2018

Catalytic Transformation of Ethanol to 1,3-Butadiene over MgO/SiO2 Catalyst

William E. Taifan
Lehigh University

Recommended Citation

Taifan, William E., "Catalytic Transformation of Ethanol to 1,3-Butadiene over MgO/SiO2 Catalyst" (2018). *Theses and Dissertations*. 4255.
https://preserve.lehigh.edu/etd/4255

Catalytic Transformation of Ethanol to 1,3-Butadiene over MgO/SiO_2 Catalyst

by

William E. Taifan

A Dissertation
Presented to the Graduate and Research Committee
of Lehigh University
in Candidacy for the Degree of
Doctor of Philosophy

in

Chemical Engineering

Lehigh University

May 2018

CERTIFICATE OF APPROVAL

Approved and recommended for acceptance as a dissertation in partial fulfillment of the requirements for the degree of Doctor of Philosophy.

Date

Dissertation Director:

Accepted Date

Dr. Jonas Baltrusaitis, Ph.D.
Advisor and Committee Chairperson
Assistant Professor of Chemical Engineering
Lehigh University

Date

Committee Members:

Dr. Israel E. Wachs, Ph.D.
G. Whitney Snyder Professor of Chemical Engineering
Lehigh University

Date

Dr. Hugo Caram, Ph.D.
Professor of Chemical Engineering
Lehigh University

Date

Dr. Nicholas C. Strandwitz, Ph.D.
Assistant Professor of Materials Science and Engineering
Lehigh University

Date

ACKNOWLEDGEMENTS

This dissertation is made possible by the experiences I have had during my graduate school, where I have had encounters with wonderful individuals that have been impactful in their own rights. I am dedicating this page to demonstrate my gratefulness for the encouragement, stimulation, and motivation that I had from these individuals.

I am eternally grateful for my family's support for my PhD endeavor. Unsurpassed love, passion, and attention from both my mother and father have been a driving force to overcome the potential (mental) barrier at difficult times during my research days. I am thankful that, if not for my father, I would not have even chosen chemical engineering as my major. I am thankful that, if not for him, I would not have pursued my doctoral degree. While my father had been the light that I follow, my mother had been my best supporters throughout my graduate study. My brother has played an instrumental part in my life, as we share a lot of secrets that are impossible to share with our parents. These secret-sharing sessions had been accompanied by advices sharing, where giving him advices had made me a more mature, better human being. I am grateful of my grandmother and grandfather for their unwavering support, and for their nagging me to find a wife for myself. Since the wife is finally here, you rest assured that your first grandson will give you some great grandchildren. I love you all, and I can never envision completing my PhD without the support from all of you.

Lehigh has not only given me an opportunity for a graduate study, instead, it has given me my life partner. The encounter we had in Taylor Gym made my dream of having a spouse with similar passion came true. If there was a little bright side of living in Lehigh, that would be you. You are my first in a lot of aspects, such as being a medical emergency contact during your surgery and taking care of your leg. Those experiences changed me as a person, for the better. I love you very much, so much that I had decided to commit a lifetime's worth of opportunities to experience all the steakhouses and sushi places in Japan and New York City.

To all of my collaborators. Tomáš Bučko (forgive me if I mistyped the accent on your name), my first ever collaborator, I can't imagine how my first ever manuscript would be possible without your help. I gained a lot of insights on DFT calculation, including few tricks to stabilize those *explosive* transition states. Dr. Yuanyuan Li and Prof. Anatoly Frenkel from Brookhaven National Lab, I'm eternally grateful for giving me a free ride on your XAS proposal to finally nail down the active sites on my catalyst. The sleepless nights we spent during Thanksgiving break (yes, during that break), finally paid off and hopefully the manusript got accepted without a lot of revisions. I'm also acknowledging Dr. Nebojsa Marinkovic, Nicholas Marcella, Amani Ebrahim, for your help in the beamline.

To my lifting dudes Tony Chang, Henry Choo, Steven Rodriguez, I'm grateful for the knowledge we share during our lifting sessions. From Candito to Sheiko, from percentages to RPE. I'm grateful for our meet together, it was a very profound experience. Powerlifting had been a part of my graduate school life. My love for this sport is a causal relationship with my research, where the former has been a therapy to the detrimental effects of the latter. I’m grateful as well that this sport has introduced me to a bunch of wonderful people, Shane Del Bianco, Johnny Luczkovich, Mark Herndon, and my coach, Samuel Bernstein. May we all be relentless in our pursuit of strength and power. May our backs arch beautifully during our bench, may we squat lower than our GPA, and may our deadlifts be three times our bodyweight.

During the early dark days of the research I have also taken solace in my friendships with great individuals at this university. With no particular order: George Xu Yan, Benjamin Moskowitz, Fan Ni, Aaron Zhang, Daniyal Kiyani, Chris Keturakis, Yoona Yang, Leah Spangler, Sagar Sourav, Chris Curran, Evan Koufos, and Lohit Sharma. My mentors from Wachs’ lab: Minghui Zhu, Soe Lwin, Jih-Mirn Jeng, and Ivan Santos. Please accept my apologies for missing your names in this list, as you see I have made efforts to include everyone’s names, but you all are very meaningful to me.

Lastly I would also like to thank the two Professors that are very influential to me during my PhD study. Professor Israel E. Wachs, for the meaningful discussion and wonderful lectures on the *operando* catalyst characterization, emphasizing the importance of under reaction condition characterization. I gained a lot of knowledge from our discussions during the lecture and about my PhD work. My adviser, Jonas Baltrusaitis, with whom I have formed a long-lasting relationship, though I’m a bit bitter that he couldn’t hood me on my graduation day. He had given me opportunities to travel and attend the biggest conferences throughout my PhD study. From him I acquired my knowledge, attitude, and mindset of a hybrid engineer-scientist. I have grown much since I first came here in terms of both personal and professional development. I am eternally grateful for your advises and guidance throughout my graduate study, as they all said, you only have one Ph.D. advisor for the rest of your life.

TABLE OF CONTENTS

CHAPTER 1 | Introduction

CHAPTER 2 | Experimental Methods

CHAPTER 3 | Computational Study of Ethanol to 1,3-BD Reaction Mechanisms

CHAPTER 4 | Combined In-situ DRIFTS and DFT study of Ethanol to 1,3-BD Reaction Mechanism over MgO/SiO2 catalysts

CHAPTER 5 | Active Sites Determination of MgO/SiO$_2$ Catalysts for Ethanol to 1,3-BD Reaction

CHAPTER 6 | Role of transition metal promoters (Cu, Zn) on MgO/SiO$_2$ catalyst for Lebedev reaction

CHAPTER 7 | Conclusions and Future Outlook

LIST OF TABLES

Chapter 1

Chapter 3

Chapter 4

Chapter 5

Chapter 6

LIST OF FIGURES

Chapter 1

Chapter 2

Chapter 3

Chapter 4

Chapter 5

Chapter 6

Abstract

Increasing concerns regarding global warming, which is caused by growing CO_2 emissions, have led to efforts focused on discovering alternatives to petroleum for energy and commodity chemical production. (Bio)ethanol has been seen as a platform molecule with increasing production and versatility for upgrading to various high-value fuels and chemicals. Among those high-value chemicals is 1,3-butadiene (1,3-BD), which has demonstrated widespread applications in polymer synthesis and as an organic chemistry intermediate. Its conventional methods of production rely on oil as a feedstock, hence suggesting the need for alternative and more sustainable routes. Interest in the catalytic conversion of ethanol to 1,3-BD, introduced in the 1940s by Lebedev, has been revived and is now focused on the development of selective catalysts, thus minimizing the need for the high cost separation between 1,3-BD and other (by)products, such as C2 and C4 olefins and oxygenates. The main components of the catalyst for this system are MgO and SiO_2, where its reactivity and selectivity depend heavily on the method of preparation. This system is still at an early stage of development, with a lot of disagreements on structure of the catalyst, optimum ratio of Mg:Si, reactive intermediates, reaction mechanisms, and kinetics.

Reaction mechanism was studied intensively using both theoretical (DFT) and experimental (spectroscopy) methods. Initial screening of the reaction mechanism using DFT with MgO defect site, i.e. kink, demonstrated that aldol condensation is more viable thermodynamically than Prins condensation. In the reaction mechanism, dehydrogenation of ethanol to acetaldehyde, an important reactive intermediate, is shown to be the rate-determining step (RDS) of the reaction. Comparison of the potential energy barrier also

shows that acetaldol, the product of acetaldehyde self-aldolisation, dehydration competes with its hydrogenation with an ethanol molecule. This mechanistic study is also supported by comprehensive *in-situ* DRIFTS. MgO/SiO_2 catalyst is synthesized using a wet-kneading method, with equivalent oxide mass ratio and thoroughly characterized with HS-LEIS, DRIFTS, and XRD. Chemical probing was also done with different probe molecules, such as pyridine, NH_3, CO_2, and methanol. Combination of several reactants and intermediate shows that acetaldehyde is spontaneously transformed to crotonaldehyde under constant reactant flow, while *in-situ* ethanol DRIFTS requires contribution from the gas-phase ethanol to make 1,3-BD. Furthermore, the crotonaldehyde does not transform to 1,3-BD under inert flow, it requires the presence of ethanol to complete the transformation to 1,3-BD.

The resulting catalyst was extensively probed and characterized, revealing a silica-rich surface, where comparison with incipient wetness impregnation catalyst shows a rather Mg-rich surface. Surface silicate that is formed is confirmed by *in-situ* DRIFTS, where new OH groups were formed. The basicity of the catalyst also varies significantly with different methods of preparation and calcination temperature. All strong, medium, and weak basic sites were found on the catalysts surface. More superior performance, however, is shown to be enforced by lower amount of strong basic sites. Ammonia probing reveals the presence of both *open* and *closed* Lewis acid sites (LAS) and limited amount of Brønsted acid sites (BAS). Pyridine, on the other hand, could not identify any BAS, which is due to its larger molecule size. This further demonstrates that the LAS on the catalyst is much more accessible than the BAS.

Promotion of the catalyst with transition metal was shown to have a significant enhancement on the reactivity. Since the RDS was determined to be the dehydrogenation of ethanol, transition metal sites lower this barrier, and shift the RDS. Zn and Cu, two very promising ethanol dehydrogenation catalysts, were separately impregnated on the uncalcined wet-kneaded MgO/SiO_2 support at low loadings, 2.5 and 1%, respectively. The catalysts were thoroughly characterized using *in-situ* UV-Vis, methanol *operando* DRIFTS, *in-situ* XANES and EXAFS, TEM, TPSR, and *in-situ* DRIFTS. Cu(II) exists as a surface species coordinated in a tetrahedral geometry, where it has 0.8 (or ~1) nearest neighbor, i.e. number of Cu-O-Cu bonds. The transition metal also possesses Cu-O-Mg bond, hinting to formation of solid solution. Similar interaction was also observed for Zn, suggesting the stronger interaction with Mg, instead of Si. This structural change affects the basicity and acidity of the catalyst. Both CO_2 and methanol probing with DRIFTS show that the promoted catalysts have less affinity with CO_2, while the BAS was eliminated, replaced with another distinct LAS. Redox capability was also modified, shown by the enhanced strength of the redox site in expense of its reduced quantity. During the reaction, Cu(II) is reduced to Cu(0) via an intermediate Cu species, before the catalyst deactivates after long hours of experiment. Zn, on the other hand, maintained its structure even after extensively tested.

Chapter 1

Introduction

1. Background

The growing environmental concerns caused by the increasing CO_2 emissions have incentivized endeavors on discovering alternatives for energy and chemical production. While potential alternatives such as wind, solar, and nuclear had been able to partially replace the need for power generation, biomass remains one the only options to mitigate the petroleum consumption in chemical production section.[1] Biomass valorization had been extensively studied, with focuses on lignin depolymerization, sugar modification, and hemicellulose fermentation to ethanol.[2,3] The target molecules varied from aromatics, alcohols, to new molecules that were envisioned to replace the incumbent from petroleum.[2] While the fight for biomass upgrading is still far from over, (bio)ethanol has presented a very interesting alternative, due to its abundance[3] and its versatility to be upgraded to different other higher-valued platform molecules or commodity chemicals. **Figure 1.1** shows the ever-increasing production of ethanol and its upgradeability to different molecules.

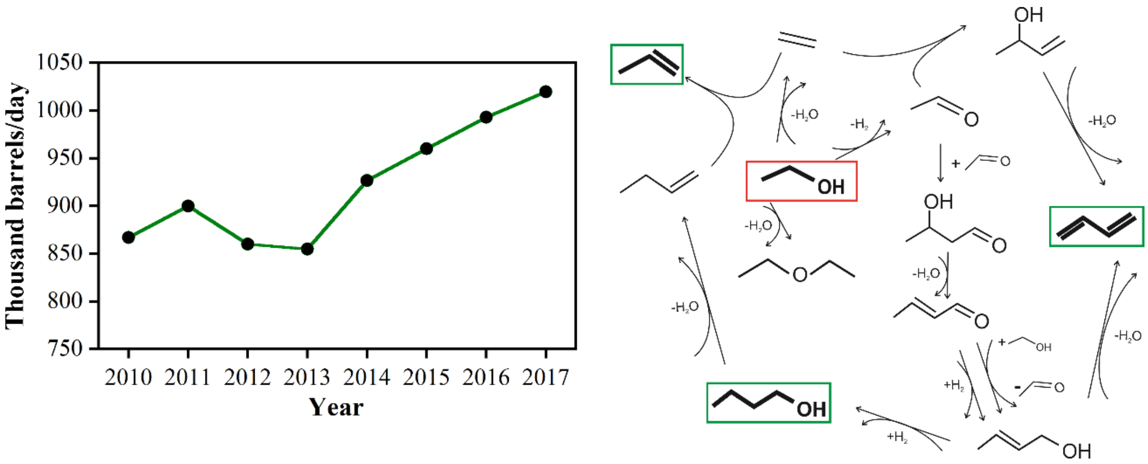

Figure 1.1. Ethanol production rate increase from 2010 to 2017 (adapted from U.S. Energy Information and Administration) (left) and ethanol upgrading map to different highly valued chemicals (right).

Ethanol upgrading to higher-valued chemicals has recently been pursued.[4,5] It is fairly reactive, and the fact that it has two carbons makes it relatively selective to even-numbered carbon containing molecules. Different target were investigated, such as hydrogen,[5–7] n-butanol,[8–13] ethylene and diethyl ether (DEE),[14–20] propylene,[21–25] isobutene,[26–28] ethylene oxide,[29,30] acetaldehyde,[31–35] ethyl acetate,[36–42] and 1,3-butadiene (1,3-BD). Steam reforming had also been explored to replace the current energy-intensive methane steam reforming processes. The ethanol to chemical processes is different from methanol to olefin, where the latter is initiated by carbon pooling mechanism, activating the surface methoxide and breaking the stable C-H bond. Most of the proposed mechanisms for ethanol upgrading involve acetaldehyde formation, which can be activated by enolate formation. This reaction itself opens a new pathway for the C-C bond formation, which is also extensively studied.[43]

Hydrogen is a very clean fuel energy source, where its application will give off water as the only product.[44] Current hydrogen production is dominated by methane steam reforming over Ni catalyst, which is also followed by water-gas shift reaction.[45] However, such reaction generally applies severe condition, 700-1100 °C, leading to the very high capital costs for its facilities.[45] Another pathway to make hydrogen is the photocatalytic process, where water is split into hydrogen and oxygen. However, charge recombination and thermodynamics stand as a major obstacle in achieving respectable yield.[46] Ethanol steam reforming, on the other hand, possesses a major advantage in the much lower reaction temperature, <600 °C, some of the processes even had reaction temperatures of 250 °C.[5–7] Partial oxidation of ethanol, i.e. autothermal reforming, is also another alternative that is being investigated, due to it being much less energy intensive than the endothermic steam reforming. Major challenge in this reaction remains the expected carbonaceous deposit on the catalyst surface, which will lead to catalyst deactivation. This carbonaceous deposit, however, can be mitigated to a certain extent by using suitable supports, such as MgO, ZnO, CeO_2, and La_2O_3.[6]

Other endeavors had been focused on valorizing ethanol into ethylene, propylene, ethylene oxide, 1,3-BD, and n-butanol, which are among the top 30 industrial organic chemicals based on weight produced in the USA.[1] Ethylene is typically produced from oil cracking, which also produces 1,3-BD as the byproduct. Popular alternative of this process has been the dehydrogenation of ethane, due to the increasing production of ethane from both shale gas and the byproduct of the paraffin from the oil cracking.[4] Ethanol dehydration was touted as a possible route for the production of bioethylene, where it has recently been made economically possible due to the recent advances in the heterogenous catalysts, as well as the lowered ethanol price.[4] The dehydration of ethanol is carried out over solid acid catalysts, such as SAPO-34,[17] γ-Al_2O_3,[14–17] and zeolites.[14,17,18] γ-Al_2O_3 is the most stable catalyst, whereas other catalysts were found to give higher ethylene yield and operate at lower temperature. Promotion with transition metals, such as Ni[17] and Mo,[18] were found to have prolonged the catalysts' life, where the latter was shown to be more of a sacrificial transition metal oxide to be reduced during the reaction.[18] Lewis acid sites (LAS) were observed to be the main site for ethanol conversion, while ethylene production was maximized by the presence of medium and weak acid sites.[16,17] Water, byproduct of the ethanol dehydration, however, plays an important role in deactivating the catalyst, since it was found to block the neighboring site, which prevents the C-H bond breaking to make the C=C bond.[19] The major challenge remains in limiting the bimolecular dehydration route to make diethyl ether, which is much more thermodynamically favored than ethanol. This can be done by using catalyst with confinement effects.[20]

Another C2 molecule that can be directly synthesized from ethanol is acetaldehyde. This molecule had traditionally been used as an intermediate that is further converted to other chemicals, mainly to acetic acid. However, this process was largely abandoned due to the more selective Monsato and Cativa processes from methanol.[47] Production of acetaldehyde from ethanol follows two routes, partial oxidation and non-oxidative dehydrogenation. The latter is becoming more attractive due to the production of hydrogen as its byproduct, even though the presence of oxygen significantly enhances the activity. Non-oxidative dehydrogenation of the catalyst was studied with different Cu catalysts, including Cu/SiO_2,[31] Cu-Cr_2O_4,[32,33] and CuO/RHA (rice husk ash).[34,35] The presence of chromium stabilized the catalyst by preventing sintering during both reduction and reaction.[32,33] Significant improvement of acetaldehyde yield was achieved when Cu was supported on rice husk ash, a silica-rich byproduct of domestic agriculture, resulting in lowered Cu particle size and high surface area catalyst.[34,35]

Related to acetaldehyde, ethyl acetate is another product of ethanol upgrading that involves the acetaldehyde as the reactive intermediate. Important catalysts that were developed are Cu-Zn-Zr-Al-O, [36–38] supported Pd catalysts,[39] Au/TiO_2,[40] and supported Cu catalysts.[41] The presence of different metals were reported to have different effects on the catalyst.[42] Zr and Al, for instance, enhanced the conversion of ethanol, with Zr favored ethyl acetate, while Al favored dehydration products such as DEE and methyl ethyl ketone (MEK). Collaborative effects of Zn and Zr were touted to limit the MEK, which is an unwanted byproduct, while Cu increased the dehydrogenation reaction, resulting in high ethyl acetate yield.[42] There is still a lot of room for improvement for this system, since the reaction mechanism is yet to be proven. Rational design of the catalysts is still far from reach, shown by the previous investigators' attempts to use various different transition metals in their catalysts.

C4 molecules that are upgraded by creating new C-C bond, such as isobutene, n-butanol, and 1,3-BD, are very attractive due to its higher value and its multiple applications. Isobutene is an important commodity chemical, in particular as an additive to jet fuel and as a raw material for various polymers. Pathway from ethanol was recognized by converting it into acetone, and further converting acetone into isobutene. The highlighted two-step reaction, however, requires basic and acidic catalysts. Bifunctional catalysts containing balanced amount of base/acid sites were synthesized at Pacific Northwest National Laboratory (PNNL).[26–28] The catalysts, possessing two different sites, were able to catalyze the two reactions in one pot, with basic and redox sites catalyzing the ethanol to acetone, while the acid sites condensing the acetone into isobutene. Detailed study of the catalysts revealed the importance and detrimental effects of Brønsted acid sites (BAS), which catalyzed the second reaction, as well as isomerizing and polymerizing isobutene into other butenes and coke.[28]

N-butanol has a lot of advantages over ethanol as a drop-in fuel. It has higher solubility in gasoline (longer chain) and significantly higher calorific value (29.2 vs 19.6 MJ/dm^3). Upgrading ethanol to n-butanol had been a focus of several research groups,[8–13] and had converged into two classes of catalysts: hydroxyapatite and hydrotalcite. N-Butanol has been traditionally produced from aldol condensation of acetaldehyde followed by the catalytic hydrogenation and from oxo process.[47] Revisiting the process is of paramount interest due to the lowered ethanol price. Just like isobutene, the catalyst needs to be bifunctional in nature. Very early attempts used combination of strong basic and acids, such as alkali cation-exchanged zeolites[48] and Na-promoted zirconia.[49] Magnesia-based catalysts present a unique class of bifunctional catalysts, in which they do not necessarily possess strong basic sites, but still provide weak acid sites. Magnesia alone was observed to give respectable n-butanol yield,[8,10] while combination with alumina gave a hydrotalcite structure, which increased the activity significantly.[50–52] More improvement was achieved by hydroxyapatite catalysts, calcium phosphate material, which was done by tuning the Ca/P ratio, as stronger basic sites were shown to increase the n-butanol yield.[53] Latest works had focused on the study of the material, where kinetic models and active sites were determined using combination of several methods, such as SSITKA and *in-situ* titration with probe molecules.[12,13]

Among all of the higher-valued target molecules, 1,3-BD represents the most interesting target molecule. Back in the 1940s, both the US and the USSR produced 1,3-BD from ethanol via two-step[54,55] and one-step processes,[56] respectively. In the two-step process, ethanol was first converted into acetaldehyde before the product and a separate ethanol feed were flowed to a second reactor containing a supported tantalum oxide catalyst.[54,55] The one-step process, however, incorporated all reactions in one-pot, using a catalyst that was revealed to have both magnesia and silica.[56] The process was abandoned when catalytic cracking of oil became popular, since 1,3-BD were produced efficiently as a byproduct of ethylene production. However, in the recent year, the shift of raw material for ethylene production from oil to shale gas had decreased the availability of 1,3-BD, prompting the revisiting of this old process. Improving the catalyst's activity and stability had been the main focus of the research, where new systems had also been established, such as promoted MgO/SiO_2,[57–60] and solid Lewis acid catalyst systems.[61,62]

This chapter provides a review of ethanol to 1,3-BD (ETB) reaction system. This review includes proposed reaction mechanisms, current state-of-the-art of the catalysts, and the proposed active sites. Following the review, this chapter will discuss the techniques that were used to study the system, as well as an outline of the thesis.

1.1. ETB Reaction Network

1.1.1. Reaction Intermediates and Byproducts

As shown in Figure 1.1, ethanol can be converted to a variety of other chemicals. Optimizing ethanol to 1,3-BD requires analysis of thermodynamics to select the reaction temperature and contact time, i.e. space velocity. Byproducts that are most commonly found during the reactions are ethylene, CO_2 and acetaldehyde.[63] Other byproducts that were occasionally observed are diethyl ether, butenes, propylene, C2-C4 paraffins, diols, acetone higher alcohols and heavy oxygenates, such as n-butanol, n-hexanol, crotonaldehyde, and hexadienal.[58,64] Dictation by thermodynamics also depends on the catalysts employed. At different reaction temperature, acid catalysts, such as γ-Al_2O_3,[65] will give different product distributions from transition metal catalysts, such as CuO/SiO_2.[35]

Optimizing the performance of the catalyst also means suppressing the formation of unwanted byproducts, such as butenes, ethylene, and acetaldehyde. Butenes are particularly unwanted, since at high concentration, they will form azeotrope with 1,3-BD, which makes separation costly.[60] Ethylene, on the other hand, is of much lower-value, and its formation is followed by the production of water, which was found to poison the catalyst by competitive adsorption.[19] Another byproduct of this system is acetaldehyde, shown to be a reactive intermediate during the reaction, which will be explained in subsequent subchapters. Thermodynamics also determines the selectivity between acetaldehyde and ethylene, since ethanol dehydrogenation was found to be much more endergonic reaction than ethanol dehydration.[66] Furthermore, the reactivity of acetaldehyde to undergo further reactions, such as polymerization, esterification, and aldol condensation, requires a careful design of the catalyst to minimize the unwanted reactions.[63,67]

1.1.2. Proposed Reaction Mechanisms

Various byproducts produced during the reaction led to different reaction mechanisms being proposed. In general, there had been five proposed reaction mechanisms. The first two mechanisms, proposed by Lebedev[4,56] and Ostromislensky[68,69] were ruled out due to the improbable steps in their mechanisms. Briefly, Lebedev proposed a reaction mechanism involving free radicals in a very complex sequence, while Ostromislensky's mechanism entailed reaction between ethanol and acetaldehyde, which is followed by rearrangement of the hemiacetal to diols. **Equation 1.1** shows the stoichiometry of the reaction:

$$2\ C_2H_5OH \rightarrow C_4H_6 + 2\ H_2O + H_2 \tag{1.1}$$

Subsequently, Toussaint, *et al.* proposed reaction mechanism which involved dehydrogenation of ethanol to acetaldehyde, followed by aldol condensation of two acetaldehyde molecules, and dehydration of the aldol to give crotonaldehyde, which would further undergo Meerwein-Ponndorf-Verley (MPV) reduction with ethanol and dehydration to give 1,3-BD.[55] Other reaction mechanisms that had been proposed were called Prins condensation, proposed by Gruver, *et al.*,[70] and carbanion mechanism, very recently proposed by Chieregato, *et al.*[71] **Figure 1.2** comprehends the proposed reaction mechanisms by Toussaint, *et al.*, Gruver, *et al.* and Chieregato, *et al.*

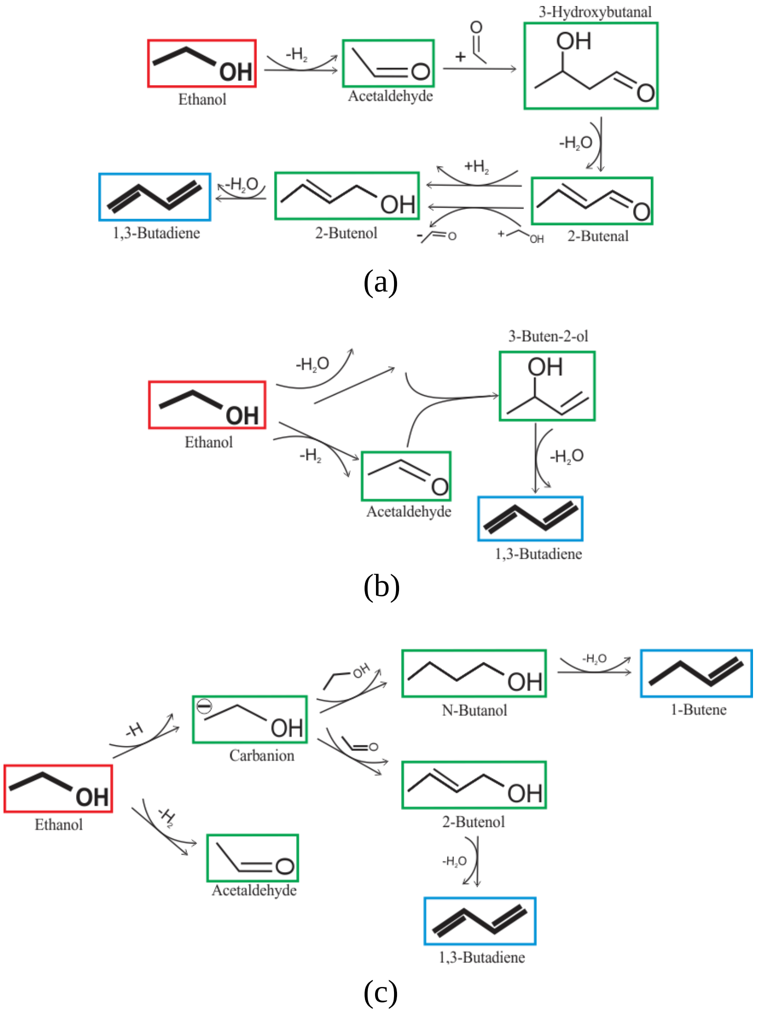

Figure 1.2. Proposed reaction mechanisms for ethanol conversion to 1,3-BD: (a) Toussaint’s aldol condensation; (b) Gruver’s Prins condensation; (c) Cavani’s carbanion mechanism.

The reaction mechanism proposed by Toussaint had been touted as the generally accepted mechanism.[4,5,72,73] Aldol condensation and the subsequent dehydration steps were reported to be facile, while the rate of ethanol dehydrogenation and MPV reduction step of crotonaldehyde depends on the catalyst. Over MgO/SiO_2 catalysts, for instance, the rate-determining step was ethanol dehydrogenation,[66] while for Lewis acid catalysts, MPV reduction of crotonaldehyde with ethanol as the hydrogen source was thought to be the rate-limiting step.[72] There are still, however, several issues with the mechanism, including the very rare occurrences of the reactive intermediates mentioned.[71] Furthermore, acetaldol was also shown to decompose to two acetaldehyde molecules when introduced to Ta/SiO_2 catalyst.[55] The very rare occurrence of the reactive intermediates was due to the rapid reaction steps at the mostly employed reaction temperature. Second, acetaldol is a very unstable molecule, it could either dehydrate to crotonaldehyde and water when heated, and therefore, data analysis of the reaction should be carried out with extra caution.

The other rejected mechanism is the Prins mechanism, where ethanol undergoes two parallel reactions, i.e. dehydrogenation to acetaldehyde and dehydration to ethylene.[70] The problem with this mechanism is the ethylene protonation, an indispensable step during the Prins mechanism, that leads to a highly unstable carbocation,[4] and when this step was not involved, the coadsorption of both ethylene and acetaldehyde on the surface is very unstable.[66] An alternative mechanism was proposed by Chieregato, *et al.*, where ethanol dehydrogenation resulted in two different entities.[71] If the step was preceded by dissociative adsorption, ethanol would be converted to acetaldehyde. Otherwise, a physisorbed ethanol molecule would break a C-H bond and be converted to a stabilized carbanion.[71] This carbanion would further react with acetaldehyde to make 1,3-BD or with ethanol to make n-butanol and 1-butene. Several issues were readily identified with this mechanism. First issue was the use of bare MgO as the catalyst, which, if not hydrothermally treated, would not give off 1,3-BD.[71] Second, our attempts of using bare MgO as the catalyst for Diffuse Reflectance Infrared Fourier Transformed Spectroscopy (DRIFTS) study did not show any formation of the surface intermediates that were demonstrated by their reports.[63] Bare MgO exhibits very high absorption of CO_2, which would hamper identification of the surface intermediates that are located at similar wavenumber ranges. Third, the experiment was carried out under inert flow, and due to the nature of the cascade reaction, the amount of ethanol would be insufficient to convert further into 1,3-BD, given all the ethanol will be consumed to acetaldehyde. Furthermore, the peak fittings were done with solely focusing on the intermediates, without considering the possibility of the side reactions of acetaldehyde, such as acetate formation, aldol condensation, and polymerization. Finally, the model used in the density functional study (DFT) study did not necessarily represent the true condition of the surface. The DFT calculation was done on a cluster MgO, with a small number of atoms used to represent the catalyst. Stability calculation was not done either in choosing the right defect site, with corner MgO being the model site. Later attempt by our group demonstrated that the postulated carbanion formation does not take place when C-H bond is broken, instead, the resulting TS further broke the C-O bond to give-off ethylene, which disputed their proposed mechanism.[66]

1.2. Catalytic Systems

There had been a lot of efforts to improve the catalytic performance of the catalysts for the synthesis of 1,3-BD from ethanol.[72,73] As mentioned previously, apart from the use of MgO/SiO_2-based catalysts,[57,74–77] efforts had been carried out for other classes of catalysts, such as zirconia-based catalysts,[61,78] and mixed metal oxide catalysts.[79–83] The complex reaction mechanism calls for a very demanding catalyst specification; the catalysts have to possess balanced amount of basic, acidic, and redox sites. Typically, there are several ways to improve the catalysts' performance, by promotion with other metal oxides, hydrothermal or chemical post-synthesis treatment, and modification of the preparation methods. This section will thoroughly discuss the current state-of-the-art of the catalytic system.

1.2.1. Reaction Conditions and Catalytic Performance

1,3-BD had been the most realistic target molecule for ethanol upgrading, mainly due to the abundance in ethanol supply and decline in 1,3-BD supply.[60,84] Once a competitive process, the catalytic cracking of petroleum feed had taken over the production method, which in turn, demanded the green chemistry process to be a lot more efficient. For the process to be competitive, there are several factors that have to be considered. Among of these factors, 1,3-BD productivity and catalyst stability are the most important factors. The minimum requirement for 1,3-BD productivity was suggested to be 0.15 g_{BD} g_{cat}^{-1} h^{-1},[83] while the catalyst needs to be stable for long hours of production, since catalyst regeneration can also be very costly. Deactivation typically was due to coke deposition on the catalyst, coupled with poisoning from water formed by the dehydration reaction.

Another factor that also plays important role is the reaction temperature, where typically, the reaction takes place at 300 and 400 °C for low weight-hourly space velocity (WHSV) of 0.2-1 h^{-1}. The optimum reaction condition itself varied due to the nature of different catalysts employed. For instance, unpromoted MgO/SiO_2 catalysts typically require higher operating temperature than promoted MgO/SiO_2 catalysts, due to the higher activation temperature for ethanol dehydrogenation to acetaldehyde.[58,59] Other relevant conditions are pressure and WHSV, which is essentially a unit to define catalyst to reactant ratio. The reaction had been carried out under atmospheric pressure in a fixed bed reactor, with the exception from Bhattacharyya, *et al.*, who have used fluidized-bed reactor.[85] Additional consideration is the ethanol to acetaldehyde ratio in reactant feed. This parameter is also important for one-step process, since it will be favorable to recycle some of the acetaldehyde back to the reactor. **Table 1.1** shows the catalytic performances of recently investigated catalysts.

Table 1.1 Catalytic performance of different catalysts studied for one-step ethanol to 1,3-BD conversion. [a] Contact (residence) time; WHSV (weighted-hourly space velocity); TOS (time-on-stream); X (ethanol conversion), Y (yield); P (productivity)

No	Catalyst	T (°C)	WHSV (h^{-1})	TOS (h)	X (%)	Y_{BD} (%)	P_{BD} (g_{BD} g_{cat}^{-1} h^{-1})	Ref.
				MgO/SiO2 catalysts				
1	MgO hydrothermally-treated	400	0.2	7.0	36.6	17.2	0.02	86
2	WK $MgO-SiO_2$ (1:1)	425	1.1	4.0	52.0	17.7	0.23	58
3	MC $MgO-SiO_2$ (1:1)	400	1.2	3.3	10.0	3.6	0.02	59
4	SG $MgO-SiO_2$ (4:1)	400	0.4 s[a]	N/A	53.0	14.6	N/A	87
5	WK $MgO-SiO_2$ (1:1)	400	0.1	3.0	65.9	32.5	0.19	88
6	MC $MgO-SiO_2$ (1:1)	400	1.0	N/A	41.2	23.6	0.14	89
7	IWI $MgO-SiO_2$ (1:1)	300	1.1	3.3	~3.5	~1	0.01	60
8	WK $MgO-SiO_2$ (13:7)	450	4.1	1.0	95.0	73.2	1.15	77
9	1% $CuO/MgO-SiO_2$	425	1.1	4.0	74.0	36.3	0.48	58
10	2% $Ag/MgO-SiO_2$	400	1.2	3.3	50.0	20.5	0.15	59
11	5%$Ga/MgO-SiO_2$ (1:1)	400	0.1	3.0	98.8	52.4	0.31	88
12	2% $Zn/MgO-SiO_2$	425	1.0	3.0	84.6	45.0	0.26	57
13	0.1% $Na/MgO-SiO_2$	350	0.2	N/A	100.0	87.0	0.08	90
14	1.2% Zn/Talc	400	8.4	7.0	41.6	21.3	1.06	86
15	3% $Au/MgO-SiO_2$ (1:1)	300	1.1	3.3	45.0	27.0	0.14	60
16	1.5% Zr 1% $Zn/MgO-SiO_2$ (1:1)	375	0.6	3.0	40.0	30.4	0.13	91
17	1.2% $K/ZrZn/MgO-SiO_2$ (1:1)	375	0.6	3.0	26.0	27.1	0.12	91
				Zr/SiO2 catalysts				
1	2% Ag/4% Zr/SiO_2	320	0.31	5.0	55.2	39.4	0.07	62
2	1% Ag/Zr/BEA (Si/Zr=263)	320	0.64	3.0	30.1	19.2	0.07	61
3	3.5% Ag/Zr/BEA	320	1.2-3	3.0	-	-	0.59	92
4	2000 ppm Na $Zn_1Zr_{10}O_n$	350	6.2	30.0	54.4	14.1	0.49	93
5	2% ZnO/7% La_2O_3/1% ZrO_2/SiO_2	400	2	N/A	100.0	60.2	0.71	94
				Other catalysts				
1	3% Hf/9.3% Zn/HM	360	0.64	10.0	98.6	68.4	0.26	79
2	1% Cu/1% Ta/SiBEA (Si/Al=1300)	325	0.5	3.5	87.9	63.9	0.19	95

1.2.2. MgO/SiO_2 Catalysts

The original catalyst employed by Lebedev in his one-step process was disclosed by Natta and Rigamonti to contain MgO and SiO_2.[96] MgO by itself is a very strong basic catalyst,[97,98] and its interaction with SiO_2 were suggested to have formed distinct LAS, making it a bifunctional catalyst.[99] Furthermore, the defect sites of MgO are essentially a very strong electron acceptor, making it a very strong Lewis acid-base pair.[66] Proper amount of acid-base sites was determined by changing the MgO to SiO_2 ratio[75,77,87,99] and by different preparation methods.[60,99,100] A contradicting result, however, was recently reported by Baba, *et al.*, where a bare MgO that was hydrothermally treated resulted in a conversion of 36% and 1,3-BD selectivity of 47%.[86] This MgO was reported to have a very distinct showed that SiO_2 presence was not indispensable to the catalyst.

The main issue with the catalyst system is that it is highly influenced by the Mg to Si ratio and preparation methods. Discrepancies can be found on every considered parameters, including the Mg to Si ratio and which preparation methods that yielded the best performing catalysts. For instance, wet-kneading (WK),[58,99] incipient-wetness impregnation (IWI),[60] mechanical mixing,[59,89] sol-gel,[87] and hydrothermal synthesis,[86] were each reported as the best preparation method. Reports for optimum Mg to Si ratio also contained a lot of disagreements, even for the same preparation method. For sol-gel catalyst this parameter was reported to be between 9 to 15,[87] both 1:1[89] and 2:1[59] for dry milling, and 1:1[58,99] (17:3)[75] for wet-kneading. In the case of promotion with transition metals, the order of promoters impregnation and calcination also altered the activity.[57,58,60]

Works on unpromoted MgO/SiO_2 catalysts mainly concerned the method of preparation and oxide ratio. Wet-kneading method had been reported as the best preparation method.[58,77,99] Wet-kneading was defined as "a process in which two or more solid precursor materials are combined and stirred (mechanically or magnetically) thoroughly in a liquid medium."[76,101] This method was first used by Natta in 1947,[101] and maintained its relevance through the work of Niiyama, *et al.*,[75] Ohnishi, *et al.*,[90] Kvisle, *et al.*,[99] and Angelici, *et al*.[76] The wet-kneading was typically done with either MgO[102] or $Mg(OH)_2$[58,90] as the starting material, and typically in water, since other solvent, such as ethanol, had exhibited unwanted effect.[101]

Study by Weckhuysen's group showed that wet-kneading method is superior to co-precipitation and mechanical mixing.[58] Wet-kneading method resulted in 1,3-BD yield of ~17%, significantly higher than co-precipitated catalysts (~8%) and mechanically mixed catalyst (<1%), with 24 h time-on-stream (TOS). Co-precipitated catalyst produced significantly higher amount of ethylene, attributed to its higher ethylene selectivity. On the other hand, wet-kneading resulted in a layered magnesium silicate phase, which was correlated to the higher activity of the catalyst.[76] A detailed acid-base characterization using Hammett indicator, DRIFTS with probe molecules, and TPD further produced certain criteria for a good catalyst.[100] In particular, strong basic sites have to be limited, with participation of mostly medium and weak basic sites, in combination with some Lewis acidity. Co-precipitated catalyst possessed combination of both strong acid-base sites, which are shown to have increased the generation of ethylene.[100]

Mechanical mixing (dry milling) with different silica materials were studied by Jannsens, *et al.*[59] Two ordered mesoporous materials (COK-12 and MCM-41) were used along with amorphous mesoporous SiO_2. MgO was first hydrated to form $Mg(OH)_2$, which was followed by dry milling with the SiO_2 material. The resulting dry mixture was then wetted with water before being dried and calcined. The wetting process appeared to have a significant effect on the acidity-basicity of the catalyst. This process dispersed MgO, further creating additional Lewis acid-base sites.[59] Characterization of the catalyst showed silica support covered by magnesia flakes in the case of SiO_2. The other silica supports, i.e. COK-12 and MCM-41, showed a loss of mesoporous structure when mixed with magnesia with this preparation method. These catalysts did not show significant activity toward 1,3-BD, with the MgO/COK-12 and MgO/MCM-41 being the worst catalyst due to their collapsed structure. The diffusion of MgO into the lattice was suggested to limit access of reactant to the active sites, which was also aggravated by the presence of large magnesium silicate phases.[59]

Sol-gel was another explored preparation method.[87] Starting from Mg/Si oxide ratio of 2 up to 9, significant fosterite, a magnesium silicate, phase was identified using X-ray diffraction (XRD) and attenuated total reflectance infrared spectroscopy (ATR-IR). This fosterite phase, however, was detrimental to the process, since it possessed more acid sites, leading to an enhanced ethylene yield. High amount of Mg, i.e. Mg/Si > 15 accumulated the alkenol intermediate, due to the limited amount of acid sites. The best performing catalysts exhibited combination of a limited number medium-strength acid sites with strong basic properties, which contradicted Weckhuysen's finding.[87,100] The LAS, however, was observed to be transformed into BAS when water was formed as the byproduct.

MgO/SiO_2 with various MgO loading was synthesized using IWI method.[60] For loading between 10-80%, a magnesium silicate hydrate (MSH) phase was observed at ~50% loading. Higher loading at 80% showed a crystalline MgO phase, presumably formed by excessive MgO formation covering SiO_2. ^{29}Si magic-angle spinning (MAS)

NMR spectroscopy showed that at lower loading at 10 and 30% MgO, SiO_2 still retaine its support characteristics, where Mg^{2+} cations mainly interact with the isolated silanol groups. The Q3 feature was caused by silanol groups [$Si^*(OSi)_3(OH)$] and [$Si^*(OSi)_4$]. However, at higher loading, new peaks associated with [$Si^*(OMg)(OSi)_3$], [$Si^*(OMg)(OSi)_2(OH)$], and [$Si^*(OMg)_2(OSi)_2$] were formed. As expected, higher MgO loading increased the basicity of the catalyst, demonstrated by CO_2 DRIFTS. The reactivity study showed that higher loading significantly reduced the catalyst's conversion while increasing selectivity toward both acetaldehyde and 1,3-BD. The high silanol content for lower loading was suggested to be responsible for ethanol dehydration at lower loading.

Other unpromoted MgO/SiO_2 systems that have been studied are clay materials and talc.[86,103,104] Without promotion with transition metal oxides, clay, a naturally occurring magnesium silicate mineral, favored dehydration of ethanol to produce ethylene.[103,104] Talc is a 1:2 layered structure, where a unit cell includes six octahedral sites and eight tetrahedral sites. Mg^{2+} ions represent the former, while cations for the latter are Si^{4+}. Significant improvement of these magnesium silicate materials was attained by promotion with different transition metal catalysts. Nickel,[104] manganese,[103] and zinc[86,105] were all incorporated into the catalyst to achieve higher conversion. Characterization of Zn/talc carried out using ICP, XRD, and XPS suggested that Zn was incorporated into the lattice. The Zn site in the catalyst was shown to be responsible for the enhanced ethanol dehydrogenation step, which increases the overall 1,3-BD yield.[86]

Promotion using other metal oxides were very commonly done to improve 1,3-BD activity. Mainly, this was done to add redox sites to the catalysts and hence, to reduce the energetic barrier of the rate-limiting step. Larina, et al. published a study on the role of

ZnO as a promoter for magnesia/silica catalyst on the ethanol conversion to 1,3-BD.[57] The amount of both Lewis and BAS were investigated using pyridine adsorption spectroscopy. The experiment revealed that there are two types of LAS in the catalyst, one in MgO-SiO_2 contact phase and one in ZnO-SiO_2. When tested over MgO single oxide, the formation of 1-butanol was preferred, indicating the necessity of both acidic and basic sites in the catalysts. However, the excessive silica content would lead to the preferential formation of ethylene, since the number of acid sites would significantly be increased. Catalytic testing conducted demonstrated the enhanced yield of 1,3-BD attributed to the ZnO role in catalyzing dehydrogenation of ethanol as the first step of the reaction. The author postulated this step to be the rate-determining step for the complete mechanism [57].

Other transition metal oxides have also been used in the past to improve the MgO/SiO_2 catalysts' performance. Angelici thoroughly studied 1%CuO/MgO/SiO_2 catalysts, where they saw an enhanced improvement, with Cu^0 as the active sites suggested by *operando* X-ray absorption near edge structure (XANES) spectroscopy.[106] Deposition-precipitation (DP) of Au onto MgO/SiO_2 catalyst also saw significant increase in the MgO/SiO_2 catalyst.[60] DP of AuCl-based precursor surprisingly completely transformed the bulk MgO into MSH phase. This phenomenon was attributed to the Cl^- effect from the Cl^- ion produced from the precursor's hydrolysis, since acetate precursor did not transform the MgO into MSH. *In-situ* titration experiment with propionic acid, a very weak acid, showed that 1,3-BD production considerably decreased, and did not recover when propionic acid was not fed anymore. The dehydrogenation reaction to acetaldehyde recovered, however, indicating the presence of weak basic sites to catalyze dehydrogenation and strong basic sites to catalyze the subsequent reactions.[60] Another transition metals that were used to improve 1,3-BD yield is Ag.[59] Silver was dispersed on silica phase when impregnated over calcined MgO/SiO_2 catalyst, as shown by ambient SEM and EDS analysis. Synergistic effect was observed, where Ag catalyzed the dehydrogenation of ethanol, while $MgO\text{-}SiO_2$ phase catalyzed the subsequent reactions. However, increase in Ag loadings seemed to have created aggregated, larger Ag particles, which in turn deactivated the catalyst.[59]

Other types of metals had been used as well as promoters. Ohnishi, *et al.*, for instance, prepared three $MgO\text{-}SiO_2\text{-}Na_2O$ and $MgO\text{-}SiO_2\text{-}K_2O$ by impregnating aqueous NaOH and KOH with $MgO\text{-}SiO_2$ catalysts prepared from different raw materials using different methods.[90] They found out that the (0.01%) Na_2O promoted magnesia-silica catalyst prepared from ethyl orthosilicate and magnesium nitrate (1:1) by wet-kneading produced the highest catalytic activity (100%) and selectivity (87%) for formation of 1,3-BD at 350 ºC for the one-step process.[90] The origin of this alkali metal promotion, however, is not known since there was no characterization reported on how Na and K is coordinated to the surface. Zirconia, another class of catalyst that will be discussed below, is another non-redox promoting metal that was used to improve 1,3-BD formation.[91] Jones, *et al.* found that IWI over an uncalcined MgO/SiO_2 gives a higher surface area, since there were more OH groups to interact with the promoter. Zn itself improved the dehydrogenation reaction but lagged the aldol condensation, demonstrated by accumulation of acetaldehyde in the product stream. Co-promotion with zirconia, another solid Lewis acid, was shown to significantly improve this, since it further provided additional aldol sites on top of the support's native sites. The authors suggested that both ZnO and ZrO_x were more readily dispersed over Mg-O-Si linkages, and coprecipitation method was shown to generate more of this linkage, as shown by ^{29}Si MAS NMR. Furthermore, $CHCl_3$ and NH_3 DRIFTS experiments suggested that post-treatment of the catalyst with alkali metals, such as Na, Li, and K, poisoned the stronger acid sites, without introducing strong basic sites. This poisoning effect significantly removed ethylene from byproduct, and therefore opening possibilities of recycling the product back to the system.[91]

1.2.3. ZrO_x –based Catalysts

Study on ethanol to 1,3-BD over ZrO_x-based catalysts had been extensively studied recently. Toussaint, *et al.*,[55] Jones, *et al.*,[78] and Ivanova, *et al.*,[62] screened a number of different Lewis acid catalysts that would work on aldol condensation and MPV reduction. The Lewis acid material can then be combined with redox metal catalyst that would improve the conversion of the dehydrogenation of ethanol. Jones, *et al.* suggested the use of ZnO and ZrO_x,[78] while Ivanova, *et al.* identified AgO/ZrO_x as the most active catalyst.[62]

The complete reaction network for the catalytic conversion of ethanol into 1,3-BD over metal-containing (M=Ag, Cu, Ni) oxide catalysts (MO_x=MgO, ZrO_2, Nb_2O_5, TiO_2, Al_2O_3) supported on silica was investigated by Sushkevich, *et al.*[62] From the reaction network above, these authors narrowed down their catalyst selection to target the dehydrogenation of ethanol, aldol condensation of acetaldehyde, and MPV-reduction of the crotonaldehyde. Their experiments demonstrated the superior Ag and Cu-promoted catalysts over Ni-promoted. Nb and Al-based oxide catalysts developed higher selectivity toward ethylene due to the BAS, while magnesia and titania oxide catalysts were prominent in catalyzing aldol condensation. The best performing catalyst was found out to be 1% Ag/10%ZrO_2 on silica reaching 88% conversion and 74% yield of 1,3-BD at 593 K, with WHSV of 0.04 g g^{-1} h^{-1} and time on stream (TOS) of 5 hours.[62]

Optimization of the Ag/ZrO_x catalysts was subsequently done by fine-tuning the composition of both Zn and Zr.[61] Catalysts employed were ZrBEA zeolites with various Zr/Si ratios and zirconia supported on silica, all promoted with silver. Characterization of the acid sites of the catalysts was conducted by FTIR spectra of deuterated acetonitrile. The silanol group of the catalysts contributed to the high number or the BAS, giving peaks at 2275 cm^{-1} that readily disappeared upon evacuation, pointing to the weak interaction of the OH group. The LAS were also determined using the same technique, particularly by looking at the band centered at 2303 cm^{-1}. The number of LAS apparently played significant role in determining which reaction pathways to take place; catalyst with the highest yield turned out to be the one with the highest LAS. The best catalyst performance was observed for Ag-promoted ZrBEA (Si/Zr = 100), with 1,3-BD selectivity of 56% and conversion of 48% under the following conditions: T = 593 K, WHSV = 0.32 g g^{-1} h^{-1}, observed after TOS = 3 h.[61]

DFT calculation, in combination with CO-DRIFTS study, elucidated the nature of the LAS on the catalyst.[107] Two active sites, open and closed isolated LAS, were shown to be available on the surface. The open site, where there is one terminal hydroxyl group coordinated to Zr (HO-Zr-$(OSi)_3$), was found to be the main catalytic active sites.[107] Over series of synthesized catalyst, direct correlation was made between the 1,3-BD productivity and the relative amount of open LAS. The reaction mechanism over this catalyst was further probed using combination of SSITKA and isotope labeling.[108] As expected, two sites were available for the reaction, the silver sites that were responsible for ethanol dehydrogenation, and Zr LAS that catalyzed the subsequent aldol and MPV reactions. Deuterated ethanol CH_3CD_2OH and CH_3CH_2OD showed that ethanol dissociatively adsorbed on silanol site, followed by C-H bond breaking over Ag/Si-OH site. The resulting acetaldehyde was then desorbed from the surface.[109] Enolization of acetaldehyde was made possible by Zr LAS and Zr-O pair sites, and reaction with vapor-phase acetaldehyde molecule was carried out according to Eley-Rideal mechanism. Facile dehydration of acetaldol then followed, where crotonaldehyde was produced. MPV reduction by ethanol was then determined to follow the Langmuir-Hinshelwood mechanism by fitting of kinetic data.[108]

Combination of Zn and Zr for ETB reaction had also been explored.[93,110] Similar to previously published endeavors, Zn/Zr mixed oxides were used. From IR-pyridine probing experiment, it was found that the acidity of the catalyst as a function of Zn/Zr ratio had a maximum at Zn/Zr = 1:10. The use of Na as a promoter to control the surface acid-base properties was confirmed by NH_3-TPD and IR-Py as well. When 2000 ppm if Na was used as a promoter, the balanced basic sites and weak BAS exhibited selectivity of 47% at 97% conversion, with higher productivity per grams of catalyst. Another alkali metal oxide, cesium oxide, was studied as well as a promoter that eliminates acid sites and reduces ethylene formation.[110] The similarity between Zn/Zr and Ag/Zr catalysts suggested similar reaction mechanism and active sites. Zn/Zr catalysts, however, required a third promoter in the form of very small amount of alkali metal to eliminate the acidity it provided, unlike Ag/Zr catalyst, which did not provide improved Lewis acidity.[107]

1.2.4. Other Catalysts

This subsection will discuss other metal oxide catalysts that had been used/investigated in the past. Discussion will cover some of the catalysts that have similar characteristics with Zn(Ag)/Zr catalyst, i.e. Lewis acid combined with dehydrogenation catalysts, such Hf-based catalyst[79] and Ta-based catalyst.[82,95] Due to the extensive work carried out by Sushkevich and Ivanova, Zr-based catalysts were classified as a different class of catalyst.[43,61,62,107–109]

Bhattacharyya and Ganguly performed one-step catalytic conversion of ethanol to 1,3-BD in a fixed bed reactor on various single oxide catalysts of aluminum, thorium, magnesium, iron (III), and zirconium.[111] The maximum process yield of 1,3-BD was achieved at 36.1% using thorium oxide prepared from thorium nitrate and ammonia carbonate with flow rate at 1.256 mL/g h^{-1} at 450 ºC. All metal oxides were selected based on their capabilities of catalyzing both dehydration and dehydrogenation reactions.[111] Few years later, Bhattacharyya and Avasthi conducted exhaustive experiments on the conversion of ethanol to 1,3-BD via the one-step process on single alumina oxide and binary alumina-zinc/calcium/chromium/magnesium oxide catalysts. They reported maximum yield of 72.8% on a fluidized bed reactor using the binary alumina-zinc oxide catalyst (60:40) as opposed to 55.8% yield on a fixed bed reactor at 425 ºC.[85]

Work on hafnium oxide catalyst, promoted with Cu and Zn as dehydrogenation promoter, was done by Baerdemaeker, *et al.*[79] Building on Jones' catalyst screening,[78] slight modification was performed to understand which element contribute to which step of the mechanisms. Switching the precursors from nitrate to chloride already contributed in higher 1,3-BD selectivity, stability, and lower ethylene selectivity. Replacing zirconium with hafnium, a softer material but still in the same group as Zr, suppressed the formation of ethylene more significantly. Their study also revealed Zn's superiority in catalyzing dehydrogenation of ethanol, since when Zn single oxide was used, acetaldehyde accumulated without significant formation of 1,3-BD. It was inferred that, the addition of Hf suppressed ethanol dehydration, while also promoted the C-C coupling step, i.e. aldol condensation.

Tantalum oxide, a rare transition metal material, was among the first catalysts used to catalyze the reaction in the two-step process.[68,81] Its use had been revisited following the renewed interest in the Lebedev process.[82,95,112–114] Kyriienko, *et al.*, synthesized a TaSiBEA zeolite material by dealuminating the starting AlSiBEA with HNO_3, followed by the introduction of tantalum into the framework. [95] The tantalum itself was present as isolated mononuclear in the framework, as confirmed by UV-Vis and XRD. The catalyst was further promoted with Ag, Cu, or Zn to introduce dehydrogenation sites. UV-Vis characterization suggested that Ag was present as Ag(I) and oxidized silver cluster, Cu was available as isolated mononuclear and oxidized cluster, while Zn was suggested to be in the framework and as a polynuclear zinc oxide in the extra-framework position.[95] Incorporation of Cu and Zn is suggested by pyridine DRIFTS to give higher amount of LAS, as compared to Ag promotion, while ZnO incorporation exhibited higher BAS content in the catalyst than the rest. Further deuterated chloroform DRIFTS also suggested that incorporation of the transition metals into the TaSiBEA catalysts had eliminated medium strength basic sites, replacing them with weaker ones.[95] Mechanistic study for Ta-SiBEA catalyst,[82] and subsequently on Ag-Zr-BEA,[114] was done by Müller, *et al*.[82,114] *Operando* modulated DRIFTS-MS was used to control the ratio of ethanol to acetaldehyde, maintaining sufficient ethoxy coverage to keep replenishing acetaldehyde formation by both dehydrogenation and MPV reduction.[114] The presence of Ag was reduced nanoparticles enabled reduction of crotonaldehyde in two possible mechanisms, direct hydrogenation by hydrogen molecule under low ethanol pressure, and MPV reduction under high ethanol pressure.[114]

2. Approach

2.1. Approach

The recent emergence of combined dehydrogenating/Lewis acid catalysts has opened an alternative for the Lebedev's process. Despite this, the traditional MgO/SiO_2 catalysts are still very interesting, due to the lack of suitable characterization methods. Mg to Si ratio and other synthesis parameters for the available preparation methods are the most enticing part of the research. Additionally, the catalytic system is still not well-understood, despite attempts to characterize the system. This is mainly due to the nature of the catalyst itself that limits the use of several *in-situ (operando)* spectroscopic methods. In this study, MgO/SiO_2 catalysts were used as the investigated catalysts, where reaction mechanisms, role of promoters, and catalyst characterization are integral parts of this dissertation. The approach taken to achieve these objectives consisted of the following steps:

1. Perform DFT calculation as a preliminary study on proposed reaction mechanisms over an ideal model MgO surface.
2. Synthesize MgO/SiO_2 catalyst with wet-kneading method, fixing Mg to Si ratio to 1 with varying calcination temperature at 500 and 800 °C.
3. Perform reactivity study and reaction mechanism study, both surface and vapor-phase intermediates.

4. Intensively characterize the catalyst using probe molecules and *in-situ* spectroscopy, correlate the catalytic active sites with activity and selectivity.
5. Promote the MgO/SiO_2 catalyst with transition metal (Cu and Zn), characterize the system, and investigate the catalytic consequences.

DFT calculation was performed using VASP software package, with MgO (100) surface termination chosen as the model catalyst. Specifically, a kink site, $Mg^{2+}{}_{3C}\,O^{2-}{}_{4C}$ pair were chosen as the active site, since defects had been suggested to have a very high catalytic activities.[115] This first approximation simplified the current state-of-the-art, where Lewis acidity and basicity were represented by the lower coordinated ionic pairs on the surface. In reality, the Lewis acidity and basicity were suggested to be provided by the Mg-O-Si linkages, and promotional effect on the redox site was provided by transition metal sites on the catalyst.

Experimentally, MgO/SiO_2 catalysts were synthesized by wet-kneading in water. $Mg(OH)_2$ from hydrothermal-NaOH assisted precipitation of magnesium nitrate precursor and Cab-O-Sil EH5 fumed silica were used as a starting material. Wet-kneading was done for 4 hours, before separation, drying, and impregnation/calcination. All final catalysts were calcined at elevated temperature to transform the material into oxides. Experimental study comprised *in-situ* and *operando* spectroscopy, kinetic experiment using fixed bed, and other bulk and surface ambient characterization such as TEM, SEM, XPS, and XRD. Materials used were ethanol in inert, such as N_2, He, and Ar. Probe molecules were used to investigate the reaction mechanism, acidity, and basicity of the catalyst.

2.2. DFT Calculation

Theoretical (computational) chemistry methods provided an alternative to predict reaction mechanisms, thermodynamics, kinetics, and even catalyst design by creating potential energy landscape. The potential energy surface (PES) was created by optimization of different minima and maxima (TS). This iterative step is essentially solving the Schrödinger's equation,

$$\hat{H}\Psi(R,r)=E\Psi(R,r) \tag{1.2}$$

The Hamiltonian in this equation can be separated into two terms, one to account for the electron and the other for the nucleus. This separation is made possible by using the Born–Oppenheimer approximation.[116] Consequently, the wavefunction is represented as a product of the electronic and nuclear wavefunctions. Further simplification is also made by ignoring the nuclear kinetic energy and only taking into account the nuclear's potential energy and electron's kinetic energy. *Ab-initio* methods and DFT study aim to solve the Schrödinger's equation by using electronic wavefunctions in the forms of single electron molecular orbitals.[116]

DFT is less computationally expensive than post-HF calculations. It uses electron (probability) density, ρ(r) to compute the electronic energy. A functional is used to represent the energy, because energy is a function of electron density, which is a function of position. This electron density is represented by a sum of one electron orbitals in the Kohn-Sham equation, $\rho = \sum_i^N \varphi_i(r)$. The DFT energy is further calculated in the Kohn-Sham equation,

$$E[\rho] = T_s[\rho] + \int d\boldsymbol{r}\, v_{ext}(\boldsymbol{r})\rho(\boldsymbol{r}) + E_H[\rho] + E_{XC}[\rho] \tag{1.3}$$

The terms on the right-hand side represent the (electronic) kinetic energy, external potential acting on the interacting system, Hartree (or Coulomb) repulsion energy, and the exchange-correlation energy.[116] The exchange-correlation energy is approximated, and several approximations have been developed, such as the local density approximation (LDA), local spin density approximation (LSDA), and generalized gradient approximations (GGA). The generalized gradient approximation (GGA) is an adaptation of the LDA that accounts for inhomogeneity of the electron density, in which the non-local correction of the gradient of the electron density (moving away from the coordinate) is added to the exchange-correlation energy.[116] In this work, GGA was used to approximate the exchange-correlation energy, specifically the simplified Perdew-Burke-Ernzerhof (PBE) GGA. More details of the computational calculation are provided in Chapter 2

2.3. *In-situ* and *Operando* Spectroscopy

In-situ spectroscopy is defined as spectroscopic characterization under relevant, operating condition.[117] The dynamics of the reaction and catalysts at different temperature can be studied by manipulating the temperature and pressure in a controlled manner. *Operando* spectroscopy, on the other hand, is essentially *in-situ* spectroscopy with monitoring of the vapor-phase product identification.[118,119] Typical setup for *operando* spectroscopy comprises a reaction cell with a temperature and/or pressure controller. The use of this reaction cell enables probing using optical light source, such as Raman and FTIR spectroscopy, at reaction condition, with flowing gas. The output of this reaction cell is then connected to product identification system, either GC-MS or MS. **Figure 1.3** shows a typical setup for *operando* spectroscopy.

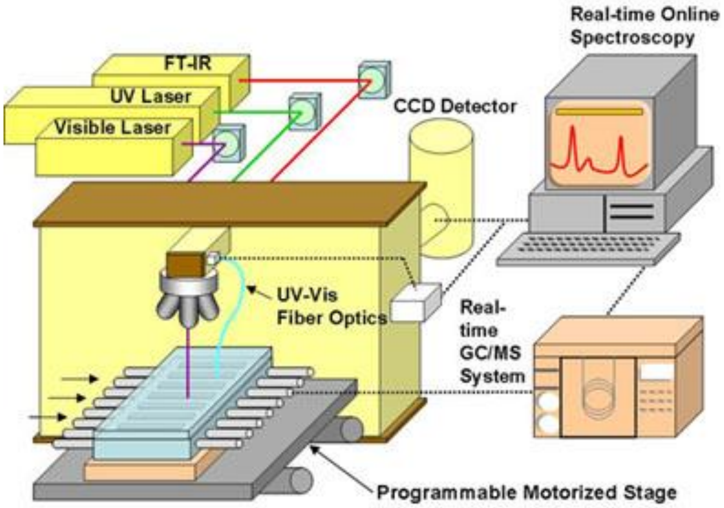

Figure 1.3. *Operando* spectroscopy setup, flow reaction cell temperature/pressure controller equipped with FTIR, UV-Vis and Raman spectroscopy that enables real-time online measurement. Output is connected to real-time GC/MS system. Adapted from: http://www.lehigh.edu/operando

2.3.1. Infrared Spectroscopy

Infrared (IR) spectroscopy is based on the radiation absorption by the characterized compounds. When an IR beam is passed through a sample, the compound absorbs radiation at a specific wavelength, resulting in a decrease of the transmitted radiation. In the spectra, the absorption is reflected as a dip in transmission, or a peak in absorbance. Upon absorbing the IR radiation, the molecules' oscillation amplitude will increase, hence the molecule is excited to a higher vibrational state. Vibrational states are quantized energy levels, and the particular wavelength of absorption by a specific bond depends on the energy difference between the ground level and the excited state. Hence, different bonds produce different peaks/dips, which also vary depending on the different oscillation modes, in the IR spectra at different wavenumbers.

Monitoring the molecular events taking place at a certain reaction temperature or pressure, i.e. in situ IR spectroscopy, is now possible and widely used. A substrate, or catalyst, can be put into a reaction chamber, where a reactant is flown over it. The spectroscopy is then used to continuously monitor the surface species present on the substrate while the surface is heated up to a certain desired temperature. This characterization method is very powerful because one can get information on the bonds created or destroyed during the temperature ramping, which, when properly analyzed, could give information on the possible transition states during the reaction.

Vibration spectroscopic measurements of the solid/gas interface can be effectively carried out using reaction chamber equipped with optical windows enabling measurements in transmission mode, attenuated total reflectance (ATR) and total or diffuse reflectance modes. Fourier transform infrared spectroscopy (FTIR) is generally limited to powdered (submicron-sized) materials, given limitations in throughput.

2.3.2. UV-Vis-NIR Spectroscopy

UV-Vis-NIR spectroscopy is another powerful tool to study catalysts. UV, Vis (visible), NIR (near infrared) regions cover 200-400 nm, 400-800 nm, and 800-2500 nm wavelength, respectively.[120,121] The UV-Vis region is very useful since it probes the electronic transitions, while NIR can discover overtones and combination bands of fundamental vibrational vibrations. This spectroscopy technique is especially useful when studying the transition metal ions, such as Cu and Zn in this dissertation study. In particular, two types of bands can be identified in the spectra, charge transfer (CT) bands and d-d transition bands. CT bands are usually associated with the highest oxidation state, while d-d transition bands represent reduced states. Bands associated with plasmon resonance are also available at higher wavelength region, which signifies the presence of a metallic state.

Coordination number of the transition metal species can be determined as well using UV-Vis spectroscopy.[122] This is done by comparing the optical absorption edge energies or band gaps in metal compounds with properties resembling crystalline or amorphous semiconductors. Several references with known coordination numbers, i.e. isolated, dimer, trimer, are tested and plotted against the band gap. The band gaps themselves are obtained from the hν-intercept value $[(\alpha h\nu)1/\eta = 0]$ by extrapolating a straight line from the linear region near the edge on the Tauc plot, where α is absorption coefficient, hν is the energy of the incident photon, E_0 is the optical absorption edge energy, and for crystalline semiconductors, η is 0.5, 1, 2, and 3, when the optical transitions caused by photon absorption are direct-allowed, direct-forbidden, indirect-allowed, and indirect-forbidden, respectively, whereas for amorphous, homogeneous semiconductors, η is typically 2.[122]

2.3.3. *Operando* XANES and EXAFS

High energy X-ray spectroscopy comprises X-ray absorption near edge spectroscopy (XANES) and extended X-ray absorption fine structure (EXAFS). Sample is irradiated with a tunable source of high intensity monochromatic x-rays from a synchrotron radiation facility. The bulk of the solid is penetrated by the x-ray, and only materials with nearly all the atoms on the surface give surface information. Oxidation state and coordination information can be extracted using this characterization method. The characterization can also be done in *operando* mode, which allows correlation with catalytic activity.

Not only does XANES give information for oxidation states, but it also discriminates tetrahedral and octahedral coordination of metal oxides by identification of the pre-edge features. Octahedral coordination has a center of symmetry (unlike tetrahedral), and transitions between states of g symmetry are not dipole allowed. Hence, octahedral coordination will not exhibit a pre-edge feature. EXAFS, on the other hand, provides information on the bond length and coordination number of different atoms on the molecules. With the correct reference, interpretation can be made to correlate the change in the bond length, oxidation states, coordination number, or change of coordination type during the reaction.

2.3.4. Temperature-Programmed Reaction Spectroscopy

Temperature-Programmed reaction spectroscopy (TPRS), often called TPD (temperature-programmed desorption), TDS (thermal desorption spectroscopy), and TPSR (temperature-programmed surface reaction), is a very powerful method to characterize a catalyst.[123] When only desorption is taking place, it is either called TDS or TPD, and when there is a reaction involved, i.e. decomposition, reduction, oxidation, it is called TPRS or TPSR. This technique requires a very simple infrastructure; a tube with a furnace containing the catalyst sample and mass spectrometer (MS) that is equipped with vacuum pump. Typically, the heating rate applied is constant, and hence, partial pressure of the vapor-phase can be related to the desorption (reaction) temperature. Redhead had shown that for fast pump rate, the desorption rate is proportional to the pressure in the chamber.[124] The desorption kinetics can also be determined, with the desorption activation energy estimated from the peak temperature. For the first-order kinetic, the following equation is applicable:

$$\frac{E_a}{RT_p^2} = \frac{\upsilon}{\beta} e^{\left(-\frac{E_a}{RT_p}\right)} \tag{1.4}$$

In this study, this method was used to identify the intermediates desorbed from the surface, further confirming the reaction mechanism and rate-determining steps. Ethanol or other reactants were adsorbed on the surface, flushed to remove the physisorbed species, and finally temperature was ramped under reactant flow or under inert flow. Depending on the reaction mechanism, activation energy can be determined, as discussed by Redhead. Deconvolution of the curve of a m/z number is particularly important. A m/z number can represent more than one molecules. For instance, m/z = 31 could originate from 1,3-butanediol, n-butanol, 2-butanol, crotyl alcohol, ethanol, and diethyl ether. Therefore, it is very important to deconvolute the curve and to consider the important m/z and discard the others.

2.4. High Sensitivity Low Energy Ion Scattering Spectroscopy (HS-LEIS)

High Sensitivity-Low Energy Ion Scattering (HS-LEIS), was used to probe the outermost layer of the catalyst, since reaction takes place on the catalyst surface. Quantitative, elemental information of the outermost layer is probed by bombarding the surface perpendicularly with noble gas ions. The noble gas ions, which are lighter than the elements on the surface, will be backscattered, recorded, and analyzed based on the classic laws of mechanics (conservation of momentum and conservation of energy).[125] The equation can be seen below:

$$\mathrm{E}_f = \mathrm{k}^2 \left(\frac{m_2}{m_1} \theta\right) E_i \tag{1.5}$$

Ei is the initial energy carried by the noble gas ion, m1, θ is the backscatter angle, m2 is the scattering surface atom, k is a known function of m_2/m_1 and θ, and E_f is the final energy of the scattered atom that is analyzed by the analyzer. The m_2 can hence be determined from the equation and the element can be determined.[125] Elemental composition calculation can further be estimated using quantum chemical method, by first deconvoluting the curve using Gaussian fitting and integrating the area under the curve to get I_i and use the following formula:

$$C_i = \frac{I_i/\sqrt{m_i}}{\sum I_i/\sqrt{m_i}} \tag{1.6}$$

2.5. Probe Molecules

Characterization of (supported) metal oxide catalysts often involves the use of probe molecules. Probe molecules, combined with spectroscopic techniques, such as DRIFTS and TPD, can provide a lot of insights on the catalysts surface. This characterization technique can be conveniently done at relevant reaction temperatures, which further provides the most relevant information regarding the chemical nature of the catalyst. In the case of bifunctional catalysts such as MgO/SiO_2 catalysts, acidic and basic probe molecules are indispensable for the acid-base characterization. Two probe molecules are typically used to characterize the acid sites of a catalysts: ammonia and pyridine. Ammonia is the most common probe molecule, since it is a very small molecule with relatively strong basic characteristic, allowing it to penetrate the small pore of the catalysts. Furthermore, ammonia adsorbs on both BAS as ammonium ion NH_4^+ and as NH_3 by donating its excess electron pairs to LAS. DRIFTS spectroscopy can be used to qualitatively and semi-quantitatively determine the acidity of the catalyst. Pyridine, on the other hand, is a weak but bigger basic molecule. This weak base can differentiate between LAS and BAS, and is more sensitive to the strong acid sites.

The basicity of the catalysts were probed with various acid probe molecules. CO_2 remains the most popular probe molecules, due to its slightly acidic nature and its versatility to bond with basic sites with different strengths. Monodentate, bidentate, symmetrical, and polydentate (bridged) carbonates are readily formed on the surface with different splitting values, while bicarbonate can also help identify the presence of weaker basic sites.[126] Methanol can also be used as a reactive probe molecule. On metal oxides, methanol adsorbs both as a Lewis-bound molecule and as a methoxy species. Upon thermal treatment, these two species desorb as both molecular methanol and as its reaction product, depending on which sites it is adsorbed to. On acid sites, methanol undergoes dehydration to yield dimethyl ether, while on basic sites, CO_2 will be produced by consecutive C-H bonds breaking. Redox site, when available, will transform methanol into formaldehyde. This versatility is very important when considering a catalyst that possesses different functional active sites.

2.6. Product Determination with GC-MS/FID

Gas chromatography (GC)-mass spectrometry (MS)/flame ionization detector (FID) is a very important tool to identify volatile chemical products. The setup essentially consists as a gas chromatography, coupled with MS or FID as the detector for product analysis. A GC is an oven box containing capillary or packed column that is internally coated with a polar solute, which is defines as stationary phase. The oven box will controllably heat up the column for separation purpose. On top of the oven, there is a sample loop that functions as a sample storage. At one state, the GC valve will allow sample to be continuously flown to the sample loop for a storing purpose. At another state, the GC valve will allow carrier gas, or mobile phase, to flush the sample loop into the GC column for product identification purpose.

When the carrier gas introduces sample to the GC, molecules will be adsorbed on the stationary phase, while the mobile phase keep flowing through the column. Separation is based on two variables, the affinity of the molecules (based on polarity) to the column and boiling point of each molecules. Separation is aided by the heating oven which will desorb each molecule based on their boiling point. Separation of molecules with similar boiling points will be based on the affinity to the column. The separated, desorbed molecules will be carried to the detector, MS and/or FID. Mass spectrometry detects volatile products by ionizing them and analyzing their mass-to-charge ratio, which is very specific to different molecules. The ionized molecules are then accelerated to the same kinetic energy by charged plates down the MS. The ions are deflected using a magnetic field selectively allowing one m/z to hit the detector. Simultaneous product identification is made possible by rapidly changing the magnetic field. However, MS is not inherently quantitative.[127]

For quantification purpose, FID detector was used in this work. FID detects the ions formed during combustion of organic compounds in a hydrogen flame.[126] These ions are proportional to the concentration of organic species in the sample. Since this detection method is based on combustion, the detectable molecules are limited to organic molecules with C-H bonds. Unlike MS, where the peaks can be identified as a specific molecule, there is no qualitative way of identifying a single molecule without the use of a standard molecule. Standard molecules can be used to determine the order of the GC retention time, and then calibrated to the area recorded by the GC-FID, and response factor for each molecule can be determined as the area/concentration.

3. Thesis Outline

Chapter 2

The complete experimental methods were presented in this chapter, which covers all experiments/computation done in this work. Results and discussions were presented in the following chapter accordingly.

Chapter 3

This chapter discusses the study of relevant reaction mechanisms by DFT simulation. Three previously proposed reaction mechanisms were investigated over a kink site of MgO (100) crystal model catalyst. This study was represented by comparison of kinetics and thermodynamics of the three reaction mechanisms, demonstrated by plotted potential energy surfaces. This work was published in *J. Catal.* **2017**, *346*, 78–91.

Chapter 4

This chapter follows up the mechanistic study using *in-situ* DRIFTS to investigate the surface reaction mechanism on the surface of MgO/SiO_2 catalyst. Detailed study using different feed, such as crotonaldehyde/ethanol, acetaldehyde, ethanol/inert, and ethanol/ethanol, were used in combination with GC-MS to identify the product stream. This work was published in *Catal. Sci. Technol.* **2017**, *7* (20), 4648–4668.

Chapter 5

This chapter discusses the catalyst characterization of MgO/SiO_2, as well as the kinetics of the reaction. Identification of the active sites were done by titration of the catalyst, as studied using DRIFTS and fixed-bed reactor with GC-MS. Characterization was done using XRD, HS-LEIS, and probe molecules. This work was submitted to *Journal of Physical Chemistry C* journal.

Chapter 6

The catalyst was promoted with transition metal, i.e. Zn and Cu. Initial computational study using a first approximation for the catalyst model was done to compare the reaction mechanisms on promoted catalysts. Promotional effect was briefly discussed by comparison of reactivity data, which is followed by characterization using UV-Vis spectroscopy, TEM and DRIFTS of CO_2 and NH_3. Subsequently, the chemical nature of the catalyst was studied by *operando* methanol DRIFTS to probe the chemical change of the catalyst brought about by promoting the catalyst with transition metals. The catalysts were further studied for its reaction. *In-situ* DRIFTS and cofeeding with different poison probe molecules were carried out to study the active sites of the catalyst. This study was completed by *operando* XANES/EXAFS to investigate the chemical change of the promoter materials during reaction. Part of this work was submitted to *ACS Catalysis* journal.

Chapter 7

A summary of the whole work for this dissertation is presented. Future outlook was discussed as well, presenting works that need to be further done.

References

(1) McCoy, M.; Reisch, M. S.; Tullo, A. H.; Short, P. L.; Tremblay, J. F.; Storck, W. J. *Chem. Eng. News* **2007**, *85*, 29.

(2) Werpy, T.; Petersen, G. *Top Value Added Chemicals from Biomass. Volume 1. Results of Screening for Potential Candidates from Sugars and Synthesis Gas*; US Department of Energy: Washington DC, 2004.

(3) Keturakis, C. Operando Molecular Spectroscopy during Catalytic Biomass Pyrolysis, Lehigh University, 2015.

(4) Angelici, C.; Weckhuysen, B. M.; Bruijnincx, P. C. a. *ChemSusChem* **2013**, *6* (9), 1595–1614.

(5) Sun, J.; Wang, Y. *ACS Catal.* **2014**, *4* (4), 1078–1090.

(6) Ni, M.; Leung, D. Y. C.; Leung, M. K. H. *Int. J. Hydrogen Energy* **2007**, *32* (15), 3238–3247.

(7) Haryanto, A.; Fernando, S.; Murali, N.; Adhikari, S. *Energy & Fuels* **2005**, *19* (5), 2098–2106.

(8) Hanspal, S.; Young, Z. D.; Shou, H.; Davis, R. J. *ACS Catal.* **2015**, 1737–1746.

(9) Morrill, M. R.; Thao, N. T.; Shou, H.; Davis, R. J.; Barton, D. G.; Ferrari, D.; Agrawal, P. K.; Jones, C. W. *ACS Catal.* **2013**, *3* (7), 1665–1675.

(10) Birky, T. W.; Kozlowski, J. T.; Davis, R. J. *J. Catal.* **2013**, *298* (0), 130–137.

(11) Kulkarni, N. V; Brennessel, W. W.; Jones, W. D. *ACS Catal.* **2017**, 997–1002.

(12) Young, Z. D.; Hanspal, S.; Davis, R. J. *ACS Catal.* **2016**, *6* (5), 3193–3202.

(13) Ho, C. R.; Shylesh, S.; Bell, A. T. *ACS Catal.* **2016**, *6* (2), 939–948.

(14) Takahara, I.; Saito, M.; Inaba, M.; Murata, K. *Catal. Letters* **2005**, *105* (3), 249–252.

(15) Bi, J.; Guo, X.; Liu, M.; Wang, X. *Catal. Today* **2010**, *149* (1), 143–147.

(16) Phung, T. K.; Busca, G. *Catal. Commun.* **2015**, *68*, 110–115.

(17) Zhang, X.; Wang, R.; Yang, X.; Zhang, F. *Microporous Mesoporous Mater.* **2008**, *116* (1–3), 210–215.

(18) Han, Y.; Lu, C.; Xu, D.; Zhang, Y.; Hu, Y.; Huang, H. *Appl. Catal. A Gen.* **2011**, *396* (1–2), 8–13.

(19) DeWilde, J. F.; Chiang, H.; Hickman, D. A.; Ho, C. R.; Bhan, A. *ACS Catal.* **2013**, *3* (4), 798–807.

(20) Phung, T. K.; Proietti Hernández, L.; Lagazzo, A.; Busca, G. *Appl. Catal. A Gen.* **2015**, *493*, 77–89.

(21) Gayubo, A. G.; Tarrío, A. M.; Aguayo, A. T.; Olazar, M.; Bilbao, J. *Ind. Eng. Chem. Res.* **2001**, *40* (16), 3467–3474.

(22) Gayubo, A. G.; Alonso, A.; Valle, B.; Aguayo, A. T.; Olazar, M.; Bilbao, J. *Fuel* **2010**, *89* (11), 3365–3372.

(23) Iwamoto, M. *Molecules* **2011**, *16* (9), 7844–7863.

(24) Meng, T.; Mao, D.; Guo, Q.; Lu, G. *Catal. Commun.* **2012**, *21* (0), 52–57.

(25) Song, Z.; Takahashi, A.; Nakamura, I.; Fujitani, T. *Appl. Catal. A Gen.* **2010**, *384* (1–2), 201–205.

(26) Liu, C.; Sun, J.; Smith, C.; Wang, Y. *Appl. Catal. A Gen.* **2013**, *467* (0), 91–97.

(27) Sun, J.; Zhu, K.; Gao, F.; Wang, C.; Liu, J.; Peden, C. H. F.; Wang, Y. *J. Am. Chem. Soc.* **2011**, *133* (29), 11096–11099.

(28) Sun, J.; Baylon, R. A. L.; Liu, C.; Mei, D.; Martin, K. J.; Venkitasubramanian, P.; Wang, Y. *J. Am. Chem. Soc.* **2016**, *138* (2), 507–517.
(29) Lippits, M. J.; Nieuwenhuys, B. E. *Catal. Today* **2010**, *154* (1), 127–132.
(30) Lippits, M. J.; Nieuwenhuys, B. E. *J. Catal.* **2010**, *274* (2), 142–149.
(31) Tu, Y.-J.; Chen, Y.-W. *Ind. Eng. Chem. Res.* **1998**, *37* (7), 2618–2622.
(32) Tu, Y.-J.; Li, C.; Chen, Y.-W. *J. Chem. Technol. Biotechnol.* **1994**, *59* (2), 141–147.
(33) Tu, Y.-J.; Chen, Y.-W.; Li, C. *J. Mol. Catal.* **1994**, *89* (1), 179–189.
(34) Chang, F.-W.; Yang, H.-C.; Roselin, L. S.; Kuo, W.-Y. *Appl. Catal. A Gen.* **2006**, *304* (0), 30–39.
(35) Chang, F.-W.; Kuo, W.-Y.; Lee, K.-C. *Appl. Catal. A Gen.* **2003**, *246* (2), 253–264.
(36) Gaspar, A. B.; Barbosa, F. G.; Letichevsky, S.; Appel, L. G. *Appl. Catal. A Gen.* **2010**, *380* (1–2), 113–117.
(37) Inui, K.; Kurabayashi, T.; Sato, S. *Appl. Catal. A Gen.* **2002**, *237* (1–2), 53–61.
(38) Inui, K.; Kurabayashi, T.; Sato, S.; Ichikawa, N. *J. Mol. Catal. A Chem.* **2004**, *216* (1), 147–156.
(39) Sánchez, A. B.; Homs, N.; Fierro, J. L. G.; Piscina, P. R. de la. *Catal. Today* **2005**, *107–108* (0), 431–435.
(40) Jørgensen, B.; Egholm Christiansen, S.; Dahl Thomsen, M. L.; Christensen, C. H. *J. Catal.* **2007**, *251* (2), 332–337.
(41) Santacesaria, E.; Carotenuto, G.; Tesser, R.; Di Serio, M. *Chem. Eng. J.* **2012**, *179* (0), 209–220.
(42) Inui, T.; Matsuda, H.; Yamase, O.; Nagata, H.; Fukuda, K.; Ukawa, T.; Miyamoto, A. *J. Catal.* **1986**, *98* (2), 491–501.
(43) Palagin, D.; Sushkevich, V. L.; Ivanova, I. I. *J. Phys. Chem. C* **2016**, *120* (41), 23566–23575.
(44) Chalk, S. G.; Miller, J. F. *J. Power Sources* **2006**, *159* (1), 73–80.
(45) Taifan, W.; Baltrusaitis, J. *Appl. Catal. B Environ.* **2016**, *198*, 525–547.
(46) Ni, M.; Leung, M. K. H.; Leung, D. Y. C.; Sumathy, K. *Renew. Sustain. Energy Rev.* **2007**, *11* (3), 401–425.
(47) Matar, S.; Hatch, L. F. F. *Chemistry of Petrochemical Processes*; Elsevier, 2001.
(48) Yang, C.; Meng, Z. Y. *J. Catal.* **1993**, *142* (1), 37–44.
(49) Kozlowski, J. T.; Davis, R. J. *J. Energy Chem.* **2013**, *22* (1), 58–64.
(50) León, M.; Díaz, E.; Ordóñez, S. *Catal. Today* **2011**, *164* (1), 436–442.
(51) Carvalho, D. L.; de Avillez, R. R.; Rodrigues, M. T.; Borges, L. E. P.; Appel, L. G. *Appl. Catal. A Gen.* **2012**, *415–416* (0), 96–100.
(52) Marcu, I.-C.; Tichit, D.; Fajula, F.; Tanchoux, N. *Catal. Today* **2009**, *147* (3–4), 231–238.
(53) Tsuchida, T.; Kubo, J.; Yoshioka, T.; Sakuma, S.; Takeguchi, T.; Ueda, W. *J. Catal.* **2008**, *259* (2), 183–189.
(54) Quattlebaum, W. M.; Toussaint, W. J.; Dunn, J. T. *J. Am. Chem. Soc.* **1947**, *69*, 593–599.
(55) Toussaint, W. J.; Dunn, J. T.; Jachson, D. R. *Ind. Eng. Chem.* **1947**, *39* (2), 120–125.
(56) Lebedev, S. V. *Zh Obs. Khim* **1933**, No. 3, 698–717.

(57) Larina, O.; Kyriienko, P.; Soloviev, S. *Catal. Letters* **2015**, 1–7.

(58) Angelici, C.; Velthoen, M. E. Z.; Weckhuysen, B. M.; Bruijnincx, P. C. A. *ChemSusChem* **2014**, *7* (9), 2505–2515.

(59) Janssens, W.; Makshina, E. V. V.; Vanelderen, P.; De Clippel, F.; Houthoofd, K.; Kerkhofs, S.; Martens, J. A. A.; Jacobs, P. A. A.; Sels, B. F. B. F. *ChemSusChem* **2014**, *8* (6), 994–1008.

(60) Shylesh, S.; Gokhale, A. A.; Scown, C. D.; Kim, D.; Ho, C. R.; Bell, A. T. *ChemSusChem* **2016**, *9* (12), 1462–1472.

(61) Sushkevich, V. L.; Ivanova, I. I.; Taarning, E. *Green Chem.* **2015**.

(62) Sushkevich, V. L.; Ivanova, I. I.; Ordomsky, V. V; Taarning, E. *ChemSusChem* **2014**, *7* (9), 2527–2536.

(63) Taifan, W.; Yan, G. X.; Baltrusaitis, J. *Catal. Sci. Technol.* **2017**, *7* (20), 4648–4668.

(64) Ordomsky, V. V.; Sushkevich, V. L.; Ivanova, I. I. *J. Mol. Catal. A Chem.* **2010**, *333* (1), 85–93.

(65) Phung, T. K.; Lagazzo, A.; Rivero Crespo, M. Á.; Sánchez Escribano, V.; Busca, G. *J. Catal.* **2014**, *311*, 102–113.

(66) Taifan, W. E.; Bučko, T.; Baltrusaitis, J. *J. Catal.* **2017**, *346*, 78–91.

(67) Georgieff, K. K. *J. Appl. Polym. Sci.* **1966**, *10* (9), 1305–1313.

(68) Wang, Z. In *Comprehensive Organic Name Reactions and Reagents*; John Wiley & Sons, Inc., 2010.

(69) Ostromislenskiy, I. *J. Russ. Phys. Chem. Soc.* **1915**, No. 47, 1472 –1506.

(70) Gruver, V.; Sun, A.; Fripiat, J. J. *Catal. Letters* **1995**, *34* (3–4), 359–364.

(71) Chieregato, A.; Velasquez Ochoa, J.; Bandinelli, C.; Fornasari, G.; Cavani, F.; Mella, M. *ChemSusChem* **2014**, *8* (2), 377–388.

(72) Makshina, E. V; Dusselier, M.; Janssens, W.; Degreve, J.; Jacobs, P. A.; Sels, B. F. *Chem. Soc. Rev.* **2014**, *43* (22), 7917–7953.

(73) Pomalaza, G.; Capron, M.; Ordomsky, V.; Dumeignil, F. *Catalysts* **2016**, *6* (12), 203–237.

(74) Makshina, E. V.; Janssens, W.; Sels, B. F.; Jacobs, P. A. *Catal. Today* **2012**, *198* (1), 338–344.

(75) Niiyama, H.; Morii, S.; Echigoya, E. *Bull. Chem. Soc. Jpn.* **1972**, *45* (3), 655–659.

(76) Chung, S.-H.; Angelici, C.; Hinterding, S. O. M.; Weingarth, M.; Baldus, M.; Houben, K.; Weckhuysen, B. M.; Bruijnincx, P. C. A. *ACS Catal.* **2016**, *6* (6), 4034–4045.

(77) Huang, X.; Men, Y.; Wang, J.; An, W.; Wang, Y. *Catal. Sci. Technol.* **2017**, *7* (1), 168–180.

(78) Jones, M. D.; Keir, C. G.; Iulio, C. Di; Robertson, R. A. M.; Williams, C. V; Apperley, D. C. *Catal. Sci. Technol.* **2011**, *1* (2), 267–272.

(79) De Baerdemaeker, T.; Feyen, M.; Müller, U.; Yilmaz, B.; Xiao, F.-S.; Zhang, W.; Yokoi, T.; Bao, X.; Gies, H.; De Vos, D. E. *ACS Catal.* **2015**, 3393–3397.

(80) Bhattacharyya, S. K.; Sanyal, S. K. *J. Catal.* **1967**, *7* (2), 152–158.

(81) Corson, B. B.; Jones, H. E.; Welling, C. E.; Hinckley, J. A.; Stahly, E. E. *Ind. Eng. Chem.* **1950**, *42* (2), 359–373.

(82) Müller, P.; Burt, S. P.; Love, A. M.; McDermott, W. P.; Wolf, P.; Hermans, I. *ACS Catal.* **2016**, *6* (10), 6823–6832.

(83) Jones, M. D. *Chem. Cent. J.* **2014**, *8* (1), 53.
(84) Posada, J. A.; Patel, A. D.; Roes, A.; Blok, K.; Faaij, A. P. C.; Patel, M. K. *Bioresour. Technol.* **2013**, *135*, 490–499.
(85) Bhattacharyya, S. K.; Avasthi, B. N. *Ind. Eng. Chem. Process Des. Dev.* **1963**, *2* (1), 45–51.
(86) Hayashi, Y.; Akiyama, S.; Miyaji, A.; Sekiguchi, Y.; Sakamoto, Y.; Shiga, A.; Koyama, T.; Motokura, K.; Baba, T. *Phys. Chem. Chem. Phys.* **2016**, *18* (36), 25191–25209.
(87) Velasquez Ochoa, J.; Bandinelli, C.; Vozniuk, O.; Chieregato, A.; Malmusi, A.; Recchi, C.; Cavani, F. *Green Chem.* **2016**, *18*, 1653–1663.
(88) Velasquez Ochoa, J.; Malmusi, A.; Recchi, C.; Cavani, F.; Ochoa, J. V.; Malmusi, A.; Recchi, C.; Cavani, F. *ChemCatChem* **2017**, *9* (12), 2128–2135.
(89) Larina, O. V.; Kyriienko, P. I.; Trachevskii, V. V.; Vlasenko, N. V.; Soloviev, S. O. *Theor. Exp. Chem.* **2016**, *51* (6), 387–393.
(90) Ohnishi, R.; Akimoto, T.; Tanabe, K. *J. Chem. Soc. Chem. Commun.* **1985**, No. 22, 1613–1614.
(91) Da Ros, S.; Jones, M. D.; Mattia, D.; Pinto, J. C.; Schwaab, M.; Noronha, F. B.; Kondrat, S. A.; Clarke, T. C.; Taylor, S. H. *ChemCatChem* **2016**, *8*, 1–12.
(92) Sushkevich, V. L.; Ivanova, I. I. *ChemSusChem* **2016**, *9* (16), 2216–2225.
(93) Baylon, R. a. L.; Sun, J.; Wang, Y. *Catal. Today* **2015**, 1–7.
(94) Larina, O. V; Kyriienko, P. I.; Soloviev, S. O. *Theor. Exp. Chem.* **2016**, *52* (1), 51–56.
(95) Kyriienko, P. I.; Larina, O. V; Soloviev, S. O.; Orlyk, S. M.; Calers, C.; Dzwigaj, S.; Pisarzhevsky, L. V. *ACS Sustain. Chem. Eng.* **2017**, *5* (3), 2075–2083.
(96) Natta, G.; Rigamonti, R. *Chim. E Ind.* **1947**, *29*, 195–201.
(97) Ruckenstein, E.; Khan, A. Z. *J. Catal.* **1993**, *141* (2), 628–647.
(98) Cavalleri, M.; Pelmenschikov, A.; Morosi, G.; Gamba, A.; Coluccia, S.; Martra, G. In *Oxide-based Systems at the Crossroads of ChemistrySecond International Workshop October 8-11, 2000, Como, Italy*; A. Gamba, C. C. and S. C. B. T.-S. in S. S. and C., Ed.; Elsevier, 2001; Vol. Volume 140, pp 131–139.
(99) Kvisle, S.; Aguero, A.; Sneeden, R. P. A. *Appl. Catal.* **1988**, *43* (1), 117–131.
(100) Angelici, C.; Velthoen, M. E. Z.; Weckhuysen, B. M.; Bruijnincx, P. C. A. *Catal. Sci. Technol.* **2015**.
(101) Natta, G.; Rigamonti, R. *Chim. Ind.* **1947**, *29*, 239–243.
(102) Lewandowski, M.; Babu, G. S.; Vezzoli, M.; Jones, M. D.; Owen, R. E.; Mattia, D.; Plucinski, P.; Mikolajska, E.; Ochenduszko, A.; Apperley, D. C. *Catal. Commun.* **2014**, *49*, 25–28.
(103) Kitayama, Y.; Michishita, A. *J. Chem. Soc., Chem. Commun.* **1981**, No. 9, 401–402.
(104) Kitayama, Y.; Satoh, M.; Kodama, T. *Catal. Letters* **1996**, *36* (1–2), 95–97.
(105) Sekiguchi, Y.; Akiyama, S.; Urakawa, W.; Koyama, T.; Miyaji, A.; Motokura, K.; Baba, T. *Catal. Commun.* **2015**, *68*, 20–24.
(106) Angelici, C.; Meirer, F.; van der Eerden, A. M. J.; Schaink, H. L.; Goryachev, A.; Hofmann, J. P.; Hensen, E. J. M.; Weckhuysen, B. M.; Bruijnincx, P. C. A. *ACS Catal.* **2015**, *5* (10), 6005–6015.
(107) Sushkevich, V. L.; Palagin, D.; Ivanova, I. I. *ACS Catal.* **2015**, 4833–4836.

(108) Sushkevich, V. L.; Ivanova, I. I. *Appl. Catal. B Environ.* **2017**, *215*, 36–49.
(109) Sushkevich, V. L.; Ivanova, I. I.; Taarning, E. *ChemCatChem* **2013**, *5* (8), 2367–2373.
(110) Patil, P. T.; Liu, D.; Liu, Y.; Chang, J.; Borgna, A. *Appl. Catal. A Gen.* **2017**, *543*, 67–74.
(111) Bhattacharyya, S. K.; Ganguly, N. D. *J. Appl. Chem.* **1962**, *12* (3), 97–104.
(112) Kim, T.-W.; Kim, J.-W.; Kim, S.-Y.; Chae, H.-J.; Kim, J.-R.; Jeong, S.-Y.; Kim, C.-U. *Chem. Eng. J.* **2014**.
(113) Chae, H.-J.; Kim, T.-W.; Moon, Y.-K.; Kim, H.-K.; Jeong, K.-E.; Kim, C.-U.; Jeong, S.-Y. *Appl. Catal. B Environ.* **2014**, *150–151*, 596–604.
(114) Müller, P.; Wang, S.-C.; Burt, S. P.; Hermans, I. *ChemCatChem* **2017**, *9* (18), 3572–3582.
(115) Branda, M. M.; Rodríguez, A. H.; Belelli, P. G.; Castellani, N. J. *Surf. Sci.* **2009**, *603* (8), 1093–1098.
(116) Jensen, F. *Introduction to Computational Chemistry*, 2nd ed.; John Wiley & Sons Ltd., 2006.
(117) Weckhuysen, B. M. *Phys. Chem. Chem. Phys.* **2003**, *5* (20), 4351–4360.
(118) Chakrabarti, A.; Ford, M. E.; Gregory, D.; Hu, R.; Keturakis, C. J.; Lwin, S.; Tang, Y.; Yang, Z.; Zhu, M.; Bañares, M. A.; Wachs, I. E. *Catal. Today* **2017**, *283*, 27–53.
(119) Bañares, M. A. *Catal. Today* **2005**, *100* (1), 71–77.
(120) Jentoft, F. C. B. T.-A. in C. Academic Press, 2009; Vol. 52, pp 129–211.
(121) Schoonheydt, R. A. *Chem. Soc. Rev.* **2010**, *39* (12), 5051–5066.
(122) Bravo-Suarez, J. J.; Subramaniam, B.; Chaudhari, R. V. *J. Phys. Chem. C* **2012**, *116* (34), 18207–18221.
(123) Gorte, R. J. *Catal. Today* **1996**, *28* (4), 405–414.
(124) Redhead, P. a. *Vacuum* **1962**, *12* (4), 203–211.
(125) ter Veen, H. R. J.; Kim, T.; Wachs, I. E.; Brongersma, H. H. *Catal. Today* **2009**, *140* (3), 197–201.
(126) McWilliam, I. G.; Dewar, R. A. *Nature* **1958**, *181*, 760.
(127) Doerr, A. *Nat. Methods* **2008**, *6*, 34.

Chapter 2

Experimental Methods

1. Introduction

This chapter is dedicated for both computational details and experimental methods used throughout the research work.

2. Computational Details

2.1. Electronic structure calculations.

Periodic DFT calculations have been performed using the VASP code.[1–4] The Kohn–Sham equations have been solved variationally in a plane-wave basis set using the projector-augmented-wave (PAW) method of Blochl,[5] as adapted by Kresse and Joubert.[5] The exchange-correlation energy was described by the PBE generalized gradient approximation.[6] Brillouin-zone was sampled using 2x2x1 k-point mesh. The plane-wave cutoff was set to 400 eV. The convergence criterion for the electronic self-consistency cycle, measured by the change in the total energy between successive iterations, was set to 10^{-6} eV/cell.

2.2. Structural optimization calculations.

Transition states have been identified using the DIMER method,[7] as improved by Heyden *et al.*[8] Atomic positions were considered to be relaxed if all forces acting on the atoms were smaller than 0.005 eV/Å. Transition states were proven to be first-order saddle points of the potential energy surface using vibrational analysis. The intrinsic reaction coordinates[9,10] (IRCs) for the forward and backward reaction steps were identified using the damped velocity Verlet algorithm.[11] The structures corresponding to potential energy minima along the IRC were further relaxed using a conjugate-gradient algorithm such as to satisfy the same optimization criterion as for transition states. Vibrational analysis was performed to ensure that the relaxed structures correspond to true potential energy minima. This procedure guarantees that reactant and product states are linked by a path with a single transition state.

The Gibbs free-energy calculations have been performed using the harmonic/rigid rotor approximation to the transition state theory[12] for the temperature of 723 K. The detailed calculations for the Gibbs energy estimations are provided in subchapter 2.4. All relative energies were referenced to the sum of the relaxed MgO slab, and three molecules of gas phase ethanol. The first-order reaction constants were computed using:

$$k(T) = \frac{k_B T}{h} e^{-\frac{\Delta G_A(T)}{RT}} \tag{2.1}$$

where k_B – 1.380662x10^{-23} m^2 kg/s^2 K^1, T = 723 K, h - 6.626176x10^{-34} m^2 kg/s, R - 1.987 cal/K mol, and $\Delta G_A(T)$ is molar Gibbs free-energy of activation defined for the forward and reverse reactions as follows:

$$\Delta G_{A,forward} = G_{TS} - G_{IS} \tag{2.2}$$

$$\Delta G_{A,reverse} = G_{TS} - G_{FS} \tag{2.3}$$

with subscripts TS, FS and IS representing transition state, final state, and initial state, respectively. Similarly, the reaction free energy (ΔG_{Rx}) is defined as follows:

$$\Delta G_{Rx} = G_{FS} - G_{IS} \tag{2.4}$$

The rate constants for the forward and reverse reaction steps are labelled as k_f and k_r, respectively.

2.3. Structural model.

Under normal conditions, MgO crystallizes in the rocksalt crystal structure, with (001) being the most prominent surface. For the specific reaction of ethanol to 1,3-butadiene, the original working catalyst is MgO/SiO_2 [13,14]. The addition of MgO to SiO_2, regardless of the methods used to synthesize the catalysts, does not result in the formation of $MgSiO_4$ solid solution.[13,15–17] It was found that MgO crystalline phase was the only phase found on the amorphous surface. In contrast, a study by Angelici *et al.*[18] claims that

$MgSiO_4$ phase was indeed formed and it was suggested to be responsible for the aldol condensation of the acetaldehyde intermediates. The authors argued that FTIR shows the presence of a hydroxyl group which coincides with that found in talc. This statement contradicts their previous study, in which the presence of the silicate was not confirmed by XRD.[19] The addition of MgO to amorphous silica combined with increased surface area of the catalyst is also known to create more defects on the MgO itself, which clearly contributes to the higher activity and selectivity of the catalyst. The unsaturated surface oxygen atoms, e.g. corner and edge O, are unfavorable energetically leading to the tendency to release an electron and to turn into O^- species. Hence these unsaturated oxygen atoms act as donors of an electron pair, i.e. as Lewis bases.[20] Cube corners,[21] terraces, steps, corners, and reverse corners were studied extensively.[22]

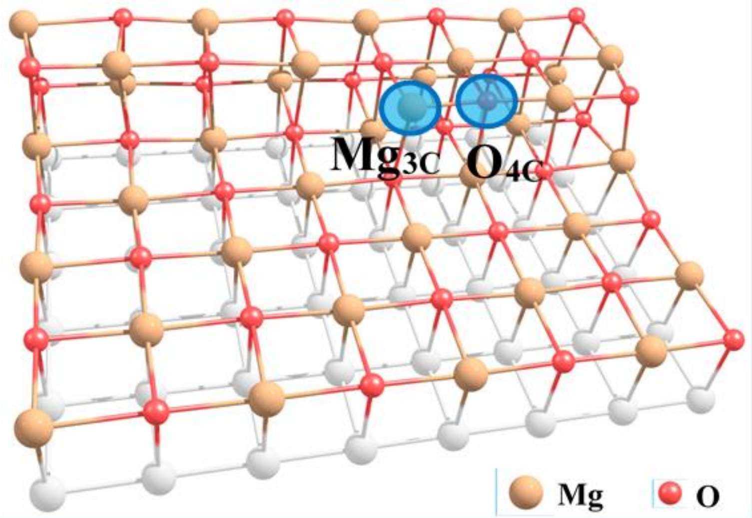

Figure 2.1 Periodic MgO slab used throughout the calculations. The whited out bottom layer indicates the atoms whose positions were kept frozen during calculations.

Periodic three layer slab of MgO consisting of 8 x 6 x 3 primitive cells was used throughout all the calculations. Previous investigations have identified defect sites of MgO catalysts, most notably the three- and four-fold coordinated surface atoms (Mg^{2+}_{3C} O^{2-}_{4C}), as the active sites[22–27] whereas atoms at surface terraces were found to be relatively unreactive.[28] The positions of atoms in the bottommost layer were fixed while remaining atoms were relaxed. PBE lattice parameter of 4.255 Å was used to construct the slab. This value is similar to values of 4.261 (PBE) and 4.186 Å (experimental).[29] In this work we considered the Mg_{3C} coordinated to O_{4C} in the form of stepped kink, depicted in Figure 2.1, as the active sites for the reaction. The large slab is used to accommodate several intermolecular reactions that might include interactions of C2 and C4 intermediates and also to avoid significant interaction between molecules in the neighboring unit cells.

2.4. Free-energy calculation

The free-energy calculations have been performed using a static approach based on harmonic and rigid rotor approximations to vibrational and rotational degrees of freedom. Although this methodology is described in detail in many textbooks,[12] we find it useful to summarize the working equations in this text.

2.4.1. Working equations

Within the static approximation used in this study, Gibbs free energy for each state is expressed as a sum of contribution of electronic (el), vibrational (vib), rotational (rot), and translational (tr) degrees of freedom (DOF):

$$G = G_{el} + G_{vib} + G_{rot} + G_{tr} \tag{2.5}$$

Discussion of partitioning of atomic degrees of freedom in the case of interacting and non-interacting systems is provided in section 1.2.

The electronic contribution for a system in a singlet electronic state (all systems discussed in this work) takes a form:

$$G_{el} = E_{DFT} \tag{2.6}$$

where E_{DFT} is a Kohn-Sham energy computed by solving Schrödinger equation at the DFT level. The vibrational contribution is expressed as

$$G_{vib} = \frac{3}{2}k_B T - T k_B \sum_{i=1}^{N_{vib}} \left(\frac{h\nu_i}{k_B T} \frac{1}{e^{\frac{h\nu_i}{k_B T}} - 1} - \ln\left(1 - e^{-\frac{h\nu_i}{k_B T}}\right) \right) \tag{2.7}$$

where k_B and h are fundamental constants (Boltzmann and Planck, respectively), T is thermodynamic temperature (723 K), N_{vib} is the number of vibrational degrees of freedom, and ν is a harmonic vibrational frequency. The rotational contribution is expressed as

$$G_{rot} = -k_B T \ln\left(\frac{\sqrt{\pi}}{\sigma} \left(\frac{8\pi^2 k_B T}{h^2} \right)^{3/2} \sqrt{I_1 I_2 I_3} \right) \tag{2.8}$$

where σ is a symmetry index, and I_1, I_2, and I_3 are moments of inertia of a molecule. The values of σ for molecules considered in this study are compiled in Tab.S1. Finally, the term G_{tr} is expressed as follows

$$G_{tr} = -k_B T \ln\left(V_m \left(\frac{2\pi M k_B T}{h^2} \right)^{3/2} \right) \tag{2.9}$$

where $V_m = k_B T/p$ is a volume occupied by one particle of ideal gas at given external pressure p (101325 Pa) and temperature (723 K), and M is the total molecular mass.

Table 2.1. Symmetry indices σ for gas-phase molecules considered in this study.

Molecule	$\boldsymbol{\sigma}$
acetaldehyde	1
crotonaldehyde	1
ethanol	1
butadiene	2
dihydrogen	2
water	2

2.4.2. Partitioning of atomic degrees of freedom in interacting and non-interacting systems

For a system consisting of $N_{s,free}$ free substrate atoms (in our model $N_{s,free}$ corresponds to all substrate atoms except of the bottommost layer of the slab, see subchapter 2.3 and Figure 2.1) and N_M atoms forming molecules adsorbed on the substrate, the number of vibrational degrees of freedom is $N_{vib} = 3(N_{s,free} + N_M)$. There are no rotational and translational degrees of freedom in such a case and hence also the contribution of G_{rot} and G_{tr} to Gibbs free energy is zero. In the case of systems consisting of a substrate and P molecules that neither interact with each other nor they interact with the substrate, the total number of vibrational degrees of freedom is $3N_{s,free} + \sum_{i=1}^{P}(3N_{M_i} - 3 - N_{rot,i})$, where N_{M_i} and $N_{rot,i}$ are the number of atoms and the number of rotational degrees of freedom in the molecule i. Each molecule has 3 translational and 2 (linear molecules) or 3 (nonlinear molecules) rotational degrees of freedom.

2.4.3. Calculation of harmonic vibrational frequencies

The harmonic vibrational frequencies have been computed using the finite differences method implemented in VASP. The numerical differentiation has been done using the a differences formula with displacement of size 0.02 Å. Even the use of quite stringent relaxation criterion (maximal force smaller than 0.005 eV/ Å) does not ensure the correct eigenvalue spectrum of dynamical matrix (i.e. zero imaginary vibrational frequencies in the case of minima and one imaginary vibrational frequency in the case of first-order saddle) in all cases. In order to obtain correct vibrational spectrum in such a problematic case, several iterations consisting of line-minimization of energy along the incorrect unstable directions, followed by a full relaxation of the atomic positions and dynamical matrix calculations was performed.

3. Experimental Methods

3.1. Catalyst synthesis

3.1.4. Synthesis of magnesium oxide, MgO, catalyst

MgO catalyst was synthesized using a modified thermal decomposition method.[30] In a typical synthesis, 2.23g (8.7 mmol) of $Mg(NO_3)_2{\cdot}6H_2O$ (Sigma-Aldrich) were dissolved in 40 ml methanol and then 1 ml water was added. A 30 ml methanol solution containing 0.7 g (17.4 mmol) of NaOH was added drop-wise to the resulting solution under reflux temperature. After 30 minutes a white precipitate was collected by centrifugation (Thermo Sorvall™ Legend™ XT). The isolated precipitate was washed three times using a 1:1 ratio solution of ethanol/water and then separated using centrifugation. The resulting wet samples were dried at 80 °C overnight. The resulting dry magnesium hydroxide solid was ground using a mortar and pestle and calcined at 800 °C in a calcination oven (Thermo Lindberg™ Blue M). Here, a ramping rate of 10 °C/min for 3 hours was used under an oxidizing atmosphere with an air flow rate of 50 ml/min. Natural convection was used to cool down the samples.

3.1.5. Synthesis of MgO/SiO_2 catalysts

Two methods of preparation are investigated in this study, i.e. incipient wetness impregnation (IWI) and wet-kneaded (WK). The incipient wetness impregnation was done using final Mg/Si mass ratio of 1. Precursor used in this method is $Mg(NO_3)_2{\cdot}6H_2O$ (Sigma-Aldrich) in water, impregnated on fumed silica (Cabot). The solid is then dried overnight under ambient condition, followed by drying at 80°C overnight, before further calcined at 800 °C. The wet-kneaded MgO/SiO_2 catalysts were prepared by utilizing some of the magnesium hydroxide material obtained in Section 3.1.1 by a thermal decomposition method before its calcination. Instead of calcining, the hydroxide was wet-kneaded with fumed silica (Cabot).[13] The corresponding amounts of silica and magnesium hydroxide were wet-kneaded in deionized water for 4 hours, centrifuged, dried overnight at 80 °C and calcined. In Chapter 4 and 5, 800°C was chosen as calcination temperature for both catalysts. In Chapter 4, the catalyst is labeled as WK (1:1), while in Chapter 5, the catalysts are labeled as MgSi-WK and MgSi-IWI for comparing between WK and IWI methods, and a WK catalyst calcined at 500°C is labeled as MgSi-WK2. In Chapter 6, for comparison between unpromoted and promoted WK catalysts calcined at 500°C, the unpromoted catalyst is simply referred to as MgSi.

3.1.6. **Synthesis of promoted wet-kneaded MgO/SiO_2 catalysts.**

Following synthesis the wet-kneaded MgO/SiO_2 (1:1) catalyst, drying is instead carried out at room temperature overnight, and the catalyst was then impregnated with transition metals, i.e., Cu or Zn. Copper nitrate trihydrate (Alfa Aesar) and zinc nitrate hexahydrate (Sigma) were used as precursors. The catalysts were then dried at room temperature overnight and further calcined at 500 °C for 3 hours. For comparison purpose, an unpromoted catalyst is also calcined at 500 °C for 3 hours. These catalysts are labeled as CuMgSi and ZnMgSi, while the corresponding binary reference catalysts, e.g. Cu(Zn)-SiO_2, Cu(Zn)-MgO, are labeled as CuSi, ZnSi, CuMg and ZnMg, respectively.

3.2. Catalytic reactivity study

The catalytic tests were performed in a Microactivity-Reference fixed bed reactor from PID Eng Tech (Spain). A quartz tube reactor was used with the quartz wool positioned so as to support the catalyst bed (0.1 g, pelletized, crushed and sieved to 100-150 µm particle size). Additional SiO_2 powder (Sigma) was used to increase the bed length so as to maintain the plug flow condition. Ethanol was delivered with helium gas by bubbling the gas through a chilled ethanol saturator with a total flow of 50 ml/min. The bubbler temperature was varied to manipulate the weight hourly space velocity (WHSV). The hot box temperature in the reactor was set at 100 °C to prevent any reactant or product condensation. Prior to the reaction, the catalyst was activated by heating it to 500 °C at a heating rate of 10 °C/min and then held at that temperature for 1 hour under 30 ml/min He flow. The reactions were performed at 375 °C. The products were kept in the vapor phase and then analyzed using a gas chromatograph equipped with an FID detector and Restek RT-Q-Bond column. The reactant ethanol and principal products, i.e., ethylene, acetaldehyde and 1,3-BD, were quantified based on the calibration carried out using a standard reference mixture (Praxair).

Titration experiment was carried out to poison both basic and acidic sites. To poison basic sites, probe molecules, i.e. CO_2 and propionic acid, were used. Poisoning acidic sites were carried out by using NH_3 as the probe molecule, and by post-treatment using NaOH. For this post-treatment method, the catalyst was impregnated with a very dilute NaOH solution, with final catalysts containing 250, 500, and 1000 ppm NaO, and let dry at room temperature without further thermal treatment. In a typical titration experiment, the catalyst was let to achieve a steady-state condition at a selected WHSV and reaction temperature. Probe molecules were then co-fed into the reactor using MFC for CO_2 and 1% NH_3 in N_2, while propionic acid was delivered using a chilled saturator containing mixture of propionic acid/ethanol (3:7). After a new steady-state is achieved, the feed was reverted back to only ethanol to check for the activity recovery.

3.3. Catalyst characterization

Unpromoted catalysts, i.e. MgSi-IWI and MgSi-WK, were characterized using HS-LEIS, XRD, BET surface area measurement, and combination of *in-situ* IR and UV-Vis measurements. TPRS experiments were also run using MgSi-WK. Transition metal-promoted catalysts were characterized using XRD and BET surface area measurement, ICP-OES, XPS, STEM, *in-situ* IR and UV-Vis, and also *operando* XAS experiments.

3.3.1. High-sensitivity low energy ion scattering (HS-LEIS)

The unpromoted IWI and WK catalysts (1:1), calcined at 800 °C, were prepared for analysis by dispersing into an appropriate sample crucible for a heatable sample holder for the LEIS spectrometer, ION-TOF Qtac^{100}, and then compacting it with a sample press. The crucible was then affixed to a sample holder with an integrated cartridge heater and a thermocouple was placed in a hole on the crucible.

After being placed in vacuum, the temperature of a sample was raised to about 50°C for outgassing. O2 was then introduced into the preparation temperature at an unmeasured pressure likely between 100 and 300 mbar. The temperature of the sample was then increased at a rate of 10°C/min to a maximum temperature of 500°C. This temperature was held for 60 min, at which time the temperature was allowed to decrease and the preparation chamber was evacuated. The sample was then transferred into the analysis chamber. Charge neutralization was invoked during spectra acquisition and sputtering. For primary ion beam, the following parameter was used: 3.0 keV He^+, 1500 × 1500 μm raster, at 2 x 10^{14} ions cm^{-2} cyc^{-1}, 3000 eV pass energy. The following conditions were applied during sputtering: 1.0 keV Ar^+, 2000 x 2000 μm raster, 5 x 10^{14} ions cm^{-2} cyc^{-1}.

3.3.2. XRD and BET surface area

Bulk structural information of the catalysts was characterized using XRD. XRD patterns were obtained using PANalytical Empyrean powder X-ray diffractometer using Cu $K_{\alpha1,2}$ with λ=1.5418 Å operating at 45 kV. Measurements were carried out between $2\theta=10°$ and 100° using a step size of 0.05°. The BET specific surface areas of the catalysts were determined by nitrogen adsorption at 77 K on a Micromeritics ASAP 2010 instrument. All samples were degassed under nitrogen flow at 623 K for 12 h before the measurements.

3.3.3. Transition metal concentration measurements.

The weight transition metal concentration of Cu- and Zn-promoted MgO/SiO_2 catalysts was determined using Inductively Coupled Plasma-Optical Emission Spectroscopy (ICP-OES, PerkinElmer Optima 2000 DV). About 10 mg of catalyst was digested using 40 ml solution containing 1:1:1 H_2O, HCl and HNO_3. Cu concentration was measured to be 0.8%, similar to that used by Weckhuysen and coworkers[18,19] while Zn was 2.5%, close to that reported by Larina *et al.*[15]

The XPS measurements were carried out to corroborate the results of ICP-OES with a PHI 5600ci instrument using a non-monochromatized Al Kα X-ray source. The pass energy of the analyzer was 58.7 eV, acquisition area with diameter of ~800 um and the scan step size was 0.125 eV. Binding energies were corrected for charging by referencing to the C 1s peak at 284.8 eV. Atomic concentrations were calculated from the areas under individual high-resolution XPS spectra using manufacturer-provided sensitivity factors.

3.3.4. Scanning transmission electron microscopy

The morphology of the catalyst particles was investigated using a dedicated Scanning Transmission Electron Microscope (STEM) (Hitachi 2700C) operating at 200 kV.

3.3.5. *In-situ* spectroscopy

Diffuse Reflectance Infrared Spectroscopy (DRIFTS) was used to probe the composition and changes in hydroxyl (OH) groups on the catalyst surface under dehydrated conditions. A Thermo Nicolet iS50 infrared spectrometer equipped with a Mercury-Cadmium-Tellurium (MCT) liquid nitrogen cooled detector was used in combination with a Harrick Praying Mantis™ diffuse reflection accessory equipped with ZnSe windows. About 30 mg of <100 µm catalyst samples were loaded into the DRIFTS cell. The smaller particle size was used to ensure a uniform catalyst bed surface for spectroscopy. Similar to the steady state reaction testing, the catalyst activation was carried out by heating it up to 500 °C at 10 °C/min and keeping it at that temperature for 1 hour under 30 ml/min He flow. The catalyst was then cooled down to 100 °C under 30 ml/min N_2 (Praxair) flow. During the cooling reference spectra of the catalysts were acquired at 400°C, 300°C, 200°C and 100 °C. All spectra were averaged over 96 scans at a resolution of 4 cm^{-1}.

In-situ UV-vis DRS measurements were performed using an Agilent Technologies Cary 5000 UV-Vis- NIR spectrophotometer equipped with a Praying Mantis TM diffuse reflection accessory. Finely ground samples (< 100µm) of supported catalyst powders were loaded into the environmental cell (Harrick, HVC-DR2) and then UV-vis spectra were collected in the 200-800 nm region. An MgO reflectance standard was used as the baseline. The experimental protocol used for DRIFTS experiments was also used in the *in-situ* UV-

VIS DRS experiments. The Kubelka-Munk function was calculated from the absorbance of the UV-vis DRS. The edge energy (E_g) for allowed transitions was determined by finding the intercept between the straight line and the abscissa on the Tauc plot derived from the UV-Vis spectra.

3.3.6. Acid-*base* characterization using pyridine, NH_3, CO_2, and methanol as probe molecules

A Thermo Nicolet iS50 infrared spectrometer equipped with a Mercury-Cadmium-Tellurium (MCT) liquid nitrogen cooled detector was used with a Harrick **Praying Mantis™ diffuse reflection accessory and ZnSe windows** to study the acidity and basicity of the catalyst. About 30 mg of sample was pressed and loaded into the DRIFTS cell. Catalyst activation was carried out by heating it up to 773 K at a rate of 10 K/min and then held at that temperature for 1 hour under 30 ml/min air flow, in agreement with the fixed bed experiment catalyst preparation procedure. The catalyst was then cooled down to 373 K under 30 ml/min nitrogen (Praxair) flow. During the cooling, reference spectra of the catalysts were acquired every 50 K. All spectra were averaged over 96 scans at a resolution of 4 cm^{-1}. Probe molecules, i.e. NH_3, CO_2 and pyridine, were used to characterize the acidity and basicity of the catalyst. In general, the probe molecule is adsorbed on the surface for 15 minutes shortly after the catalyst temperature is brought down to 373 K. This step is followed by extensive purging using 30 ml/min N_2 (Praxair) for 45 minutes. Spectra were then continuously recorded every minute during which time the temperature was increased to 723 K under 30 ml/min N_2 flow. CO_2 and NH_3 (Praxair) gas cylinder is used for delivery method, while pyridine delivery method involved bubbling N_2 through the pyridine saturator.

Methanol *operando* temperature programmed DRIFTS-MS sample preparation was carried out in a similar manner. The product was continuously monitored using a Cirrus 2 benchtop atmospheric pressure gas analysis system (MKS Instruments). Methanol was used because it can test and yield products formed at the acidic, basic and redox sites.[31] Briefly, after the catalyst activation step, the CH_3OH was preadsorbed on the sample surface as a saturated vapor at 4 °C using 50 ml/min helium as a carrier gas with a cell temperature of 100 °C for 30 minutes. The catalyst was subsequently flushed with pure helium at 30 ml/min for 1 hour. Spectra were then continuously recorded every minute, while the temperature was ramped up to 450 °C at a rate of 10 °C/min under He flow. Unless stated otherwise, reference spectra obtained at the corresponding temperatures were subtracted from the acquired spectra to eliminate contribution from the catalysts. Calibration of methanol and CO_2 was performed using a mixture of both products with He at different concentrations, while formaldehyde - by reactive calibration of methanol dehydrogenation over Cu/SiO_2 catalyst. The reaction was kept at low conversion to limit the occurrence of secondary reactions, forming such molecules as dimethoxymethane and methyl formate. A mass balance for the reaction system was then calculated to determine the response factor of the formaldehyde.

3.4. Reaction mechanism study using *in-situ* DRIFTS spectroscopy and TPRS

A Thermo Nicolet iS50 infrared spectrometer equipped with a Mercury-Cadmium-Tellurium (MCT) liquid nitrogen cooled detector was used with a Harrick **Praying Mantis™ diffuse reflection accessory and ZnSe windows** to study the nature of the hydroxyl groups, as well as the adsorbates on the catalyst surface. Catalyst activation is carried out according to the procedure mentioned in Section 2.3. To monitor reactive surface intermediates, ethanol was pre-adsorbed onto the sample surface as a saturated vapor at 298 K using 30 ml/min nitrogen as a carrier gas at 373 K for 20 minutes. Physisorbed molecules were removed with pure nitrogen at 30 ml/min for 40 minutes. Liquid ethanol (200 proof, Koptec), crotonaldehyde (Acros organics, +99%) and crotyl alcohol were used (Sigma, 96%). For acetaldehyde DRIFTS experiments, a gaseous mixture of 5% acetaldehyde in nitrogen (Praxair) was used. Crotonaldehyde and crotyl alcohol were handled with extra caution due to their toxicity. In particular, transporting the chemical was done in the hood to an enclosed, chilled bubbler (2-4°C). The enclosed, chilled bubbler was then installed to the gas flow delivery system while still being chilled. Chilled bubbler lowered the partial pressure of crotonaldehyde and crotyl alcohol, further limiting exposure to the vapor. Spectra were then continuously recorded every minute during which time the temperature was increased to 723 K with or without the continuous vapor flow of the reactants.

Four types of infrared spectra subtractions were applied. First, only instrumental background was subtracted from the catalyst spectra acquired. This method was used in **Figure 4.3**. Second, dehydrated catalyst spectra at 100 °C was subtracted from the spectra of the adsorbed reactants at different temperature. This method was used in **Figure 4.5**. Third, in temperature programmed desorption DRIFTS experiments, dehydrated catalyst spectra at the exact same temperature were subtracted from the spectra of the adsorbed reactant. This method was used in **Figures 4.4-7**. Fourth, in temperature programmed desorption DRIFTS experiments, in the presence of the vapor reactant, a spectrum containing catalyst and adsorbed surface species at 373 K was subtracted from the spectra containing contributions of the catalyst, adsorbed surface species and the vapor-phase at specific temperature. This method was used in **Figures 4.9-11**.

Temperature-programmed reaction spectroscopy (TPRS) was carried out using an Altamira Instruments system (AMI-200) connected to Dymaxion Dycor mass spectrometer (DME200MS). Approximately 30 mg of catalyst was loaded into a glass U-tube fixed-bed reactor and held in place by quartz wool. Prior to measurement, the catalyst was first pre-treated under 10% O2/Ar (Airgas, certified, 9.99% O2/Ar balance) at 500°C for 1 hour. After pretreatment, the catalyst temperature was brought down to 100°C. At this temperature, ethanol was preadsorbed for 15 minutes, followed by degassing using argon for 45 minutes. The vapor delivery system followed that of *in-situ* DRIFTS study. Finally, the fixed-bed reactor was heated at ~10°C/min to 450°C in the flowing reactant gases and the evolution of the products was monitored with the online mass spectrometer. Acetaldehyde was delivered using a mixture of 5% acetaldehyde in nitrogen (Praxair). Another experiment involved preadsorbing acetaldehyde on the surface of catalyst, followed by degassing with argon for 45 minutes, and temperature increase at 10°C/min to 450°C under constant ethanol/argon flow. The ethanol saturator is chilled at 2°C using ice bath at all times.

3.5. *Operando* XANES and EXAFS spectroscopy during ethanol reaction to 1,3-BD over Cu- and Zn-promoted MgO/SiO_2 catalysts

Operando X-ray absorption spectroscopy (XAS) was performed at the beamline BL2-2 at Stanford Synchrotron Radiation Lightsource (SSRL), SLAC National Accelerator Laboratory. The Cu and Zn K-edge data were collected in transmission mode. For the measurements, the sample powder was loaded into a quartz tube with 0.9 mm inner diameter and 1.0 mm outer diameter which was then mounted into the Clausen plug-flow reaction cell.[54] Ethanol vapor was delivered into the system using a temperature-controlled saturator to manipulate the space velocity. He was bubbled through the saturator and fed into the reactor. Prior to the spectroscopy study under reaction condition, the catalyst was pretreated at 450 °C for 1 hour under constant He flow. The *operando* measurements were done at 100, 200, 300 and 400 °C under constant ethanol flow. After reactor temperature reached 400 °C, the system was allowed to equilibrate for 2 hours and XAS spectra were repeatedly taken. The *operando* condition was ensured by allowing the vapor-phase into a dedicated RGA Mass Spectrometer (RGA, Stanford research system). Standard reference compounds, CuO (Alfa Aesar), ZnO (Alfa Aesar), Cu_2O (Alfa Aesar) and synthesized reference materials, i.e. CuMg, ZnMg, CuSi, and ZnSi, were pressed into the pellets and measured under ambient conditions.

References

(1) Kresse, G.; Hafner, J. *Phys. Rev. B* **1994**, *49* (20), 14251–14269.

(2) Kresse, G.; Furthmüller, J. *Comput. Mater. Sci.* **1996**, *6* (1), 15–50.

(3) Kresse, G.; Furthmüller, J. *Phys. Rev. B* **1996**, *54* (16), 11169–11186.

(4) Kresse, G.; Hafner, J. *Phys. Rev. B* **1993**, *48* (17), 13115–13118.

(5) Blöchl, P. E. *Phys. Rev. B* **1994**, *50* (24), 17953–17979.

(6) Perdew, J. P.; Burke, K.; Ernzerhof, M. *Phys. Rev. Lett.* **1996**, *77* (18), 3865–3868.

(7) Henkelman, G.; Jónsson, H. *J. Chem. Phys.* **1999**, *111* (15), 7010–7022.

(8) Heyden, A.; Bell, A. T.; Keil, F. J. *J. Chem. Phys.* **2005**, *123* (22), 224101/1-224101/14.

(9) Fukui, K. *J. Phys. Chem.* **1970**, *74* (23), 4161–4163.

(10) Fukui, K. *Acc. Chem. Res.* **1981**, *14* (12), 363–368.

(11) Hratchian, H. P.; Schlegel, H. B. *J. Phys. Chem. A* **2001**, *106* (1), 165–169.

(12) Jensen, F. *Introduction to Computational Chemistry*, 2nd ed.; John Wiley & Sons Ltd., 2006.

(13) Kvisle, S.; Aguero, A.; Sneeden, R. P. A. *Appl. Catal.* **1988**, *43* (1), 117–131.

(14) Angelici, C.; Weckhuysen, B. M.; Bruijnincx, P. C. a. *ChemSusChem* **2013**, *6* (9), 1595–1614.

(15) Larina, O.; Kyriienko, P.; Soloviev, S. *Catal. Letters* **2015**, 1–7.

(16) Zhang, M.; Gao, M.; Chen, J.; Yu, Y. *RSC Adv.* **2015**, *5* (33), 25959–25966.

(17) Janssens, W.; Makshina, E. V.; Vanelderen, P.; De Clippel, F.; Houthoofd, K.; Kerkhofs, S.; Martens, J. A.; Jacobs, P. A.; Sels, B. F. *ChemSusChem* **2014**, *8* (6), 994–1008.

(18) Angelici, C.; Meirer, F.; van der Eerden, A. M. J.; Schaink, H. L.; Goryachev, A.; Hofmann, J. P.; Hensen, E. J. M.; Weckhuysen, B. M.; Bruijnincx, P. C. A. *ACS Catal.* **2015**, *5* (10), 6005–6015.

(19) Angelici, C.; Velthoen, M. E. Z.; Weckhuysen, B. M.; Bruijnincx, P. C. A. *ChemSusChem* **2014**, *7* (9), 2505–2515.

(20) Che, M.; Tench, A. J. *Adv. Catal.* **1982**, *31*, 77–133.

(21) Sushko, P. V.; Shluger, A. L.; Catlow, C. R. A. *Surf. Sci.* **2000**, *450* (3), 153–170.

(22) Kantorovich, L. N.; Holender, J. M.; Gillan, M. J. *Surf. Sci.* **1995**, *343* (3), 221–239.

(23) Chizallet, C.; Petitjean, H.; Costentin, G.; Lauron-Pernot, H.; Maquet, J.; Bonhomme, C.; Che, M. *J. Catal.* **2009**, *268* (1), 175–179.

(24) Chizallet, C.; Bailly, M. L.; Costentin, G.; Lauron-Pernot, H.; Krafft, J. M.; Bazin, P.; Saussey, J.; Che, M. *Catal. Today* **2006**, *116* (2), 196–205.

(25) Di Valentin, C.; Del Vitto, A.; Pacchioni, G.; Abbet, S.; Wörz, A. S.; Judai, K.; Heiz, U. *J. Phys. Chem. B* **2002**, *106* (46), 11961–11969.

(26) Branda, M. M.; Rodríguez, A. H.; Belelli, P. G.; Castellani, N. J. *Surf. Sci.* **2009**, *603* (8), 1093–1098.

(27) Bailly, M.; Chizallet, C.; Costentin, G.; Krafft, J.; Lauronpernot, H.; Che, M. *J. Catal.* **2005**, *235* (2), 413–422.

(28) Baltrusaitis, J.; Hatch, C.; Orlando, R. *J. Phys. Chem. A* **2012**, *116* (30), 7950–7958.

(29) Haas, P.; Tran, F.; Blaha, P. *Phys. Rev. B* **2009**, *79* (8), 85104.

(30) Wu, C.-M.; Baltrusaitis, J.; Gillan, E. G.; Grassian, V. H. *J. Phys. Chem. C* **2011**, *115* (20), 10164–10172.
(31) Badlani, M.; Wachs, I. E. *Catal. Letters* **2001**, *75* (3–4), 137–149.

Chapter 3

Computational Study of Ethanol to 1,3-BD Reaction Mechanisms

Abstract

In this work, we performed periodic Density Functional Theory calculations and explored reactive pathways of ethanol catalysis to catalytically form 1,3-butadiene on undoped MgO surface. We have identified critical reactive intermediates, as well as thermodynamic and kinetic barriers involved in the overall reactive landscape. The overall free energy surface was explored for the highly debated reaction mechanisms, including Toussaint’s aldol condensation mechanism, Fripiat’s Prins mechanism and mechanism based on Ostromislensky’s hemiacetal rearrangement. Thermodynamics and kinetics data calculated showed four rate limiting steps in the overall process. In particular, ethanol

dehydration to form ethylene possessed lower energy barrier than dehydrogenation to yield acetaldehyde suggesting competing reactive pathways. C-C bond coupling to form acetaldol (3-hydroxybutanal) is preceded with 16 kcal/mol forward reaction barrier. Direct reaction of ethylene and acetaldehyde proceeds with a free energy barrier of 29 kcal/mol suggesting that Prins condensation is an alternative route. Finally, thermodynamic stability of 1-ethoxyethanol prevents further reaction via hemiacetal rearrangement. The results here provide a first glimpse into the overall 1,3-butadiene formation mechanism on undoped MgO reactive sites in light of the vast literature discussing variety of the proposed mechanistic pathways mostly based on conventional homogenous organic chemistry reactions.

1. Introduction

Since the rapid expansion of coal industry in the 18th century World has relied on non-renewable sources for organic chemicals [1]. Currently, petroleum and natural gas are the main feedstocks of relatively inexpensive carbon source [2]. Biomass can serve as a sustainable and renewable carbon source to generate chemicals and bio derived ethanol catalytic upgrading has been proposed as a viable route for biomass valorization [3,4]. In particular, ethylene, propylene, ethyl acetate, n-butanol and isobutene are some of the high value chemicals that can be derived from ethanol [5–14]. Furthermore, 1,3-butadiene, the most important monomer for synthetic rubber, has been produced via catalytic processing of ethanol during World War II in USSR and USA, using Lebedev and Ostromislensky processes, respectively [15]. The former utilized catalytic conversion of ethanol to 1,3-

butadiene via one-step on MgO/SiO_2 catalysts [16], while the latter utilized a two-step process with the first step ethanol dehydrogenation to acetaldehyde over Cu/SiO_2 catalysts [3,17] followed by acetaldehyde and ethanol coupling to 1,3-butadiene over a tantalum-based catalyst. Catalysts for the one-step process were reported to have achieved ~50-60% yield [18,19], while the two-step process could attain over 60% yield, with purity of about 98-99% at 300-350°C. Recent abundance of shale gas resulted in a different catalytic cracker product distribution dominated by ethylene [3]. This caused a worldwide shortage of C4 hydrocarbons, such as 1,3-butadiene. Since ethanol can be produced using variety of biomass sources including fermentation and gasification, it recently emerged as the green route to catalytically form 1,3-butadiene [3,4].

The biggest obstacle in ethanol catalysis to form 1,3-butadiene is relatively low selectivity and the resulting yields of the desired product. Angelici *et al.* reported 74% conversion with 49% selectivity on $CuO/MgO\text{-}SiO_2$, while Makshina *et al.* described a similar catalyst that attained 97.5% conversion with 58.2% selectivity [18,20]. Most recently, a CuO/HfO/ZnO catalyst was reported to have achieved 99% conversion with 71.1% selectivity, e.g. ~70% yield [19]. In general, doped-MgO supported on silica [18,20–29] (Lebedev's catalyst) or mixed (supported) oxides [16,19,30–36] were used. Various transition metal dopants (Zn, Cu, and Ag) were used to improve MgO/SiO_2 catalyst performance, as well as different synthesis methods and composition of MgO/SiO_2 were investigated, such as Kvisle's wet kneading method [26] and the utilization of clay and sepiolite as the support [21,28]. However, multitude of byproducts, including ethylene, C4 oxygenates and olefins, diethyl ether, acetaldehyde and even acetone are still detected implying high separation. This lack of the kinetic control over the ethanol-to-1,3-butadiene catalytic process and poor understanding of the fundamental mechanistic steps involved have hindered the development of catalysts with reasonable performance. The generally accepted one-step catalytic mechanism involves dehydrogenation of ethanol to acetaldehyde which then undergoes C-C coupling via aldol condensation mechanism to yield crotonaldehyde. Crotonaldehyde is further hydrogenated via MPV (Meerwein-Ponndorf‑Verley) reduction with ethanol and the resulting crotyl alcohol is dehydrated give butadiene[37,38] as shown in **Figure 3.1a**. In addition, Fripiat and Ostromislensky proposed two other possible reaction pathways [39,40]. Fripiat suggested Prins-like mechanism involving both dehydration and dehydrogenation reactions producing ethylene and acetaldehyde, as shown in **Figure 3.1b**. The C=O group is hydroxylated in the presence of Brønsted acid and reacts with ethylene opening the double bond. The resulting 3-buten-2-ol is then dehydrated to yield 1,3-butadiene [40]. Ostromislensky's version of the reaction mechanism shown in **Figure 3.1c** involves the hemiacetal rearrangement between ethanol and acetaldehyde to yield 1-ethoxyethanol that later converts to butane-1,3-diol [3]. Two computational studies by Chieregato *et al.* [41] and Zhang *et al.* [42] attempted to unravel the overall reaction mechanism. Zhang *et al.* performed calculations using density functional generalized gradient approximation (GGA) and focused on the very first step of the mechanism, e.g. dehydrogenation of the alcohol. Stepped MgO surface was predicted to have lower energy barrier than flat surface for this reaction [42]. Chieregato *et al.*, on the other hand, proposed an entirely different mechanism using cluster type calculations and Gaussian basis set. They ruled out crotonaldehyde and crotyl alcohol as possible intermediates and concluded that acetaldehyde would react with a carbanion resulting from ethanol C-H cleavage. In this work we performed ethanol catalytic coupling to 1,3-butadiene using a kink Mg atom at a step-edge MgO (100) as a model catalyst surface in accordance with the recent works that suggest MgO as a bifunctional catalyst [43–53]. The energetics and structure of key reactive intermediates, e.g. acetaldehyde, crotonaldehyde, and crotyl alcohol, for Lebedev's reaction [16] based on the proposed mechanism by Toussaint *et al*. [38,54], as well as the proposed Fripiat's Prins and Ostromislensky mechanistic pathways were explored to determine the kinetic limitations of ethanol catalytic coupling to 1,3-butadiene on MgO.

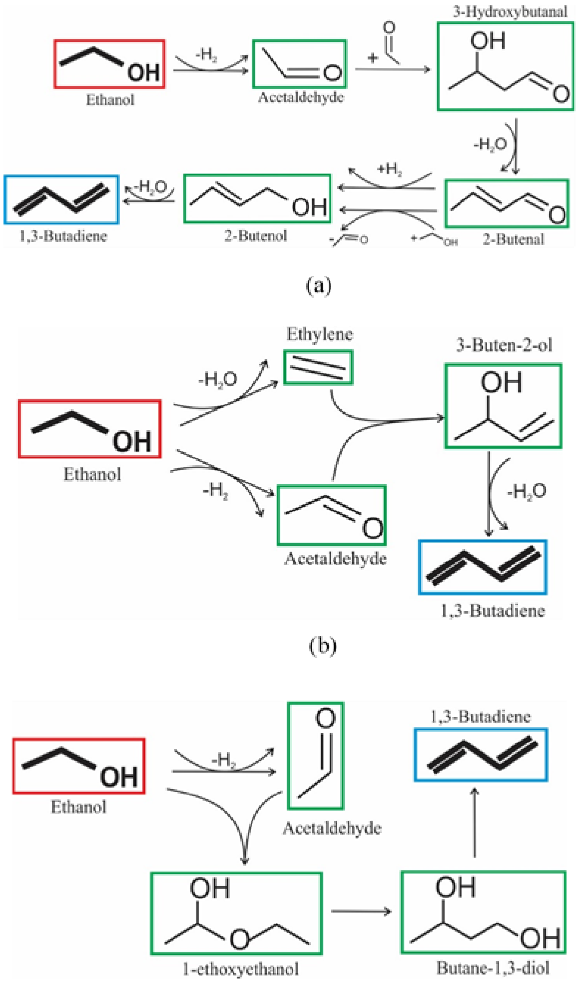

(a)

(b)

(c)

Figure 3.1. Reaction mechanisms proposed for ethanol to 1,3-butadiene; (a) Toussaint's generally accepted mechanism, (b) Fripiat's Prins mechanism, (c) Ostromislensky's hemiacetal rearrangement.

2. Computational results

2.1. Reaction Pathways

2.1.1. Ethanol Dehydrogenation and Dehydration

We begin with the first step of ethanol catalytic transformation into acetaldehyde or into ethylene for which the computed free-energy profiles are shown in **Figure 3.3**. States 1A-1C and 5A-5C in **Figure 3.2** demonstrate the reaction pathways for ethanol dehydrogenation and dehydration to form acetaldehyde and ethylene, respectively. The corresponding TSs are labelled as 1B(TS) and 5B(TS). In both cases the reaction starts from the structures formed upon spontaneous dissociative adsorption of ethanol whereby proton is abstracted either by the edge or terrace oxygen atoms. The calculated relative free energies for the configurations 1A and 5A are -13.5 and -10.5 kcal/mol, respectively, at 450 ^{o}C. In 1B TS, the surface bound proton becomes coordinated to the proton leaving α-carbon atom. The H….H distance is 0.84 Å, which is 0.07 Å longer than the equilibrium H-H bond distance in hydrogen molecule in 1C. Compared to 1A, the distance between the hydrogen atom and lattice O_{4C} has significantly increased from 0.98 Å to 1.61 Å. Furthermore, acetaldehyde is coordinated to Mg_{3c} via oxygen atom while also accepting some electron density from in the terrace O_{5c} resulting in a distorted chemisorbed structure. During the dehydration step hydrogen atom is adsorbed on terrace oxygen atom as shown in Fig. 3.2 (5A). During the reaction over transition state 5B one of the β-hydrogen atoms becomes oriented towards O_{4C} with C-H and O_{4C}-H of 1.45 and 1.22 Å, respectively. The final state 5C results in two hydroxyl groups formed on the MgO surface with ethylene molecule loosely coordinated to the surface. Relative electronic energies at T=0 K and the corresponding free energy values at 450 ^{o}C for the reaction profile shown in **Figure 3.3** are provided in **Table 3.1**. In particular, at 450°C the forward free-energy barrier for the reaction 1A → 1C is 39.6 kcal/mol while the barrier for the reverse barrier is only 20.5 kcal/mol suggesting that the acetaldehyde formation is endergonic. Ethylene formation via 5A → 5C has barrier 33.5 kcal/mol but the reverse barrier is higher with 38.3 kcal/mol. While both acetaldehyde and ethylene are typically observed as reaction byproducts of ethanol catalytic coupling [18,20,22–25], the stability of ethylene vs acetaldehyde is intriguing but not surprising. Ethanol is known to undergo intramolecular dehydration in the presence of acidic and basic surface sites [55], while acetaldehyde formation in general needs redox metals [56]. Hence for undoped MgO catalyst ethylene generation is expected and preferred over acetaldehyde.

The reaction pathways of ethanol dehydration and dehydrogenation products further proceed via two main reaction mechanisms discussed in detail in Sec.3.1.2 and 3.1.3: aldol condensation and Prins condensation reaction. The aldol condensation pathway entails acetaldehyde transformation into its enolate form followed by the reaction with the molecular acetaldehyde to form a C-C bond. The resulting C4 intermediate then undergoes several steps of intermolecular proton transfer with the surface and ethanol to yield 1,3-butadiene. Prins condensation entails C-C bond formation via reaction of acetaldehyde and ethylene followed by proton transfer steps. In these mechanisms, the proton diffusion through the surface leads to water release from the surface.

Table 3.1 Electronic and free energy values of the stationary points calculated at 0 K and 723 K, respectively.

State	Electronic energy (kcal/mol)	Referenced free energy (kcal/mol)	State	Electronic energy (kcal/mol)	Referenced free energy (kcal/mol)
1A	-40.6	-13.5	4F	-45.3	-8.1
1B	3.9	26.2	4G	-43.2	-6.1
1C	-16.6	5.6	4H	-52.0	-46.2
2A	-14.3	-8.5	4I	-37.8	-37.7
2B	4.1	7.4	4J	-5.5	-5.3
2C	-22.2	-20.3	4K	-18.7	-24.0
2D	-17.7	-17.3	5A	-39.9	-10.5
2E	-26.2	-28.8	5B	-2.6	23.0
2F	-22.5	-23.7	5C	-32.0	-15.3
2G	-15.9	-7.6	6A	11.6	-0.2
2H	-19.4	-10.8	6B	25.6	28.6
2I	-12.5	-1.6	6C	-34.8	-22.9
2J	-11.4	-1.6	6D	3.7	15.8
2K	-6.2	4.2	6E	-26.8	-18.9
2L	-15.4	-8.2	6F	9.5	15.3
2M	9.3	15.7	6G	-6.0	-0.7
2N	2.2	3.2	6H	-4.4	-2.9
2O	6.8	-18.2	6E i	-21.8	-16.0
3A	-24.1	-18.8	6E ii	-30.5	-27.2
3B	-14.6	-6.8	6E iii	-32.5	-27.3
3C	-19.8	-15.2	6E iii 1	2.2	5.6
3D	-27.3	-27.8	6E iii 2	-13.8	-9.6
3E	-1.3	-0.2	6E iii 3	-11.5	-12.7
3F	-15.4	-15.4	6E iv	43.9	44.3
3G	-15.6	-20.4	6E v	-21.4	-25.4
4A	-53.1	-14.6	7A	-51.2	-26.4
4B	-52.5	-4.8	7B	-30.6	2.5
4C	-64.4	-22.1	7C	-33.4	3.9
4D	-68.3	-32.0	7D	-30.5	6.4
4E	-42.5	-5.8	7E	-44.8	-8.7

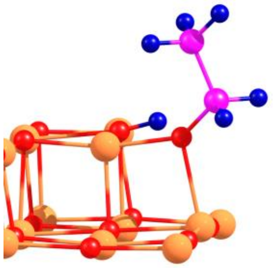	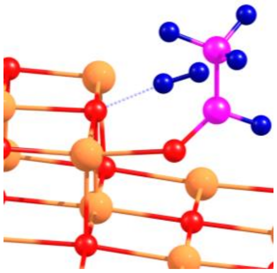	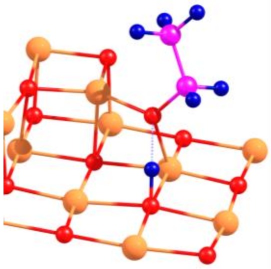	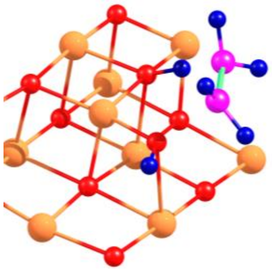
1A	1B (TS)	5A	5B (TS)
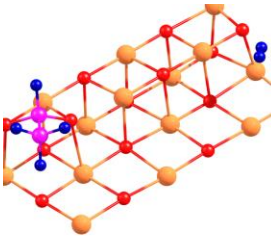		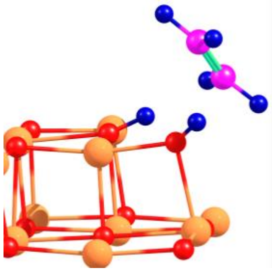	
1C		5C	
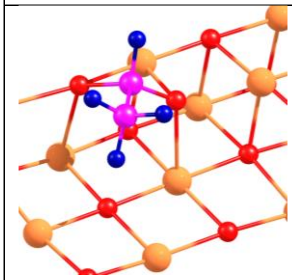	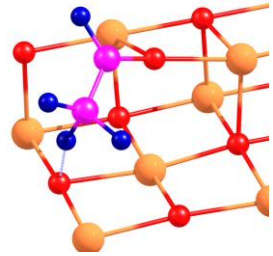	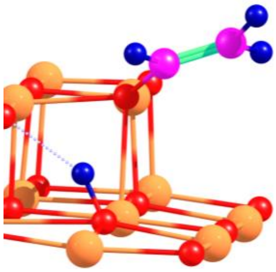	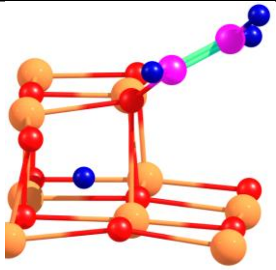
2A	2B (TS)	2C	2D (TS)
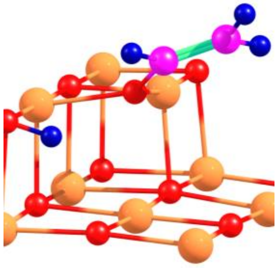	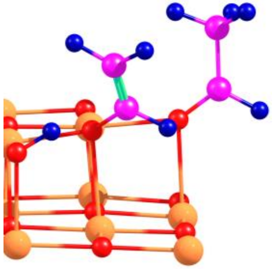	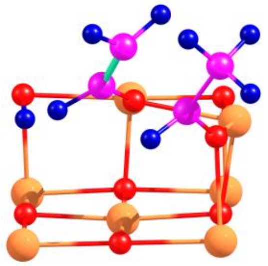	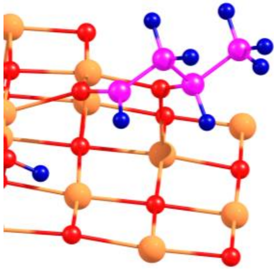
2E	2F	2G (TS)	2H
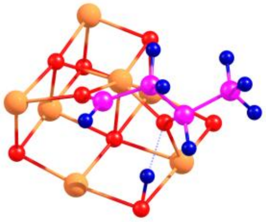	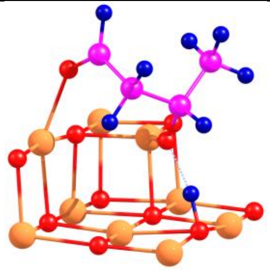	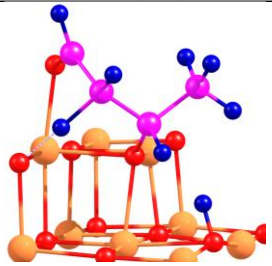	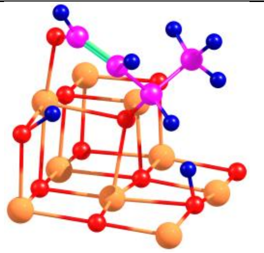
2I	2J	2K (TS)	2L

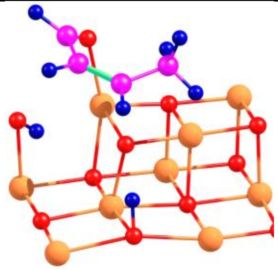	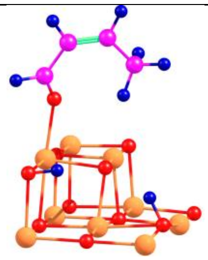	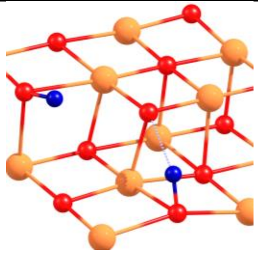	
2M (TS)	2N	2O	
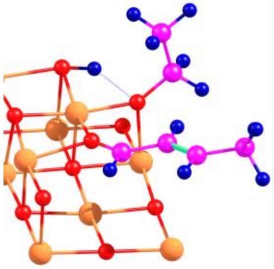	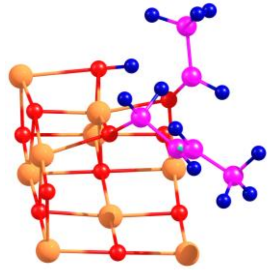	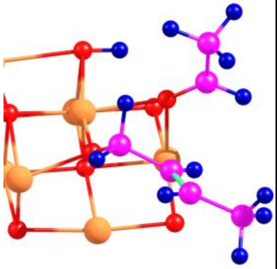	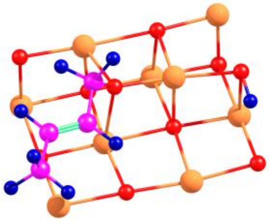
3A	3B (TS)	3C	3D
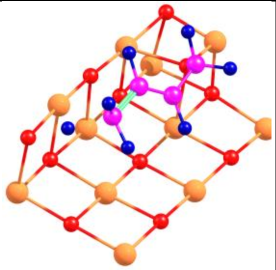	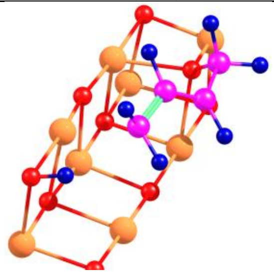	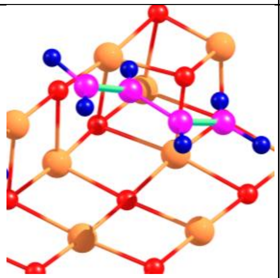	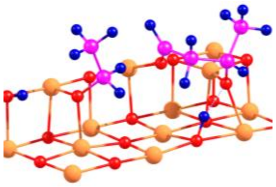
3E (TS)	3F	3G	4A
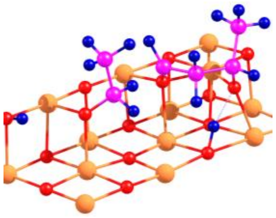	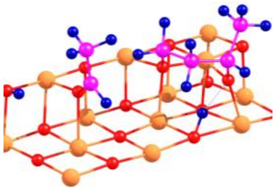	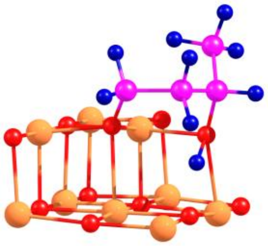	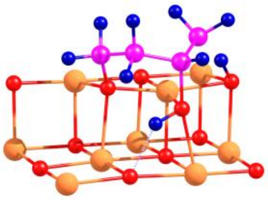
4B (TS)	4C	4D	4E (TS)
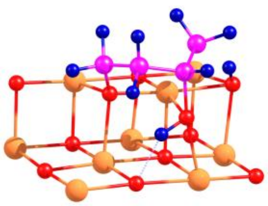	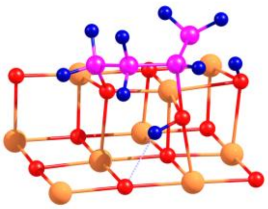	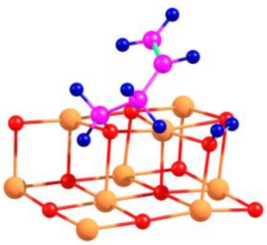	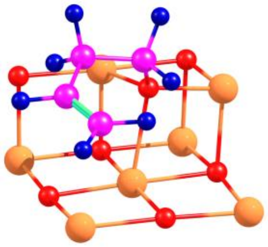
4F	4G (TS)	4H	4I

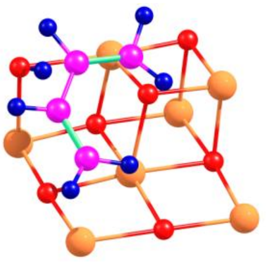	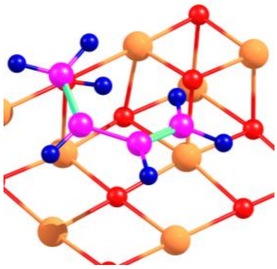		
4J (TS)	4K		
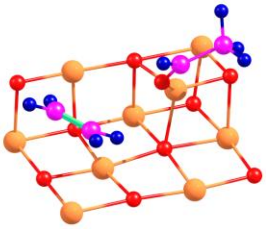	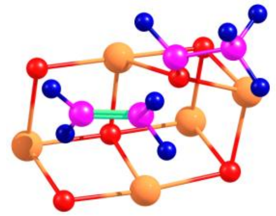	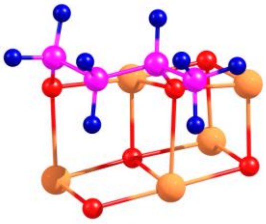	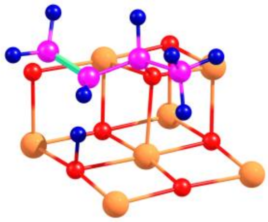
6A	6B (TS)	6C	6D (TS)
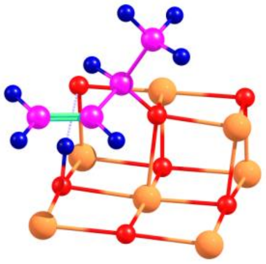	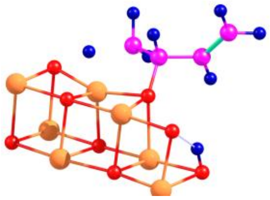	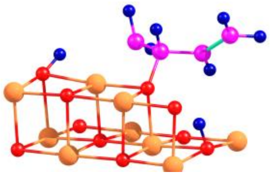	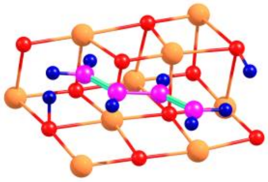
6E	6F (TS)	6G	6H
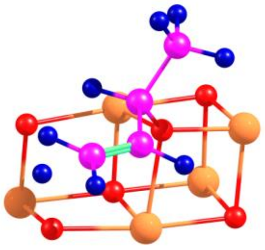	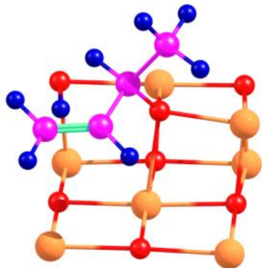	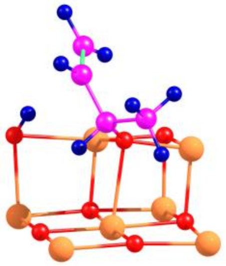	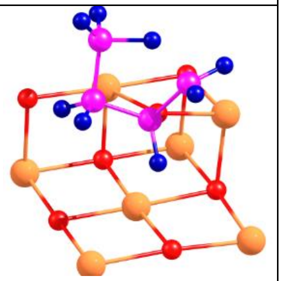
6E i (TS)	6E ii	6E iii	6E iv (TS)
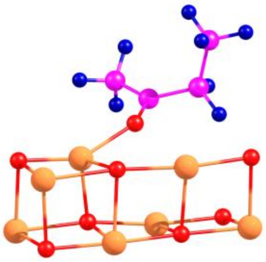	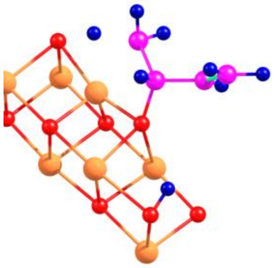	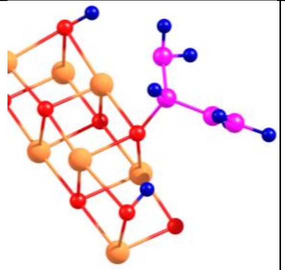	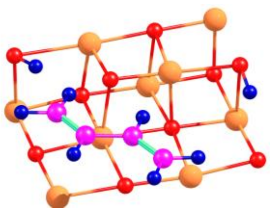
6E v	6E iii 1 (TS)	6E iii 2	6E iii 3

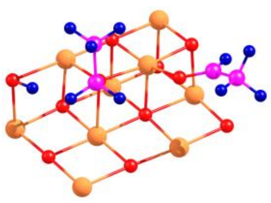	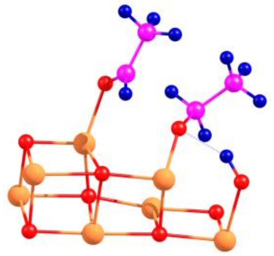	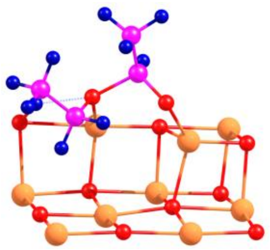	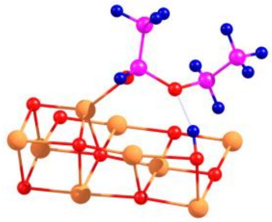
7A	7B (TS)	7C	7D (TS)
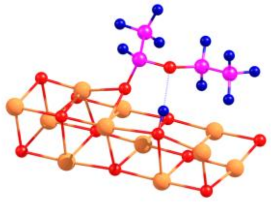			
7E			

Figure 3.2 All stable intermediates and transition states calculated following the reaction pathways. (1A-1C): ethanol dehydrogenation to acetaldehyde; (2A-2O): acetaldehyde aldol condensation to 3-hydroxybutanal (acetaldol) followed by proton transfer to crotonaldehyde; (3A-3G): MPV (Meerwein–Ponndorf–Verley) reduction of crotonaldehyde to 1,3-butadiene; (4A-4K): acetaldol MPV reduction to butadiene; (5A-5C): ethanol dehydration to ethylene; (6A-6E iii 3): Prins condensation of acetaldehyde and ethylene; (7A-7E): ethanol and acetaldehyde nucleophilic addition reaction (Ostromislensky's hemiacetal rearrangement).

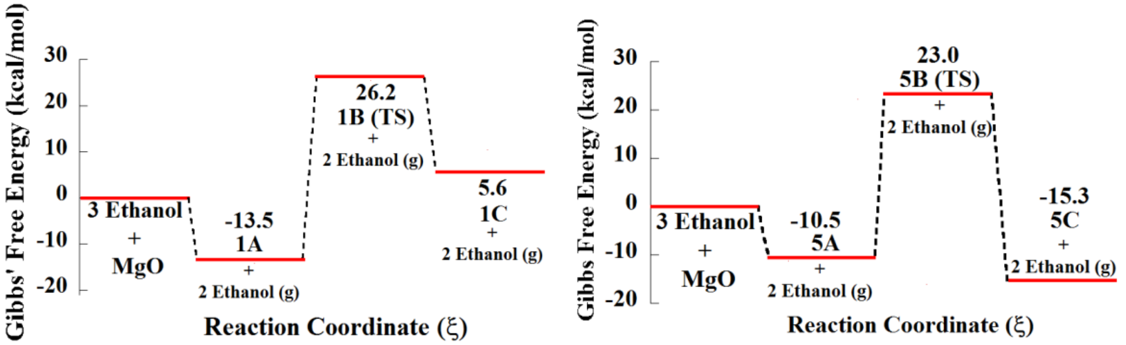

(a) (b)

Figure 3.3 Free-energy profiles for (a) ethanol dehydrogenation to form acetaldehyde and (b) ethanol dehydration to ethylene.

2.1.2. Aldol condensation

Classical aldol condensation mechanism requires one of the acetaldehyde molecules to be in its enolate state.[57] In this work the enolate state 2C (see Fig. 3.2) was obtained via proton transfer of β-hydrogen to terrace atom O_{5C} yielding a hydroxyl group via low energy barrier 2B TS from the initial stable strongly adsorbed acetaldehyde molecule in 2A with free-energy of -8.5 kcal/mol relative to the reference state. The forward barrier for the reaction step 2A → 2C is 16 kcal/mol as shown in **Figure 3.4**. This mechanism is facilitated by the C=O bond elongated from 1.21 Å[58] to 1.43 Å due to strong interaction with the surface oxygen atoms. In TS configuration, one of hydrogen atoms from the methyl group establishes a hydrogen bond with surface oxygen atom causing an elongation of the corresponding C-H bond from 1.10 to 1.29 Å. State 2C represents a stable configuration with sp^2 hybridized carbon enolate atoms and surface hydroxyl group.

For the aldol condensation to take place, the hydrogen atom bound to the surface needs to be in a close proximity to the enolate molecule requiring it to diffuse to the edge O_{4C} atom. This transition proceeds via transition state structure 2D with the forward barrier of only 3 kcal/mol. The next step is the physisorption of a second acetaldehyde molecule on the surface in 2F, preceding the C-C bond formation via aldol condensation (2F-2H). The TS for this step (the structure 2G) shows the coordination between enolate and acetaldehyde with the reactive β-carbon of enolate and the α-carbon of acetaldehyde adsorbed on surface site Mg_{3C} establish a C-C bond of length of 2.07 Å. The forward IRC analysis for this reaction shows the formation of C-C bond between the two reactive carbon atoms. The length of the latter bond in the stable structure 2H is 1.64 Å. Formation of the acetaldol (3-hydroxybutanal) in 2H is preceded with forward reaction barrier of 16.1 kcal/mol.

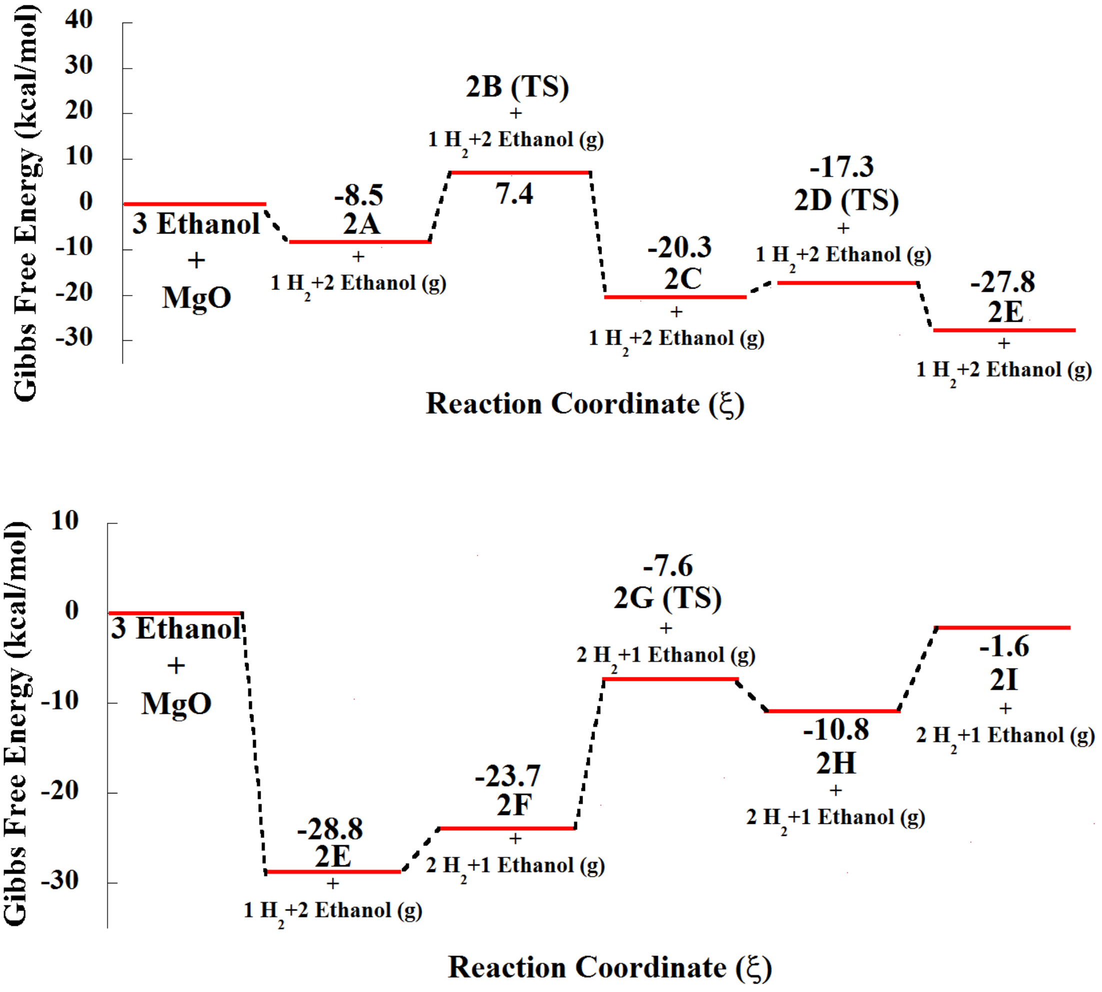

Figure 3.4 Free-energy profiles for aldol condensation

Once 3-hydroxybutanal is formed, the aldol needs to lose a hydrogen atom to the surface to undergo dehydration to yield crotonaldehyde. For this step to take place, a reactive O_{4C} is required. Assuming transient proton diffusion between O_{4C} and O_{5C} atoms, proton abstraction takes place followed by the transformation of the trans-isomer, as depicted in 2I, into 2J via aergonic steps. The activation energy from cis- to trans-crotonaldehyde reported is ~13 kcal/mol [59]. The molecule subsequently loses hydrogen atoms to the MgO surface via step 2J→2L ($\Delta G_{A,forward}$ = 5.9 kcal/mol) and desorbs from the surface after breaking the C-O bond via sequence 2L→2M(TS)→2O ($\Delta G_{A,forward}$ = 24 kcal/mol) yielding the structure 2O with a newly formed surface site O_{3c} which under reactive conditions can recombine with protons to form H_2O reforming the original Mg_{3c} site.

Formation and desorption of crotonaldehyde in 2N-2O agrees very well with the occasional gas phase byproduct observations [22,37]. Formation of the O_{3C} surface site in 2O is followed by the water molecule formation, which is another product of ethanol coupling reactions. The next step in the overall mechanism is the MPV reduction of crotonaldehyde by ethanol (3A→3C) to form adsorbed acetaldehyde in 3C followed by its desorption and proton transfer to the surface (3C→3G) to form 1,3-butadiene. The corresponding free-energy profile (2H → 2O → 3A → 3G) is shown in **Figure 3.5**. The highest barrier that we determined within this sequence was that of proton transfer to the surface in 3E TS with 27.6 kcal/mol. Reduction of the unsaturated aldehyde by hydrogen was assumed not to take place as confirmed by the measured hydrogen content in the reaction products [30] and due to the gas-phase thermodynamic calculation which favors the reduction by ethanol [3]. Dissociation of hydrogen on the defected MgO surface itself is a non-spontaneous process with a relatively low activation barrier of 2.8 kcal/mol [60] whereas ethanol dissociation on Mg_{3c} is spontaneous as shown in Figure 3.2. Additionally, the heterolytic dissociation can only be stabilized on a high density of 3-coordinated sites which suggests small amount of surface hydrogen [61].

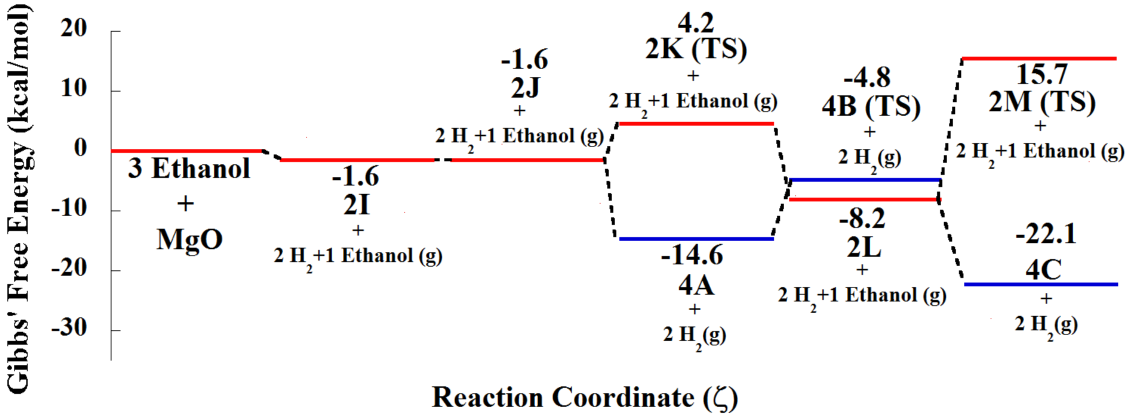

Gibbs' Free Energy (kcal/mol)
20
10
0
-10
-20
-30
Reaction Coordinate (ζ)
3 Ethanol + MgO
-1.6 2I + 2 H_2+1 Ethanol (g)
-1.6 2J + 2 H_2+1 Ethanol (g)
4.2 2K (TS) + 2 H_2+1 Ethanol (g)
-14.6 4A + 2 H_2(g)
-4.8 4B (TS) + 2 H_2(g)
-8.2 2L + 2 H_2+1 Ethanol (g)
15.7 2M (TS) + 2 H_2+1 Ethanol (g)
-22.1 4C + 2 H_2(g)

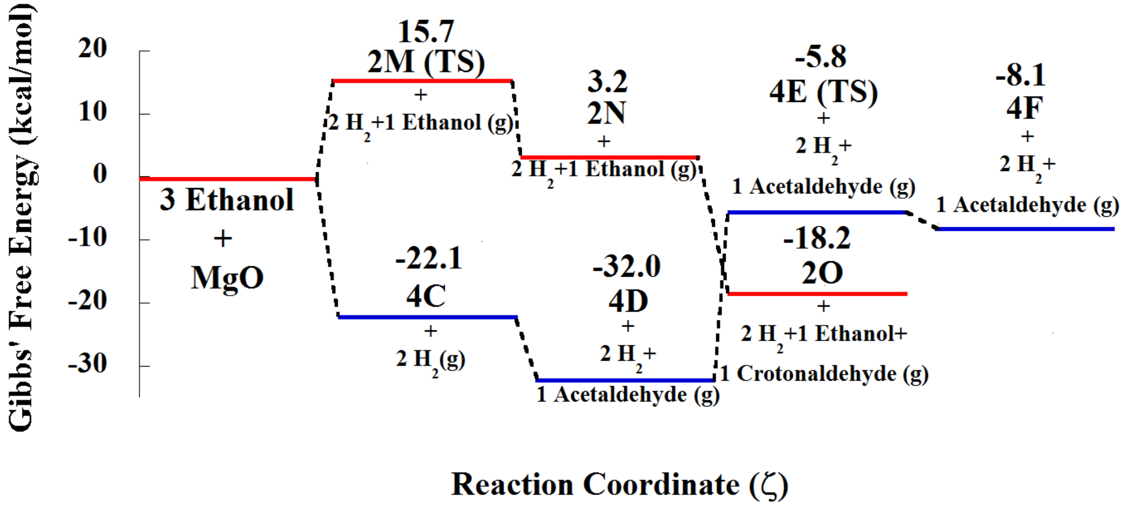

Gibbs' Free Energy (kcal/mol)
20
10
0
-10
-20
-30
Reaction Coordinate (ζ)
3 Ethanol + MgO
15.7 2M (TS) + 2 H_2+1 Ethanol (g)
-22.1 4C + 2 H_2(g)
3.2 2N + 2 H_2+1 Ethanol (g)
-32.0 4D + 2 H_2+ 1 Acetaldehyde (g)
-5.8 4E (TS) + 2 H_2+ 1 Acetaldehyde (g)
-18.2 2O + 2 H_2+1 Ethanol+ 1 Crotonaldehyde (g)
-8.1 4F + 2 H_2+ 1 Acetaldehyde (g)

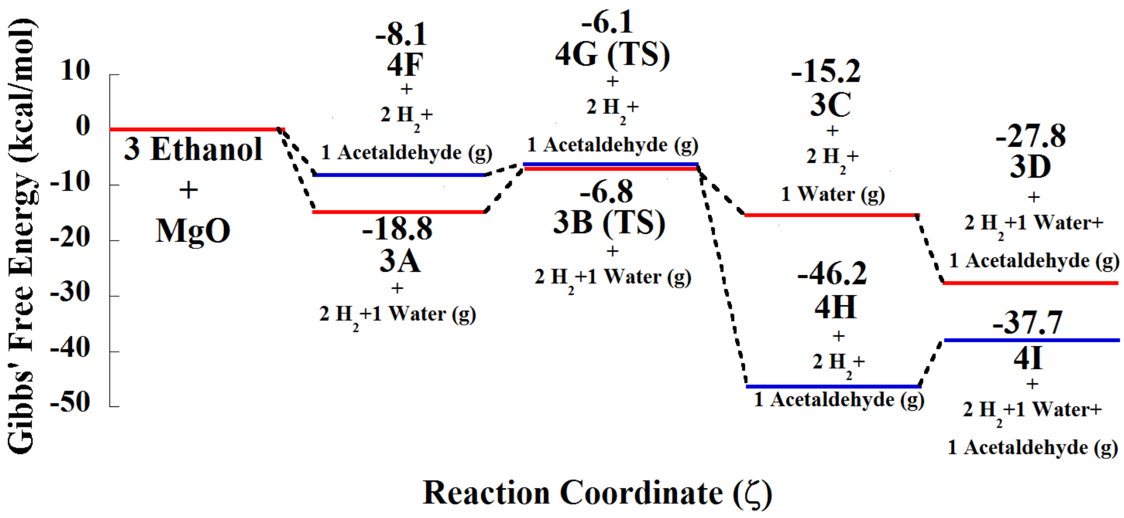

Gibbs' Free Energy (kcal/mol)
10
0
-10
-20
-30
-40
-50
Reaction Coordinate (ζ)
3 Ethanol + MgO
-8.1 4F + 2 H_2+ 1 Acetaldehyde (g)
-18.8 3A + 2 H_2+1 Water (g)
-6.1 4G (TS) + 2 H_2+ 1 Acetaldehyde (g)
-6.8 3B (TS) + 2 H_2+1 Water (g)
-15.2 3C + 2 H_2+ 1 Water (g)
-46.2 4H + 2 H_2+ 1 Acetaldehyde (g)
-27.8 3D + 2 H_2+1 Water+ 1 Acetaldehyde (g)
-37.7 4I + 2 H_2+1 Water+ 1 Acetaldehyde (g)

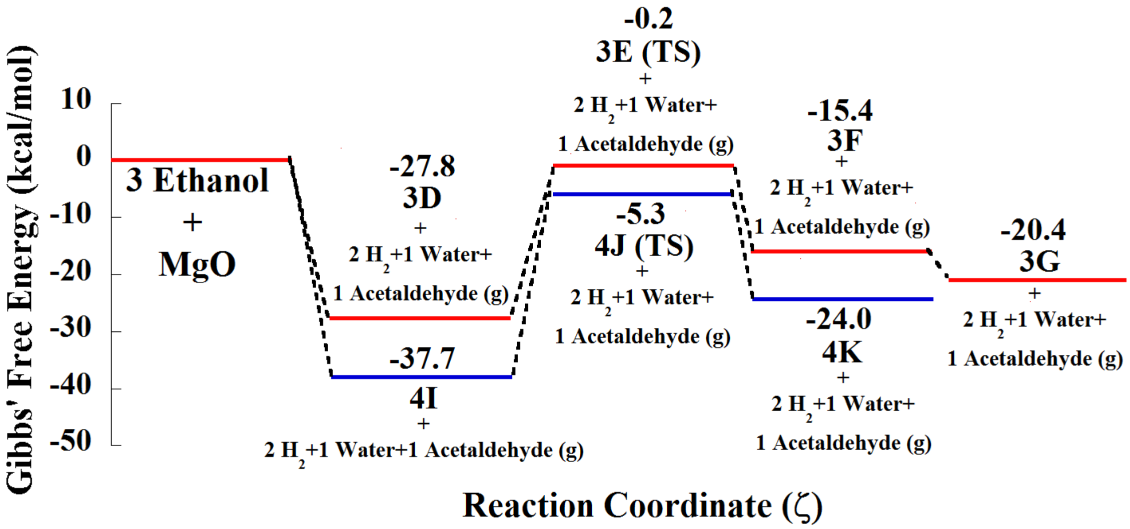

Figure 3.5 Free-energy profiles for the MPV reduction of the resulting molecule from aldol condensation. Red pathway indicates subsequent proton transfer of acetaldol followed by MPV reduction of the crotonaldehyde; Blue pathway shows the direct MPV reduction of the resulting acetaldol.

Alternatively, the 1,3-butadiene formation mechanism proposed earlier by Ostromislensky (also *vide infra*) involves the hemiacetal rearrangement [39]. It was argued that ethanol can react with acetaldehyde to form 1-ethoxyethanol which will then undergo rearrangement to butane-1,3-diol and further dehydrate to 1,3-butadiene. However, this mechanism has been rebuffed by Quattlebaum *et al.* [37]. The formed C-O-C bond, if it is to be rearranged to make C-C bond, would lead to its dissociation. The identified butane-1,3-diol, however, could be formed when acetaldol is reduced by ethanol, as shown in **Figure 3.5** 4A-4C. State 4C is effectively dissociated (adsorbed) butane-1,3-diol which is formed via series of exergonic steps 2J-4A-4B TS-4C with a very low forward free-energy barrier of 9.8 kcal/mol. The resulting adsorbed butane-1,3-diol can further undergo several steps of proton transfer to yield 1,3-butadiene (4C-4K). In this situation, there are three competing processes with transition states 4E, 4G, and 4J. The reaction channel with TS 4G breaks a C-O bond of the adsorbed butane-1,3-diol. The reaction 4F→4H is extremely exergonic with very low free-energy of activation (~2 kcal/mol). It is preceded by the 4E TS and the free-energy of activation of 26.2 kcal/mol, which is a typical value to that of sp^3 proton transfer to the reactive surface O4c atoms. The last step of this condensation mechanism is the simultaneous C-O bond breaking and proton transfer to the surface (4I→4K). Fig. 3.2 (4J) depicts a transition state where the 1,3-butadiene is desorbing from the surface. Interestingly, the two different MPV reduction steps yield two different conformations of 1,3-butadiene. MPV reduction of crotonaldehyde gives s-trans conformation, while that of acetaldol results in s-cis conformation (structures 3G and 4K, respectively, see Fig. 3.2). The stable conformation is, however, trans 1,3-butadiene, which makes an additional step for acetaldol reduction necessary. This last step will be cis/trans isomerization to trans 1,3-butadiene with rather low free-energy of activation of only ~4 kcal/mol [62].

2.1.3. Prins condensation

Our data shown in Figure 3.2 suggest that on undoped MgO the ethylene formation from ethanol will compete with that of acetaldehyde. Prins condensation is among the early proposed mechanisms for ethanol reaction to 1,3-butadiene.[40] The explicit ethanol reaction mechanism on MgO via Prins mechanism is studied in this work and the corresponding results are presented in this section. The corresponding structures are shown in **Figure 3.2** (6A-6E) whereas the free-energy reaction profiles are displayed in **Figure 3.6**. The Prins condensation pathway is the formation of C-C bond by opening the double C=C and C=O bonds of both ethylene and acetaldehyde, respectively (6A-6C). 6B TS represents the double bond opening of C=O with the oxygen coordinated between two surface Mg atoms (Mg_{4C} and Mg_{3C}). This charge transfer to the MgO surface makes the α-carbon susceptible to attack by the sp^2 carbon molecule. The intermolecular C-C distance is now 1.90 Å, while that of the aldehyde C-O bond is elongated by 0.1 Å. The double bond opening results in a C4 structure bound to the surface, as shown in Fig. 3.2 (6C). The corresponding forward free-energy barrier is 28.8 kcal/mol. This C-C coupling step is then followed by the proton transfer to the surface atom O_{5c} and the simultaneous C-$O_{lattice}$ bond breaking (see Fig. 3.2 (6C-6E)) followed by another proton transfer from the terminal sp^3 carbon to the O_{4c} surface atom (see Fig. 3.2 (6E-6G)). The free-energy barriers for these steps are of 38.7 and 34.1 kcal/mol, which are typical values for proton transfer reactions considered in this work. The structure 6H represents the desorbed structure of 1,3-butadiene.

An alternative pathway for transformation of the structure 6E is that via transition state 6E i leading to the product 6E ii (see Fig. 3.2). Here instead of the subsequent proton transfer from the terminal carbon (as in the reaction 6E→6G) the surface proton diffuses from planar surface atom O_{5c} to a nearby edge atom O_{4c} via low forward barrier of 2.9 kcal/mol. The terminal proton transfer then takes place, as depicted in Fig. 3.2 (6E iii, 6E iii 1, 6iii 2) and the computed free-energy of activation (32.9 kcal/mol) is comparable to that for steps alternative pathway (6C→6E and 6E→6G). Interestingly, a cyclic TS can also be established in another variant of this mechanism, see Fig. 3.2 (6E iv). This mechanism yields a physisorbed molecule as a product, which is similar to methylethyl ketone (MEK) shown in Fig. 3.2 (6E v). However, this step has rather large forward activation energy of 71.6 kcal/mol.

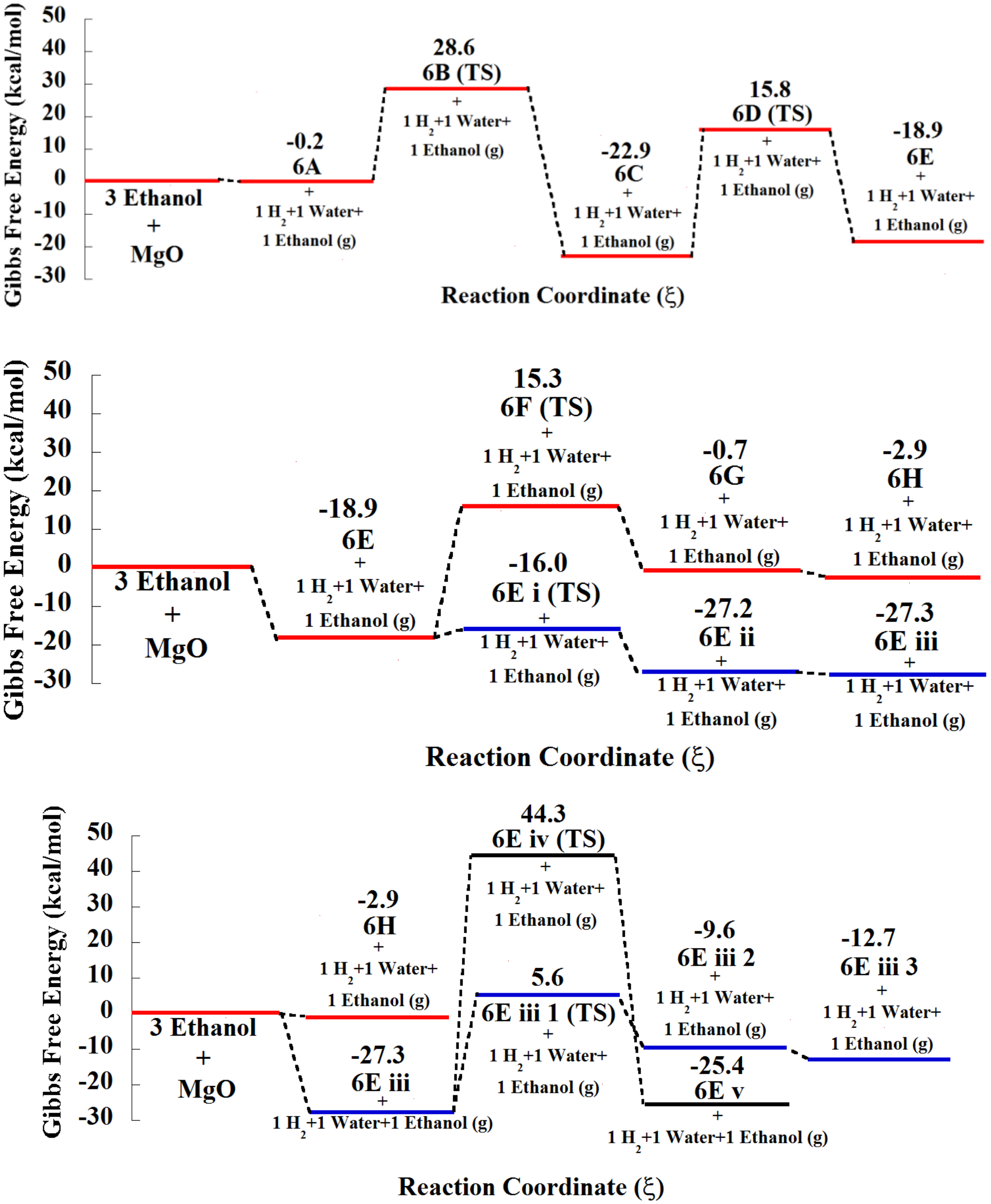

Figure 3.6 Free-energy profiles for the Prins condensation between ethylene and acetaldehyde. Red pathway indicates a typical route of Prins condensation; Blue pathway shows an additional proton diffusion step in between the reaction steps; Black pathway shows the unlikely formation of MEK.

2.1.4. 1-ethoxyethanol formation

Final major reaction mechanism considered in this study is the Ostromislensky's hemiacetal rearrangement which will be discussed in this section. The very first step in this case is the reaction of ethanol and acetaldehyde to yield 1-ethoxyethanol, which was further postulated to undergo a molecular rearrangement to form butane-1,3-diol. The very first step was investigated and it was found to proceed via stationary structures 7A to 7E shown in **Figure 3.2.** The free-energy profile for these steps is shown in **Figure 3.7**. The initial structure 7A contains an ethoxy species formed during the chemisorption of ethanol, as well as a molecule of acetaldehyde physisorbed to the MgO surface. The C-O bond formation to yield 1-ethoxyethanol (via transition state 7B) has a forward barrier of 28.9 kcal/mol with several nearly isoexergonic molecular rearrangements followed by the stabilized 7E structure with former aldehyde C-O that is still coordinated to the surface atom Mg_{3c}. It is apparent from **Figure 3.7** that reverse barrier for the 1-ethoxyethanol formation is almost zero. In this case 1-ethoxyethanol can behave as a thermodynamical sink that would form in a transient fashion before reacting via other discussed pathways to form 1,3-butadiene. Surprisingly, the free energy computed for the structure 7C, which is a minimum on potential energy surface (PES), is slightly higher than that for the structure 7B – TS that is a first-order saddle point on PES. This unexpected result is clearly due to a failure of the harmonic approximation used in this work to determine free-energies. This level of theory implies that the positions of stationary points on PES and on the free-energy surfaces are identical which is generally not true (see Ref.[63] for discussion of the limitations of harmonic transition state theory). Furthermore, this level of theory is unsuitable to describe soft degrees of freedom such as hindered molecular rotations or long-wave lattice vibrations which contribute to harmonic free-energies more than the hard ones. In our case, the free energy for the first-order saddle point structure 7B is 28.9 kcal/mol higher than that for the minimum 7A and, importantly, the reaction coordinate for the whole sequence 7A→7E consists of hindered rotations of the CH_3CH_2O- and CH_3CHO- groups with the imaginary frequencies for the TS structures 7B and 7D that are smaller than 100 cm^{-1}. We note, however, that the free-energies for the sequence of structures between two stable configurations 7A and 7E (i.e. the structures 7B, 7C and 7D) are all within 4 kcal/mol and this number is relatively small compared to the free-energy difference with respect to the stable structure 7A. As the configuration 7D is the one with the highest free-energy on the sequence of steps 7A→7E, we consider the difference G(7D)-G(7A)=32. 8 kcal/mol as the effective free-energy barrier for the whole process 7A→7E.

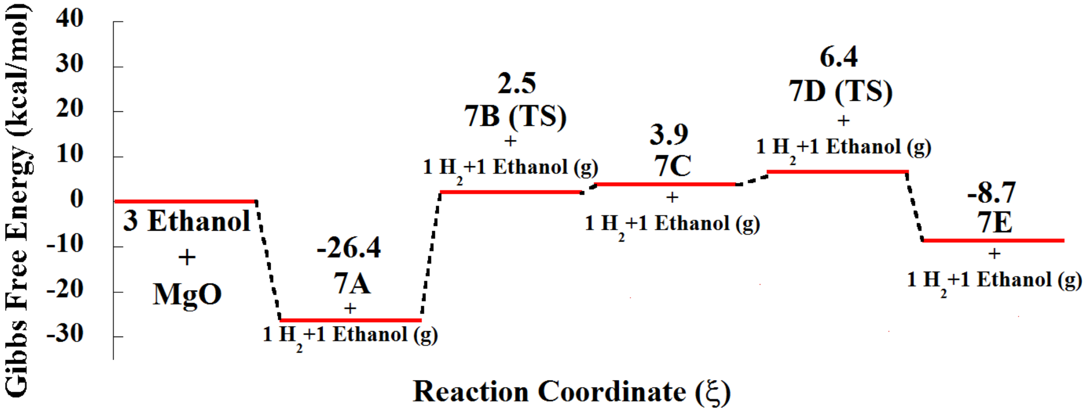

Figure 3.7 Free-energy profile for ethanol and acetaldehyde nucleophilic addition reaction.

2.2. Details of the Free-energy profiles

Three particular steps will be discussed here, namely elimination/redox reactions of ethanol, C-C bond formation, and proton transfer.

2.2.1. Elimination/redox reaction of ethanol

Elimination reaction takes place when a substituent leaves the molecule, e.g. water leaving ethanol, while redox reaction is defined as a reaction where a molecule loses or gains hydrogen. [64] Dehydrogenation reaction of ethanol (redox) is the first and foremost reaction step in all mechanisms proposed for the 1,3-butadiene formation. This oxidation step yields hydrogen as a byproduct while also transforming ethanol into acetaldehyde, a more reactive intermediate. The transformation 1A→1C shows a rather high free-energy barrier, 39.6 kcal/mol, while the reaction itself is endergonic in nature, with ΔG_{Rx}=20.5 kcal/mol. On the other hand, ethanol dehydration to ethylene has slightly lower activation barrier, 33.5 kcal/mol, and it is slightly exergonic with ΔG_{Rx}=-4.9 kcal/mol. Comparison of both reactions shows that ethanol is more likely to lose water than hydrogen on undoped MgO catalyst surface, which means that ethylene should be produced in higher amounts than acetaldehyde. This is in agreement with the experimental reports where small amounts of Ag, Cu or Zn are typically incorporated into the lattice structure to enhance acetaldehyde formation [23,65–71].

2.2.2. C-C bond formation

Two C-C bond formation pathways are presented in this study. Namely, aldol condensation and Prins condensation. The pathway 2F→2H possesses a favorable activation energy, lower than that of Prins, 16.1 v 28.8 kcal/mol. However, this reaction is thermodynamically limited, as shown by the endergonic nature of the reaction, with ΔG_{Rx}=12.9 kcal/mol. This suggests that aldol condensation step is kinetically favored on undoped MgO samples, with arguably one of the most favorable steps in the whole reaction landscape, while the exergonic nature of the Prins mechanism makes it thermodynamically favored. The activation energy of the latter is also similar to the energetic barrier to other steps, comparable to that of ethylene formation, and even lower than the activation energy of ethanol dehydrogenation. However, the overall picture is more complex since ethylene formed is only physisorbed onto the surface and adsorption of both reactants, i.e. ethylene and acetaldehyde, is only -0.2 kcal/mol lower in free-energy than the reference state suggesting that both molecules can desorb as byproducts. In accord with implications of these results, both ethylene and acetaldehyde have been seen as byproducts of ethanol catalytic coupling to form 1,3-butadiene.[18,20,22–25]

2.2.3. Proton transfer

Proton transfer steps can be further subdivided into three categories. The proton transfer steps of the first category are those that take place between the organic molecule and the surface, e.g. 2J→2L, 3D→3F, 4D→4F, 4I→4K, 6C→6G. The second type of proton transfer reactions is the MPV reduction taking place between two organic molecules, e.g. 3A→3C and 4A→4C. The last type is the proton diffusion from one site of the MgO surface to another, e.g. 6E→6E i→6E ii, 2C→2E, and also the understated proton diffusion steps between 2H and 2I.

The first type of proton transfer typically exhibits moderate activation energy. Most of the cases have $\Delta G_{A,forward}$ = ~30 kcal/mol with only one case, i.e. 2J→2L, possessing very low activation energy of ~6 kcal/mol, possibly due to the very saturated nature of the organic C4 compound. In the case of the MPV reduction, hydrogen atom moves from an alcohol α-carbon to open up the C=O bond of a molecule. This reduction reaction does not have a typical activation energy but rather it depends on the nature of the C=O containing molecule itself. The values computed for crotonaldehyde and acetaldol are ~12 kcal/mol and ~10 kcal/mol, respectively. Finally, the last type of the proton transfer reaction is proton diffusion from one MgO surface site to another. This reaction has typically very low activation energy of ~3 kcal/mol which suggests that the water formation and desorption are easily facilitated by the MgO catalyst.

3. Discussion

Adsorption of ethanol on both perfect and defect sites of MgO surface had been studied previously using cluster calculation [47]. It was shown that ethanol dissociated on defect sites but not on the perfect surface. Moreover, the adsorption energy decreased with the coordination number of the adsorption site [47]. This finding also aligns well with our calculations which show two modes of ethanol dissociation on the defect sites, i.e. 1A and 5A. In the state 1A, adsorbed molecules are coordinated on Mg_{3C} (corner) and O_{4C} (edge), while in the configuration 5A the ethanol molecule is chemisorbed on Mg_{3C} and O_{5C} (terrace). The energy of the former is lower than the latter (both electronic energy and Gibbs' free energy), indicating the difference in stability of both states. The lower coordination O_{4C} is very reactive and hence the spontaneous chemisorption of ethanol [45,52]. **Figure 3.2** structure 5A, however, depicts the adsorption of ethanol on the same Mg atoms (Mg_{3C} and Mg_{5C}), but proton adsorbing on O_{5C}. The highly-coordinated O_{5C} does not possess similar deprotonation ability to its lower-coordinated counterparts, as it is already stabilized by coordination with the neighboring atoms [45,50]. This situation causes the ethoxy oxygen to interact less strongly with the surface in Figure 5A, resulting in a relatively more unstable state compared to **Figure 3.2** structure 1A. Similarly, two new hydroxyl groups are formed during the dehydration process and only weakly bound acetaldehyde and molecular hydrogen during the dehydrogenation process in **Figure 3.2** structures 5C and 1C, respectively, with the former being more stable.

A study by Zhang *et al.* showed a peculiar finding where ethanol dissociated on both perfect and defected sites with energy barriers of 1.63, 1.42, and 1.30 eV, for terrace, kink, and edge, respectively [42]. Surprisingly, the molecule needed to surpass higher barrier for kink which consisted of two low coordinated ions (Mg_{3C}-O_{3C}), than for stepped Mg_{4C}-O_{4C}. This is in contrast to findings reported in this work and those of Branda where strong dissociation on the defect sites takes place without any barrier [47]. Finally, Chieregato *et al.* [41] showed that ethanol dehydrogenation over corner site of the MgO surface had an energetic barrier of 44.7 kcal/mol on Mg_{3C} site, as determined using cluster B3LYP/6-31++G(d,p) DFT calculations. Furthermore, the reaction was also postulated to be slightly exergonic with respect to the gas phase reference components, with ΔE of -1.4 kcal/mol. Our periodic calculations, on the other hand, predict that ethanol to acetaldehyde has a rather high energetic barrier, and it essentially represents rate-limiting step in the overall mechanism. The free-energy barrier, based on our calculation was 39.6 kcal/mol at 450°C. The ΔG_{Rx} for this reaction is also calculated to be +19.1 kcal/mol, which is highly endergonic.

The free-energy values for the profiles presented in **Figure 3.3-7** are listed in **Table 3.2,** along with the computed reaction rate constants. Based on the results presented in **Figure 3.3,** ethylene is more likely to be produced than acetaldehyde due to the lower activation energy and the exergonic nature of the reaction. As depicted in **Figure 3.4** only one TS structure has barrier higher than the desorption energy of the molecules in the reference state, namely that for enolate formation (2A-2C). In the subsequent step C-C bond coupling takes place between the enolate and the physisorbed acetaldehyde (2F-2H). This transition state (2G) is facilitated by enol, acetaldehyde as well as the resulting C-C product bonded by low-coordinated Mg atoms.

The resulting acetaldol, after several steps of proton diffusion and isomerization to cis conformer, can either lose proton to the surface or undergo MPV reduction, as shown in **Figure 3.5** for steps 2J→2L and 2J→4C, respectively**.** The two different pathways show that MPV reduction of acetaldol can be more favorable with a sharp decrease in its energy when ethanol is adsorbed, i.e. ethanol adsorption is much more favorable than a proton transfer from acetaldol to the surface. One should note that the overall MPV reduction pathway of acetaldol is below the reference state, which means that all the reaction steps are more favorable than the desorption of any adsorbates. State 4D, which results from the subsequent acetaldehyde desorption from state 4E, is essentially an adsorbed butane-1,3-diol. This is the basis of Ostromislensky's reaction mechanism supported by our calculations, although the rearrangement step from 1-ethoxyethanol to this diol has been previously rejected.[39] As mentioned before, MPV reduction of acetaldol pathway would require an additional step to convert the *cis*-1,3-butadiene to *trans*-1,3-butadiene (ΔG_{Rx} = ~4kcal/mol), which is the more stable molecule.

The adsorption of crotonaldehyde on the defected surface shows that the C=O bond is now lengthened from 1.25 Å (gas-phase) to 1.27 Å. This bond lengthening, also noticed by Boronat, *et al.*, is attributed to the back-donation of the surface antibonding orbital π^*(CO) of crotonaldehyde [72]. These authors calculated three main pathways for MPV reduction of cycohexanone by 2-butanol over a tin-zeolite catalyst and reported the most favorable pathway ($\Delta G_{A,forward}$ = ~15 kcal/mol) proceeding via formation of alkoxy species on the surface, although their calculation was carried out on a single metal center model [72]. Furthermore, both direct MVP and H-transfer facilitated by metal hydride formation have been reported with the former taking place over alkali-catalysts while the latter over transition metal catalysts [73,74]. A direct MPV reduction mechanism was also reported to take place during the 5-HMF reduction by methanol on Mg_{3c} site of MgO cluster model, as reported by Pasini, *et al.* [73] with electronic energy of 27.5 kcal/mol.

Table 3.2 Computed forward and reverse reaction barriers and the corresponding reaction rate constants.

Reaction	**ΔG_A (kcal/mol)**		**K (s^{-1})**	
	Forward	**Reverse**	**Forward**	**Reverse**
1A → 1C	39.6	20.5	15.9	9.37 10^{6}
2A → 2C	16.0	27.7	2.26 10^{8}	6.26 10^{4}
2C → 2E	3.0	10.5	1.84 10^{12}	9.93 10^{9}
2F → 2H	16.1	3.2	2.04 10^{8}	1.60 10^{12}
2J → 2L	5.9	12.5	2.52 10^{11}	2.59 10^{9}
2L → 2N	24.0	12.5	8.66 10^{5}	2.44 10^{9}
3A → 3C	12.1	8.5	3.35 10^{9}	4.17 10^{10}
3D → 3F	27.6	15.3	6.88 10^{4}	3.67 10^{8}
4A → 4C	9.8	17.3	1.69 10^{10}	8.74 10^{7}
4D → 4F	26.2	2.4	1.77 10^{5}	2.86 10^{12}
4F → 4H	2.1	40.2	3.57 10^{12}	11.0
4I → 4K	32.5	18.8	2.26 10^{3}	3.18 10^{7}
5A → 5C	33.5	38.3	1.15 10^{3}	38.9
6A → 6C	28.8	51.5	3.07 10^{4}	4.11 10^{-3}
6C → 6E	38.7	34.7	29.6	4.93 10^{2}
6E → 6G	34.1	2.3	7.45 10^{2}	3.14 10^{12}
6E → 6E ii	2.9	11.3	2.00 10^{12}	6.00 10^{9}
6E iii → 6E v	71.6	69.7	3.43 10^{-9}	1.26 10^{-8}
6E iii → 6E iii2	32.9	15.2	1.76 10^{3}	3.92 10^{8}
7A → 7E	32.8	15.1	1.86 10^{3}	4.24 10^{8}

Free-energy profile for the Prins pathway is depicted in **Figure 3.6.** Both acetaldehyde and ethylene (6A) have rather low adsorption energies, i.e. the two C2 species can easily desorb from the surface before going to the anticipated TS (6B). Notably, all transition states in this mechanism have positive relative energy with respect to the reference state. The blue pathway indicates a Prins mechanism that includes proton diffusion which results in a slightly lower free energy of the last transition state (6E iii 1) compared to the original red pathway, of which last transition state has a higher free energy (6F). The final state in both variants of Prins mechanism is *trans*-1,3-butadiene detached from the surface. Another step considered within the discussion of Prins mechanism is the formation of highly energetically unfavorable cyclic TS (6E iv). Not only does it have a large activation barrier, but it also goes to another minimum (6E v) which has a slightly higher relative energy than the initial state (6E iii).

The Prins mechanism was originally suggested by Gruver *et al.* [40]. The authors used aluminated sepiolites (both ammonium-exchanged and silver-exchanged) for the butadiene production from ethanol. On the silver exchanged catalyst, the production of ethylene and 1,3-butadiene increased exponentially with increasing contact time, while acetaldehyde production was linear [40]. The adoption of the same mechanism for MgO can be attributed to the fact that both catalysts possess almost exclusively Lewis acid sites [75] as Prins is a mechanism that mostly takes place on Lewis acid sites [76]. The reason that this mechanism has not been considered viable was the postulated step of ethylene protonation, which was supposed to result in a highly unstable carbocation [3]. As shown in this work, there is another type of intermediate/transition state for Prins mechanism which does not require protonation of ethylene. This intermediate was also identified by Yamabe, *et al.* [77]. In their theoretical work, propylene and formaldehyde were reacted via a novel C4 intermediate. Finally, other evidences of reaction between olefin and aldehyde were shown in US Patent no 2377025 A for 1,3-butadiene production, albeit through an acetylene intermediate, on alumina-silver and Cr- and Mo-oxide catalyst[78], isobutylene and pentenes with formaldehyde on KU-2 cation exchanged resin to make dioxanes [79] and 1,3-butanediol production via reaction of propylene and formaldehyde over ceria catalysts that contain mostly Lewis acid sites [80].

Work presented here for the enol formation step also shows a much lower free-energy barrier, compared to ethanol dehydrogenation, with a much more negative ΔG_{Rx} of reaction, 16 and -11.8 kcal/mol, respectively. Chieregato *et al.* suggested a novel mechanism with ethanol releasing a proton from its β-carbon and yielding a carbanion with ~33-36 kcal/mol forward barrier and negligible reverse barrier. This carbanion would then react with either ethanol or acetaldehyde to yield 1-butanol or crotyl alcohol, respectively, which subsequently dehydrate to produce 1,3-butadiene[41]. The carbanion has an interesting configuration in which the ethanol is not deprotonated, rather the hydroxyl group is interacting with a proton detached from β-carbon. From their overall mechanism, the rate-limiting step was predicted to be the reaction of acetaldehyde and carbanion with the electronic energy barrier of 11.4 kcal/mol with respect to the adsorbed reactants. The reaction to form C4 hydrocarbons is exergonic. Our attempt on cleaving the proton from β-carbon, however, lead to another pathway, namely to dehydration to form ethylene in 5A, 5B TS and 5C in **Figure 3.2** ($\Delta G_{A,forward}$ =33.5 kcal/mol, ΔG_{Rx}=-4.9 kcal/mol). The unstable carbanion situation that would lead to C-O bond scission was not encountered in the case of diol transformation to 1,3-butadiene (Figure 3.2D-K). As a result, Figure 3.3F shows a C4 molecule with two oxygen atoms bound to the surface. The terminal carbon, however, is in distorted sp^2 configuration and thus, represents a carbanion. Similarly, on the investigated Prins mechanism, a stabilized C4 carbanion, which leads to the desorption of 1,3-butadiene, is also observed in Figure 3.5G and 3.5E iii 2.

Interesting observation stemming from our work was that the Prins mechanism for C-C bond formation was thermodynamically more favorable than aldol C-C coupling step, and with the calculated barrier of 28.8 kcal/mol, i.e. ~10 kcal/mol lower than ethanol dehydrogenation. The activation energy is, however, still larger than that of aldol condensation (16.1 kcal/mol). Another fact complicating our conclusions further is that adsorption of both C2 intermediates on the surface is almost unfavorable thermodynamically (adsorption free energy (ΔG_{Ads}) = -0.2 kcal/mol), and the transition state is located above the reference state. This step was similar to the carbanion/acetaldehyde reaction, which is also a double bond opening of two sp^2 carbon atoms in acetaldehyde and ethylene. The suggested carbanion/acetaldehyde reaction involved butane-1,3-diol as an intermediate which subsequently deprotonates, as opposed to but-3-en-2-ol (state 5C) suggested by our calculation. 1,3-butanediol, however, still appears in our mechanism as a product of MPV reduction on the resulting acetaldol from aldol condensation.

4. Conclusion

A complex reactive mechanism of ethanol to form 1,3-butadiene was explored using periodic quantum chemical methods. Overall free energy surface was explored for the highly debated reaction mechanisms, including Toussaint's aldol condensation mechanism, Fripiat's Prins mechanism and mechanism based on Ostromislensky's hemiacetal rearrangement. Based on the thermodynamic and kinetic data determined within this study we identified four rate limiting steps in the overall process. In particular, ethanol dehydration to form ethylene possessed lower energy barrier than dehydrogenation to yield acetaldehyde suggesting competing reactive pathways. Aldol condensation step to form acetaldol is preceded with forward free-energy barrier of 16.1 kcal/mol but limited thermodynamically with endergonic reaction free energy of 12.9 kcal/mol. This calculation also offers another viable route in the form of Prins condensation, which has a free energy barrier of 28.8 kcal/mol with exergonic reaction free energy of -22.7 kcal/mol. Finally, thermodynamic stability of 1-ethoxyethanol prevents further reaction via hemiacetal rearrangement. The results presented here provide a first glimpse into the 1,3-butadiene formation mechanism on undoped MgO reactive sites in light of the vast literature discussing variety of the proposed mechanistic pathways mostly based on conventional homogenous organic chemistry reactions. While the surface model employed in this work utilized most reactive MgO site, presence of H_2O as a reaction product suggests that other surface sites, based on reactive hydroxyls, can also affect the overall reactive pathways and will be the focus of the future studies. However, based on the present calculations alone several mechanisms appear possible. Reactivity experiments are needed to discriminate between the different hypothesis, and we hope that our calculations will stimulate such studies.

References

(1) Matar, S.; Hatch, L. F. *Chemistry of Petrochemical Processes*; Elsevier, 2001.

(2) McCoy, M.; Reisch, M. S.; Tullo, A. H.; Short, P. L.; Tremblay, J. F.; Storck, W. J. *Chem. Eng. News* **2007**, *85*, 29.

(3) Angelici, C.; Weckhuysen, B. M.; Bruijnincx, P. C. a. *ChemSusChem* **2013**, *6* (9), 1595–1614.

(4) Sun, J.; Wang, Y. *ACS Catal.* **2014**, *4* (4), 1078–1090.

(5) Han, Y.; Lu, C.; Xu, D.; Zhang, Y.; Hu, Y.; Huang, H. *Appl. Catal. A Gen.* **2011**, *396* (1–2), 8–13.

(6) Zhang, X.; Wang, R.; Yang, X.; Zhang, F. *Microporous Mesoporous Mater.* **2008**, *116* (1–3), 210–215.

(7) Meng, T.; Mao, D.; Guo, Q.; Lu, G. *Catal. Commun.* **2012**, *21* (0), 52–57.

(8) Song, Z.; Takahashi, A.; Nakamura, I.; Fujitani, T. *Appl. Catal. A Gen.* **2010**, *384* (1–2), 201–205.

(9) Sun, J.; Zhu, K.; Gao, F.; Wang, C.; Liu, J.; Peden, C. H. F.; Wang, Y. *J. Am. Chem. Soc.* **2011**, *133* (29), 11096–11099.

(10) Liu, C.; Sun, J.; Smith, C.; Wang, Y. *Appl. Catal. A Gen.* **2013**, *467* (0), 91–97.

(11) Jørgensen, B.; Egholm Christiansen, S.; Dahl Thomsen, M. L.; Christensen, C. H. *J. Catal.* **2007**, *251* (2), 332–337.

(12) Carotenuto, G.; Tesser, R.; Di Serio, M.; Santacesaria, E. *Catal. Today* **2013**, *203* (0), 202–210.

(13) Birky, T. W.; Kozlowski, J. T.; Davis, R. J. *J. Catal.* **2013**, *298* (0), 130–137.

(14) Tsuchida, T.; Sakuma, S.; Takeguchi, T.; Ueda, W. *Ind. Eng. Chem. Res.* **2006**, *45* (25), 8634–8642.

(15) Lebedev, S. V. *Zh Obs. Khim* **1933**, No. 3, 698–717.

(16) Jones, M. D. *Chem. Cent. J.* **2014**, *8* (1), 53.

(17) Chang, F.-W.; Yang, H.-C.; Roselin, L. S.; Kuo, W.-Y. *Appl. Catal. A Gen.* **2006**, *304* (0), 30–39.

(18) Makshina, E. V.; Janssens, W.; Sels, B. F.; Jacobs, P. A. *Catal. Today* **2012**, *198* (1), 338–344.

(19) De Baerdemaeker, T.; Feyen, M.; Müller, U.; Yilmaz, B.; Xiao, F.-S.; Zhang, W.; Yokoi, T.; Bao, X.; Gies, H.; De Vos, D. E. *ACS Catal.* **2015**, 3393–3397.

(20) Angelici, C.; Velthoen, M. E. Z.; Weckhuysen, B. M.; Bruijnincx, P. C. A. *ChemSusChem* **2014**, *7* (9), 2505–2515.

(21) Ohnishi, R.; Akimoto, T.; Tanabe, K. *J. Chem. Soc. Chem. Commun.* **1985**, No. 22, 1613–1614.

(22) Sekiguchi, Y.; Akiyama, S.; Urakawa, W.; Koyama, T.; Miyaji, A.; Motokura, K.; Baba, T. *Catal. Commun.* **2015**, *68*, 20–24.

(23) Larina, O.; Kyriienko, P.; Soloviev, S. *Catal. Letters* **2015**, 1–7.

(24) Sushkevich, V. L.; Ivanova, I. I.; Ordomsky, V. V; Taarning, E. *ChemSusChem* **2014**, *7* (9), 2527–2536.

(25) Janssens, W.; Makshina, E. V.; Vanelderen, P.; De Clippel, F.; Houthoofd, K.; Kerkhofs, S.; Martens, J. A.; Jacobs, P. A.; Sels, B. F. *ChemSusChem* **2014**, *8* (6), 994–1008.

(26) Kvisle, S.; Aguero, A.; Sneeden, R. P. A. *Appl. Catal.* **1988**, *43* (1), 117–131.

(27) Kitayama, Y.; Satoh, M.; Kodama, T. *Catal. Letters* **1996**, *36* (1–2), 95–97.

(28) Kitayama, Y.; Michishita, A. *J. Chem. Soc., Chem. Commun.* **1981**, No. 9, 401–402.

(29) Niiyama, H.; Morii, S.; Echigoya, E. *Bull. Chem. Soc. Jpn.* **1972**, *45* (3), 655–659.

(30) Bhattacharyya, S. K.; Sanyal, S. K. *J. Catal.* **1967**, *7* (2), 152–158.

(31) Bhattachariya, S.; Gangooli, N. D.; Avastkhi, B. N. *J. Catal.* **1965**, *4* (6), 736.

(32) Bhattacharyya, S. K.; Avasthi, B. N. *Ind. Eng. Chem. Process Des. Dev.* **1963**, *2* (1), 45–51.

(33) Sushkevich, V. L.; Ivanova, I. I.; Taarning, E. *Green Chem.* **2015**.

(34) Baylon, R. a. L.; Sun, J.; Wang, Y. *Catal. Today* **2015**, 1–7.

(35) Bhattacharyya, S. K.; Ganguly, N. D. *J. Appl. Chem.* **1962**, *12* (3), 97–104.

(36) Jones, M. D.; Keir, C. G.; Iulio, C. Di; Robertson, R. A. M.; Williams, C. V; Apperley, D. C. *Catal. Sci. Technol.* **2011**, *1* (2), 267–272.

(37) Quattlebaum, W. M.; Toussaint, W. J.; Dunn, J. T. *J. Am. Chem. Soc.* **1947**, *69*, 593–599.

(38) Toussaint, W. J.; Dunn, J. T.; Jachson, D. R. *Ind. Eng. Chem.* **1947**, *39* (2), 120–125.

(39) Ostromislenskiy, I. *J. Russ. Phys. Chem. Soc.* **1915**, No. 47, 1472 –1506.

(40) Gruver, V.; Sun, A.; Fripiat, J. J. *Catal. Letters* **1995**, *34* (3–4), 359–364.

(41) Chieregato, A.; Velasquez Ochoa, J.; Bandinelli, C.; Fornasari, G.; Cavani, F.; Mella, M. *ChemSusChem* **2014**, *8* (2), 377–388.

(42) Zhang, M.; Gao, M.; Chen, J.; Yu, Y. *RSC Adv.* **2015**, *5* (33), 25959–25966.

(43) Chizallet, C.; Costentin, G.; Che, M.; Delbecq, F.; Sautet, P.; Surface, D.; Marie, P. *J. Am. Chem. Soc.* **2007**, No. 19, 6442–6452.

(44) Shalabi, A. S.; El-Mahdy, A. M. *Phys. Lett. A* **2001**, *281* (2–3), 176–186.

(45) Chizallet, C.; Bailly, M. L.; Costentin, G.; Lauron-Pernot, H.; Krafft, J. M.; Bazin, P.; Saussey, J.; Che, M. *Catal. Today* **2006**, *116* (2), 196–205.

(46) Di Valentin, C.; Del Vitto, A.; Pacchioni, G.; Abbet, S.; Wörz, A. S.; Judai, K.; Heiz, U. *J. Phys. Chem. B* **2002**, *106* (46), 11961–11969.

(47) Branda, M. M.; Rodríguez, A. H.; Belelli, P. G.; Castellani, N. J. *Surf. Sci.* **2009**, *603* (8), 1093–1098.

(48) Kantorovich, L. N.; Holender, J. M.; Gillan, M. J. *Surf. Sci.* **1995**, *343* (3), 221–239.

(49) Sushko, P. V.; Shluger, A. L.; Catlow, C. R. A. *Surf. Sci.* **2000**, *450* (3), 153–170.

(50) Chizallet, C.; Petitjean, H.; Costentin, G.; Lauron-Pernot, H.; Maquet, J.; Bonhomme, C.; Che, M. *J. Catal.* **2009**, *268* (1), 175–179.

(51) Aramendia, M. a.; Borau, V.; Jimenez, C.; Marinas, J. M.; Porras, A.; Urbano, F. J. *J. Mater. Chem.* **1996**, *6* (12), 1943.

(52) Bailly, M.; Chizallet, C.; Costentin, G.; Krafft, J.; Lauronpernot, H.; Che, M. *J. Catal.* **2005**, *235* (2), 413–422.

(53) Cornu, D.; Guesmi, H.; Krafft, J. M.; Lauron-Pernot, H. *J. Phys. Chem. C* **2012**, *116* (11), 6645–6654.

(54) Corson, B. B.; Jones, H. E.; Welling, C. E.; Hinckley, J. A.; Stahly, E. E. *Ind. Eng. Chem.* **1950**, *42* (2), 359–373.

(55) Zhang, M.; Yu, Y. *Ind. Eng. Chem. Res.* **2013**, *52* (28), 9505–9514.

(56) Redina, E. A.; Greish, A. A.; Mishin, I. V; Kapustin, G. I.; Tkachenko, O. P.;

Kirichenko, O. A.; Kustov, L. M. *Catal. Today* **2015**, *241, Part*, 246–254.
(57) Fessenden, R. J.; Fessenden, J. S. In *Organic Chemistry*; Dodson, K., Ed.; Brooks/Cole Publishing Company, 1995; pp 713–748.
(58) Harmony, M. D.; Laurie, V. W.; Kuczkowski, R. L.; Schwendeman, R. H.; Ramsay, D. A.; Lovas, F. J.; Lafferty, W. J.; Maki, A. G. *J. Phys. Chem. Ref. Data* **1979**, *8* (3), 619.
(59) Yang, Y.-J.; Teng, B.-T.; Liu, Y.; Wen, X.-D. *Appl. Surf. Sci.* **2015**, *357, Part,* 369–375.
(60) Chen, H.-Y. T.; Giordano, L.; Pacchioni, G. *J. Phys. Chem. C* **2013**, *117* (20), 10623–10629.
(61) Cavalleri, M.; Pelmenschikov, A.; Morosi, G.; Gamba, A.; Coluccia, S.; Martra, G. In *Oxide-based Systems at the Crossroads of ChemistrySecond International Workshop October 8-11, 2000, Como, Italy*; A. Gamba, C. C. and S. C. B. T.-S. in S. S. and C., Ed.; Elsevier, 2001; Vol. Volume 140, pp 131–139.
(62) Barborini, M.; Guidoni, L. *J. Chem. Phys.* **2012**, *137* (22).
(63) Bučko, T.; Benco, L.; Hafner, J.; Ángyán, J. G. *J. Catal.* **2011**, *279* (1), 220–228.
(64) Fessenden, R. J.; Fessenden, J. S. In *Organic Chemistry*; Dodson, K., Ed.; Brooks/Cole Publishing Company, 1995; pp 275–308.
(65) Musolino, V.; Selloni, A.; Car, R. *J. Chem. Phys.* **1998**, *108* (12), 5044.
(66) Pacchioni, G. *J. Chem. Phys.* **1996**, *104* (18), 7329.
(67) Zhukovskii, Y. F.; Kotomin, E. a.; Borstel, G. *Vacuum* **2004**, *74* (2), 235–240.
(68) Matveev, A.; Neyman, K.; Yudanov, I.; Rösch, N. *Surf. Sci.* **1999**, *426* (1), 123–139.
(69) Rodriguez, J. a.; Jirsak, T.; Chaturvedi, S. *J. Chem. Phys.* **1999**, *111* (17), 8077.
(70) Rodriguez, J. a.; Jirsak, T.; Freitag, A.; Larese, J. Z. *J. Phys. Chem. B* **2000**, *2* (100), 7439–7448.
(71) Angelici, C.; Meirer, F.; van der Eerden, A. M. J.; Schaink, H. L.; Goryachev, A.; Hofmann, J. P.; Hensen, E. J. M.; Weckhuysen, B. M.; Bruijnincx, P. C. A. *ACS Catal.* **2015**, *5* (10), 6005–6015.
(72) Boronat, M.; Corma, A.; Renz, M. *J. Phys. Chem. B* **2006**, *110* (42), 21168–21174.
(73) Pasini, T.; Lolli, A.; Albonetti, S.; Cavani, F.; Mella, M. *J. Catal.* **2014**, *317*, 206–219.
(74) Assary, R. S.; Curtiss, L. A.; Dumesic, J. A. *ACS Catal.* **2013**, *3* (12), 2694–2704.
(75) Angelici, C.; Velthoen, M. E. Z.; Weckhuysen, B. M.; Bruijnincx, P. C. A. *Catal. Sci. Technol.* **2015**.
(76) Arundale, E.; Mikeska, L. A. *Chem. Rev.* **1952**, *51* (3), 505–555.
(77) Yamabe, S.; Fukuda, T.; Yamazaki, S. *Beilstein J. Org. Chem.* **2013**, *9*, 476–485.
(78) Miller, H. Conversion of a mixture of acetaldehyde and ethylene to butadiene. US2377025 A, 1945.
(79) Isagulyants, V. I.; Safarov, M. G. *Pet. Chem. U.S.S.R.* **1966**, *5* (3), 203–208.
(80) Wang, Y.; Wang, F.; Song, Q.; Xin, Q.; Xu, S.; Xu, J. *J. Am. Chem. Soc.* **2013**, *135* (4), 1506–1515.
(81) Towns, J.; Cockerill, T.; Dahan, M.; Foster, I.; Gaither, K.; Grimshaw, A.; Hazlewood, V.; Lathrop, S.; Lifka, D.; Peterson, G. D.; Roskies, R.; Scott, J. R.; Wilkins-Diehr, N. *Comput. Sci. Eng.* **2014**, *16* (5).

Chapter 4

Surface Reaction Mechanisms Study of MgO/SiO_2 for Lebedev Process

Abstract

1,3-butadiene is an important commodity chemical and new, selective routes of catalytic synthesis using green feedstock, such as ethanol, is of interest. For this purpose, surface chemistry of MgO/SiO_2 catalyst synthesized using wet-kneading was explored during the reaction of ethanol and the corresponding reactive intermediates, including acetaldehyde, crotonaldehyde, crotyl alcohol using temperature programmed *in situ* DRIFT spectroscopy combined with DFT calculations. Ethanol adsorption yielded several physisorbed and chemisorbed surface species. Acetaldehyde exhibited high reactivity to form crotonaldehyde. However, aldehyde intermediates resulted in strongly bound surface species stable even at high temperatures, assigned to surface acetate, and/or 2,4-hexadienal or polymerized acetaldehyde. Crotonaldehyde was reduced by ethanol to yield crotyl alcohol via MPV mechanism. Crotyl alcohol, on the other hand, showed to be very reactive and yield two different species on the surface, namely physisorbed and deprotonated that would further desorb as 1,3-BD. Presence of gas phase hydrogen containing molecules, such as ethanol, proved to be key in several reactive steps, including acetaldehyde condensation step and crotonaldehyde reduction. Altogether, these data suggested a complex reactive interactions between the surface hydroxyl groups, gaseous reactants and surface bound reactive intermediates during the 1,3-BD formation. Future work is needed to correlate vapor phase product evolution with the transient reactive surface intermediates to examine trends leading to higher overall 1,3-BD selectivity.

1. Introduction

1,3-butadiene (1,3-BD) is an important commodity chemical with widespread applications in polymer synthesis and as an organic chemistry intermediate.[1] It is commonly produced via crude oil cracking. 1,3-BD production can be affected by market instability triggered by oil price fluctuations. This difficulty is compounded by the emergence of shale gas, which suggests a need for an alternative and more sustainable production method.[2] For this reason, there has been a renewed interest in utilizing ethanol as a feedstock for 1,3-BD synthesis. Production from ethanol was used during World War II by the USA and the USSR with a two-step process and a one-step catalytic process, respectively, as demonstrated by Ostromislensky and Lebedev.[3,4] Several reports since then have highlighted the economic viability of the overall synthesis process with the one-step catalytic process recently becoming a focal point.[1,2,5] This single step process originally utilized MgO/SiO_2 catalyst with a 30-40% yield. Ethanol dehydrogenation to yield acetaldehyde was identified as the rate-determining step in the generally accepted complex reaction mechanism,[6] with a large body of experimental work performed for elucidating the reaction pathways.[7–12] However, there is only a limited number of studies that focus on the adsorbed reactive surface intermediates on MgO catalysts that utilize *in-situ* spectroscopy to characterize the reaction intermediates under operating conditions.[8,10,13,14]

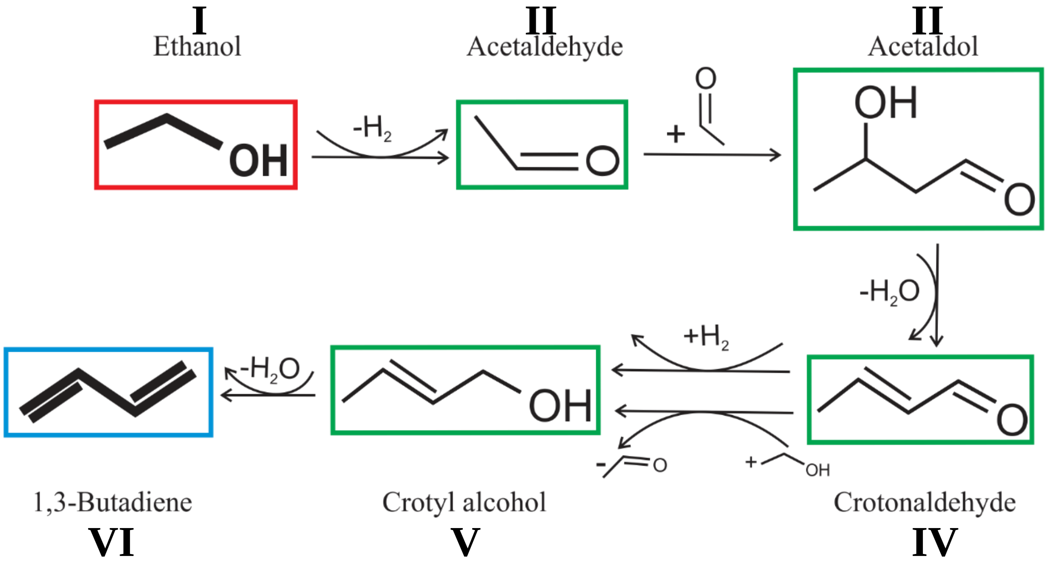

Figure 4.1. Main reaction mechanism proposed for ethanol to 1,3-butadiene via Toussaint's aldol condensation.

A one-step catalytic mechanism, as summarized in **Figure 4.1**, involves dehydrogenation of ethanol to acetaldehyde on basic MgO sites[1,10,15], followed by C-C coupling via the aldol condensation mechanism to yield crotonaldehyde.[6,16,17] Crotonaldehyde can be further hydrogenated via MPV (Meerwein–Ponndorf–Verley) reduction, either with ethanol or molecular H_2 and the resulting crotyl alcohol dehydrated to give 1,3-BD.[16,18] Three computational studies by Chieregato *et al.* [10], Zhang *et al.*[11] and Taifan *et al.*[17] attempted to unravel the reaction mechanism and the structures of the reactive surface intermediates. Zhang *et al.* performed calculations using periodic density, functional generalized, gradient approximation (GGA), with a focus on the very first step of the overall reaction mechanism, the dehydrogenation of ethanol. A stepped MgO surface was predicted to have a lower energy barrier than a flat surface for this reaction.[11] The dissociation of ethanol on that surface was studied for three different surface sites, i.e., $Mg_{5C}O_{5C}$, $Mg_{4C}O_{4C}$, and $Mg_{3C}O_{3C}$ and on the stepped surface, i.e. $Mg_{4C}O_{4C}$ was shown to have the lowest potential energy barrier for this reaction. Chieregato *et al.*, on the other hand, proposed an entirely different mechanism based on cluster type calculations and a Gaussian basis set. They ruled out crotonaldehyde and crotyl alcohol as possible intermediates and concluded that acetaldehyde would react with a carbanion, which resulted from ethanol C-H bond cleavage.[10] Taifan *et al.*, for the first time, outlined a complete reactive pathway for ethanol conversion to 1,3-BD by using periodic GGA calculations. The pathways explored included an alternative Fripiat's Prins mechanism and a mechanism based on Ostromislensky's hemiacetal rearrangement. They showed ethanol dehydration to have an energetic barrier comparable to that of dehydrogenation. The dehydration proceeded on Mg_{3c} with surface O_{5c} responsible for the initial proton transfer and the resulting low coordination O_{2c} and O_{4c} hydroxyl group formation. Dehydrogenation, on the other hand, took place in the vicinity of Mg_{3c} and step O_{4c}.

Acetaldol (3-hydroxybutanal) formation proceeded via a 16 kcal/mol free energy barrier, as calculated at 450 °C using harmonic/rigid rotor approximation. That took place when acetaldehyde molecules were coordinated to Mg_{3c}, Mg_{4c} and Mg_{5c} surface sites. Acetaldol was not identified as a stable intermediate on a PES surface, as it immediately deprotonated on reactive O_{4c} sites. While computational modelling utilized low saturation Mg_{3c} and O_{4c} sites for the overall reaction cycle, spectroscopic identification of the corresponding sites and the reactive surface intermediates was less utilized. In particular, an adsorbed ethoxy group on MgO was identified at 1119-1132 cm^{-1} in the temperature regime between 200 and 400 °C, when adsorbed ethanol was heated suggesting ethanol chemisorption.[10] New bands appeared at 1718 and 1143 cm^{-1} already at 150 °C and these bands were attributed to acetaldehyde and new C-O containing surface species assigned to carbanion, respectively. A transient peak at 1653 cm^{-1} together with one at 2957 cm^{-1} were assigned to acyl or acetyl species. The reactive adsorbed intermediate at 1620 cm^{-1} was observed and assigned to crotyl alcohol.[19] C=O and C=C stretching vibrations at 1672 and 1649 cm^{-1} observed above 350 °C were assigned to other C_4 products, such as 1,3-BD, crotonaldehyde and butanol. No adsorbed crotonaldehyde or acetaldol intermediates (the latter one in agreement with Taifan *et al.*)[17] were observed at lower (>250 °C) temperatures but 1,3-BD formation was identified, suggesting that the aldol condensation mechanism was not a key. *In-situ* DRIFTS was also the preferred technique used by Davis' group[13,14] and Ordomsky *et al.*[8] to monitor the surface species during the reaction to n-butanol and 1,3-butadiene, respectively. Ethanol strongly adsorbed on MgO as both dissociated ethoxide and a molecularly adsorbed ethanol. Dissociated ethanol exhibited a major peak at 1132-1119 cm^{-1}, while molecularly adsorbed ethanol was detected at 1058 cm^{-1}. At higher temperatures, no aldol condensation was detected during the experiment, possibly due to the very low conversion which was also supported by a small acetaldehyde formed at 1711 cm^{-1}.[13,14] Aldol condensation of acetaldehyde was studied over MgO/SiO_2 catalyst and was suggested to instantaneously take place on the surface once acetaldehyde was introduced to the IR cell, as shown by the band at 1643 cm^{-1}, attributed to C=C stretch of crotonaldehyde. Other than aldol condensation, acetaldehyde undergoes other side reactions, namely condensation on the basic sites, as well as aldol condensation with crotonaldehyde yielding 2,4-hexadienal, an unsaturated aldehyde.[8]

In this work we report a detailed study of wet-kneaded MgO/SiO_2 catalyst surface reactive sites and reactive intermediates during the ethanol conversion to 1,3-BD. Where necessary, data are also reported for pure MgO model catalyst. Wet kneading (WK) of MgO/SiO_2 catalyst has been shown to result in an active catalysis towards 1,3-BD formation from ethanol.[1,15,20–23] In this study, we prepared calcined MgO and MgO/SiO_2 catalysts using a wet kneading method with an $MgO:SiO_2$ mass ratio of 1:1. We used *in situ* Diffuse Reflectance Infrared Spectroscopy (DRIFTS) and the corresponding proposed reactants and proposed reactive intermediates, including ethanol, acetaldehyde, crotyl alcohol, crotonaldehyde, as shown in **Figure 4.1**. To aid in the observed peak assignment, quantum chemical calculations using periodic boundary conditions and PBE functional were used.

2. Results and Discussion

2.1. Catalyst activity and selectivity testing

Figure 4.2 depicts the catalytic activity testing of the synthesized wet-kneaded MgO/SiO_2 catalyst, WK (1:1). The experiment were carried out at 723 K (450°C) at several WHSV (hr^{-1}) ranging from 0.78 to ~2 hr^{-1}. WHSV plays a very important role in determining the catalyst's activity, since it represents the catalyst-to-reactant ratio. The conversion decreased with increasing WHSV from ~87% to ~60%. Selectivities of selected products, i.e. acetaldehyde, ethylene, and 1,3-butadiene, were relatively unaffected by WHSV. At very high conversion, there were several other byproducts, such as butenes, propene, ethers and some aromatic compound that coked the catalyst; this led to carbon balance of 60-80%. High 1,3-butadiene selectivity was achieved with this catalyst, 35-40%, without the addition of routinely used transition metal oxide promoter.[1,2] Similar conversion-yield values were previously reported by Weckhuysen's group, where different methods of preparation and precursors were explored to find the best working catalyst.[21] **Table 4.1** shows comparison between catalyst in this work and previously used wet-kneaded MgO/SiO_2 catalysts.

Table 4.1. Catalytic activity comparison of WK (1:1) with previously investigated wet-kneaded synthesized catalysts.

Catalyst	T (K)	WHSV (h^{-1})	X_{EtOH} (%)	Y_{BD} (%)	P_{BD} (gBD g^{-1}cat h^{-1})	Ref
WK (1:1)	723	1.1	~84	33	0.4	This work
WK-a	623	0.15	50	42	0.06	Makshina *et al.*[23]
WK-b	698	1.1	~67	35	0.25	Angelici *et al.*[21]

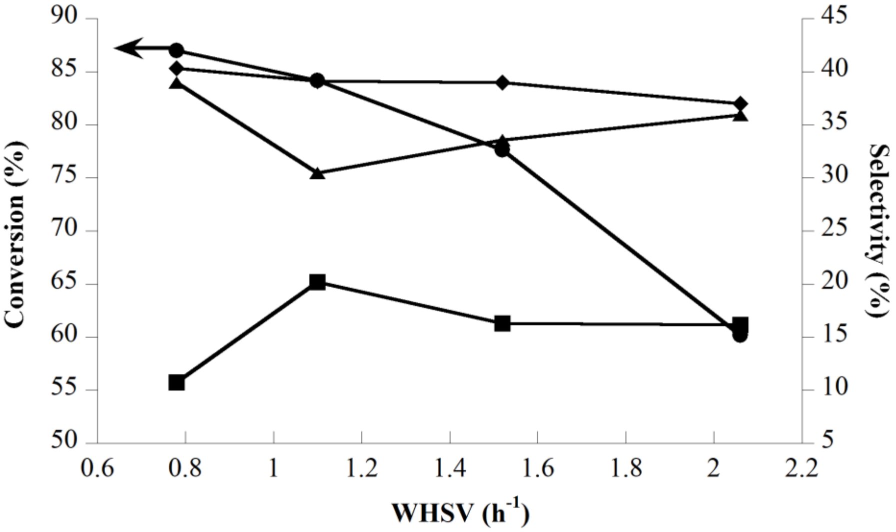

Figure 4.2. Conversion (●) and selectivity of main products (■ acetaldehyde; ▲ ethylene; ♦ 1,3-butadiene) at different WHSV. Reaction conditions: T=723 K, Q_{tot} = 50 cm^3/min, M_{cat}=0.2 g, P^0_{EtOH} = 2.72; 3.77; 5.15; 6.96 kPa.

2.2. *In-situ* DRIFT spectroscopy of MgO based catalyst surface hydroxyl groups.

We begin by investigating the hydroxyl groups present on a dehydrated WK (1:1) surface by comparing them with MgO and SiO_2. *In-situ* IR spectroscopy results for the pure MgO surface shown in **Figure 4.3** were obtained after heating (dehydrating) the sample at 773 K, typical for the ethanol catalytic reaction to form 1,3-BD, in air and cooling down to 373 K temperature. Spectra show two high basicity (low coordination) peaks in the hydroxyl region at 3765 and 3745 cm^{-1}, while several broad peaks are also present at 3700-3400 cm^{-1}, namely, 3660, 3547 and 3465 cm^{-1}. The higher stretching frequency is related to a more isolated (and basic) hydroxyl group, while the lower one is often assigned to multi-coordinated hydrogen bonded hydroxyls.[27,39–43] In general, there have been six structural hydroxyl group models proposed to exist on MgO. Anderson *et al.* proposed two kinds of hydroxyl groups on the MgO surface: hydrogen bond acceptor and hydrogen bond donor.[41] Their model was subsequently refined by Shido *et al.,* where the two regions could be classified in further detail based on the coordination numbers of the Mg and O atoms.[42] Coluccia, Morrow, and Knozinger each proposed three different models with one uniting characteristic: the inclusion of an isolated hydroxyl group as the sharp band at the high wavenumber region and hydrogen bond donor - multicoordinated hydroxyl groups in the lower wavenumber region.[39,40,43] Most recent models combined DFT and infrared spectroscopy studies to show that the most isolated single coordinated (O_{1C}-H) group does not exist: it immediately transforms into O_{3C}-H and O_{4C}-H at a lower temperature and into O_{2C}-H at an elevated desorption temperature, and thus a new model was proposed.[44] The bands observed at 3765 and 3745 cm^{-1} in our work agree well with those reported in the literature. Those bands have been assigned to low coordinated O_{1c}-H or O_{2c}-H *hydrogen bond acceptors* or O_{4c}-H and O_{5c}-H coordinated *isolated* groups on valleys and edges of the MgO crystallites.[39,44] The peaks below 3650 cm^{-1} are in general attributed to multi-coordinated hydrogen bond donor hydroxyl groups[44], thus presenting a rather complex picture of the reactive MgO surface.

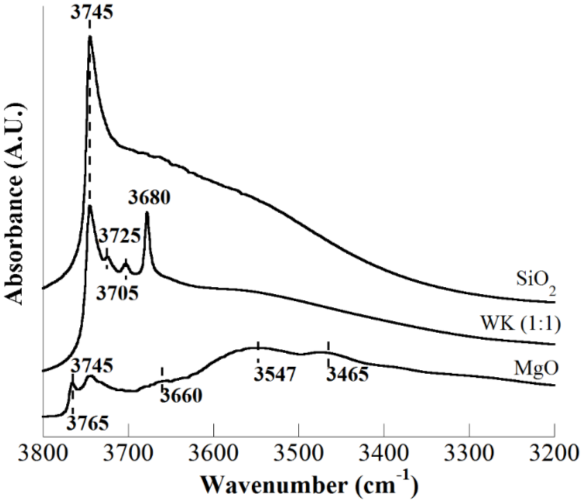

Figure 4.3. *In-situ* DRIFTS spectra acquired of dehydrated (temperature programmed to 773 K at 10 ^{o}C/min under air and cooled down to 100 ^{o}C) MgO, MgO WK (1:1) catalysts and SiO_2. Only hydroxyl region of 3800 to 3200 cm^{-1} is shown. Spectra are acquired at 100 °C.

The WK (1:1), on the other hand, exhibited four major peaks at 3745, 3725, 3705, and 3680 cm^{-1}. For comparison, dehydrated spectra of calcined SiO_2 are also shown. There are two bands present for SiO_2, a sharp one at 3745 cm^{-1} and a broad band at 3700-3450 cm^{-1}. The sharp peak is typical for the isolated silanol (Si-OH) vibration with a small contribution from the geminal silanol group (HO-Si-OH), while the broad band is formed from the contribution of the hydrogen bonded vicinal silanol groups.[45] The 3745 cm^{-1} peak is also observed in WK (1:1), albeit at the lower intensity, which suggests that isolated silanol groups are consumed during the wet-kneading interaction with MgO. The other three peaks present, 3725, 3705, and 3680 cm^{-1}, are unique to the WK (1:1) structure. The latter peak has previously been assigned to magnesium silicates, due to its formation in the presence of silica.[7,19,46] It has previously been observed as a mineral lizardite hydroxyl group at 3686 cm^{-1}.[47] The relatively low FWHM (Full Width at Half Maximum) of the peak suggests that this group might be isolated, rather than hydrogen bonded, consistent with the crystalline structure of the lizardite.[48] Peaks at 3725 and 3705 cm^{-1} are more difficult to assign directly, since none of the magnesium silicate compounds exhibit hydroxyl stretches above 3700 cm^{-1}.[47] It can be proposed that the interaction of MgO and SiO_2 during wet kneading increases the formation of hydroxyl groups that are already present on MgO itself, i.e., wet-kneading results in more defects that produce the said hydroxyl group or that peaks could originate from Mg-OH interacting with nearby SiO_2 surface sites. The peak at 3725 cm^{-1} is rather intriguing due to the fact that it was not observed by other groups. We tentatively assign the peaks at 3725 and 3705 cm^{-1} to the isolated O_{4c}-H and O_{5c}-H coordinated groups formed in the presence of the amorphous SiO_2 ($SiMg_{4c}O_{4c}$ and $SiMg_{4c}O_{5c}$). This is also consistent with the decrease in intensity of the 3765 and 3745 cm^{-1} hydroxyl groups present on MgO but not on WK (1:1), where incorporation of amorphous Si-O-Mg linkages could result in the frequency shift towards lower wavenumbers.

2.3. Acid-base characterization of WK (1:1) catalyst using CO_2 and pyridine as probe molecules

Characterization of the basic sites present on WK (1:1) was carried out by performing *in-situ* DRIFTS using CO_2 as a probe molecule. **Figure 4.4a** depicts the spectra of adsorbed CO_2 species at different temperatures. The basicity was previously reported to originate from MgO, and with no contribution from SiO_2.[2] There are three broad, main peaks present on the spectra, located at 1650, 1531, and 1405 cm^{-1}. Judging from the carbonate υ_3 frequency split, the last two peaks originate from monodentate carbonate, assigned to υ_3 as and υ_3 s, respectively.[49] The peak at 1650 cm^{-1} could originate from either bidentate carbonate or monodentate bicarbonate. However, bicarbonate would exhibit a peak at around ~1250-1200 cm^{-1}, which is non-existent in this case. Bidentate carbonate assignment is more likely than bicarbonate, given the broad peaks exhibited in this spectra, where the accompanying υ_3 s would be convoluted as a shoulder to the peak at 1405 cm^{-1}. Furthermore, the basic site strength can be determined by the surface species present. Monodentate carbonate is typically more stable than bidentate carbonate, while bicarbonate is the least stable.[2,49] Hence, the strong basic sites are assigned to monodentate carbonate, while medium-strength and weak basic sites are assigned to bidentate carbonate and bicarbonate, respectively. From the spectra, the bidentate carbonate is far less intense than monodentate carbonate, indicating the more basic nature of the MgO/SiO_2 WK (1:1). Several other methods of preparation, such as sol-gel[19] and incipient wetness impregnation[2], yield catalysts with limited amount of strong basic sites. However, it should be noted that at the reaction temperature, ~673-723 K, the CO_2 species in our catalyst are mostly absent. This indicates that the basic sites present on the catalyst gradually lose strength at elevated temperature.

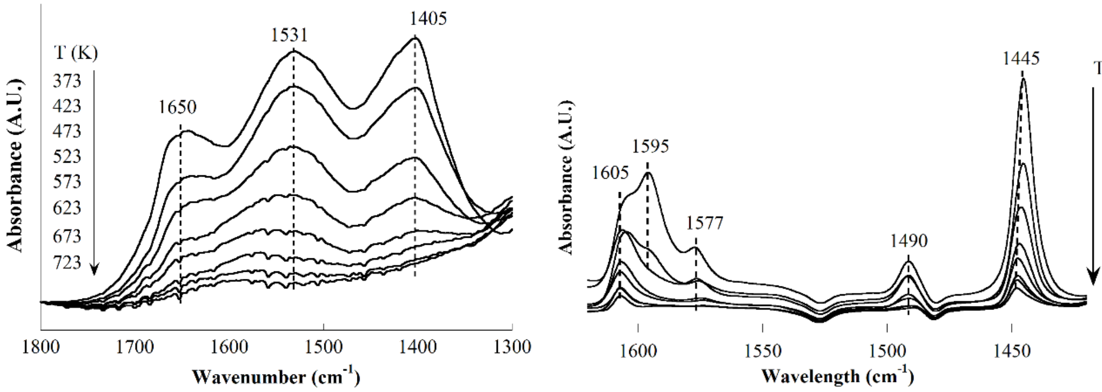

(a) (b)

Figure 4.4. DRIFTS spectra of adsorbed (a) CO_2 and (b) pyridine on WK (1:1) catalyst at different temperatures to probe the catalyst's basicity and acidity at relevant temperatures.

The acidity of the catalyst was characterized using pyridine as the probe molecule (**Figure 4.4b).** Peaks at 1445 and 1605 cm^{-1} indicates the presence of strong Lewis acid sites, while the peak at 1577 cm^{-1} is for weak Lewis acid sites.[50] Peak at 1490 cm^{-1} is assigned to a combination band of Lewis and Brønsted acid sites, while Brønsted acid site itself should exhibit a peak at 1540 cm^{-1}, which is not present on our catalyst. The peak at 1595 cm^{-1} does not represent any acid sites, instead, it was assigned to hydrogen-bound pyridine.[50] The absence of Brønsted acid sites were also observed by previous investigators, given the basic nature of the catalyst.[2,7,19,51] However, the intensity of the strong Lewis acid sites is a dominant feature on this spectra indicating that the catalyst possess a significant amount of strong Lewis acid sites, relative to the weaker Lewis acid sites. SiO_2 by itself is known to be slightly acidic, contributing to the weak Lewis acid sites, while the rest of the Lewis acid sites are combination of defect sites of MgO and the interaction between SiO_2 and MgO.[1,2,10,51]

2.4. *In-situ* DRIFT spectroscopy to monitor hydroxyl group reactivity during the ethanol, acetaldehyde, crotonaldehyde and crotyl alcohol adsorption and subsequent reaction on a WK (1:1) catalyst surface.

Spectra for those hydroxyl groups in the 3800 to 3200 cm^{-1} regions during WK (1:1) reaction with ethanol, acetaldehyde, crotonaldehyde and crotyl alcohol are shown in **Figure 4.5** and tabulated in **Table 2**. Subtracted adsorbed molecule spectra as a function of temperature are shown in black, while red dotted spectra are for 373 K hydroxyl groups reacting upon vapor phase molecule adsorption with catalyst spectrum subtracted. Notably, the catalyst sample surface was treated at 773 K beforehand; thus, the hydroxyl groups observed in **Figure 4.5** are transient reactive groups formed and released during the organic molecule adsorption/reaction. Upon adsorption of organic molecules, negative peaks appeared on all the assigned WK (1:1) hydroxyl groups, i.e. 3747, 3725, 3705, and 3680 cm^{-1}. The adsorption behavior is very different for alcohols – ethanol and crotyl alcohol – and for aldehydes – acetaldehyde and crotonaldehyde, as shown by the different intensities of the negative peaks. The alcohols have less affinity to the peaks at 3705 and 3680 cm^{-1}, while aldehydes have no preference on which hydroxyl group to coordinate.

Alcohols' interactions with MgO surfaces include both molecular adsorption on native hydroxyl groups[52], as well as their displacement via chemisorption, which involves basic site – Lewis acid site pairs, that will produce adsorbed water as the byproduct.[19,53] Positive hydroxyl peaks in the alcohol cases can indicate new hydroxyl vibrations, due to the newly formed groups via displacement, while the increased hydrogen bonding demonstrates that some of the native hydroxyl groups only weakly-bind the molecular ethanol. Aldehyde adsorption, on the other hand, typically takes place via two surface species: on a surface hydroxyl group via an unstable, protonated intermediate and on a lone pair of oxygen atoms as a more stable species, typically indicated by the red-shifted C=O stretching vibration at 1650-1680 cm^{-1}.[54] **Figure 4.5** shows that acetaldehyde adsorbs differently from crotonaldehyde, that the peak at 3725 cm^{-1} is not significantly consumed, as compared to that of crotonaldehyde. We assume that this is due to crotonaldehyde's π-electron cloud, which makes the molecule more activated toward consuming the hydroxyl group related to the 3725 cm^{-1} peak. For all experiments, the adsorption results in the positive peak at ~3684 cm^{-1}, indicating different hydroxyl group coordination, or a more intense hydrogen bonding. This positive peak is more intense for acetaldehyde and crotonaldehyde, possibly due to the formation of new alcoholic species, rather than in the case of alcohols, which are simply hydroxyl groups displacement.

Table 4.2. Surface hydroxyl group vibrational frequencies during ethanol, acetaldehyde, crotonaldehyde and crotyl alcohol adsorption on WK (1:1).

	Experimental (cm^{-1})				
	Ethanol	**Acetaldehyde**	**Crotonaldehyde**	**Crotyl alcohol**	**Assignment**
ν (Mg-OH)	3748 (3761) 3725 (3721) - 3680	3755 (3757) 3721 3710 3680	3740 3721 3710 3680	3751 3723 - 3678	Mg$_{4c}$O$_{4c}$ SiMg$_{4c}$O$_{4c}$ SiMg$_{4c}$O$_{5c}$ Mg$_3$Si$_3$O$_5$(OH)$_4$

According to **Figure 4.3**, the peak at 3747 cm^{-1} is a combination of both a silica isolated silanol peak and the basic MgO hydroxyl group. As the temperature is increased, the former sharply loses intensity, while the latter slowly gains intensity. This trend is true for all the intermediates adsorbed on the surface. Furthermore, this MgO peak splits at a higher temperature, indicating the presence of a second peak, at lower wavenumber, which translates to higher coordination. This further splitting was previously observed by Knözinger *et al.*[39] All other surface hydroxyl groups undergo a significant decrease in intensity, while also being accompanied by the emergence of their shoulders at a lower wavenumber as the temperature is increased. One intriguing observation is that those neighboring hydroxyl peaks are all red-shifted from the native hydroxyl peaks. The thermal effect on the surface seems to rearrange the hydroxyl group coordination to achieve more thermodynamically stable configurations, i.e., there are no new hydroxyl groups being formed.

Putting the rearrangement of the hydroxyl groups aside, increasing the temperature also led to desorption of the surface species. The release of the hydroxyl groups can be explained by the flattening shoulder at ~3684 cm^{-1}. These hydroxyl groups were made during the alcohol/acetaldehyde adsorption. However, native hydroxyl peaks that were consumed during the initial adsorption keep decreasing in intensity as well. This continuous decrease indicates that these peaks, in particular at 3747 and 3680 cm^{-1}, are not fully consumed during the adsorption, i.e. they are relatively less reactive. The remaining, unconsumed hydroxyl groups of these types undergo further thermal change by achieving thermodynamically more stable coordination, shown by the increase of the neighboring hydroxyl peak. For the case of aldehydes, increasing the temperature would both convert the unstable protonated intermediate into the more stable compound, which is coordinated to Lewis acid sites.

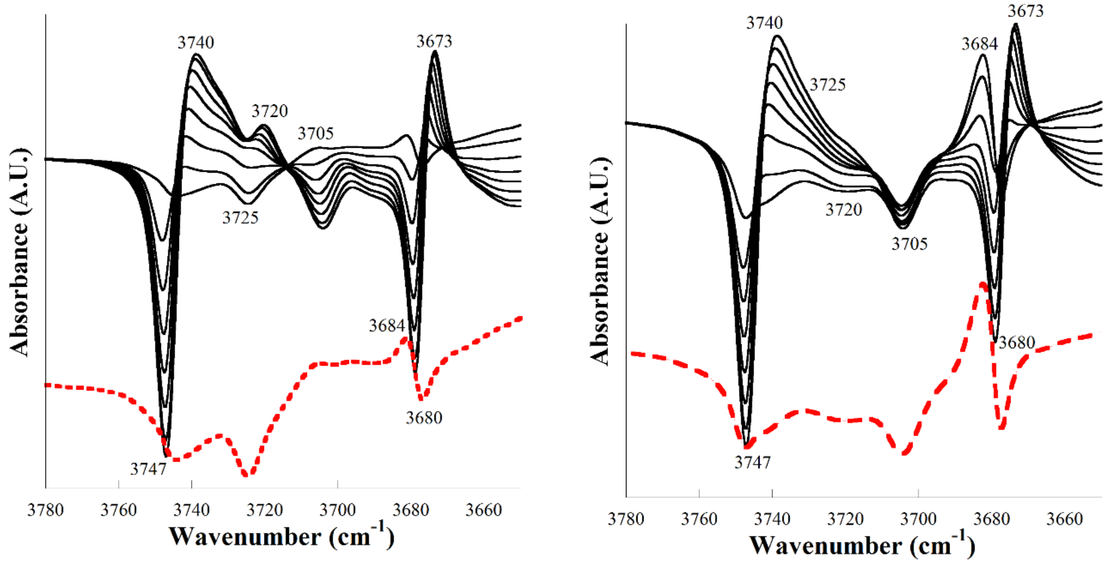

Ethanol **Acetaldehyde**

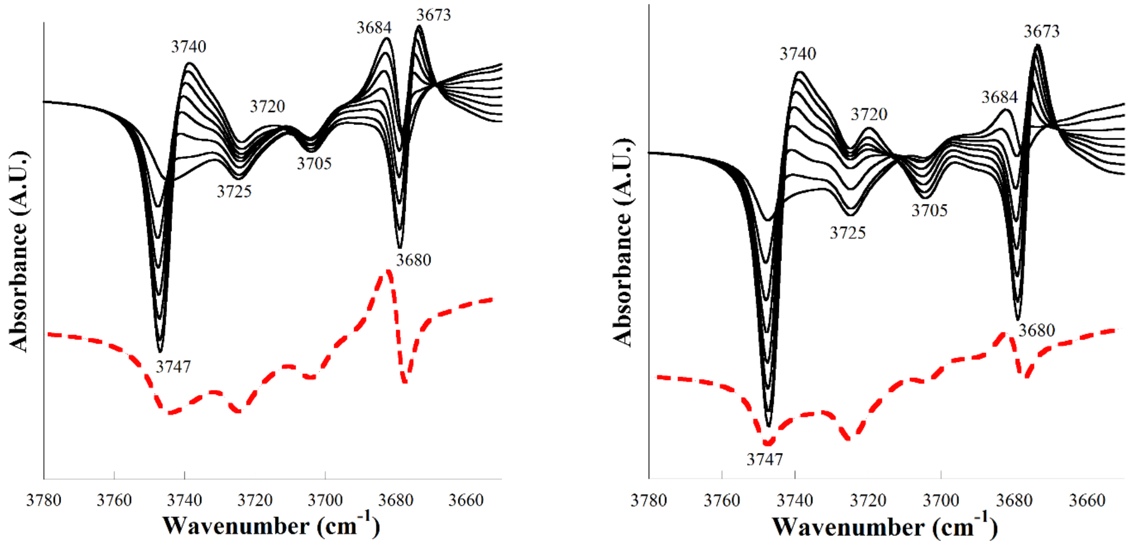

Crotonaldehyde **Crotyl alcohol**

Figure 4.5. *In-situ* DRIFTS spectra in the hydroxyl group region of 3800 – 3200 cm^{-1} acquired of ethanol, acetaldehyde, crotonaldehyde and crotyl alcohol on WK (1:1) catalyst. Sample vapor was adsorbed on the sample surface and temperature ramped up from 373 to 723 K while spectra being recorded. *In-situ* DRIFTS dehydrated catalyst spectrum at 100 °C was used as a reference.

2.5. *In-situ* DRIFT spectroscopy of C_2 (ethanol, acetaldehyde) and C_4 (crotonaldehyde and crotyl alcohol) adsorption and reaction on WK (1:1) catalyst surface as a function of temperature.

2.5.1. C_2 reactants and intermediates.

When ethanol was adsorbed on WK (1:1), several peaks in the C-H region were observed between 2985 and 2907 cm^{-1}, as well as at 2720 cm^{-1}, as shown in **Figure 4.6** and tabulated in **Table 4.3**. The former peaks were attributed to the combination of ν (CH_3) and ν (CH_2) vibrational modes with the corresponding bending modes located at 1454 and 1418 cm^{-1}, while the assignment of the latter peak is not straightforward. While generally within the ν (CH_3) spectral region, it can't be unambiguously assigned. As later shown by DFT calculations, that peak can be assigned to a frustrated ν (OH) mode of dissociated (chemisorbed) ethanol on a Mg_{4c} site. Peaks at 1380 and 1338 cm^{-1} can be assigned to the wagging modes of CH_2 and CH_3. Interestingly, a peak at 1624 cm^{-1} was observed at 373 K together with a negative peak at ~1670 cm^{-1} after physisorbed ethanol adsorption. The peak at 1670 cm^{-1} is the native bidentate carbonate asymmetric ν_3 vibration that persisted during the sample treatment, which we propose to be displaced due to the reactive ethanol adsorption on the surface.[49] This bidentate carbonate peak would typically be accompanied by its asymmetric counterpart at ~1370 cm^{-1},[49] however, this spectral region also shows adsorbed ethanol vibrations. The splitting of the ν_3 vibration is typically used to identify the coordination of the carbonate, since the degree of symmetry lowering caused by surface coordination is well-known to split the vibration differently.[55] For instance, the monodentate split is ~100 cm^{-1} (1415 split to ~1400 and ~1500 cm^{-1}), bidentate split is ~300 cm^{-1}, and bridged carbonate split is ≥ 400 cm^{-1}.[55] While surface carbonates are typically stable under low O_2 and high CO_2 concentration, they are typically unstable under reaction conditions.[56] DFT study also showed that ethanol adsorption is thermodynamically more stable than that for CO_2, with E_D = 10.5 - 13.5 kcal/mol and 7.1 - 9.4 kcal/mol, respectively,[17,57] hence suggesting that chemisorption of ethanol can displace surface carbonate species. There are several possibilities in assigning the peak at 1624 cm^{-1}. At this wavenumber region, hydrocarbons exhibit C=C stretches, as well as a distorted C=O stretch. Stable bands at ~1580 cm^{-1} are also expected for the surface acetate, even though an accompanying peak must be present around ~1400 cm^{-1} It is unlikely, that acetate is formed at 373 K.[58] One possible explanation for this is the formation of the coadsorbed water, presumably formed by dissociation of ethanol that results in the rearrangement of the hydroxy group when ethanol is adsorbed on the surface. The formation of water on the surface was previously observed by Busca's group on γ-Al_2O_3, where vapor-phase water was formed right after ethanol was introduced to the surface.[53]

The corresponding ν(C-O) vibration at ~1100 cm^{-1} was not observed because of the predominant vibrations of SiO_2 in the spectral region of 1200 to 900 cm^{-1}. However, peaks at 1140, 1126, 1104 and 1058 cm^{-1} were observed at 373 K on pure MgO samples, as shown in the **Figure 4.6** inset. The peaks at 1140, 1104, and 1058 can be assigned to the ethanol species on the surface, both chemisorbed surface ethoxide and physisorbed ethanol, with spectral shifts observed due to the difference in interaction with and adsorption on various accessible sites. The shifts between the physisorbed, chemisorbed, and vapor-phase ethanol were also previously observed by Branda and Birky.[14,30] Peaks at 1104 and 1058 cm^{-1} were assigned to δ(OH) and ν (C-O) of surface ethoxy, respectively, as also observed by Davis and Cavani groups.[10,13,14] The peak at 1140 cm^{-1} gained intensity after the cell was evacuated and heated to 476 K. This peak was previously assigned to ρ_w (CCO) by Davis' group with the peak located at 1122 cm^{-1} on MgO.[14] Notably, the peak at 1126 cm^{-1} appears at a higher temperature, ~473 K, which indicates the formation of a new species. This peak can be assigned to C-C stretch of the adsorbed acetaldehyde.[59]

Table 4.3. Vibrational frequencies and their assignments for ethanol, acetaldehyde, crotonaldehyde and crotyl alcohol adsorption on WK (1:1)

Assignment	**Experimental (cm^{-1})**				
	Ethanol	**Acetaldehyde**	**Enolate**	**Crotonaldehyde**	**Crotyl alcohol**
ν (OH)	2720	-	-	-	-
ν (CH_3)	2985	3037, 2967, 2935	-	2967, 2935	3017, 2965
ν (CH_2)	2937, 2907, 2881	-	-	-	2949, 2840
Fermi CH_3		2882, 2845			
ν (CH)	-	2743	-	3032, 2882, 2845	
ν (C=O)	-	1716, 1680, 1633	-	1716, 1680, 1670	-
ν (C=C)	-	-	1600, 1578	1600, 1574	1602
δ (CH_2)	1454	-	-	-	1380
δ (CH_3)	1418	-	-	1456, 1434	1368
ρ_w (CH)	1380	-	-	-	-
ρ_w (CH_2)	-	-	-	-	1441
ρ_w (CH_3)	1338	1456, 1434, 1382	-	1346	1456
ρ_w (CHO)	-	1284	-	1382	-

As the temperature is increased to 723 K, the aforementioned bands start decreasing in intensity, giving rise to several new bands, including those at 2958, 1653, 1604 and 1581 cm^{-1}. The experiment was carried out under inert gas flow, which prevents chemistry beyond dehydrogenation and dehydration from happening. The inert atmosphere encouraged desorption to take place rather than surface reaction, further limiting the reaction to dehydration and dehydrogenation, which are elementary reactions of ethanol. Experiments under constant reactant flow, where ethanol is constantly supplied to the surface, were also done and discussed thoroughly in Section 3.7**.** The first two peaks appeared intermittently from 473 K up to 623 K. The peak at 1653 cm^{-1} can be assigned to the ν (C=O) of acetaldehyde[59] adsorbed on an Mg_{3c} surface site with the assignment confirmed by our DFT calculation. This peak was also previously assigned to adsorbed crotonaldehyde, since the crotonaldehyde C=O stretch frequency is also typically lowered upon adsorption.[8] The crotonaldehyde vapor-phase exhibits C=O stretch at ~1691 cm^{-1}, as shown in **Table S4.1**. The appearance of the former can then be related to acetaldehyde as well, as the CH_2 stretch was also observed by Raskó *et al.* at 2960 cm^{-1} on TiO_2 and Ordomsky *et al.* at 2950 cm^{-1} over SiO_2, ZrO_2/SiO_2, and MgO/SiO_2.[8,54] Aldehyde presence can typically be spotted by its unique carbonyl CH stretch at ~2700 cm^{-1}, however this peak does not exist in our spectra. The absence of this peak is due to the distorted acetaldehyde -CHO group, where the C-O bond is now elongated, and the band will shift to a higher wavenumber at ca. 2800 cm^{-1}, as explained later by DFT results. Ordomsky *et al.* had this same observation where the carbonyl CH stretch was only present on the spectra when there is vapor-phase acetaldehyde on the surface.[8] Upon increasing the temperature, two peaks at 1604 and 1581 cm^{-1} start gaining intensity; these speaks can be assigned to a C=C group. We have previously shown that acetaldehyde transformation to surface enolate has very low activation energy on an Mg_{3c} surface site, which becomes the basis of our assignment of one of these C=C stretching bands to surface enolate.[17] The gas-phase keto-enol tautomerization of acetaldehyde thermodynamically favors the keto (aldehyde) form.[60] However, Palagin *et al*. spectroscopically observed proton transfer from acetaldehyde to SnBEA zeolite and attributed this to the surface enolate formation. Further complicating the assignment of these C=C stretching bands is the rather low Gibbs free energy barrier of ~16 kcal/mol[17] for aldol condensation, which opens up the possibility for crotonaldehyde formation.

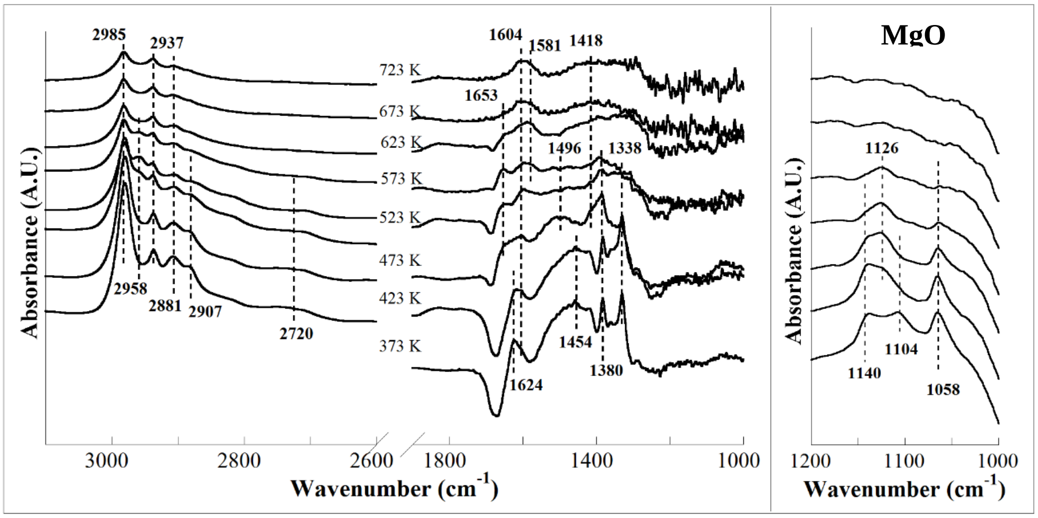

Figure 4.6. *In-situ* DRIFTS spectra acquired of ethanol on WK (1:1) catalyst in 3200 to 1000 cm^{-1} spectral region. Ethanol was adsorbed on the sample surface and temperature increased from 373 to 723 K while spectra being recorded. *In-situ* DRIFTS spectra of the sample surface with no adsorbate present at every corresponding temperature were used for reference. *In-situ* DRIFTS spectra acquired for ethanol adsorbed on MgO are shown in the inset for 1200 to 1000 cm^{-1} spectral region.

Conflicting assignments have also previously been made for the C=C stretching bands originating from ethanol adsorption on MgO, where they were also previously assigned to surface acetate,[52,58] and/or 2,4-hexadienal, aldol condensation product of crotonaldehyde and acetaldehyde.[8] The latter was actually shown to form on basic surface sites at close to dry ice temperatures.[61,62] The formation of surface acetate was previously postulated to take place through an acyl intermediate, which yields a vibrational band at ~1690 cm^{-1}.[59] There are several reasons why acyl intermediate is highly unlikely to be formed on the basic surface: the base-induced Cannizzaro reaction suggests that the aldehyde needs to be lacking hydrogen in the α-position[63], and hence, the only way acetaldehyde can form an acetate is from the strong Lewis acid-driven Tischenko reaction.[64] From the broad shape of the peak it can be concluded that surface acetaldehyde undergoes enol transformation to yield surface enolates, which then either polymerize and/or undergo aldol condensation to yield higher aldehydes and bulky aromatic structures.

Collectively, these data show that in addition to physisorption, ethanol chemisorbs as two different surface species by displacing carbonate structure and producing water as a byproduct of its adsorption. In addition to the dissociative chemisorption, ethanol adsorbs as a semi-dissociated species, where the removed proton is still interacting strongly with the ethoxide, as shown by the frustrated -OH vibration. Part of this structure further undergo dehydrogenation, which is shown by the acetaldehyde C=O peak, and further reacts to make C=C containing molecule(s).

Acetaldehyde is often cited as an important intermediate during the catalytic ethanol transformation to 1,3-BD and has been proposed to have a major role in the overall reactive mechanism.[1,6,23] To further explore the relevant surface intermediates chemistry and corroborate the assignment of the ethanol IR data, we carried out IR temperature programmed desorption experiments with acetaldehyde as the probe molecule. Acetaldehyde IR spectra typically exhibit peaks at 1716, 1680 and 1590 cm^{-1} which were related to vapor-phase C=O, adsorbed C=O, and C=C stretches, respectively.[65] Other bands stemming from acetaldehyde adsorption on bifunctional metal oxide surfaces previously observed were located in the 1450-1350 cm^{-1} region with conflicting assignments to either surface acetates[66] or, more conservatively, to bending modes of CH, CH_2, and CH_3.[65,67] Acetaldehyde adsorption was studied over MgO based catalysts, where on Ni/MgO, it was claimed to undergo several reactions, such as a Cannizzaro reaction which yielded surface acetate peaks around ~1580 and ~1425 cm^{-1} [68] aldol condensation, as previously observed on MgO/SiO_2 by IR spectroscopy.[8]

Acetaldehyde adsorption on WK (1:1) is shown in **Figure 4.7** and tabulated in **Table 4.3**. In the C-H region, several bands were observed at 3027, 2967, 2935, 2882, 2845, and 2743 cm^{-1} upon acetaldehyde introduction to the surface. The first three bands can be directly assigned to the stretching mode of CH_3, while CH_3 Fermi resonances can be assigned to 2882 and 2845 cm^{-1}, These depend on the adsorption site.[59] A possible assignment can also be made that one belongs to acetaldehyde, while the other one to crotonaldehyde. The weak band at 2743 cm^{-1} is the signature stretching mode of aldehyde -CHO group with broadening due to possible crotonaldehyde formation at the low temperature. The peaks at 1716, 1680, 1633, 1600 and 1578 cm^{-1} are all related to C=O and C=C stretches, depending on the binding site and nature of the adsorption/perturbation of the C=O group. Acetaldehyde undergoes aldol condensation[17] and polymerization[61,62] with very low energy barriers on basic surfaces, including MgO. The reactivity of acetaldehyde on the basic surface is the main reason for its rapid deactivation when acetaldehyde is present in large concentrations.[8,69] Peaks at 1456, 1434, 1382, 1346 and 1284 cm^{-1} can be used to confirm the existence of an acetaldehyde molecule and its reaction products, such as polymerized acetaldehyde and possible enolate isomerization-aldol condensation products on the surface. The first two of those peaks, along with the one at 1346 cm^{-1} , are assigned to the wagging mode of CH_3, the mode that polymerized aromatic acetaldehyde is lacking.[59] The peak at 1382 cm^{-1} and 1284 cm^{-1} can be assigned to the bending mode of the acetaldehyde CH_3 group[59] and wagging mode of the acetaldehyde CHO group, respectively. However, these bending modes can overlap with those originating from surface enolate, as a result of keto-enol tautomerization, and further detailed assignments will be made on DFT calculations. There were no peaks observed below 1300 cm^{-1} due to the strong SiO$_2$ vibrations and pure MgO data was used to investigate that spectral region, as shown in the **Figure 4.7** inset. In this region, three bands are observed at 1264, 1107, and 1066 cm^{-1} when acetaldehyde is observed on MgO. These bands were previously assigned to η (C-O), η (C-C), and ν (C-C), respectively.[59]

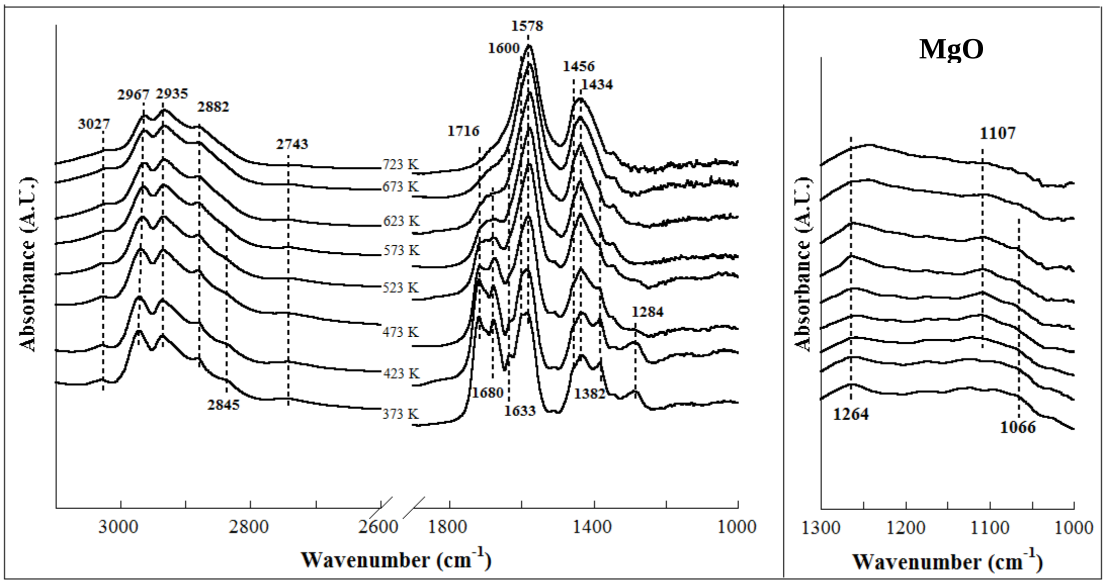

Figure 4.7. *In-situ* DRIFTS spectra acquired of acetaldehyde on WK (1:1) catalyst in 3200 to 1000 cm^{-1} spectral region. Acetaldehyde was adsorbed on the sample surface and temperature increased from 373 to 723 K while spectra being recorded. *In-situ* DRIFTS spectra of the sample surface with no adsorbate present at every corresponding temperature were used for reference. *In-situ* DRIFTS spectra acquired for acetaldehyde adsorbed on MgO are shown in the inset for 1200 to 1000 cm^{-1} spectral region.

Analysis of the IR data of both ethanol and acetaldehyde demonstrates that the surface ethoxy species react to make adsorbed surface acetaldehyde, that, in turn, further desorb, polymerize, couple, or isomerize as shown by the presence of the peaks at ~1600 and ~1580 cm^{-1}, where intensity in the ethanol spectra is much less than that of acetaldehyde. This lack of intensity is due to the fact that ethanol would also desorb from the surface and the steep activation energy, i.e. 39.6 kcal/mol for the dehydrogenation reaction.[17] The acetaldehyde formed during the experiments has higher affinity to the basic surface, which is confirmed by the intense CH stretching and CH_3 wagging modes of the molecule being on the surface even at 723 K. Ordomsky, *et al.* also acknowledged the reactivity of the basic catalyst, which, in turn, results in the strong adsorption of acetaldehyde and/or its higher self-reaction products on the surface.[8]

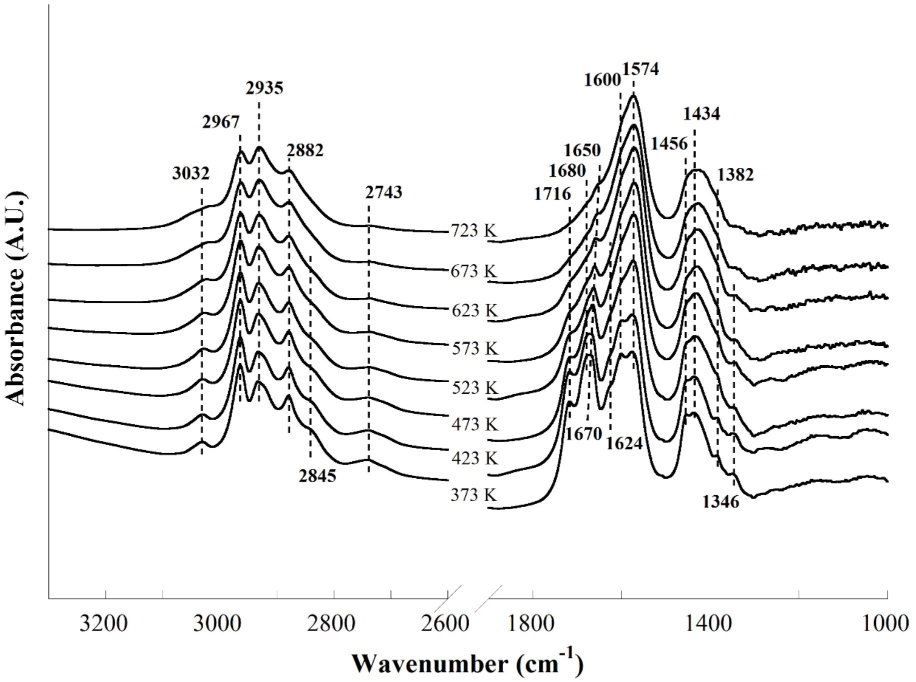

Figure 4.8. *In-situ* DRIFTS spectra acquired of crotonaldehyde on WK (1:1) catalyst in 3200 to 1000 cm^{-1} spectral region. Crotonaldehyde was adsorbed on the sample surface and temperature increased from 373 to 723 K while spectra being recorded. *In-situ* DRIFTS spectra of the sample surface with no adsorbate present at every corresponding temperature were used for reference.

2.5.2. C_4 intermediates.

DRIFT spectra of crotonaldehyde adsorbed on the WK (1:1) surface are shown in **Figure 4.8**. Notably, peaks observed in the spectra are identical with the ones found for acetaldehyde in **Figure 4.7** and tabulated in **Table 4.3**, except for the relative intensities of several peaks, such as 1716, 1680, 1650, 1456, and 1434 cm^{-1}. The similarities between the two spectra suggest potential overlaps between peaks from both aldehydes during the infrared analysis of the surface reactive intermediates. The almost identical spectra make a solid case for the deduction of acetaldehyde spontaneous coupling to crotonaldehyde via aldol condensation at 373 K followed by dehydration, which can also be confirmed by the shoulder at ~1633 cm^{-1} in **Figure 4.7**. The interpretation of aldol condensation at 373 K can be justified by our supplementary TPSR experiments (not shown), which showed that crotonaldehyde (m/z=70) appeared right when the surface became saturated with acetaldehyde. The spontaneous reaction of acetaldehyde aldol condensation to yield hydroxy-butanal and crotonaldehyde had also been previously observed over HZSM-5,[65] TiO_2, CeO_2, and Al_2O_3.[54,58,59] However, infrared spectra alone are not capable of decoupling both intermediates.

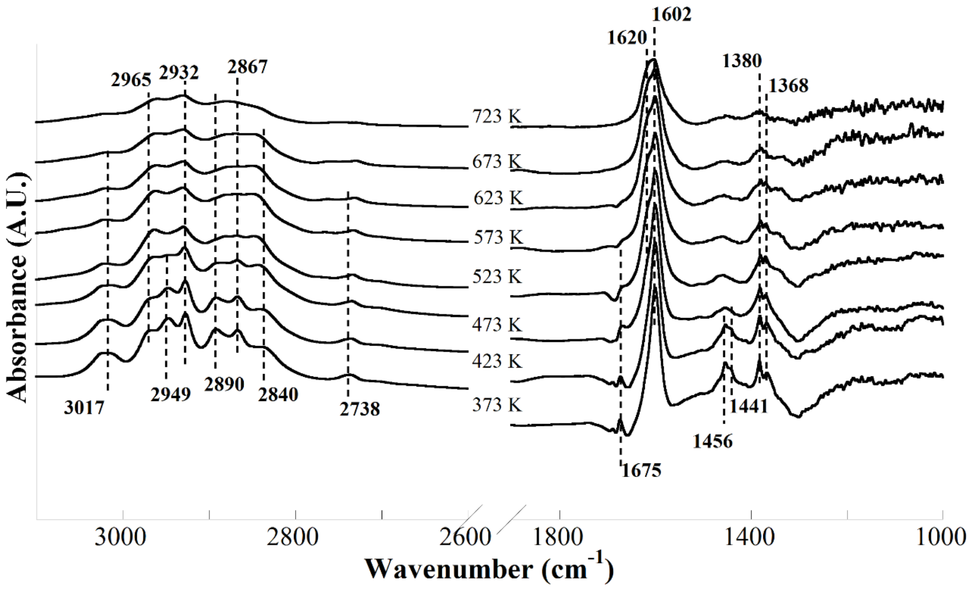

Figure 4.9. *In-situ* DRIFTS spectra acquired of crotyl alcohol on WK (1:1) catalyst in 3200 to 1000 cm^{-1} spectral region. Crotyl alcohol was adsorbed on the sample surface and temperature increased from 376 to 723 K while spectra being recorded. *In-situ* DRIFTS spectra of the sample surface with no adsorbate present at every corresponding temperature were used for reference.

The adsorption of crotyl alcohol on the WK (1:1) surface, as shown in **Figure 4.9** and tabulated in **Table 4.3,** provides more insight for the C=C vibration region. Our data show relatively few peaks and demonstrate the selective nature of the crotyl alcohol transformation on this bifunctional catalyst. Peaks at 3017, 2965, 2949 and 2840 cm^{-1} were assigned to the CH_3 and CH_2 stretches of adsorbed crotyl alcohol, while peaks at 2932, 2867 and 2738 cm^{-1} were assigned to both and also to vapor-phase crotyl alcohol.[70] Bending and wagging modes of the CH groups can also be seen in the 1400-1300 cm^{-1} region, where peaks at 1456 and 1441 cm^{-1} were assigned to $\rho_w(CH_2)$ and $\rho_w(CH_3)$ and 1380 and 1368 cm^{-1} - to $\delta(CH_2)$ and $\delta(CH_3)$. A unique feature of the adsorption is shown by the presence of an intense, sharp peak at 1602 cm^{-1} upon adsorption, which red-shifted ~70 cm^{-1} from the vapor-phase crotyl alcohol peak at 1675 cm^{-1}.[70] This peak is assigned to the C=C stretch of adsorbed 1,3-BD. This was also observed by Wenig and Schrader during their crotyl alcohol *in-situ* IR experiments over V-P-O catalyst.[71] The accompanying water peak at ~1650 cm^{-1} can be seen as a shoulder for the intense 1600 cm^{-1} peak. Our DFT calculations discussed later also show that at this adsorbed state, there was no higher CH peak observed at ~3100 cm^{-1}, due to the elongated C=C group of the C_4 structure. Following a temperature increase to 473 K, a shoulder appeared at 1620 cm^{-1} and this was assigned to 1-butene, which also was observed over V-P-O catalyst.[71] Alternatively, the peak at 1602 cm^{-1} can be assigned to the C=C mode of crotyl alcohol, while the peak at 1620 cm^{-1} could originate from the adsorbed 1,3-BD, as shown by Cavani *et al*.[10,19] In one of their experiments, however, this peak appeared when the surface temperature was increased under inert flow, which, based on our experiments, will not give any higher C_4 compounds in the vapor-phase. The peak at 1675 cm^{-1} is low enough in intensity that it would be overwhelmed if adsorbed aldehydes were present on the surface. However, **Figure 4.6** shows that there was no peak was found at that wavenumber. This is possibly due to the depleted ethanol and/or the little bit of crotonaldehyde that was being made on the surface. This argument is supported by the absence of any peaks at ~1700 cm^{-1}, indicating that there was not enough acetaldehyde on the surface to induce desorption and aldol condensation. Our observation shows that the formation of acetaldehyde, being very reactive to the WK (1:1) surface, leads to the formation of various C=C containing intermediates, including surface enolate, polymerized acetaldehyde, and aldol condensation products, i.e. crotonaldehyde and 2,4-hexadienal. The crotonaldehyde, does not, however, proceed further to produce crotyl alcohol and 1,3-BD. The unsaturated aldehyde tends to remain on the surface of the catalyst, which is why it is rarely observed in the gas-phase.

2.6. DFT calculations ethanol, acetaldehyde, crotonaldehyde and crotyl alcohol vibrational frequencies.

Disagreements in peak assignments arise mainly when interpreting the acetaldehyde adsorption spectra, where polymerization on the catalyst surface takes place at relatively low temperature,[61,62] in addition to the desired aldol condensation[8,59,65,72] and Cannizzaro reaction.[66,68] In ethanol adsorption spectra, an important peak at 1604 cm^{-1}, accompanied by a shoulder at 1581 cm^{-1}, also sparks discrepancy in assignments.[8,52,68] Peak shifts are often observed, mainly in the C-O region, where the anchoring sites vary for different catalysts and hence almost directly affect the vibration.[13,14,30,53] We used DFT structure optimized and calculated frequencies of both gas and adsorbed ethanol, acetaldehyde, crotyl alcohol and crotonaldehyde molecules to aid in *in-situ* DRIFT spectra assignments. In the calculation, a defect site on MgO (100), i.e. $Mg_{3C}^{2+}O_{4C}^{2-}$ (kink), was used for adsorbate structural optimization. Another potential active site, the OH group on

MgO, was considered since indirect correlation using XPS has pointed out that more OH groups on the MgO leads to a better conversion.[12] Our detailed analysis using *in-situ* DRIFTS, however, showed that the OH groups' involvement during the reaction is minimal with its participations limited to substitutional chemisorption and reversible thermal rearrangement. It is widely known that MgO-SiO_2 has defect sites, kinks in particular, that are stable up to the reaction condition,[15,30,31,44] not to mention the recently synthesized MgO catalyst that gives conversion as good as the SiO_2-based material, which questions the silica's role on the reaction.[12] The use of defect sites has been utilized before[10,11,17] and kink site was chosen as the active site based on the stability comparison that was carried out by Chieregato *et al.*[10] and Zhang *et al.*[11] It is well known that vibrational frequencies calculated using harmonic approximation are typically larger than the fundamental ones observed experimentally with the various scaling factors typically used.[73] We calculated these scaling factors by optimizing ethanol, acetaldehyde, crotonaldehyde, and crotyl alcohol molecules and comparing the frequencies with the experimental values.[70] Using the method of least-squares we determined the scaling factors to be 0.997, 0.9962, 0.9996, and 0.9903 for ethanol, acetaldehyde, crotonaldehyde, and crotyl alcohol, respectively. The scaling factors for all molecules are very close to unity and unscaled frequencies were used to assign FTIR peaks. The complete scaling calculation can be found in the Supplementary Information **Table S4.1**.

We performed frequency calculations for several permutations of ethanol, acetaldehyde (enolate), crotonaldehyde, and crotyl alcohol adsorbed on a defected MgO surface.[17] The optimized structures are shown in **Figure 4.10** and the calculated frequencies are tabulated in **Table 4.4**. The two ethanol (**I**) species lead to acetaldehyde on

$Mg_{3C}O_{4C}$ and ethylene on $Mg_{3C}O_{5C}$, while there are three adsorption configurations of acetaldehyde (**II**): physisorbed on Mg_{3C}, chemisorbed on $Mg_{3C}O_{4C}$ and enolate adsorbed on $Mg_{3C}O_{4C}$. For crotonaldehyde, configuration (**IV)** due to the assumed facile dehydration of acetaldol to crotonaldehyde was used.[17] The crotyl alcohol (**V**) DFT calculation leads to both the dissociated state and the coordinated 1,3-BD (**VI**) with the α-C still bound to the O atom. Structure numbers, as shown in **Figure 4.1,** refer to the particular steps in the ethanol catalytic transformation cycle. Acetaldol adsorption was not optimized in this work due to its rare observation during experiments.[1]

DFT calculations show that ethanol can be adsorbed in two separate ways: via dissociative adsorption and semi-dissociative adsorption, with the deprotonated ethoxy still interacting strongly with the resulting surface hydroxyl. Typical adsorption spectra of ethanol on an MgO surface show a peak at ~2700 cm^{-1} which was never previously discussed.[10,14,19] With the periodic DFT calculation, this peak can be assigned to the stretching mode of the surface hydroxyl group. In **Figure 4.6**, vapor-phase acetaldehyde did not appear in infrared spectra. Instead, a peak at 1653 cm^{-1} appeared at the intermediate temperatures, and this can be correlated with the DFT-calculated C-O vibration at 1657 cm^{-1}. This is accompanied by the build-up of C=C containing surface species, shown by the peak at ~1600 cm^{-1} in **Figure 4.6**.

Acetaldehyde adsorption on the basic catalyst surface results in the infrared peaks similar to those of crotonaldehyde (**Figure 4.7** and **6**). The experimental peak at 1382 cm^{-1} was previously assigned to the -CH_3 wagging mode of acetaldehyde and this may overlap with the surface crotonaldehyde, owing to the similarities between **Figure 4.7** and **6**.[59] The complexity of this peak is demonstrated by the shoulders around it and its appearance in both **Figure 4.7** and **6**. To answer this question, we looked at crotonaldehyde frequency calculation as well as the two acetaldehyde species and surface enolate (**Figure 4.10)**. DFT shows that four of the species all exhibited vibration around that wavenumber, which can be seen in **Table 4.4.** Peak at 1284 cm^{-1} was also previously assigned to the C-O vibration from acetaldehyde, and this also most likely overlaps with a vibrational mode from physisorbed acetaldehyde.[59] The peak at 1284 cm^{-1} is revealed to originate from -CHO bending of an interacting surface species, in which the C=O bond is opened with the molecule bridging two Mg atoms and one O atom, as shown in **Figure 4.10-II**. This vibrational mode is not present on the physisorbed acetaldehyde, where the analog of that vibration is presented as a peak at 1382 cm^{-1}, contradicting assignment by Singh *et al.*[59] Analysis of the C=C region inevitably presents the possibility that surface enolate is the more reactive state of acetaldehyde. This enolate is the main building block for further reactions, such as polymerization and aldol condensation.[74] The presence of the enolate is rather hard to confirm experimentally,[74] due to its subsequent spontaneous reactions, but DFT calculation reveals its presence, as verified the by C=C stretches at 1621 cm^{-1} and the -CHO bending mode at 1384 cm^{-1}. Finally, the peak at 2845 cm^{-1} in **Figure 4.8** can be assigned to the surface crotonaldehyde, blue-shifted from the vapor-phase. Our DFT calculations show that this peak can be assigned to ν (CH), calculated at 2868 cm^{-1}.

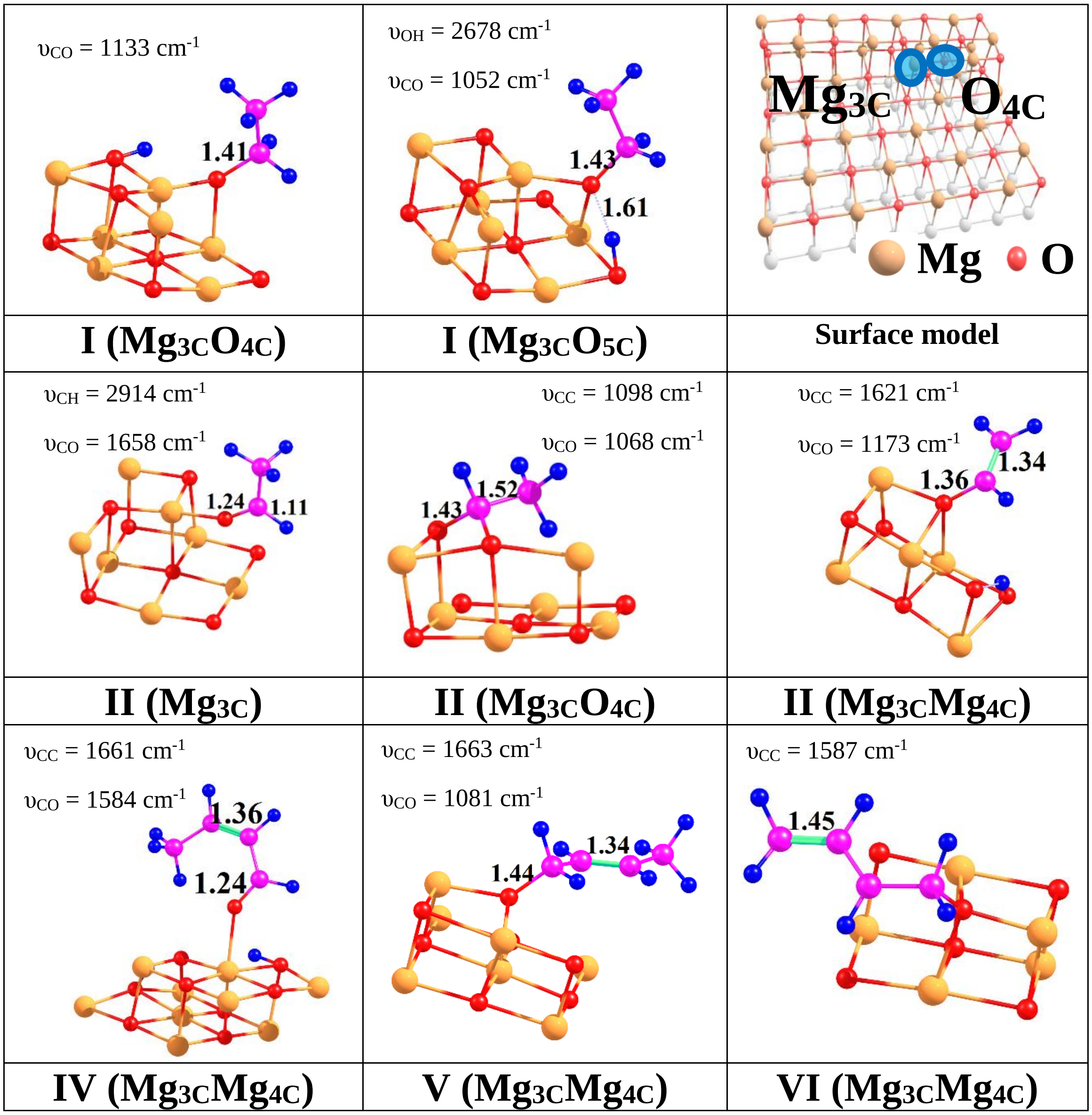

I (Mg$_{3C}$O$_{4C}$) **I (Mg$_{3C}$O$_{5C}$)** **Surface model**

II (Mg$_{3C}$) **II (Mg$_{3C}$O$_{4C}$)** **II (Mg$_{3C}$Mg$_{4C}$)**

IV (Mg$_{3C}$Mg$_{4C}$) **V (Mg$_{3C}$Mg$_{4C}$)** **VI (Mg$_{3C}$Mg$_{4C}$)**

Figure 4.10. PBE optimized structures of ethanol (**I**), acetaldehyde (**II**), its enolate conformation (**II**), crotonaldehyde (**IV**), crotyl alcohol (**V**) and 1,3-butadiene (**VI**) on MgO surface low coordination Mg$_{3c}$O$_{4c}$ or Mg$_{3c}$O$_{5c}$ surface sites. Numbers refer to the particular steps in catalytic transformation cycle shown in **Figure 4.1**.

Table 4.4 Calculated infrared frequencies of ethanol, acetaldehyde, crotonaldehyde and crotyl alcohol molecules adsorbed on low coordination model MgO surface sites. Frequencies were calculated using PBE density functional and no scaling to correct for anharmonicity was applied.

Assignment	**Ethanol**		**Acetaldehyde**		**Enolate**	**Crotonaldehyde**	**Crotyl alcohol**
Configuration	**$Mg_{3C}O_{4C}$**	**$Mg_{3C}O_{5C}$**	**Mg_{3C}**	**$Mg_{3C}O_{4C}$**	**$Mg_{3C}Mg_{4C}$**	**$Mg_{3C}Mg_{4C}$**	**$Mg_{3C}Mg_{4C}$**
ν (OH)	3574	2679	-	-	3063	-	-
ν (CH_3)	3030, 3020, 2950	3036, 3024, 2952	3096, 3019, 2965	3061, 3037, 2961	-	3000, 2943	3062, 3007, 2959
ν (CH_2)	2903, 2873	2938, 2909	-	-	3173, 3073	-	2946, 2875
ν (CH)	-	-	2914	2828	3028	3102, 3068, 3041, 2868	3056, 3040
ν (C=O)	-	-	1657	1016	1173	1664	-
ν (C=C)	-	-	-	-	1621	1581, 1010	1663
δ (CH_2)	1460	1469	-	-	1384	-	1378
δ (CH_3)	1438, 1435	1449, 1440	-	-	-	1431, 1428	1350
ρ_w (CH)	1353, 1337	-	-	1367	-	1232	-
ρ_w (CH_2)	-	1359	-	-	-	-	1434
ρ_w (CH_3)	-	1341	1408, 1402, 1320	1447, 1428, 1320	-	1349	1441, 1419
ρ_w (CHO)	-	-	1382	1292	1302	1365	-
ρ_t (CH_2)	1260	1267	-	-	-	-	-
δ (OH)	-	1116	-	-	1004	-	-
δ (CC)	-	1072	1117	1066	-	-	-
ν (CO)	1133	1052	-	-	-	-	-
ρ_w (CCO)	1132	-	-	-	-	-	1081
ν (CC)	1064	-	-	1098	-	-	-

The adsorption of crotyl alcohol provides much clarification for the entire reaction sequence. Silica possesses weak Lewis acid sites and might provide an additional dehydration site for the reaction. However, when ethanol was run on a bare silica catalyst, only a little conversion of ethanol was achieved at higher temperature.[75] The reaction yielded acetaldehyde, as well as ethylene and ether, which explains silica's role as a solid acid catalyst. MgO has the ability to dehydrate the crotyl alcohol to give 1,3-butadiene, which justifies the use of MgO defect sites for this reaction.[1,75] The interaction with silica, as shown in the Section 3.3, shows that the strong Lewis acid sites are due to the interaction of silica and MgO.[1,15] The peak at 1600 cm^{-1}, which immediately forms on the surface during experiment, indicates the presence of a C=C stretch. The vapor-phase crotyl alcohol exhibits a vibration at around ~1670 cm^{-1},[70] which is blue-shifted ~10 cm^{-1} for its adsorbed state, based on the DFT calculation and shown in **Table 4**. These peaks are also observed on the spectra in **Figure 4.9**, with the shifted peak being a shoulder to the intense, sharp 1602 cm^{-1}. This indicates the presence of another surface species, which was shown by DFT to be a coordinated 1,3-BD (**Figure 4.10, VI**). The assignment of this 1600 cm^{-1} peak is also corroborated by the absence of the sp^2 carbon C-H stretch peak, since α-C atom is still in transition from sp^3 to sp^2.

2.7. *In-situ* DRIFT spectra for the ethanol, acetaldehyde, crotonaldehyde and crotyl alcohol reaction on a WK (1:1) catalyst surface: the effect of the vapor phase presence.

Formation of the C_4 intermediates and products on MgO catalysts requires the presence of the vapor phase ethanol and does not proceed via adsorbed ethoxide intermediate catalytic conversion alone.[19] This is also supported by our experiments, as discussed in Section 3.5, where ethanol desorption did not lead to the peaks caused by acetaldehyde on the surface. Hence, we performed *in-situ* temperature programmed DRIFTS experiments, during which a continuous reactant flow was carried out over a sample containing adsorbed intermediates. DRIFT spectra for ethanol adsorbed on WK (1:1) in the presence of a continuous vapor flow are shown in **Figure 4.11**. A spectrum of the catalyst surface with the adsorbate at 373 K was used as a reference. The C-H stretching region has peaks at 2978, 2933, 2903, and 2877 cm^{-1}. These peaks are all attributed to CH_3 and CH_2 stretches. These peaks are also accompanied by the triplet at 1456, 1391 and 1061 cm^{-1} previously assigned to $\delta(CH_3)$, $\delta(OH)$ and $\upsilon(CO)$ of vapor-phase ethanol.[70,76] Two other peaks can also be observed at 1630 and 1322 cm^{-1} in the low temperature 373 to 473 K regime, while higher temperatures result in their disappearance. While the latter can be assigned to the wagging mode of the adsorbed ethoxy species, the former was previously assigned to the adsorbed crotyl alcohol.[19] It is highly unlikely, however, that crotyl alcohol was being made at such a low temperature, since no acetaldehyde was observed. Hence, we assigned the peak at 1630 cm^{-1} to adsorbed water in accordance with our assignment in Section 3.5.1. The higher temperature regime, 523 to 723 K, also consistently resulted in the greater 1575 and 1440 cm^{-1} peaks, in addition to peak broadening at ~3061 cm^{-1} which appears to be stable on the catalyst surface even at these higher temperatures. The peak broadening is indicative of the presence of olefins, i.e. ethylene and 1,3-BD. A notable increase, shown by the 1743 and 1687 cm^{-1} peaks at intermediate temperatures, can be assigned to acetaldehyde, both vapor-phase and chemisorbed, respectively. The C=O stretch peaks coincide with the emergence of a 3004 cm^{-1} peak, which is attributable to the C-H stretch of a sp^2 carbon. These two peaks are accompanied by a broad band at 1280

cm^{-1}, which is the same with the peak at 1284 cm^{-1} in **Figure 4.7**. We have assigned this peak to ρ_w of CHO. Right after the appearance of this intermediate, peaks at 1579 and 1434 cm^{-1} become very apparent, suggesting that these vibrations are from the reaction products of adsorbed acetaldehyde. These two peaks are also similar to those observed in a similar region, as shown in **Figure 4.7** and **Figure 4.8** for acetaldehyde and crotonaldehyde surface adsorption, respectively. As previously assigned, these two peaks originate from a C=C stretch (1579 cm^{-1}) and the bending modes of CH_2 or CH_3 (1434 cm^{-1}).

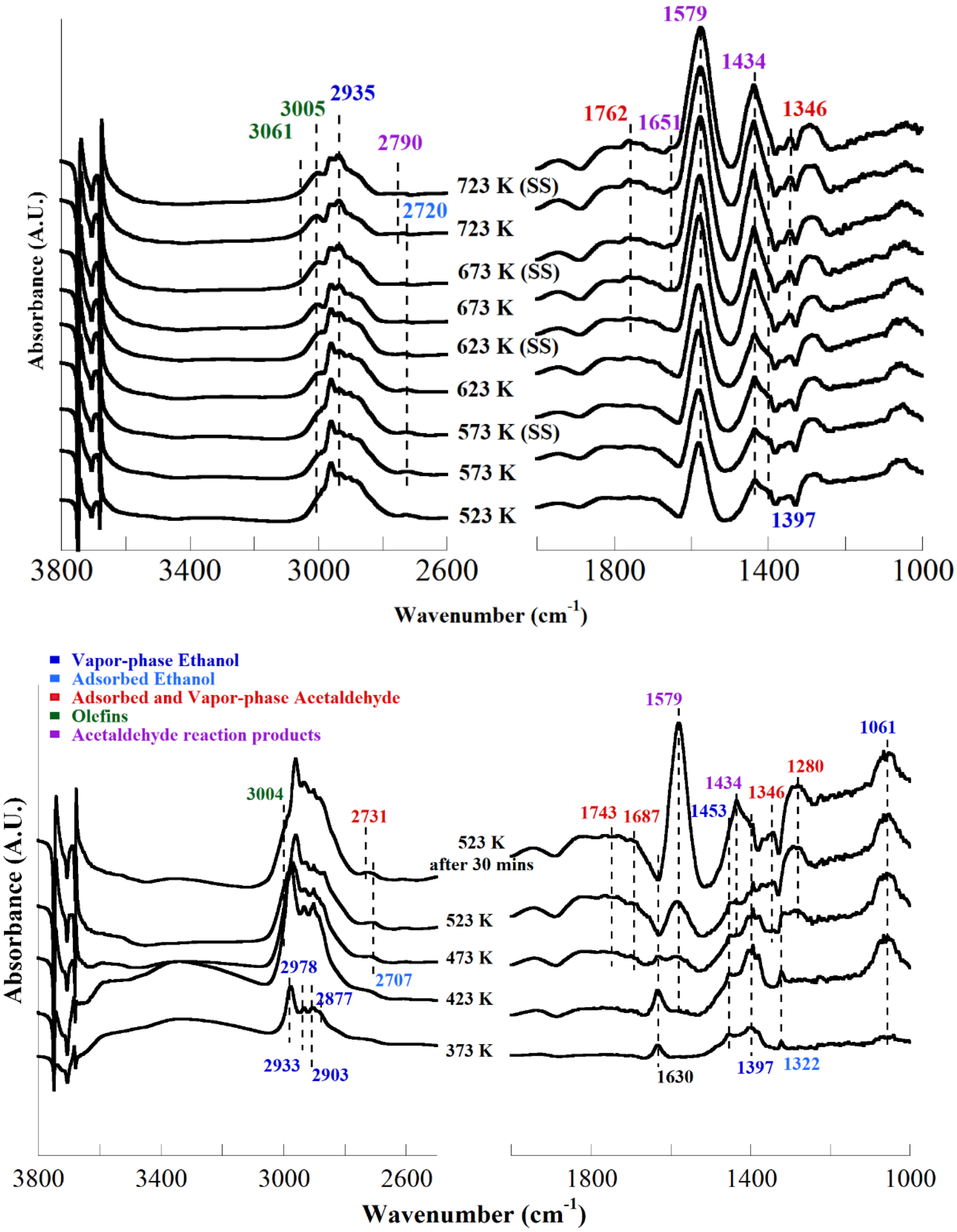

Figure 4.11. *In-situ* DRIFTS spectra acquired of ethanol on WK (1:1) catalyst. Ethanol was adsorbed on the sample surface, flown continuously and temperature increased from 376 to 723 K while spectra being recorded. *In-situ* DRIFTS spectrum of the sample surface with adsorbed ethanol present at 373 K was used for reference.

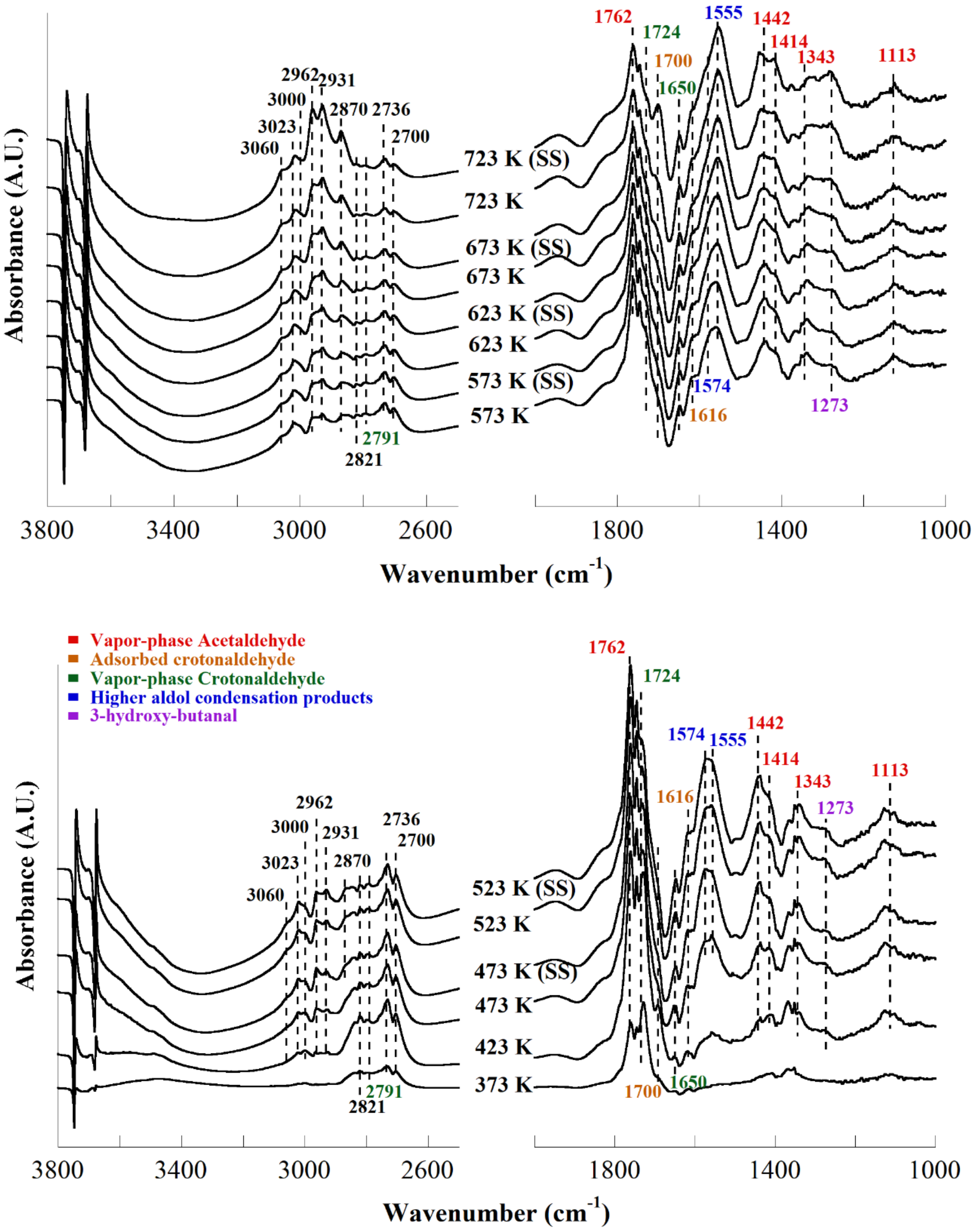

Figure 4.12. *In-situ* DRIFTS spectra acquired of acetaldehyde on WK (1:1) catalyst. Acetaldehyde was adsorbed on the sample surface, flown continuously and temperature increased from 376 to 723 K while spectra being recorded. *In-situ* DRIFTS spectrum of the sample surface with adsorbed acetaldehyde present at 373 K was used for reference.

Complementary vapor-phase composition measurements performed using gas chromatography (not shown) demonstrated that at a temperature regime above 523 K, 1,3-BD was made but no crotonaldehyde and crotyl alcohol were observed. This suggests that various C_4 intermediates to 1,3-BD tend to either react quickly with the product or remain strongly adsorbed on the surface and react further, instead of desorbing. The correlation made between the increase in 1,3-BD production by GC and the intensity increase in 1575 and 1440 cm^{-1} peak intensities implies that these two peaks are predominantly due to a C_4 intermediate, with some contributions from surface enolate and polymerized acetaldehyde, as also previously shown in Section 3.5.1. While the first peak was previously assigned to 2,4-hexadienal,[8] surface acetates from the Cannizzaro reaction would exhibit both bands due to their asymmetric and symmetric -COO stretching modes.[52] Their increasing intensity also suggests that the surface ethoxide, which dehydrogenates to acetaldehyde, is continuously replenished by the vapor-phase ethanol, as shown in **Figure 4.11**. This suggests that ethanol undergoes a catalytic transformation into acetaldehyde on WK (1:1), which can be regarded as a rate limiting step because the other important intermediates are spontaneously formed once acetaldehyde is produced. The subsequent aldol condensation proceeds rapidly even at relatively low temperatures, as shown in **Figures 4.5** and **4.6**, while crotyl alcohol is readily dehydrated, as demonstrated by the formation of 1,3-BD at 373 K.[17,71] This observation agrees with literature reports, where on a basic catalyst with little redox properties ethanol dehydrogenation is regarded as the rate limiting step.[23,77]

In-situ DRIFT spectra of acetaldehyde adsorbed on WK (1:1) in the presence of vapor are shown in **Figure 4.12**. Peaks at 3060, 3023, 3000, 2962, 2931, 2870, 2821, 2791, 2736, and 2700 cm^{-1} are readily observed on these spectra. These various CH_3, CH_2, CH sp^2 stretches indicate the presence of multiple surface species. As discussed in Sections 3.5.1 and 3.5.2 this is due to the spontaneous polymerization, aldol condensation, and keto-enol tautomerization of the acetaldehyde. A gradual increase in C-H stretching vibration from 2700 to 2821 cm^{-1} at lower temperatures is followed by their transformation into the species responsible for the peaks at 2870 to 2962 cm^{-1} and can be associated with transformation of vapor-phase acetaldehyde into chemisorbed acetaldehyde and into surface enolate and crotonaldehyde. This is different from the temperature programmed desorption experiments shown in **Figure 4.7** and suggests that vapor-phase acetaldehyde needs to be continuously supplied to replenish the surface species in order to continuously produce C_4 molecules. This experimental observation is also supported by the recent computational study where aldol condensation of acetaldehyde on an MgO Mg_{3c} site was shown to result from the interaction between surface enolate and physisorbed acetaldehyde.[17] Peak assignments provided in **Table 4.4** also suggest that peaks at 1762, 1724, 1442, 1343, and 1113 cm^{-1} can be assigned to the presence of vapor-phase acetaldehyde. Higher temperature regimes above 573 K result in the decrease to 1724 cm^{-1} as well as an enhanced 1273 cm^{-1} peak signifying the conversion of adsorbed acetaldehyde into acetaldol as an intermediate that intermittently appears before being dissociated to crotonaldehyde and water. The peak at 1273 cm^{-1} was previously observed by Singh *et al.* and assigned to δ (C-OH) of the aldol.[59] The peak at 1616 cm^{-1} is indicative of the C=C stretch that originates from enolate, crotonaldehyde or 2,4-hexadienal. The peak at 1650 cm^{-1} gradually increased with temperature, indicating the presence of adsorbed aldehyde which could belong to acetaldehyde or crotonaldehyde. The triplet peak at ~1750 cm^{-1} slowly transforms into a singlet at higher temperatures indicating the depleted vapor-phase acetaldehyde, due to the aldol condensation, confirmed by the presence of the crotonaldehyde peak at 1700 cm^{-1}. Similar to the case of ethanol, peaks at ~1574 and 1442 cm^{-1} increased with temperature. These peaks are, however, accompanied by a more prominent peak at 1555 cm^{-1}. This peak has not been observed previously in **Figures 4.5, 4.6** and **4.9**. This ~20 cm^{-1} red shift is most likely due to the interaction between the C=C molecule with vapor-phase acetaldehyde. In both ethanol and acetaldehyde reactive desorption experiments in **Figures 4.9** and **4.10** the same native hydroxyl groups at 3747, 3725, and 3680 cm^{-1} from **Table 4.2** and **Figure 4.3** are transiently involved in the catalytic transformations. Furthermore, the hydroxyl group region appears to be similar to those in **Figure 4.5** suggesting no new basic sites are formed or they are immediately consumed by the ensuing reactions. **Figure 4.12** also suggests that aldol condensation on a WK (1:1) surface proceeds quickly and is not a rate limiting step.

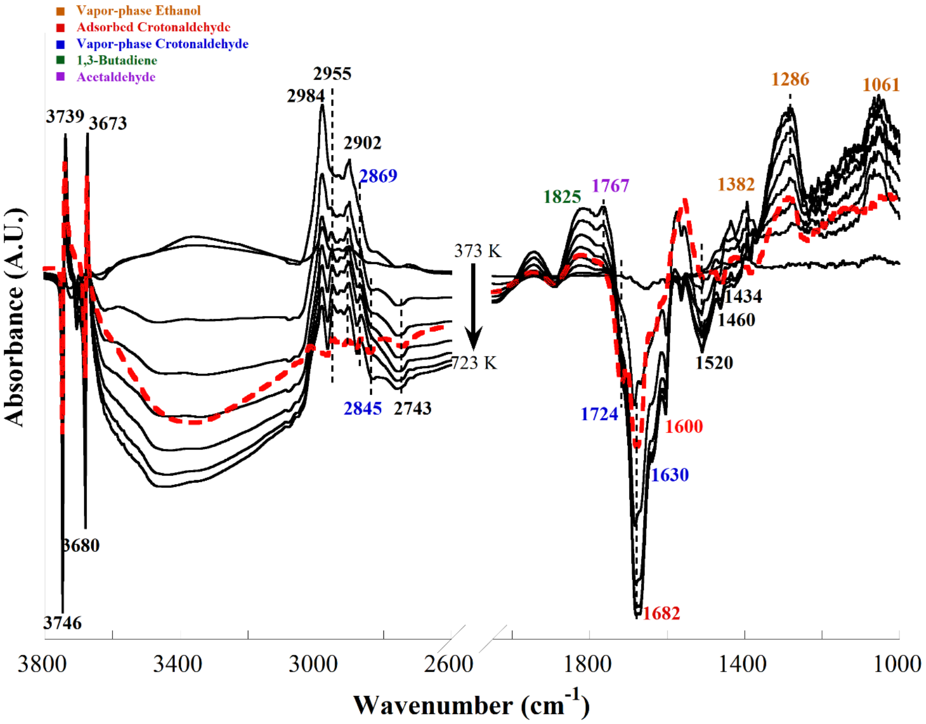

Figure 4.13. *In-situ* DRIFTS spectra acquired of crotonaldehyde on WK (1:1) catalyst under ethanol vapor flow. Crotonaldehyde was adsorbed on the sample surface, flushed with inert gas and ethanol was introduced under continuous flow with temperature increased from 376 to 723 K while spectra being recorded. *In-situ* DRIFTS spectrum of the sample surface with adsorbed crotonaldehyde at 373 K was used for reference. For comparison, 523 K spectrum of crotonaldehyde adsorbed with no gas phase present is shown in red dotted line.

Meenvein-Ponndorf-Verley (MPV) reduction is a hydrogenation process in which alcohols are used as a source of hydrogen.[78] It was postulated to take place in the reaction mechanism with ethanol hydrogenating the produced crotonaldehyde.[1,16] It is typically initiated by abstraction of an H^+ from the alcohol. It was suggested that the rate limiting step is hydride transfer from the adsorbed alcohol to the adsorbed carbonyl compound.[78] **Figure 4.13** shows the corresponding infrared spectra of the adsorbed crotonaldehyde in the presence of ethanol vapor. Peaks at 2984, 2955, and 2902 can be specifically assigned to ethanol CH_3 and CH_2 stretches with some minor contribution by other C_4 molecules. Negative peaks at 2845 and 2743 cm^{-1}, on the other hand, are due to the CH_3 Fermi resonance and ν (CH) of crotonaldehyde, respectively.[54,59] Each of these two negative peaks is accompanied by a positive shoulder at a lower wavenumber, which also increases with temperature, indicating the presence of another aldehyde, most likely acetaldehyde. The presence of the vapor-phase acetaldehyde as the side product of the MPV reduction can be confirmed by the C=O stretch at 1767 cm^{-1} , which has also been observed in previous experiments under constant acetaldehyde and ethanol vapor flow. This confirmation is shown in **Figures 4.9** and **4.10**. The peak at 1825 cm^{-1} can't be assigned to any of the alcohols or aldehydes. That peak can be found in the gas-phase 1,3-BD IR spectrum, as reported in the NIST database.[70] The signature C=C stretch of 1,3-BD is, however, impossible to observe due to its overlap with the negative peaks from crotonaldehyde. Negative peaks can readily be observed in the 1700-1600 cm^{-1} region and 1520-1400 cm^{-1} region, indicating the consumption of crotonaldehyde. A red-dotted IR spectrum is shown as a comparison for the crotonaldehyde desorption at 523 K. Comparison of the two spectra at the same temperature shows that the intensity decrease of the red plot is much less significant than when ethanol is constantly flown during the experiment. The depletion of the surface crotonaldehyde is due to temperature-induced desorption and reduction by ethanol to a certain extent. This intensity decrease is, however, not accompanied by the peak at 1587 cm^{-1}. This peak is relatively unaffected by the temperature-programmed reaction, even though there are sharp peaks at 1560 cm^{-1}, which can also be found in the red-dotted spectrum. The absence of both positive and negative peaks at 1587 cm^{-1} indicates that this peak is not part of the reactive intermediate and due mostly to the overreaction of crotonaldehyde and acetaldehyde to 2,4-hexadienal.[8] The peak at 1520 cm^{-1} signifies the presence of a C-C containing molecule, which is being consumed. Interestingly, peaks around 1460 and 1430 cm^{-1} are both initially consumed before they start increasing positively. We expect this due to the possible overlap between several CH_3 containing molecules, such as crotonaldehye, which is initially consumed. The acetaldehyde that is being produced and the vapor-phase ethanol, which is initially consumed, starts to increase in intensity due to the depleted crotonaldehyde. The intensity decrease in these peaks is also accompanied by the increasing intensity of the ethanol bands at 1061, 1286, and 1346 cm^{-1}.

3. Conclusions

Surface chemistry of WK (1:1) catalyst during the reaction of ethanol and the corresponding reactive intermediates, including acetaldehyde, crotonaldehyde, crotyl alcohol, has been investigated using *in situ* DRIFTS measurements combined with DFT calculations. The nature of the native hydroxyl groups and their reactivity was also investigated. They were found to undergo a transient reactivity via hydrogen bonded interactions with the reactive intermediates. Ethanol adsorption resulted in several physisorbed and chemisorbed surface species. Acetaldehyde exhibited high reactivity to yield crotonaldehyde but the excess resulted in strongly bound surface species assigned to surface acetate, and/or 2,4-hexadienal or polymerized acetaldehyde. Crotonaldehyde is more likely to be reduced by ethanol to yield crotyl alcohol than desorbing, even at relatively high temperatures. Crotyl alcohol, on the other hand, showed to be very reactive and adsorbs as two different species: physisorbed and deprotonated species that would further desorb as 1,3-BD. Presence of gas phase hydrogen containing molecules, such as ethanol, proved to be key in several reactive steps, including acetaldehyde condensation step and crotonaldehyde reduction. Altogether, the data presented unraveled a complex interplay between the surface hydroxyl groups, gaseous reactants and surface bound reactive intermediates of 1,3-BD formation. These complex surface processes are depicted in **Figure 4.14**. This elucidated surface reaction mechanism, combined with vapor-phase intermediate characterization, can be used as a foundation for structure-activity relationship study in combination with active sites determination. This will further lead to rational design of catalyst. Future work will attempt to correlate vapor phase product evolution with the most stable or transient reactive surface intermediates to examine trends leading to higher overall 1,3-BD selectivity.

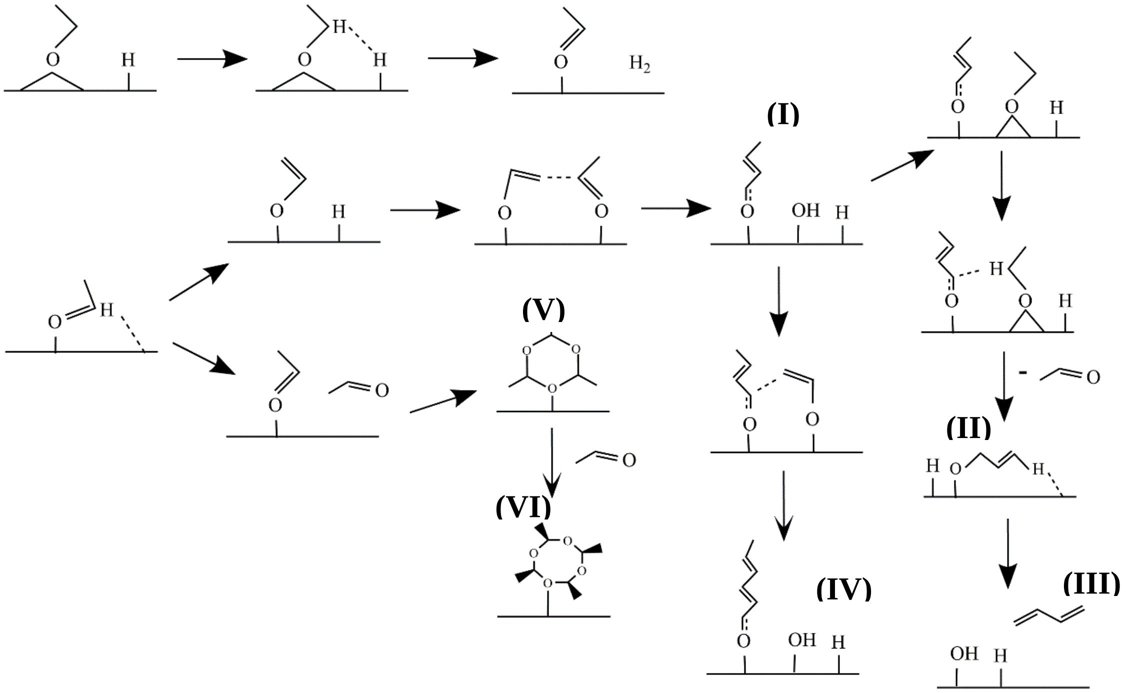

Figure 4.14. Complete surface reaction scheme on ethanol reaction over MgO/SiO2 catalyst. (I) Crotonaldehyde, (II) adsorbed crotyl alcohol, (III) 1,3-butadiene, (IV) 2,4-hexadienal, (V) paraldehyde, (VI) metaldehyde.

Chapter 4 – Supporting Information

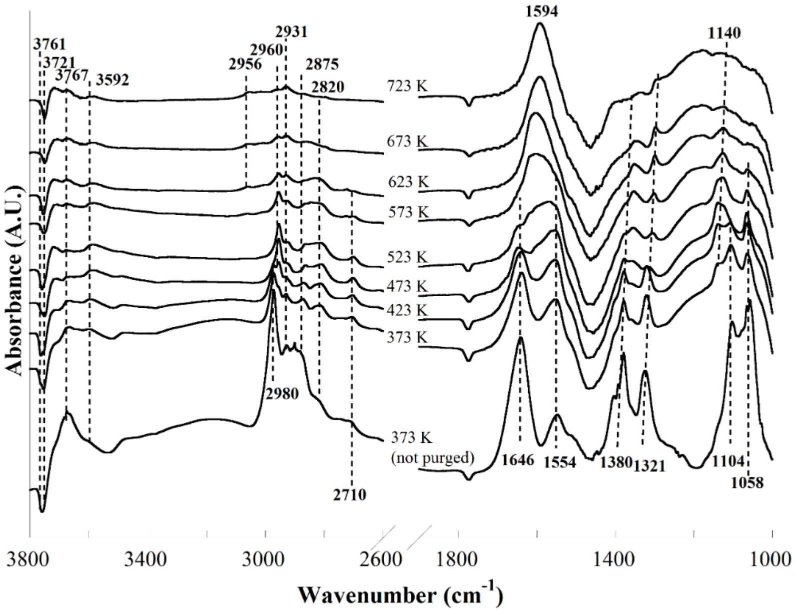

Figure S4.1. *In-situ* spectroscopy of ethanol on MgO catalyst. Ethanol was adsorbed on the sample surface and temperature ramped up from 373 to 723 K while spectra being recorded. Subtracted spectra are shown. Spectra are offset for clarity.

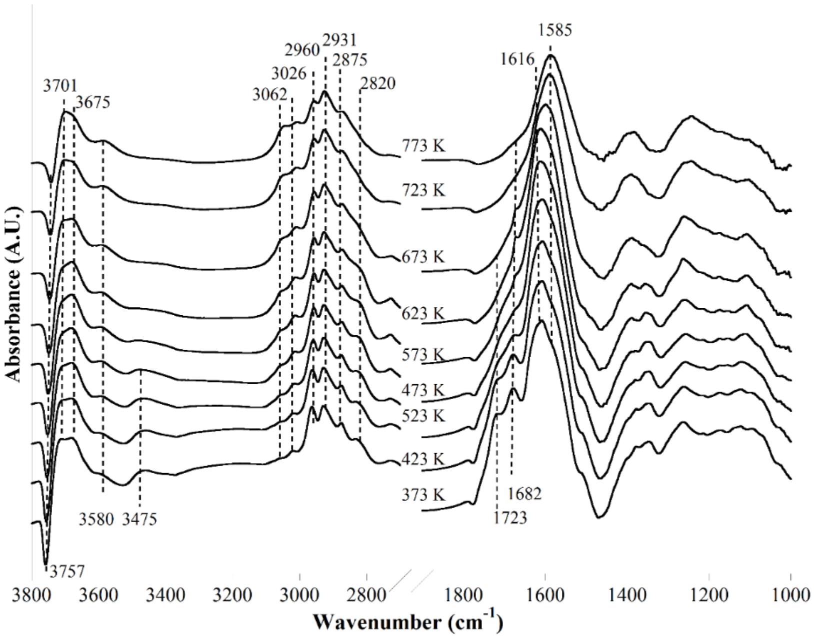

Figure S4.2. *In-situ* spectroscopy of acetaldehyde on MgO catalyst. Acetaldehyde was adsorbed on the sample surface and temperature ramped up from 373 to 723 K while spectra are being recorded. Spectra are offset for clarity.

Table S4.1. Calculated infrared frequencies of gas phase ethanol, acetaldehyde, crotyl alcohol and crotonaldehyde molecules. Frequencies were calculated using PBE density functional and no scaling to correct for anharmonicity was applied. Experimental frequencies, except for crotonaldehyde, were obtained from NIST.[68]

Vibration	**Ethanol**		**Acetaldehyde**		**Crotyl alcohol**		**Crotonaldehyde**	
	DFT Frequency (cm^{-1})	**IR (cm^{-1})**	**DFT Frequency (cm^{-1})**	**IR (cm^{-1})**	**DFT Frequency (cm^{-1})**	**IR (cm^{-1})**	**DFT Frequency (cm^{-1})**	**IR (cm^{-1})**
ν (OH)	3718	3686	-	-	3702	3665	-	-
ν CH_3	3053, 3038, 2966	3035, 3012, 2960	3092, 3025, 2967	3024, 2996, 2967	3008, 2959	2970	3068, 3011, 2965,	2984
ν CH_2	3011, 2925	3008, 2905	-	-	3000, 2928	2940, 2880	-	-
ν CH	-	-	2790	2840	3062, 3055, 3037	3030	3095, 3065, 3042, 2788	3044, 3007, 2750, 2828
ν (C=O)	-	-	1749	1743	-	-	1691	1693
ν (C=C)	-	-	-	-	1675	1675	1644	1645
δ (CH_2, CH_3)	1463	1456	1413, 1406	1410, 1390	1448, 1439, 1425, 1359	1480, 1435, 1415, 1338	1430, 1420, 1353	1449, 1398, 1381
δ (OH)	1325	1391	-	-	-	-	-	-
δ (COH)	-	-	-	-	-	-	1367	Not observed

δ (CCH)	1237	1242	-	-	-	-	1288	Not observed
Combination bending	-	-	-	-	1362, 1313, 1285, 1261, 1170, 1115, 1024	1384, 1290, 1250, 1180	1236	Not observed
Combination stretch	-	-	-	-	1075	1080	1142, 1086	1151, 1082
ν (CO)	1027	-	-	-	981	970	-	-
ν C-C (C=C)	863	-	1095	1122	-	-	-	-
Scaling factor	**0.997**		**0.9962**		**0.9903**		**0.9996**	

References

(1) Pomalaza, G.; Capron, M.; Ordomsky, V.; Dumeignil, F. *Catalysts* **2016**, *6* (12), 203.

(2) Shylesh, S.; Gokhale, A. A.; Scown, C. D.; Kim, D.; Ho, C. R.; Bell, A. T. *ChemSusChem* **2016**, *9* (12), 1462–1472.

(3) Ostromislenskiy, J. *J. Russ. Phys. Chem. Soc.* **1915**, No. 47, 1472 –1506.

(4) Lebedev, S. V. *Zh Obs. Khim* **1933**, No. 3, 698–717.

(5) Posada, J. A.; Patel, A. D.; Roes, A.; Blok, K.; Faaij, A. P. C.; Patel, M. K. *Bioresour. Technol.* **2013**, *135*, 490–499.

(6) Angelici, C.; Weckhuysen, B. M.; Bruijnincx, P. C. a. *ChemSusChem* **2013**, *6* (9), 1595–1614.

(7) Janssens, W.; Makshina, E. V.; Vanelderen, P.; De Clippel, F.; Houthoofd, K.; Kerkhofs, S.; Martens, J. A.; Jacobs, P. A.; Sels, B. F. *ChemSusChem* **2014**, *8* (6), 994–1008.

(8) Ordomsky, V. V.; Sushkevich, V. L.; Ivanova, I. I. *J. Mol. Catal. A Chem.* **2010**, *333* (1), 85–93.

(9) Müller, P.; Burt, S. P.; Love, A. M.; McDermott, W. P.; Wolf, P.; Hermans, I. *ACS Catal.* **2016**, *6* (10), 6823–6832.

(10) Chieregato, A.; Velasquez Ochoa, J.; Bandinelli, C.; Fornasari, G.; Cavani, F.; Mella, M. *ChemSusChem* **2014**, *8* (2), 377–388.

(11) Zhang, M.; Gao, M.; Chen, J.; Yu, Y. *RSC Adv.* **2015**, *5* (33), 25959–25966.

(12) Hayashi, Y.; Akiyama, S.; Miyaji, A.; Sekiguchi, Y.; Sakamoto, Y.; Shiga, A.; Koyama, T.; Motokura, K.; Baba, T. *Phys. Chem. Chem. Phys.* **2016**, *18* (36), 25191–25209.

(13) Hanspal, S.; Young, Z. D.; Shou, H.; Davis, R. J. *ACS Catal.* **2015**, 1737–1746.

(14) Birky, T. W.; Kozlowski, J. T.; Davis, R. J. *J. Catal.* **2013**, *298* (0), 130–137.

(15) Kvisle, S.; Aguero, A.; Sneeden, R. P. A. *Appl. Catal.* **1988**, *43* (1), 117–131.

(16) Toussaint, W. J.; Dunn, J. T.; Jachson, D. R. *Ind. Eng. Chem.* **1947**, *39* (2), 120–125.

(17) Taifan, W. E.; Bučko, T.; Baltrusaitis, J. *J. Catal.* **2017**, *346*, 78–91.

(18) Quattlebaum, W. M.; Toussaint, W. J.; Dunn, J. T. *J. Am. Chem. Soc.* **1947**, *69*, 593–599.

(19) Velasquez Ochoa, J.; Bandinelli, C.; Vozniuk, O.; Chieregato, A.; Malmusi, A.; Recchi, C.; Cavani, F. *Green Chem.* **2016**, *18*, 1653–1663.

(20) Velasquez Ochoa, J.; Malmusi, A.; Recchi, C.; Cavani, F.; Ochoa, J. V.; Malmusi, A.; Recchi, C.; Cavani, F. *ChemCatChem* **2017**, *9* (12), 2128–2135.

(21) Angelici, C.; Velthoen, M. E. Z.; Weckhuysen, B. M.; Bruijnincx, P. C. A. *ChemSusChem* **2014**, *7* (9), 2505–2515.

(22) Makshina, E. V.; Janssens, W.; Sels, B. F.; Jacobs, P. A. *Catal. Today* **2012**, *198* (1), 338–344.

(23) Makshina, E. V; Dusselier, M.; Janssens, W.; Degreve, J.; Jacobs, P. A.; Sels, B. F. *Chem. Soc. Rev.* **2014**, *43* (22), 7917–7953.

(24) Wu, C.-M.; Baltrusaitis, J.; Gillan, E. G.; Grassian, V. H. *J. Phys. Chem. C* **2011**, *115* (20), 10164–10172.

(25) Haas, P.; Tran, F.; Blaha, P. *Phys. Rev. B* **2009**, *79* (8), 85104.

(26) Kantorovich, L. N.; Holender, J. M.; Gillan, M. J. *Surf. Sci.* **1995**, *343* (3), 221–239.

(27) Chizallet, C.; Petitjean, H.; Costentin, G.; Lauron-Pernot, H.; Maquet, J.; Bonhomme, C.; Che, M. *J. Catal.* **2009**, *268* (1), 175–179.

(28) Chizallet, C.; Bailly, M. L.; Costentin, G.; Lauron-Pernot, H.; Krafft, J. M.; Bazin, P.; Saussey, J.; Che, M. *Catal. Today* **2006**, *116* (2), 196–205.

(29) Di Valentin, C.; Del Vitto, A.; Pacchioni, G.; Abbet, S.; Wörz, A. S.; Judai, K.; Heiz, U. *J. Phys. Chem. B* **2002**, *106* (46), 11961–11969.

(30) Branda, M. M.; Rodríguez, A. H.; Belelli, P. G.; Castellani, N. J. *Surf. Sci.* **2009**, *603* (8), 1093–1098.

(31) Bailly, M.; Chizallet, C.; Costentin, G.; Krafft, J.; Lauronpernot, H.; Che, M. *J. Catal.* **2005**, *235* (2), 413–422.

(32) Baltrusaitis, J.; Hatch, C.; Orlando, R. *J. Phys. Chem. A* **2012**, *116* (30), 7950–7958.

(33) Kresse, G.; Hafner, J. *Phys. Rev. B* **1994**, *49* (20), 14251–14269.

(34) Kresse, G.; Furthmüller, J. *Comput. Mater. Sci.* **1996**, *6* (1), 15–50.

(35) Kresse, G.; Furthmüller, J. *Phys. Rev. B* **1996**, *54* (16), 11169–11186.

(36) Kresse, G.; Hafner, J. *Phys. Rev. B* **1993**, *48* (17), 13115–13118.

(37) Blöchl, P. E. *Phys. Rev. B* **1994**, *50* (24), 17953–17979.

(38) Perdew, J. P.; Burke, K.; Ernzerhof, M. *Phys. Rev. Lett.* **1996**, *77* (18), 3865–3868.

(39) Knözinger, E.; Jacob, K.-H.; Singh, S.; Hofmann, P. *Surf. Sci.* **1993**, *290* (3), 388–402.

(40) Coluccia, S.; Lavagnino, S.; Marchese, L. *Mater. Chem. Phys.* **1988**, *18* (5), 445–464.

(41) Anderson, P. J.; Horlock, R. F.; Oliver, J. F. *Trans. Faraday Soc.* **1965**, *61* (0), 2754–2762.

(42) Shido, T.; Asakura, K.; Iwasawa, Y. *J. Chem. Soc.{,} Faraday Trans. 1* **1989**, *85* (2), 441–453.

(43) Morrow, B. A. *Stud. Surf. Sci. Catal.* **1990**, *57*, A161–A224.

(44) Chizallet, C.; Costentin, G.; Che, M.; Delbecq, F.; Sautet, P.; Surface, D.; Marie, P. *J. Am. Chem. Soc.* **2007**, No. 19, 6442–6452.

(45) Hair, M. L. *J. Non. Cryst. Solids* **1975**, *19*, 299–309.

(46) Chung, S.-H.; Angelici, C.; Hinterding, S. O. M.; Weingarth, M.; Baldus, M.; Houben, K.; Weckhuysen, B. M.; Bruijnincx, P. C. A. *ACS Catal.* **2016**, *6* (6), 4034–4045.

(47) Hofmeister, A. M.; Bowey, J. E. *Mon. Not. R. Astron. Soc.* **2006**, *367* (2), 577–591.

(48) Mellini, M. *Am. Mineral.* **1982**, *67* (5–6), 587–598.

(49) Taifan, W.; Boily, J.-F.; Baltrusaitis, J. *Surf. Sci. Rep.* **2016**, *71* (4), 595–671.

(50) Vimont, A.; Thibault-Starzyk, F.; Daturi, M. *Chem. Soc. Rev.* **2010**, *39* (12), 4928–4950.

(51) Angelici, C.; Velthoen, M. E. Z.; Weckhuysen, B. M.; Bruijnincx, P. C. A. *Catal. Sci. Technol.* **2015**.

(52) Song, H.; Ozkan, U. S. *J. Catal.* **2009**, *261* (1), 66–74.

(53) Phung, T. K.; Lagazzo, A.; Rivero Crespo, M. Á.; Sánchez Escribano, V.; Busca, G. *J. Catal.* **2014**, *311*, 102–113.

(54) Raskó, J.; Kiss, J. *Appl. Catal. A Gen.* **2005**, *287* (2), 252–260.

(55) Busca, G.; Lorenzelli, V. *Mater. Chem.* **1982**, *7* (1), 89–126.

(56) Wang, H.; Schneider, W. F. *Phys. Chem. Chem. Phys.* **2010**, *12* (24), 6367–6374.

(57) Meixner, D. L.; Arthur, D. A.; George, S. M. *Surf. Sci.* **1992**, *261* (1), 141–154.

(58) Raskó, J.; Dömök, M.; Baán, K.; Erdőhelyi, A. *Appl. Catal. A Gen.* **2006**, *299*, 202–211.

(59) Singh, M.; Zhou, N.; Paul, D. K.; Klabunde, K. J. *J. Catal.* **2008**, *260* (2), 371–379.

(60) Cederstav, A. K.; Novak, B. M. *J. Am. Chem. Soc.* **1994**, *116* (9), 4073–4074.

(61) Georgieff, K. K. *J. Appl. Polym. Sci.* **1966**, *10* (9), 1305–1313.

(62) Bevington, J. C.; Norrish, R. G. W. *Proc. R. Soc. London. Ser. A. Math. Phys. Sci.* **1949**, *196* (1046), 363 LP-378.

(63) Cannizzaro, S. *Justus Liebigs Ann. Chem.* **1853**, *88* (1), 129–130.

(64) Tishchenko, V. E. *J. Russ. Physico-Chemical Soc.* **1906**, *38* (355–418).

(65) Diaz, C. D. C.; Locatelli, S.; Gonzo, E. E. *Zeolites* **1992**, *12*, 851–857.

(66) Idriss, H.; Diagne, C.; Hindermann, J. P.; Kiennemann, A.; Barteau, M. A. *J. Catal.* **1995**, *155* (2), 219–237.

(67) Guil, J. M.; Homs, N.; Llorca, J.; De La Piscina, P. R. *J. Phys. Chem. B* **2005**, *109* (21), 10813–10819.

(68) Resini, C.; Cavallaro, S.; Frusteri, F.; Freni, S.; Busca, G. *React. Kinet. Catal. Lett.* **2007**, *90* (1), 117–126.

(69) Ho, C. R.; Shylesh, S.; Bell, A. T. *ACS Catal.* **2016**, *6* (2), 939–948.

(70) Stein, S. E. In *NIST Chemistry WebBook, NIST Standard Reference Database Number 69*; Linstrom, P. J., Mallard, W. G., Eds.; National Institute of Standards and Technology (NIST): Gaithersburg, MD, 2017.

(71) Wenig, R. W.; Schrader, G. L. *J. Phys. Chem.* **1987**, *91* (22), 5674–5680.

(72) Rekoske, J. E.; Barteau, M. a. *Langmuir* **1999**, *15* (6), 2061–2070.

(73) Scott, A. P.; Radom, L. *J. Phys. Chem.* **1996**, *100* (41), 16502–16513.

(74) Palagin, D.; Sushkevich, V. L.; Ivanova, I. I. *J. Phys. Chem. C* **2016**, *120* (41), 23566–23575.

(75) Sekiguchi, Y.; Akiyama, S.; Urakawa, W.; Koyama, T.; Miyaji, A.; Motokura, K.; Baba, T. *Catal. Commun.* **2015**, *68*, 20–24.

(76) Plyler, E. K. *J. Res. Natl. Bur. Stand. (1934).* **1952**, *48* (4).

(77) Niiyama, H.; Morii, S.; Echigoya, E. *Bull. Chem. Soc. Jpn.* **1972**, *45* (3), 655–659.

(78) Hattori, H. *Chem. Rev.* **1995**, *95* (3), 537–558.

(79) Towns, J.; Cockerill, T.; Dahan, M.; Foster, I.; Gaither, K.; Grimshaw, A.; Hazlewood, V.; Lathrop, S.; Lifka, D.; Peterson, G. D.; Roskies, R.; Scott, J. R.; Wilkins-Diehr, N. *Comput. Sci. Eng.* **2014**, *16* (5).

Chapter 5

Active Sites Determination of MgO/SiO$_2$ Catalysts for Ethanol to 1,3-BD Reaction

Abstract

Ethanol is an important renewable chemical that allows for sustainable high value product, such as 1,3-butadiene, catalytic synthesis. MgO/SiO$_2$ catalyst is typically utilized in a single step ethanol-to-1,3-butadiene catalytic conversion and the (by)product yields were shown to depend on the type, structure and strength of the catalytic active sites. The fundamental factors describing the molecular structure and binding properties of these sites is thus of critical importance but not yet fully understood. We utilized multimodal approach, including temperature programmed surface sensitive infrared, mass spectroscopy using probe molecules, such as CO_2, NH_3, pyridine and propionic acid, to unravel the structure and persistence of these catalytic sites *in situ*. In particular, Mg-O-Mg, Mg-O(H)-Mg, Mg-O-Si and Mg-O(H)-Si surface site binding configurations were interrogated using spectroscopic methods in combination with DFT calculations. Surface elemental analysis using low energy ions suggested that either Mg atoms or Si being the most abundant on the topmost surface layer, depending on the catalyst preparation method. The molecular active site structure was determined and incipient wetness prepared surface was found to be dominated with stabilized Mg-OH with little magnesium silicate (Mg-O-Si and Mg-O(H)-Si) functional groups. The wet-kneaded catalyst surface, on the other hand, contained a significant number of surface sites derived from magnesium silicates. The fundamental surface site structure proposed here can further serve as a starting point for theoretical calculations necessary to fully model the reactive pathway during ethanol catalytic transformation to 1,3-butadiene.

1. Introduction

Elucidating surface active site structure is of high importance for development of selective MgO/SiO_2 catalysts utilized for the catalytic conversion of ethanol to 1,3-butadiene (1,3-BD). Deemed as Lebedev catalyst, it is increasingly investigated due to its bifunctional nature and the variety of the (by)products that can be formed thereon.[1–4] The nature of the closed shell MgO electronic structure and diverse surface functionality provides interesting challenges as there are much fewer spectroscopic methods that allow identification of the active site properties, akin to those of solid Lewis acid catalysts, such as Ta_2O_5[5] or ZrO_2,[6] also used in ethanol-to-1,3-butadiene catalytic conversion (1,3-BD).[3,7] As a result, the surface site structure and the reactivity of MgO/SiO_2 catalysts during 1,3-BD production are still poorly understood.[8] Furthermore, discrepancies between the selectivity of the reported active catalysts are due to the intrinsic active site density, their functional nature (acidic or basic) and their strength which arise from the diverse set of preparation methods including ratio of Mg-to-Si, Mg precursor used and their deposition method. The ratio of acidic-to-basic sites was shown to affect the overall reactivity during 1,3-BD formation, as demonstrated by Angelici *et al.*[9] Shylesh *et al.* proposed that weak basic sites were responsible for ethanol dehydrogenation and other basic sites for aldol condensation.[3] Angelici *et al.* attributed higher overall reactivity to a small number of strong basic sites on the catalyst surface with an intermediate amount of acidic sites and weak basic sites.[9] Catalysts prepared using different methods, e.g. incipient wetness impregnation (IWI) and wet-kneading (WK)[3,9] resulted in a large activity difference with IWI prepared catalyst yielding only ~5% conversion at 300 °C when compared to WK catalyst ~50% conversion at 425 °C. The key to this different activity was believed to be the significant improvement of acetaldehyde production by transition metal promotion on strong basic sites.[3] In general, MgO/SiO_2 wet-kneading has consistently been shown to produce highest 1,3-BD yields[4,10,11] due to the proposed *balanced* acidic and basic catalytic site number.[9] The exact molecular structure of these acidic and basic active sites is still under debate with most analysis focused correlating the reactivity and the (bulk) crystalline catalyst phases.[1,2,12] In particular, -Mg-O-Si- linkage has been implicated to be reactive and related to the selectivity of the catalysts.[1–3] SiO_2 was proposed to indirectly catalyze the reaction due to its structural perturbation of MgO using wet-kneading.[10] Furthermore, a solid solution of MgO with SiO_2 was inferred from the experimental measurements and the amount of magnesium silicate phases, measured by ^{1}H-^{29}Si cross-polarized MAS NMR[1,3] and DRIFTS,[2] was correlated to varying overall selectivity. Ochoa *et al.* observed formation of a magnesium silicate phase with Mg^{2+} neighbored by Si^{4+} cations synthesized using sol-gel methods with Mg/Si ratio of 9 to 15 while the lower ratio led to the formation of catalytically inactive forsterite (Mg_2SiO_4) phase formation.[2] Amorphous magnesium silicate hydrous phase formed during wet-kneading of MgO and SiO_2 was found to be responsible for ethylene byproduct formation while layered magnesium silicate hydrous phase was correlated to the 1,3-BD product.[1] Furthermore, the silicate-to-MgO ratio was suggested to be the key to the appropriate balance of acidic-basic sites.[1] A different view was offered by Shylesh *et al.* where hydroxyl (OH) groups were necessary in the proximity of the strong basic Mg^{2+}-O^{2-} sites to synergistically catalyze the reaction. Finally, the correlation between the magnesium silicate hydrous phase and 1,3-BD yield was challenged by Hayashi *et al.* who reported MgO catalyst that did not require participation from SiO_2 for this reaction.[12] Said MgO catalyst was synthesized with an additional hydrothermal step using NH_4OH solution. XPS characterization of the two different MgO catalysts, i.e. with and without the additional hydrothermal step, showed that latter, i.e. the more active catalyst, exhibited a higher intensity of an unassigned O1s oxygen peak at around 532 eV.[12] The presence of this unidentified oxygen species on MgO could be related to the reactive lower-coordinated oxygen atoms on Mg-O defect sites.[13–15] Concurrently, these lower-coordinated Mg-O pairs ($Mg^{2+}{}_{3C}O^{2-}{}_{4C}$, $Mg^{2+}{}_{3C}O^{2-}{}_{3C}$, $Mg^{2+}{}_{4C}O^{2-}{}_{4C}$) were computationally shown to be involved in 1,3-BD formation from ethanol.[16–18] Analysis of Lewis acid - ZrO_2-based catalysts[19] - suggests that Lewis acid sites (LAS) can be chiefly responsible for the activity in this reaction. By definition, *closed* Lewis acid heteroatoms (M) are tetrahedrally coordinated (M-$(OSi)_4$ to the zeolite framework, while *open* Lewis acid heteroatoms are tri-coordinated (HO)-M-$(OSi)_3$ to the zeolite framework.[20–22] With this in mind, the octahedral symmetry in MgO crystal[12,23] allows to identify several LAS as part of the intrinsic acid/base pairs to be available. i.e. Mg-O-Mg, Mg-O(H)-Mg, Mg-O-Si and Mg-O(H)-Si. These combinations can further exist in open and closed acid configurations, where the oxygen is bound to SiO_2 while also coordinated to a proton to form coordinated hydroxyl groups.[24,25] Strict terminology of the *open* acid site requires an isolated hydroxyl group to be present and while it is very basic, this hydroxyl group spectroscopically has been proven to be non-existent.[25,26] In addition to these sites, the coordination of Mg is also very important, since catalysis by this metal oxide is driven by defect sites.[15,27,28] These proposed catalytic sites are shown in **Figure 5.1.**

While Zr-based catalysts mainly concerns the Zr-coordination into the framework, and consequently, characterization of the resulting LAS, i.e. open and closed,[19,29] study on MgO/SiO_2-based catalysts mostly revolves around the general acidity and basicity characterization while also discussing the importance of bulk silicate phases.[1,9,30,31] However, pyridine-DRIFTS studies concluded LAS to be the only acidic sites on the catalyst as demonstrated by the IR peaks at 1450, 1578, and 1612 cm^{-1}.[3,9,30,31] NH_3-TPD, another routinely used acidity probe method, also discriminates the acid based on the strength, without discussing the nature of the acidic sites.[9] Hence the molecular structure of these acidic sites is not well known.[1] In this work, we combined spectroscopic measurements *in-situ* using different probe molecules to identify the role of each sites during the reaction and elucidate their molecular coordination. In particular, we begin by performing bulk XRD, surface LEIS and DRIFTS analysis of native surface hydroxyl groups. We then perform steady state and kinetic temperature programmed experiments of ethanol conversion to 1,3-BD using catalysts synthesized with different methods. We then utilize temperature programmed DRIFTS to explore surface acidic and basic site structure with *ab initio* calculations to support our NH_3 adsorption site assignments and hence propose the molecular arrangements of the catalytic sites. Sodium (Na) poisoning was utilized to elucidate the role of the acidic sites during the reaction, which will further indicate the importance of strong acidic sites during the reaction. Finally, the persistence of these reactive sites is probed spectroscopically under the relevant conditions of temperature and ethanol vapor.

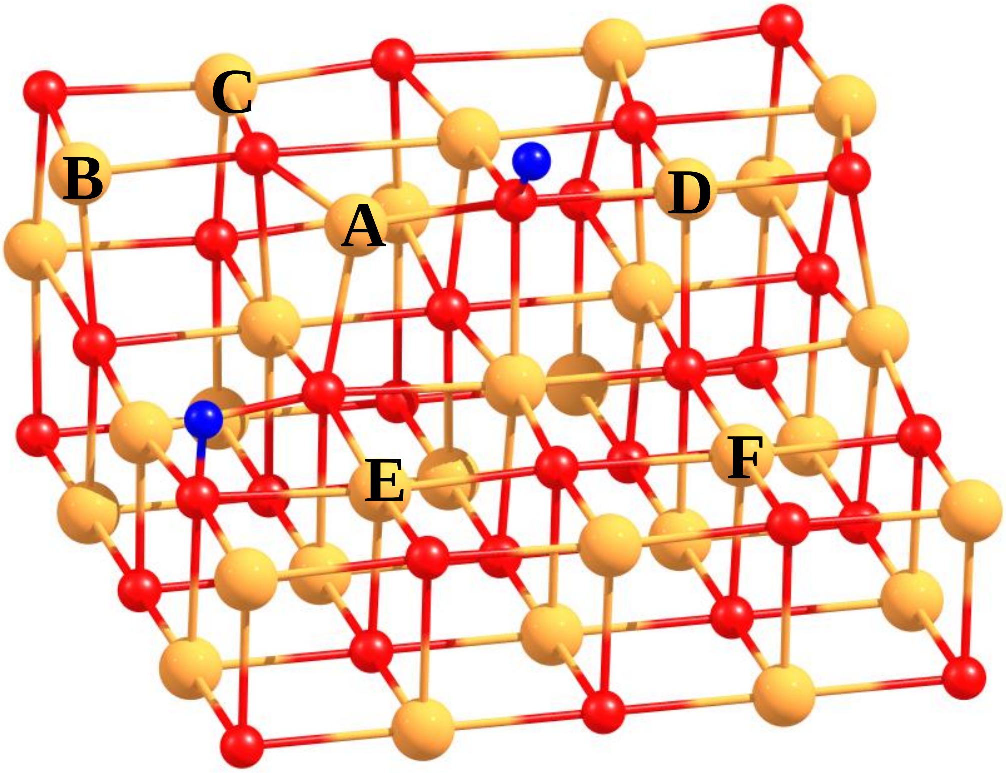

Figure 5.1. Possible combination of metal atoms that act as Lewis acid sites: A: Mg_{3C} (open), B: Mg_{3C} (closed), C: Mg_{4C} (closed), D: Mg_{4C} (open), E: Mg_{5C} (open), F: Mg_{5C} (closed).

2. Results and Discussion

2.1. Steady state ethanol catalytic conversion to 1,3-BD

Steady state reactivity of the synthesized MgO/SiO_2 catalysts was investigated using fixed-bed reactor. A catalyst calcined at 500°C was synthesized as a benchmark catalyst. This benchmark calcination temperature was based on earlier study by Zhu, *et al.*, where 500°C was the optimized calcination temperature that resulted in a balanced acidic-basic sites at 40.8 µmol/g v 49 µmol/g.[32] Activity comparison was performed at a temperature of 450 °C with the maximum 1,3-BD yield. At this reaction temperature, carbon balance for each catalyst was determined to be >80%. **Table 5.1** shows that ethylene selectivity was the highest for MgSi-WK2 which suggests the presence of acidic sites on the surface since ethanol dehydration reaction is very prominent over catalysts with very high density of BAS.[33–35] For catalysts calcined at 800 °C (MgSi-WK and MgSi-IWI) ethylene selectivity was above 50%, which is intriguing, since pyridine probing does not show the presence of BAS (*vide infra*). This ethylene formation can be proposed due to the reactive Mg-O-Mg or Mg-O-Si linkages that are inherent in the catalysts.[36] In agreement, DFT calculations have shown that ethanol dehydration competes with dehydrogenation reaction over LAS in MgO catalysts.[16]

Comparison between two catalysts calcined at 800 ^{o}C, i.e. MgSi-WK and MgSi-IWI, shows that MgSi-WK was more active and selective to 1,3-BD suggesting that the preparation method deeply affected the balance of the active sites. The accumulation of acetaldehyde on MgSi-IWI catalyst was evident from **Table 1** suggesting the active sites for further aldol condensation and MPV (Meerwein-Ponndorf-Verley) reduction – mechanistic steps taking place after ethanol dehydrogenation - were limited.[16] MgSi-WK, on the other hand, exhibited significantly higher 1,3-BD selectivity and limited acetaldehyde production suggesting more sites available for the subsequent reactions. **Figure 5.2** shows the evolution of each major (by)product with increasing temperature for reaction over MgSi-WK catalyst. 1,3-BD and ethylene exhibited almost linear increase in productivity with the calculated apparent activation energy of 12.4 and 18.02 kcal/mol, respectively. Importantly, Arrhenius plot shown in **Figure 5.2** inset of acetaldehyde formation did not show linearity due to its involvement into further reactions.

Table 5.1 Steady state reactivity of MgO/SiO_2 catalysts of different calcination temperature and preparation method. Reaction was carried out at 450 °C with catalyst mass of 0.1 g, 55 ml/min total flow rate and $p_{ethanol}$ = 2.5 kPa. Selectivity towards major (by)products ethylene, acetaldehyde and 1,3-BD is reported.

Catalyst	**Selectivity (%)**			**Conversion (%)**
	Ethylene	**Acetaldehyde**	**1,3-BD**	
MgSi-WK	55.8	14.4	29.7	77.0
MgSi-WK2	82.9	9.7	7.5	60.4
MgSi-IWI	58.0	25.6	16.4	63.9

Productivity values of MgSi-WK compared reasonably well with those found in the literature. In the present work 1,3-BD yield translated to the production rate of 0.44 $g_{BD}.g_{cat}^{-1}.hr^{-1}$, while the MgSi-WK2 yielded about 0.06 $g_{BD}.g_{cat}^{-1}.hr^{-1}$. Chung *et al.* synthesized a WK catalyst using calcination temperature of 500 °C with the reported 1,3-BD productivity of 0.23 $g_{BD}.g_{cat}^{-1}.hr^{-1}$.[1] The origin of this reactivity can be related to the high amount of layered hydrous magnesium silicate phase on the catalyst, which was highly dependent on the precursor; a nano-sized $Mg(OH)_2$ precursor was the preferred precursor.[1] The effect of MgO precursor used during the WK catalyst synthesis has recently been highlighted by Huang *et al.* where $Mg(OH)_2$ precursor synthesized using a template method yielded a very high productivity of 1.15 $g_{BD}.g_{cat}^{-1}.hr^{-1}$.[4] Since precursor was not the controlled variable in the present work, the origin of higher activity in the case of MgSi-WK, as compared to MgSi-WK2, is presumably from the higher calcination temperature. The effect of the calcination temperature has been observed previously for Zr/SiO_2 catalysts where highest 1,3-BD yield was obtained with catalyst calcined at 550 °C.[37] Study on the effect of calcination temperature on MgO/SiO_2 catalysts, on the other hand, revealed linear increase in basicity with increasing calcination temperature.[38] Pyridine testing indicated that calcination temperature of 500 °C resulted in a catalyst that exhibited the highest acidity.[38] Incipient wetness impregnation (IWI) method is not typically used for the MgO/SiO_2 catalysts synthesis for this reaction despite its popularity in supported catalyst synthesis. Typically, IWI method is utilized to obtain sub-monolayer coverage to prevent the formation of second layer of bulk oxides. The activity of this catalyst was very different yielding a much lower 1,3-BD productivity. Shylesh *et al.* investigated a similar catalyst calcined at 500 °C and reported rather low 1,3-BD yield of 0.01 $g_{BD}.g_{cat}^{-1}.hr^{-1}$ at 300 °C.[3] Surface layer compositions of this catalyst as well as MgSi-WK will further be interrogated using LEIS to better understand chemical composition changes leading to such different reactivity.

Importantly, steady state experiments suggest that ethylene and acetaldehyde are the most encountered byproducts during the reaction. As shown in **Table 5.1**, their combined selectivity makes up to more than 70% of the total activity. While acetaldehyde recycling can be utilized due to it being a reactive intermediate, ethylene production should be limited. One of the advantages of using MgO/SiO_2 is no butene byproduct production. Butenes form azeotrope with 1,3-BD and increase any separation cost. It was reported that butenes could be formed by hydrogenation of 1,3-BD over platinum catalysts, dehydration of n-butanol, and from thermal or catalytic dimerization of ethylene.[39] Hence n-butanol dehydration might not be feasible considering the high selectivity of ethylene. However, although the reactive pathway is similar, n-butanol synthesis requires a tautomerization site to convert crotyl alcohol to 1-buten-1-ol over a basic oxygen site, which further requires another MPV reduction site.[40] This pathway is not supported by our catalytic, DRIFTS[36] and TPRS data (*vide infra*) since no n-butanol was formed in the product stream and no butyraldehyde was spectroscopically observed.

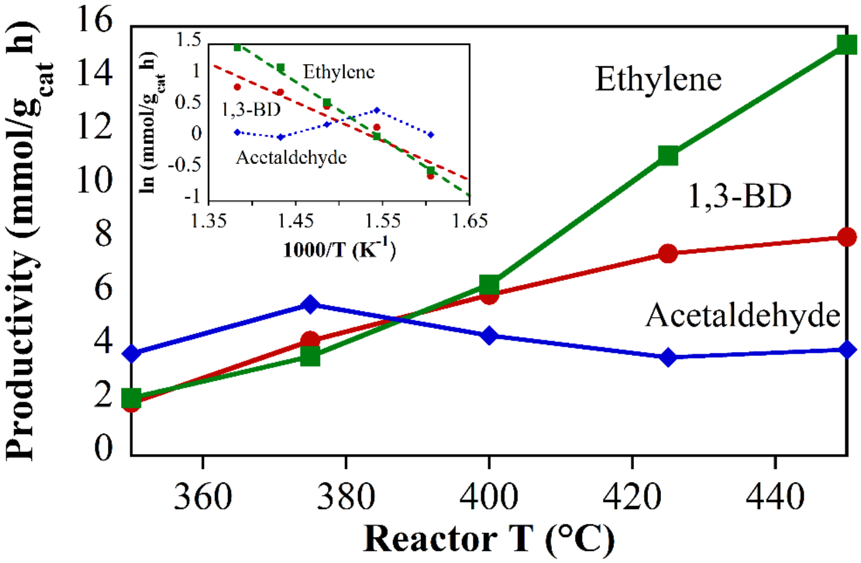

Figure 5.2. Catalytic activity of MgSi-WK between 350-450°C. Inset: Arrhenius plot of ethylene and 1,3-BD. Catalyst mass = 0.1 gr, total flow rate = 55 ml/min, $p_{ethanol}$ = 2.5 kPa.

2.2. Bulk, surface chemical and structural characterization using XRD, LEIS and DRIFTS

Bulk crystalline structure of the catalysts was characterized using XRD. XRD patterns of the selected MgSi-WK catalysts as a function of the corresponding oxide ratio as well as those for MgSi-IWI are compared in **Figure 5.3**. XRD pattern of WK catalysts indicates the formation of periclase MgO in the bulk. The intensity expectedly enhanced with higher Mg content which means that the catalyst crystallinity originated from MgO rather than any silicate material. On the other hand, IWI catalyst showed a very different crystalline structure. Several crystalline phases were identified in the XRD patterns including those that might be attributed to periclase phase of MgO. However, most of the peaks were due to the presence of different crystalline phase, potentially magnesium silicates.[41–44] While this provided implications for the varied selectivity shown in **Table 5.1**, surface chemical analysis was performed to further elucidate this effect.

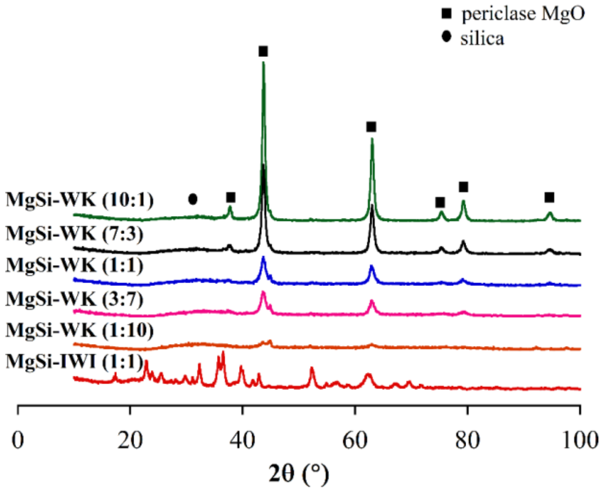

Figure 5.3. Comparison of XRD patterns of MgSi-WK and MgSi-IWI. WK with different oxide ratios are overlaid for comparison.

Topmost surface layer of the two catalysts, i.e. MgSi-IWI and MgSi-WK, was probed using LEIS. LEIS is by far the most surface sensitive characterization technique which sputters the surface with very low energy ions using ionized noble gases.[45] LEIS spectra of both catalysts are shown in **Figure 5.4.** Sputtering experiments (depth profiling) are shown as insets where surface layers were sputtered using 1 keV Ar^+ ions. The sputtering rates were on the order of one monolayer of atoms per 10^{15} Ar^+ ions/cm^2. The legend in the insets indicates the nth layer removed from the catalyst surface. Three peaks were found in the spectra corresponding to oxygen at ~1200 eV, Mg at ~1650 eV and a shoulder for Si at ~1760 eV. The increase in signal intensity for all peaks after initial sputtering may be due to some residual overlayer on the surface or perhaps to initial planarization of the catalyst granules increasing the apparent global atomic surface density. Depth profile spectra were obtained stepwise using the acquisition of the surface spectra followed by sputtering for a designated period. The resulting depth profiles show Mg-rich surface for MgSi-IWI while Si-rich surface can be for MgSi-WK. The incipient wetness impregnation method deposited the magnesium nitrate precursor on top of the fumed SiO_2 yielding a high magnesium content. The wet-kneaded method, on the other hand, provided intimate mixing between the $Mg(OH)_2$ and SiO_2 allowing for the extensive interaction between the two oxides which is reflected in the abundance of Si on the surface.[1] Based on this characterization, MgSi-IWI should contain more Mg-O-Mg linkages, while MgSi-WK would contain more Mg-O-Si linkages.

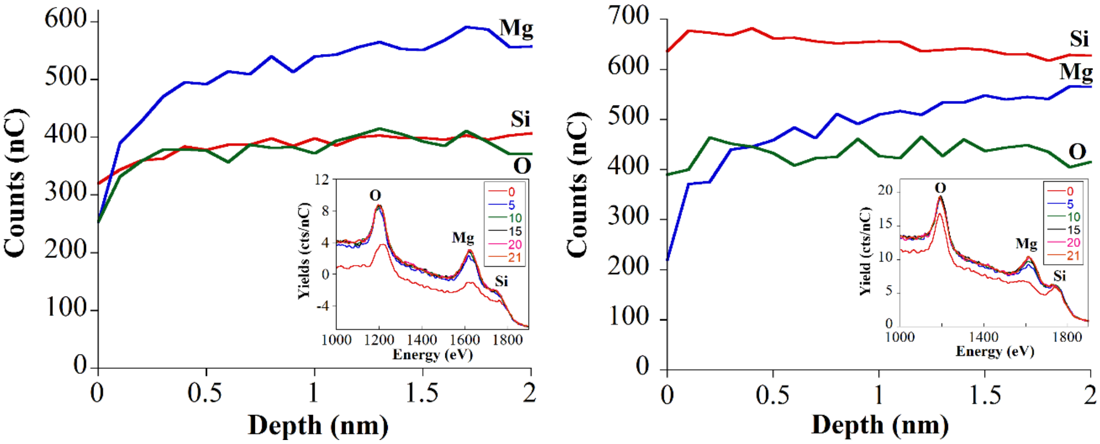

Figure 5.4. Depth-profile of (a) MgSi-IWI and (b) MgSi-WK as probed using HS-LEIS. HS-LEIS spectra of layer by layer sputtering of catalyst surface are shown in the inset.

The structure of the native OH groups of all the catalysts was investigated using DRIFTS (**Figure 5.5**). MgSi-WK shows four major peaks in the spectrum in addition to a broad peak at ~3550 cm^{-1} assigned to germinal and vicinal OH groups of the silica support.[46,47] Peak at 3745 cm^{-1} was assigned to both isolated silanol group of the SiO_2 support[46,47] which decreased in intensity when MgO was wet-kneaded and to an isolated OH group of MgO that depends on the coordination number of the Mg.[36] An intense peak at 3680 cm^{-1} was previously assigned to a magnesium silicate phase, lizardite.[1] The other peaks at 3725 and 3705 cm^{-1} were assigned to the isolated O_{4c}-H and O_{5c}-H coordinated groups formed in the presence of the amorphous SiO_2 ($SiMg_{4c}O_{4c}$ and $SiMg_{4c}O_{5c}$).[36] Formation of the peaks at 3725 and 3705 cm^{-1} was also confirmed with varying Mg/Si ratio as shown in **Figure 5.5** (right). At very high Mg content, i.e. Mg/Si > 7/3, it can be seen that a very basic Mg-OH group started to become apparent at 3765 cm^{-1}. As previously shown,[36] MgO possessed two basic OH groups that depend on the coordination number of oxygen atoms with the lower coordinated OH group at higher wavenumbers.[25,48] Interestingly, the peaks at 3705 and 3680 cm^{-1} increased with Mg content while the peak at 3725 cm^{-1} intensified at intermediate ratio and diminished at both extremes. This suggests that the peaks at 3680 and 3705 cm^{-1} were dominant at lower Si content but not in pure MgO, and hence, it can be assigned to an OH group anchored to MgSi coordination that has few Si atoms nearby. The formation of this peak confirms the XRD assignment where the catalyst is becoming increasingly crystalline MgO-like, both on the surface and in the bulk.

The OH groups that were observed on MgSi-IWI surface were very different from those found on MgSi-WK. Two new peaks at 3610 and 3571 cm^{-1}, in addition to the peaks that were also found on MgSi-WK, appeared, indicating the formation of two entirely new OH groups. From HS-LEIS experiment, the top surface layer mostly consisted of Mg atoms, which would suggest the presence of a lot of Mg-OH groups. As previously explained, the isolated OH groups from MgO exhibit peaks at both ~3760 and ~3740 cm^{-1}, depending on the coordination number. The presence of SiO_2 likely stabilized the lowest-coordinated OH group, i.e. peak at ~3760 cm^{-1}, converting it into the higher-coordinated, isolated OH group, i.e. peak at ~3740 cm^{-1}. The other peaks at 3610 and 3571 cm^{-1} are sharp with lower intensity, unlike the broad OH peaks that were assigned to multi-coordinated hydrogen-bonded OH groups,[24,25] These two peaks also were observed by Ochoa *et al.* in the catalysts structurally similar to forsterite.[2] From HS-LEIS, XRD, and DRIFTS, the surface of MgSi-IWI was confirmed to be mainly populated by Mg-OH, with significantly less magnesium silicate phases. Most of the formed magnesium silicate phases were found in the bulk of the catalyst as indicated by the XRD.

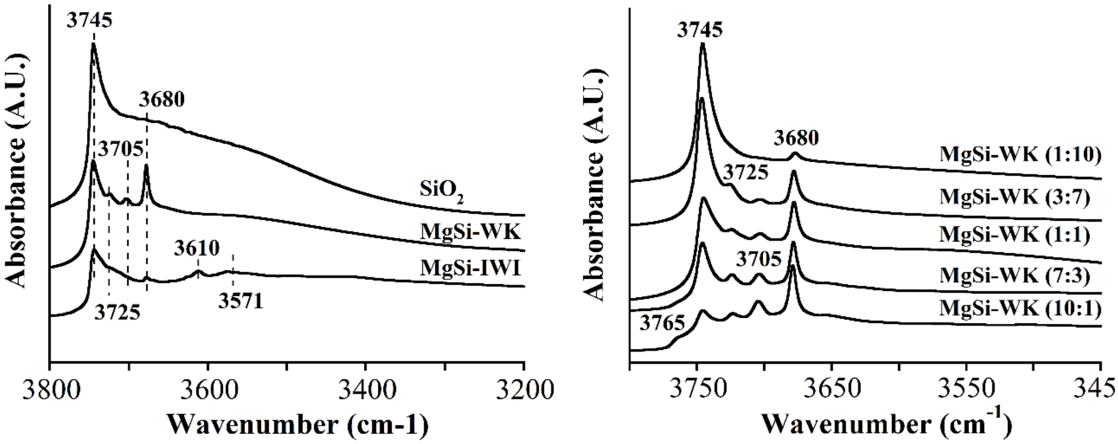

Figure 5.5. Left: Comparison of OH groups of MgSi-WK and MgSi-IWI as probed by *in-situ* dehydrated DRIFTS experiments; right: OH groups of WK catalysts with different oxide ratios.

2.3. Temperature-programmed reaction spectroscopy (TPRS) of ethanol on MgSi-WK

To further understand the reaction mechanism, temperature-programmed reaction spectroscopy (TPRS) was carried out using the ethanol reactant and intermediate reactive molecules. The TPRS was performed on MgSi-WK surface due to the higher reactivity than MgSi-IWI. Surface chemistry of this catalyst was previously interrogated using *in situ* DRIFTS[36] with the reaction mechanisms proposed based on the studied surface species formed during the reaction. TPRS provides vapor-phase analysis allowing to fully understand the mechanism as a prelude to the analysis of the catalytic sites responsible. **Table 5.2** shows the m/z utilized for reactive vapor (gas) species detection.

Table 5.2 m/z selection to identify the arising vapor-phase species from TPRS experiments

m/z	Species
46	ethanol
26	ethylene
44	acetaldehyde
2	hydrogen
54	1,3-BD
70	crotonaldehyde
57	crotyl alcohol

MgSi-WK catalyst was pretreated at 500 °C for 1 hour to simulate the real operating conditions. The adsorption of ethanol was performed at 100 °C to avoid any residual water vapor condensation and flushed with inert gas to remove loosely bound molecules. Experiment was performed under constant ethanol feed flow and shown in **Figure 5.6** (left). The ethanol signal continuously decreased during the reaction as a function of temperature without the presence of any products detected. This is consistent with the previous report where significant amount of reactive intermediates was bound strongly to the catalyst suface.[36] Ethylene was the first product to be detected at ~200 ^{o}C which can be explained by ethylene's lower desorption energy than acetaldehyde.[16] Acetaldehyde, when formed, would tend to stay on the surface to undergo several other surface reactions, such as aldol condensation and polymerization.[36] The more significant consumption of ethanol taking place at 300 °C, where acetaldehyde and hydrogen were detected at the same time around 350°C, which can be explained by the accelerated dehydrogenation reaction. Very low signal of crotyl alcohol and crotonaldehyde were also evident from the spectra which indicated the tendency of these species to undergo surface reaction than desorb off the surface.

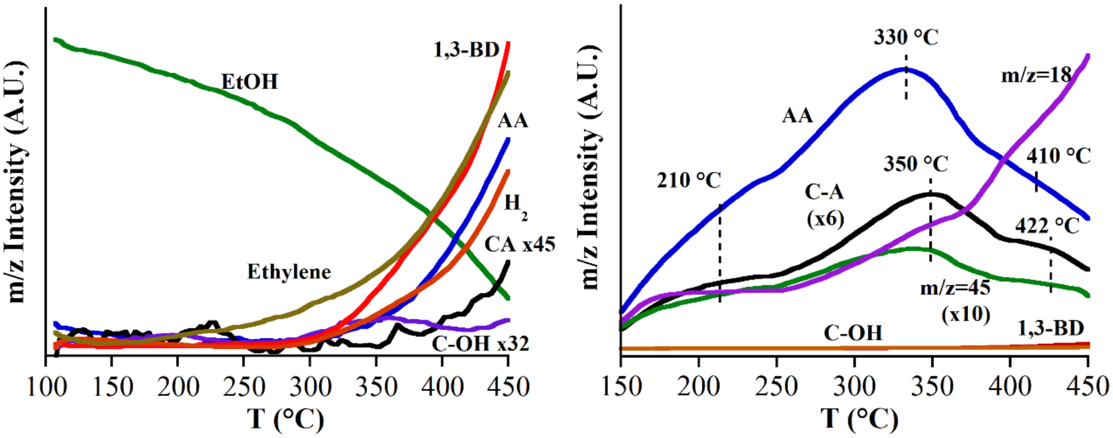

Figure 5.6. TPRS spectra of ETB reaction over MgSi-WK with ethanol as the feed (left) and acetaldehyde as the feed (right). EtOH: ethanol; AA: acetaldehyde; CA: crotonaldehyde; C-OH: crotyl alcohol.

Evolution of the reactive intermediates and byproducts during acetaldehyde temperature programmed experiment is shown in **Figure 5.6** (right). When only acetaldehyde was reacted over the sample crotonaldehyde was formed, in good agreement with DRIFTS experiments reported previously.[36] Several desorption temperature peaks were observed at 210, 330, 410 °C (acetaldehyde) and 210, 350, 422 °C (crotonaldehyde). The low temperature peak, i.e. 210 °C was due to the low temperature aldol condensation between the two acetaldehyde molecules. The presence of ethanol during the experiment imposes competitive surface MPV reduction and desorption of crotonaldehyde, as previously suggested[36] and in the absence of ethanol led to higher desorption rate of crotonaldehyde. The presence of crotonaldehyde was supported by the presence of m/z=45.

This m/z can also be associated to 3-hydroxybutanal (acetaldol). The spectrum looks very similar to that of crotonaldehyde which indicates a facile dehydration of the acetaldol formed on the surface during the aldol condensation. Reverse reaction of acetaldol on the surface was also expected when ethanol was not present on the surface since it would shift the equilibrium to the left when the resulting crotonaldehyde is not reacted.[49] This is suggested by the relatively lower intensity of the m/z=45 between 300-350 °C than that of crotonaldehyde in combination with the increasing acetaldehyde signal. The sudden change in the slope of the TP (temperature-programmed) peak of all discussed m/z, i.e. 44, 45, and 70, indicates an additional different reaction mechanism for aldol condensation. Palagin *et al.* suggested an alternative mechanism for aldol condensation without the enolization step.[50] Comparison between H-D exchange experiments of Sn-BEA, Zr-BEA and Ti-BEA demonstrated that enolized acetaldehyde was only stabilized over Sn-BEA. A separate mechanism took place where an open Lewis-bound acetaldehyde interacted with a second acetaldehyde adsorbed on the opposing OH group of the catalyst. DFT calculation showed that the activation energy of this second mechanism was more than triple than that of the enolization mechanism (~2 eV v ~0.6 eV).[50] A second peak at 330 and 350 °C for acetaldehyde and crotonaldehyde, respectively, indicated a secondary reaction that takes place. As previously suggested,[36,51] accumulation of acetaldehyde on the catalyst surface will lead to aldol condensation between crotonaldehyde and acetaldehyde to yield 2,4-hexadienal. This reaction was confirmed by the change of slope from the water signal m/z=18 which increased when the other signals decreased.

Finally, TPRS experiments were conducted with both ethanol and acetaldehyde (**Figure 5.7**). Acetaldehyde was first preadsorbed on the surface, flushed with an inert gas to remove the physisorbed molecules and temperature ramp was performed under a constant ethanol flow. This experiment mimics a two-step reactive process where acetaldehyde is cofed with ethanol. If acetaldehyde production is the rate-determining step (RDS) any accumulation of acetaldehyde on the surface would increase 1,3-BD production. Surprisingly, this experiment did not improve production of 1,3-BD as one would expect ethanol immediately undergo MPV reduction with the produced crotonaldehyde on the surface. Rather, 1,3-BD production was low until 360 °C which is much later for the ethanol alone. The sudden increase of the 1,3-BD production was accompanied by water production suggesting the dehydration of crotyl alcohol was lagging until 360 °C as well. This production onset coincided with a marked ethanol signal decline suggesting the MPV reduction becoming the RDS then acetaldehyde/crotonaldehyde is accumulated on the surface. The increase of acetaldehyde signal was mostly from both activated ethanol dehydrogenation and MPV reduction byproduct since H_2 also increased at higher temperatures.

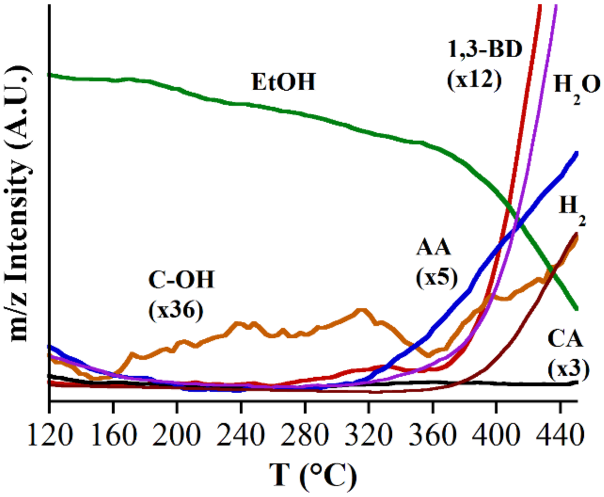

Figure 5.7. TPRS spectra of ETB reaction over MgSi-WK with ethanol and acetaldehyde as the coreactants. Acetaldehyde is pre-adsorbed on the surface and temperature ramp is under ethanol flow.

2.4. Acid-base characterization using DRIFTS

The acidity and basicity of the catalysts was investigated using CO_2 and pyridine as probe molecules (**Figure 5.8**). DRIFTS was used to qualitatively describe the acid and basic sites that are present on the surface. CO_2 adsorbs on basic surface sites as surface carbonate and bicarbonate species.[52] The formation of these surface species can be associated with the strength of the corresponding basic sites.[34,36] Adsorption of CO_2 on MgSi-WK resulted in three major, broad peaks at 1655, 1541 and 1406 cm^{-1}, while MgSi-IWI showed broad peaks at 1645, 1620, 1505, 1406 and 1385 cm^{-1}. These peaks were assigned to carbonates and bicarbonate formation on MgO site since CO_2 adsorption on SiO_2 should not yield any surface species.[3] In particular, the fundamental doubly degenerate $\upsilon_3(COO^-)$ vibration of carbonate on MgO is assigned to bidentate with ~1650 (υ_3^{as}) and ~1300 cm^{-1} (υ_3^{s}) and monodentate carbonate ~1550 (υ_3^{as}) and ~1400 cm^{-1} (υ_3^{s}) while bicarbonate is detected at ~1650 (υ_3^{as}) and ~1380 cm^{-1} (υ_3^{s}).[53,54] These three species were present on MgSi-WK catalysts, demonstrated by peaks at 1655 and 1325 cm^{-1} (bidentate carbonate), 1541 and ~1420 cm^{-1} (monodentate carbonate) and ~1670, 1406, and 1220 cm^{-1} (bicarbonate). On MgSi-WK, the dominant peaks were those originating from monodentate carbonate and bicarbonate. MgSi-IWI, on the other hand, exhibited rather different surface chemistry. Monodentate carbonate was apparent from the peaks at 1505 and 1385 cm^{-1}, while peaks at 1645 and 1406 cm^{-1} were assigned to adsorbed bicarbonate. The presence of bidentate carbonate might be signified by the peak at 1620 and a very small peak at ~1300 cm^{-1}. The strength of the same species on these two catalysts was very different, as shown by the corresponding DRIFT spectra acquired at 450 °C. At this reaction temperature, peaks at 1561 and 1368 cm^{-1} were apparent either due to the surface species rearrangement or due to the new species of lower intensity not detected at lower temperatures. These two peaks were assigned to monodentate carbonate due to the narrow υ_3 split and stability at higher temperature.[34] The stronger basicity of the MgSi-IWI originated from its Mg-rich surface, as supported by the LEIS spectra.

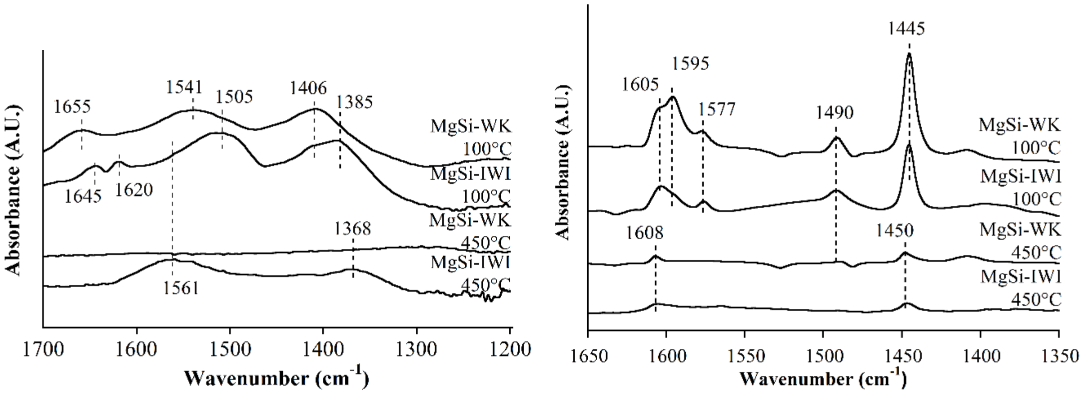

Figure 5.8. Acid-base characterization of MgSi-IWI and MgSi-WK catalysts probed using CO_2 (left) and pyridine (right). Spectra at high temperature (450°C) and low temperature (100°C) are shown.

Pyridine is a weak base and can discriminate between strong and basic site although its use is limited by its relatively large molecule size, in comparison to NH_3.[55] Pyridine adsorbs on a catalyst surface as a physisorbed molecule, Lewis-bonded species and as a pyridinium ions.[55–57] Observation of the latter two species allows to discriminate between the LAS and Brønsted acid sites (BAS).[58] BAS, which would be indicated by a peak at 1638 and 1540 cm^{-1},[58] was not observed which aligns well with the observations of Angelici *et al.* and Janssens *et al.*[9,30] Both catalysts exhibited similar Lewis acidity as shown at 450 °C as evident from peaks at 1445, 1590 and 1605 cm^{-1}. The peaks at 1445 and 1608 cm^{-1} shifted to 1450 and 1608 cm^{-1} at higher temperature, i.e. 450 °C, while the peak at 1490 cm^{-1}, which is a combination band of both LAS and BAS, disappeared. Based on both HS-LEIS and DRIFTS experiments, the origin of this Lewis acidity should be different for both catalysts where MgSi-WK would acquire its acidity from unpaired electrons of oxygen atom in the Mg-O-Si coordination while MgSi-IWI mostly from the Mg-O-Mg coordination (*vide supra*).

2.5. Reactive site persistence during ethanol-to-1,3-BD

Far less explored is reactive site acidity and basicity characterization (and persistence of the active sites) under reactive conditions of ethanol at reaction temperatures. To elucidate the role of the specific basic and acidic sites during the reaction on the aged catalyst, *in-situ* characterization experiments were performed using CO_2 and pyridine after ethanol reaction on MgSi-WK. In the first experiment ethanol was adsorbed at 100 °C for 20 min, flushed with inert gas for 1 hour and the resulting surface sites were probed with CO_2 or pyridine *in-situ*. In the second experiment, reaction with ethanol was carried out at 200 °C to initiate ethanol dehydrogenation. After 1 hour of reaction the reaction cell was flushed and CO_2 or pyridine was introduced into the cell. This way nature of the reactive sites, their persistence and availability for reaction were measured.

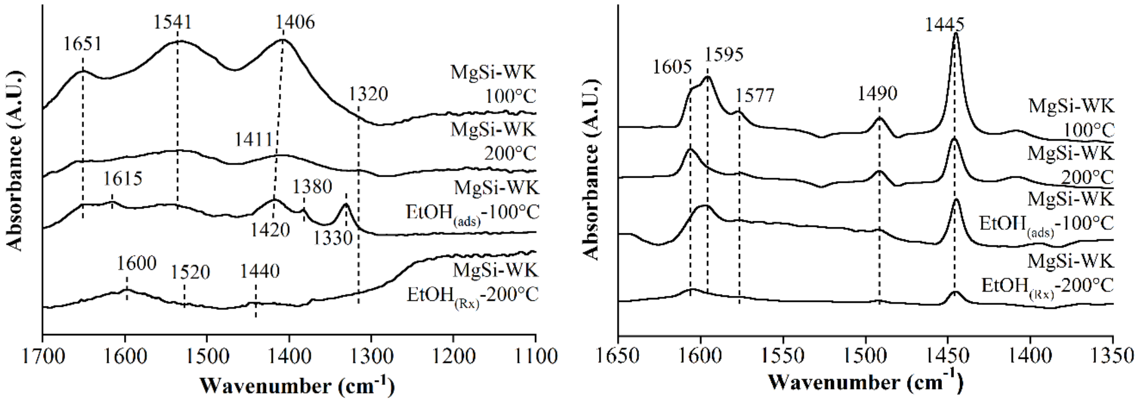

Figure 5.9. *In-situ* acid-base characterization of MgSi-WK catalyst before and after ethanol adsorption at 100°C and reaction at 200°C using CO_2 (left) and pyridine (right).

Figure 5.9 (left) shows spectra resulting from CO_2 adsorption. Three distinct peaks at 1615, 1380 and 1330 cm^{-1} appeared on the catalyst that was previously exposed to ethanol (MgSi-WK $EtOH_{(ads)}$) at 100 °C that do not originate from CO_2. While peaks at 1380 and 1330 cm^{-1} were assigned to ρ_w (CH) and ρ_w (CH_3) of surface ethoxide,[36] peak at 1615 cm^{-1} can be associated with a monodentate carbonate, accompanied by the symmetrical vibration peak at ~1320 cm^{-1}. After ethanol adsorption all peaks decreased in intensity, as compared to CO_2-only adsorption on the unreacted catalyst at the same temperature. This significant decrease indicates a competitive adsorption between ethanol and CO_2 that resulted in surface ethoxide and both monodentate and bidentate carbonate. This indicates that ethanol preferably adsorbed on the strong basic sites that would form monodentate and bidentate carbonate when exposed to CO_2. Reaction at 200 °C was performed *in-situ* before degassing with inert and adsorption of CO_2. The reaction temperature was chosen of 200 °C to limit further reactions to 1,3-BD. Extensive inert degassing was done to limit the further C4 oxygenates formed from facile aldol condensation, dehydration, and polymerization from occupying the site.[36] Comparison of the spectra between CO_2 adsorbed on activated catalyst and aged catalyst, i.e. extensively reacted at 200°C, showed decrease in intensity on all peaks related to all surface species arising from CO_2. Weak basic sites, which are represented by peaks at ~1650 and ~1400 cm^{-1} (surface bicarbonate),[53] were depleted. This indicates the consumption of the weak basic sites during the reaction. These weak basic sites on MgO/SiO_2, would be the OH groups, since the strong Mg^{2+}-O^{2-} pairs form monodentate and bidentate carbonate when exposed to CO_2.

Pyridine probing of the acidic sites shows a non-discriminative trend for both ethanol adsorption at 100 °C and reaction at 200 °C. LAS indeed were consumed during the adsorption and even more so after the reaction at 200°C, as indicated in **Figure 5.9** (right). No generation the new of BAS was observed after either adsorption or reaction as indicated by the absence of peaks at 1545 and 1638 cm^{-1}.[58] The Mg-O-Mg linkage present on MgO exhibits Lewis acidity to a certain extent, with the absence of Brønsted acidity.[50] The LAS on MgSi-WK are fundamentally represented by the Mg atoms in four groups: Mg-O(H)-Mg, Mg-O(H)-Si, Mg-O-Mg, and Mg-O-Si, with the first two groups being the open LAS. These were further distinguished by coordination number of the magnesium atoms: the lower the coordination, the stronger the atom is due to the electron deficiency of the cation. Although pyridine can't discriminate open LAS from closed sites, its combination with the conducted CO_2 DRIFTS experiment provides more information on the involved group. The two sites are distinguished by the consumed bicarbonate species, which is formed when CO_2 is adsorbed to a site containing OH group. Hence, the consumption of both LAS and bicarbonate site (weak basic site), can be traced to the open LAS. The two open sites, i.e. Mg-O(H)-Mg and Mg-O(H)-Si, were discriminated by the strength of the base pair. The former is less likely to participate during the reaction, due to its very basic nature. However, activation of this group has been observed when a bare MgO is activated using NH_3-thermally treated MgO.[12] The Mg-O-Si linkages have previously been correlated to the enhanced activity[1,2] while open LAS had been shown to be responsible for the increased 1,3-BD production.[19]

To further elucidate the role of acidic and basic sites during the reaction to 1,3-butadiene, surface site poisoning experiments were carried out using probe molecules such as CO_2, propionic acid and NH_3 in a steady state fixed bed reactor. CO_2 and propionic acid are two weak acids while NH_3 is a basic probe molecule. **Figure 5.10a** shows the effect of cofeeding with CO_2. Slow, steady decrease in acetaldehyde and 1,3-BD production before

CO_2 was introduced indicates slow catalyst deactivation. However, once the CO_2 was cofed to the system, formation rate of 1,3-BD and ethylene dramatically dropped, while acetaldehyde production increased. CO_2 is a weaker acid than propionic acid and will bind to the strongest basic sites. As shown in **Figure 5.8**, CO_2 did not typically adsorb to the surface at 450 °C. This poisoning effect suggests that CO_2 poisoned the sites that catalyzed aldol condensation and the subsequent steps, since more acetaldehyde was released into the vapor-phase without further reacting. When CO_2 flow was switched off, the production of acetaldehyde, 1,3-BD and ethylene was restored, confirming the weak interaction between CO_2 and the strong basic sites.

Figure 5.10b shows (by)product formation rates upon the introduction of propionic acid. All three products showed a decline in formation rate. When propionic acid concurrent flow was stopped, the production of acetaldehyde was restored but 1,3-BD and ethylene formation did not recover. Propionic acid interacted more strongly with the stronger base sites but also binds to any weaker basic sites. Hence, when propionic acid flow was stopped, only weak basic sites were accessible while some of the strong basic sites were permanently poisoned. From the two experiments it is evident that acetaldehyde production was catalyzed by weak basic sites and 1,3-BD - by strong basic sites. The production of acetaldehyde over the weak basic site is consistent with the DRIFTS performed using CO_2 as probe molecule (**Figure 5.9**). Similar phenomenon was observed by Shylesh, *et al.* where the 1,3-BD formation rate did not recover during propionic acid cofeeding experiment over the Au-promoted IWI MgO/SiO_2 catalyst.[3] Very interestingly, ethylene formation during the cofeeding experiments followed the trend of 1,3-butadiene. As previously suggested, ethylene formation can be carried out over both Lewis acidic oxygen atoms (LAS) in the Mg-O-Mg or Mg-O-Si sites and the acidic O-H group (BAS).[16,59] Poisoning with both CO_2 and propionic acid affected the strong and medium Lewis basic Mg atoms in the Mg-O-Mg and Mg-O-Si which inevitably perturbed the strong Lewis acid pair, i.e. oxygen anions, as well.

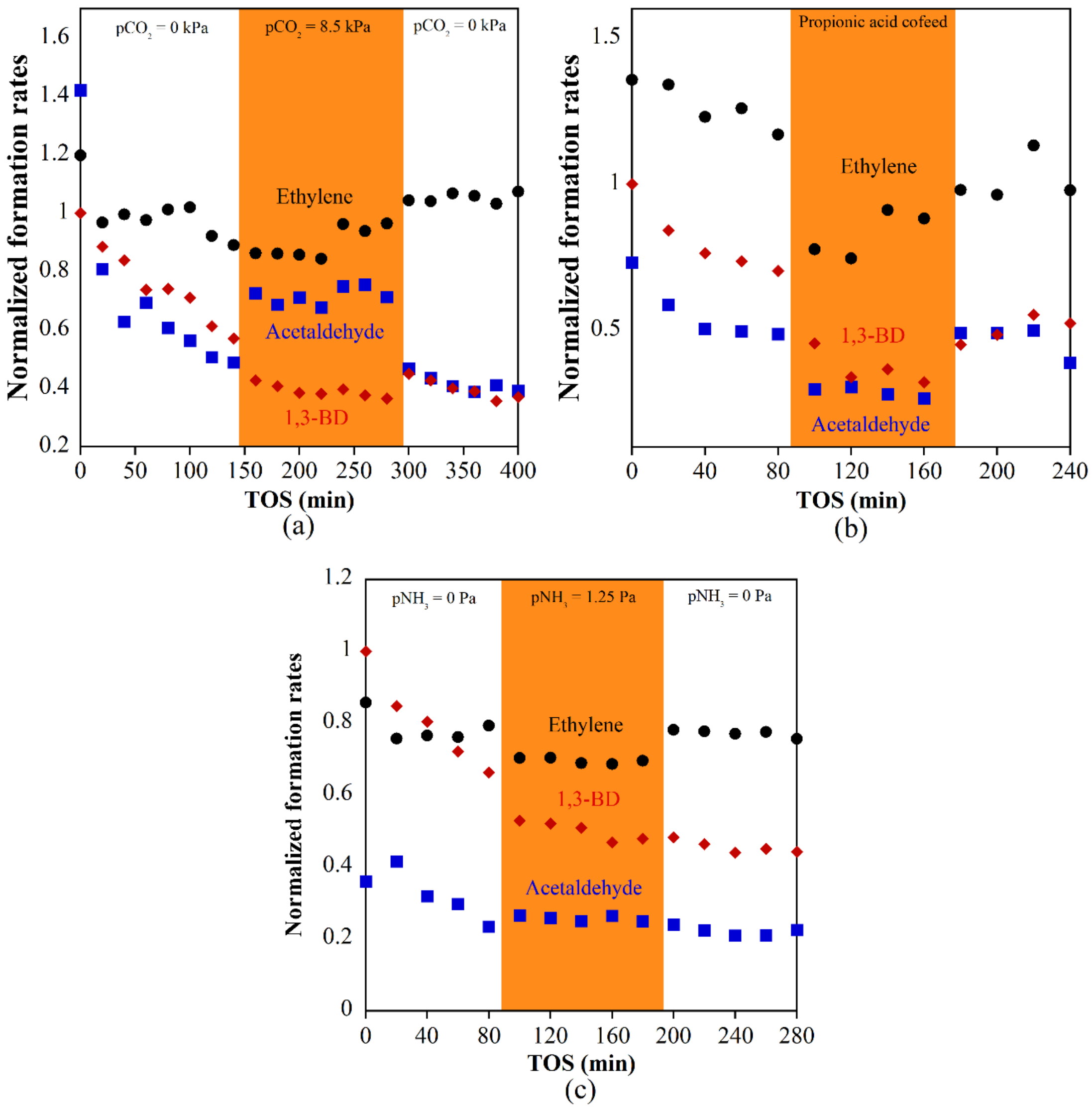

Figure 5.10. Acid-base poisoning reactivity testing using (a) CO_2, (b) propionic acid, and (c) NH_3 to determine the role of each site during ethanol conversion to 1,3-BD over WK-800 MgO/SiO_2 catalyst. Reactions are carried out at 425 °C, $m_{cat} = 0.1$ g, $p_{ethanol} = 2.5$ kPa, total flow = 55 ml/min. All formation rates are normalized to initial 1,3-BD formation rate.

NH_3 is a relatively strong gas-phase base, stronger than pyridine and other organic basic molecules, such as acetonitrile and benzenes.[55] At reaction temperature of 425 °C, NH_3 exhibits very weak adsorption on the surface and would interact with the acidic sites. Evident from **Figure 5.10c**, acetaldehyde production was hardly affected by the poisoning, as opposed to 1,3-BD and ethylene, where the decrease in production was very pronounced. While ethylene formation inhibition was reversible, 1,3-BD formation was irreversibly affected. NH_3 poisoned both strong and weak BAS and LAS but when its flow was discontinued only the strong BAS were poisoned. Ethylene synthesis trend was very similar for both propionic acid and NH_3 cofeeding which indicates the same acid-base pairs being poisoned during the experiment. 1,3-BD production involves two dehydration steps and the poisoning indicates that its production did not require participation from the site that dehydrates ethylene. From these experiments, it is evident that dehydration steps of both acetaldol and crotyl alcohol were catalyzed by strong acidic sites while ethanol dehydration was catalyzed by weaker acidic sites.

To confirm participation of the acidic sites, Na_2O, a strong basic oxide, was added to the catalyst in a post-treatment step that permanently poisoned some of the acidic sites. Three Na concentrations were chosen in this study, i.e. 250, 500, and 1000 ppm, labeled as 250NaMgSi-WK, 500NaMgSi-WK, and 1000NaMgSi-WK. Ethylene productivity was significantly limited with up to 50% suppression, as shown in **Figure 5.11b**. **Figure 5.11a** shows that sodium poisoning limited the productivity of 1,3-BD as well. The only condition that gave comparable 1,3-BD productivity to the undoped catalyst was at 450 °C and with 250NaMgSi-WK catalyst. This limitation was also reflected in the acetaldehyde production. As in 1,3-BD case there was no trend observed with varying Na content but acetaldehyde production over Na_2O-poisoned catalysts was higher than for the unpromoted catalysts. This suggests that Na_2O poisoned the acidic sites unselectively eliminating both BAS and LAS that are responsible for ethylene and 1,3-BD production. The effect of acidity modification by poisoning with alkali metal was also investigated by Da Ros *et al.*[60] However, the loss of acidic sites in their catalysts was offset by the presence of Zr and Zn which provided extra Lewis acidity, which was presumably responsible for selectively dehydrate the C4 molecules to 1,3-BD.

The origin of the poisoning effect was correlated with CO_2 and NH_3 DRIFTS experiments. **Figure 5.12a** shows the appearance of the peaks at 1643, 1463, 1372, and 1356 cm^{-1} in addition to the native basic sites of the MgSi-WK. Peaks at 1463 and 1356 cm^{-1} reached a maximum for 500NaMgSi-WK before decreasing in intensity at 1000 ppm, while the shoulder at 1372 cm^{-1} became obvious with higher Na loading. The stability of these peaks indicates the presence of bicarbonates, as shown by the peaks at 1643 and 1372 (1356) cm^{-1}. The peak at 1463 cm^{-1} is sharp and also is not stable at high temperature which indicates the presence of another weakly adsorbed CO_2 species. Na_2CO_3, on the other hand, possesses a band at this specific wavenumber, i.e. 1463 cm^{-1}.[61] Na_2CO_3 is a very stable carbonate melting prior to decomposing to Na_2O, starting at 850°C.[62] At higher temperature range, i.e. 300-450°C an interesting observation emerges from the growth of the peaks at ~1600 and ~1370 cm^{-1}, as shown in **Figure 5.12a** (top) for 1000NaMgSi-WK. The presence of the shoulders to these peaks suggests the presence of two distinct carbonate groups. From the split, i.e. ~300 cm^{-1}, these peaks are characteristics of bidentate carbonate. The growth of this peak suggests that rearrangement of (bi)carbonates took place upon thermal treatment. Furthermore, the stability of this peak at high temperature indicates the enhanced basic site when Na was introduced to the catalyst.

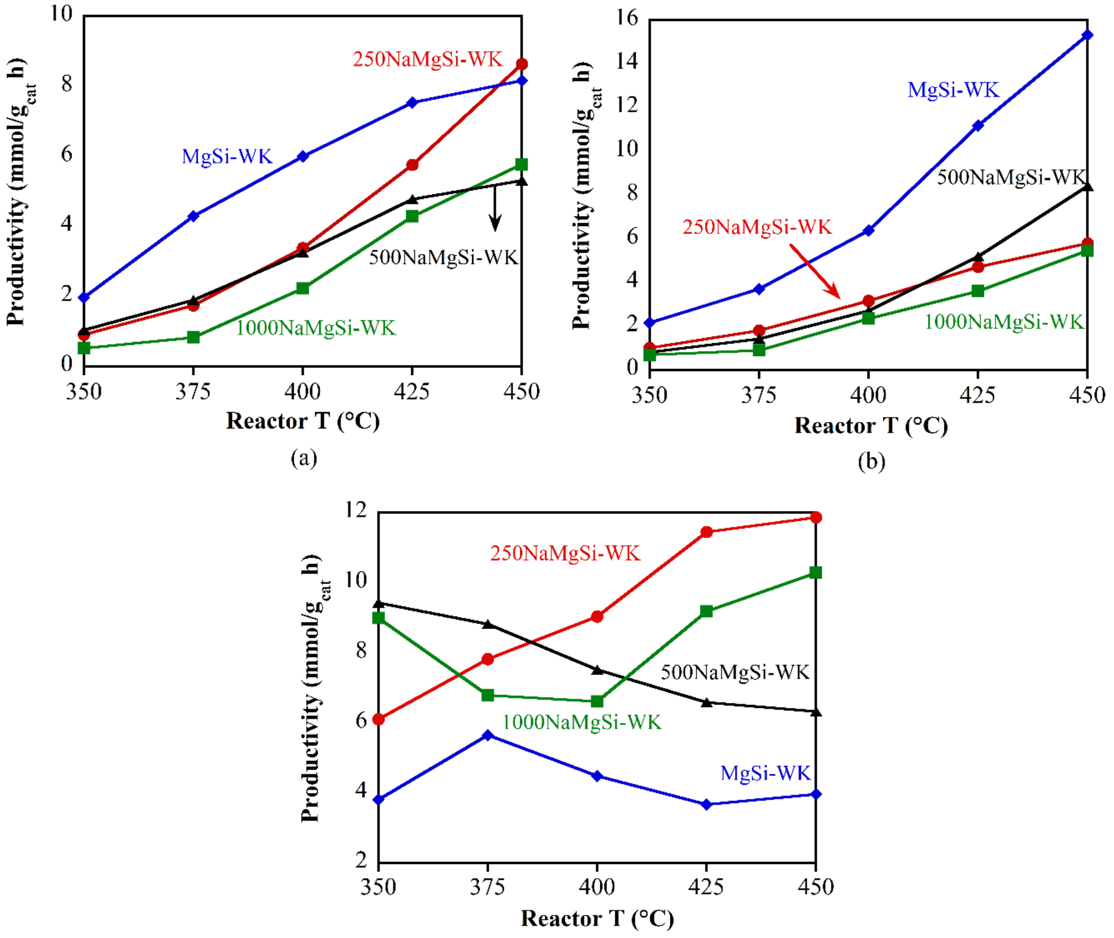

(a)

(b)

(c)

Figure 5.11. Productivity of (a) 1,3-BD, (b) ethylene, and (c) acetaldehyde of Na-poisoned MgSi-WK catalysts between 350-450°C. Catalyst mass = 0.1 gr, total flow rate = 55 ml/min, $p_{ethanol}$ = 2.5 kPa.

The acidity of the Na-modified catalysts was probed with using NH_3 as a probe molecule, as shown in **Figure 5.12b**. On pure dehydroxylated MgO, NH_3 adsorbs as physisorbed molecule, with a peak at ~1605 cm^{-1} while two different LAS exhibited vibrational peaks at >1605 and 1560 cm^{-1}.[63,64] On hydroxylated surface, however, the interaction is more complicated due to the contributions of OH groups, where hydrogen bonding between NH_2H—OH (1612 cm^{-1}) and H_3N—HO (1634 cm^{-1}) obscured the DRIFTS spectra.[63,64] The peak at 1430 cm^{-1} was assigned to ammonium ion (NH_4^+) as a result from interaction between ammonia and a BAS.[63] Physisorbed ammonia species was observed on both oxygen and hydroxyl group by the appearance of peaks at 1554 and 1605 cm^{-1}, respectively.[63,64] Presence of BAS during NH_3 but not pyridine probing had been observed in the past, where pyridine underrepresented the amount of acidic sites.[9,65] This discrepancy was due to the size of the molecule with NH_3 being more mobile.[9] The BAS that was found on the catalysts was isolated, less-accessible and hence might participate less during the reaction. Four peaks that are assignable to LAS are recognized on these catalysts by the peaks at 1560, 1580, 1600, 1620, and 1650 cm^{-1}. To aid the assignments of these peaks DFT vibrational frequency calculations performed on defect sites of MgO, i.e. $Mg_{3C}O_{4C}$ and $Mg_{4C}O_{4C}$ for both open and closed LAS (**Figure 5.13**). The corresponding vibrations were tabulated in **Table 5.3**.

Table 5.3. Comparison between observed experimental values of NH_3 adsorption on MgSi-WK catalysts with DFT calculated IR vibrations of NH_3 adsorbed on open and closed acid Mg_{3C} and Mg_{4C} sites. Scaling factor of 0.9854 was applied to the calculated values and was derived from the gas-phase NH_3 experimental and DFT calculated frequencies.

Type	**Mg coordination**	**Vibrational mode**		**Experimental values**	
		δ_{as} H-N-H	**δ_s H-N-H**	**δ_{as} H-N-H**	**δ_s H-N-H**
Open	4C	1592	1566	1600	1560
	3C	1574	1534	1570	1540
Closed	4C	1588	1571	N/A	N/A
	3C	1620	1577	1620	1580

Assuming an ideal surface and similar trend on Mg-O-Si sites, peak assignments can be readily made. For instance, experimentally, MgSi-WK (0 ppm Na) catalyst exhibited both closed and open LAS. Closed LAS were evident from the peaks at 1620 and 1580 cm^{-1} (Mg_{3C}) while open LAS from Mg_{4C} were recognized by peaks at 1600 and 1560

cm^{-1}. The presence of peak at 1540 cm^{-1} signified the presence of another open LAS (Mg_{3C}) which would be accompanied by a shoulder peak at ~1570 cm^{-1}. The assignments of these peaks here were made based on the comparison with the DFT computed values tabulated in **Table 5.3**. The shoulder at 1650 cm^{-1} is obvious and can't be ignored. Echterhoff and Knözinger attributed a peak at 1634 cm^{-1} to hydrogen bonding between ammonia and surface hydroxyl (NH_2-H—HO-Mg).[64] This vibrational mode is entirely possible due to the identified NH_4^+ on the surface indicating the presence of some BAS. Alternatively, if a Si atom replaces one Mg atom in the Mg_{3C}-O_{4C}-Mg_{4C} (closed LAS) and results in Mg-O-Si linkage then a change in electronegativity will occur and the magnesium atom becomes more positively charged which would result in the shorter bond between the Mg and N atoms. The shorter bond would result in the shift of the peak to a higher wavenumber in this case higher than 1620 cm^{-1}. Increasing Na loading resulted in the decreasing LAS and BAS, which was expected. The 250 ppm Na-poisoned catalyst, surprisingly, exhibited higher intensity of all peaks associated with LAS and BAS, indicating the enhanced acidity at this temperature. The enhanced acidity, however, was only intermittent at this temperature, since the top spectra in **Figure 5.12b** shows the better stability of NH_3 surface species on unpoisoned catalyst at elevated temperature, i.e. 300 °C.

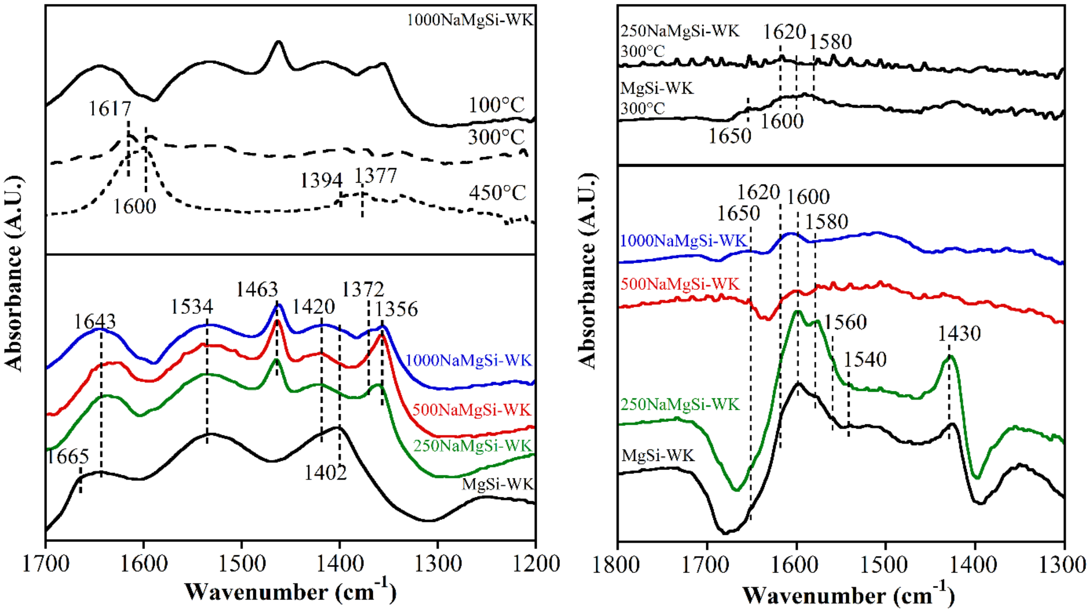

(a)

(b)

Figure 5.12. Bottom: DRIFTS characterization of Na-doped MgSi-WK using (a) CO_2 and (b) NH_3. Spectra are taken at 100°C after extensive evacuation with N_2. Top: (a) CO_2 desorption spectra of 1000 ppm Na-doped MgSi-WK at 100, 300, and 450°C and (b) NH_3 desorption on 0 ppm and 250 ppm Na-doped MgSi-WK at 300°C. Spectral subtraction was done using the spectra of the dehydrated catalysts at respective temperatures as the background.

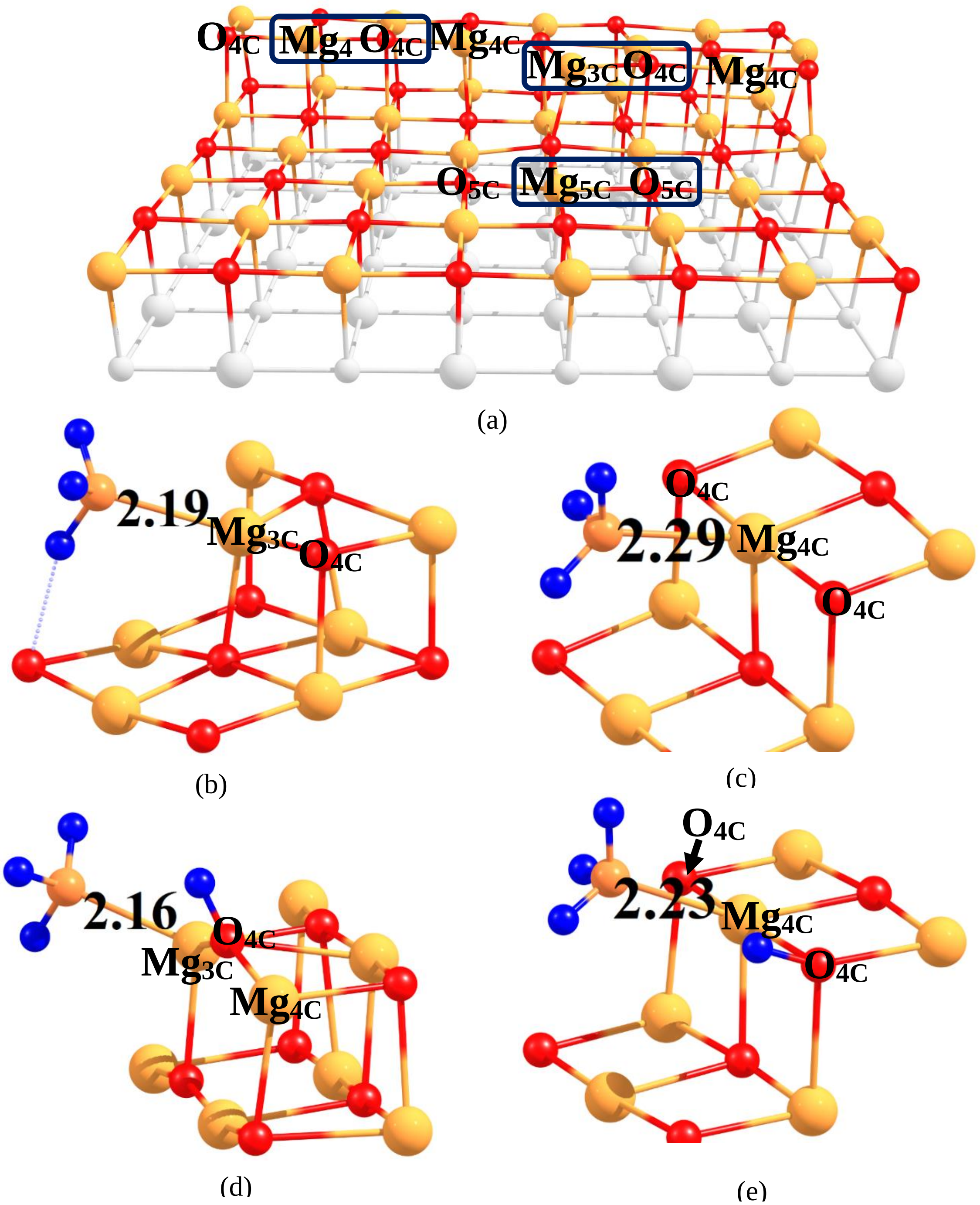

Figure 5.13. (a) MgO periodic model used for DFT simulation of NH_3 adsorption on MgO Lewis acid sites: (b) Mg_{3C}, closed, (c) Mg_{4C}, closed, (d) Mg_{3C}, open, (e) Mg_{4C}, open. Multiple possible adsorption sites, i.e. kink ($Mg_{3C}O_{4C}$), edge ($Mg_{4C}O_{4C}$), and planar ($Mg_{5C}O_{5C}$) are highlighted.

2.6. Implications for the structure-activity relationship

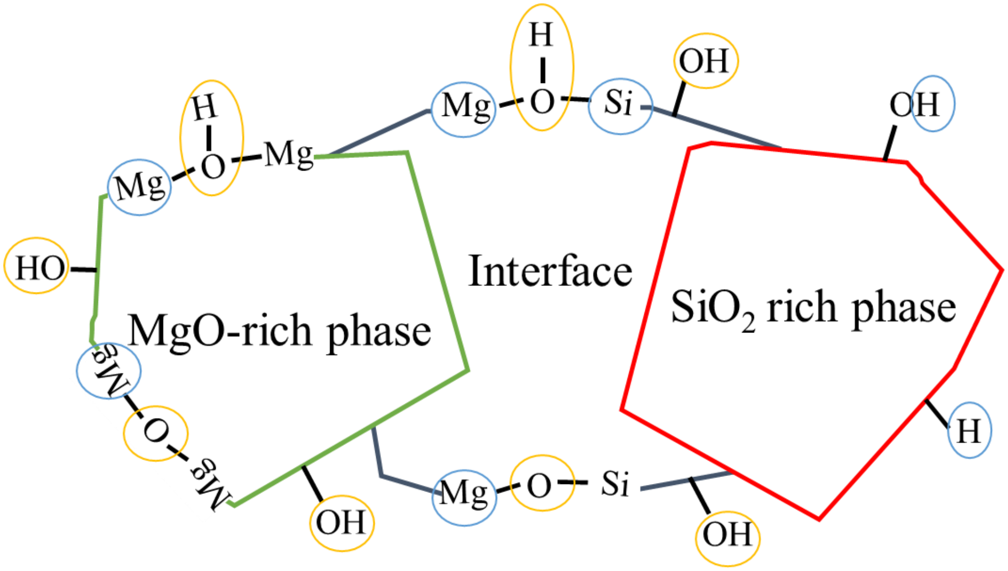

Figure 5.14. Schematic diagram to show the presence of various sites investigated with NH_3 and CO_2 DRIFTS experiments. The basic sites (orange) are shown in the figure as both Brønsted base (OH) and Lewis site (electron accepting oxygen atoms), and acid sites (blue) are represented as Brønsted acid sites (H) and Lewis acid sites (electron donating magnesium and silicon atoms).

The wet-kneading method provides a deeper, more intimate mixing between MgO and SiO_2.[1] Incipient wetness impregnation, on the other hand, is a typical synthesis method for the synthesis of supported catalyst. This method is appropriate when the target catalyst is a well-dispersed, below monolayer, metal oxide that is supported on a high surface area support. However, at ratio of 1, the 'promoter' is at similar amount with the support, which corresponds to layered metal oxide on the surface. The nature of the synthesis method would result in two different bulk phases, i.e. MgO-phase and SiO_2-phase, which are bridged by an interface that should equally contain both oxides. **Figure 5.14** schematically represents these three phases that are formed during the synthesis method. In the case of wet-kneading, the extensive interaction between MgO and SiO_2 allows the boundary phase, i.e. the middle part in **Figure 5.14**, to grow larger, as confirmed by the LEIS experiment and *in-situ* dehydrated DRIFTS of the catalysts. The MgO-rich phase that is formed on the catalyst contributes to the higher amount of strong basic sites, which is evident from CO_2-probing comparison, shown in **Figure 5.8**. The reduced amount of strong basic sites makes MgSi-WK a better catalyst than MgSi-IWI, as demonstrated by the higher 1,3-BD formation.

As confirmed by TPRS, the catalytically relevant step during the transformation of ethanol to 1,3-BD was determined to be acetaldehyde formation step. The *ex-situ* characterization alone indicated the importance of weaker basic sites during the reaction and *in-situ* poisoning experiment with CO_2 and propionic acid confirmed the need for the weaker basic sites for the reaction. In particular, poisoning the strong basic sites with CO_2 resulted in higher acetaldehyde formation rate which suggests that the weak basic sites, not poisoned by CO_2, catalyzed ethanol dehydrogenation and the stronger basic sites catalyze the subsequent reaction steps. This finding agrees that of Shylesh *et al.* where propionic acid was used as a poisoning agent.[3] The acidic sites are responsible for both 1,3-BD and ethylene formation considering the nature of the reaction steps. From NH_3 poisoning experiments it is evident that the weaker acidic sites are responsible for ethanol dehydration while the stronger sites are responsible for acetaldol and crotyl alcohol dehydration. The reasoning behind this is the strong interaction between crotyl alcohol, crotonaldehyde and the surface.[36] Poisoning the strong acidic sites resulted in the accumulation of the heavy aromatic compounds on the surface, which is also confirmed by the unprecedented amount of aromatic carbonaceous compound observed after the NH_3 reaction. The indispensable role of acidic sites on the reaction is further confirmed by Na-poisoned catalysts, where, although ethylene formation was virtually suppressed, 1,3-BD formation did not significantly benefit from the reduced acidic sites.

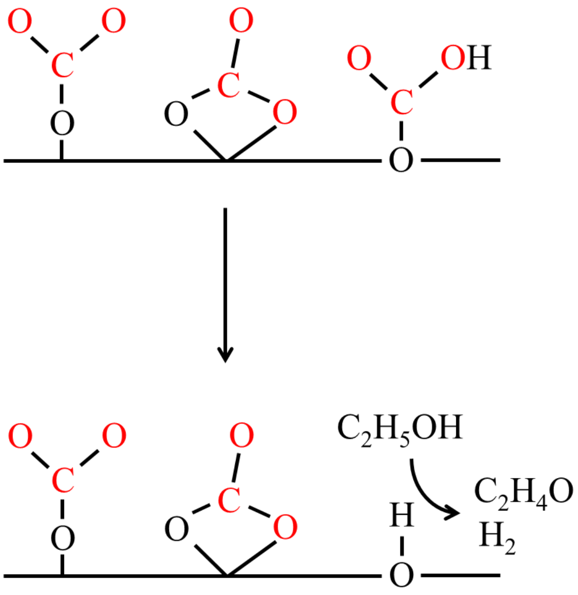

Figure 5.15. Representation of the role of basic sites during ethanol conversion to acetaldehyde. Top figure represents dehydrated (pretreated) catalyst; bottom figure demonstrates the absence of bicarbonate when CO_2 is adsorbed *in-situ* after reaction at 200 °C.

As suggested by the characterization using *in-situ* DRIFTS and LEIS, the mixing between MgO and SiO_2 would allow the formation of Mg-O-Si linkages which is consistently observed by previous investigators.[1–3] With the possibility of hydroxylation of the surface, there are four possible formation of the LASs, i.e. open and closed acid sites of both Mg-O-Mg and Mg-O-Si. The LASs, i.e. Mg^{2+} cations, will present different strength, depending on the coordination and type of linkage. Our NH_3-DRIFTS experiment demonstrated the formation of several distinct Lewis sites of different strength. The *in-situ* acid-base characterization after ethanol reaction at 200 °C showed that weak basic sites and LASs were depleted. Schematic representation of this site can be seen in **Figure 5.15.**

The weak basic sites discussed are both the Mg-O(H)-Mg and Mg-O(H)-Si. Since at 200 °C only ethylene and acetaldehyde were produced this suggested that the open sites were the most catalytically relevant active sites. It should be noted, however, that this linkage contains both acidic and basic sites in the form of Mg^{2+} cations and OH group, respectively. Hence, the strength of Mg-O(H)-Mg and Mg-O(H)-Si should be different. The basicity for the latter would be weaker, as suggested by the *in-situ* DRIFTS, where the peaks for these linkages are well below that of Mg-OH, i.e. 3680, 3705, and 3725 cm^{-1} (**Figure 5.5**). The strength of the acidic site, i.e. Mg cation, can be hypothesized to be lower as well in the case of Mg-O(H)-Si due to the electron density, since Si cations possess atomic charge of +4*e*. This leads to the proposed both Mg-O(H)-Si to be the sites that are responsible for ethanol dehydrogenation and ethylene dehydration while stronger acidic sites and basic sites are responsible for C4 dehydration and ethanol dehydrogenation. The exact molecular structure of the various open (closed) acidic and basic sites proposed is shown in **Figure 5.14** and includes both LAS and BAS.

3. Conclusions

MgO/SiO_2 catalyst active surface sites were analyzed using *in situ* DRIFTS (using complementary DFT calculations), TPRS and steady state reactor in combination with bulk XRD and surface LEIS measurements. Acid-base characterization showed that IWI synthesis method resulted in a highly basic catalyst with reactive properties originating from the abundance of Mg atoms on the topmost surface layer, as opposed to WK catalyst. The molecular active site structure was determined and MgSi-IWI surface was found to be dominated with stabilized Mg-OH with little magnesium silicate hydroxyl groups. The

MgSi-WK surface, on the other hand, contained a significant number of surface sites derived from magnesium silicates as indicated by the distinct OH groups. This fundamental site structure difference consequentially led to a different reactivity where MgSi-WK possessed a more balanced weak-strong basic sites than the basic sites present on MgSi-IWI. From various reacting molecule poisoning experiments it was determined that the weak basic sites were responsible for ethanol dehydrogenation, strong basic sites for aldol condensation and MPV reduction, while stronger acid sites catalyze acetaldol and crotyl alcohol dehydration reactions and weak acid sites catalyzed the undesired ethanol dehydration. Furthermore, through a combination of NH_3-TPD and DFT the presence of *open* and *closed* LAS was identified while further elaborating Mg coordination, as adopted from LAS classification of zeolitic materials.[20–22] The MgSi-WK catalyst was shown to have both *open* LAS with both Mg_{3C} and Mg_{4C} as the anchoring LAS, while also a very isolated *closed* LAS (Mg_{3C}).

References

(1) Chung, S.-H.; Angelici, C.; Hinterding, S. O. M.; Weingarth, M.; Baldus, M.; Houben, K.; Weckhuysen, B. M.; Bruijnincx, P. C. A. *ACS Catal.* **2016**, *6* (6), 4034–4045.

(2) Velasquez Ochoa, J.; Bandinelli, C.; Vozniuk, O.; Chieregato, A.; Malmusi, A.; Recchi, C.; Cavani, F. *Green Chem.* **2016**, *18*, 1653–1663.

(3) Shylesh, S.; Gokhale, A. A.; Scown, C. D.; Kim, D.; Ho, C. R.; Bell, A. T. *ChemSusChem* **2016**, *9* (12), 1462–1472.

(4) Huang, X.; Men, Y.; Wang, J.; An, W.; Wang, Y. *Catal. Sci. Technol.* **2017**, *7* (1), 168–180.

(5) Müller, P.; Burt, S. P.; Love, A. M.; McDermott, W. P.; Wolf, P.; Hermans, I. *ACS Catal.* **2016**, *6* (10), 6823–6832.

(6) Sushkevich, V. L.; Ivanova, I. I.; Taarning, E. *Green Chem.* **2015**.

(7) Shylesh, S.; Gokhale, A. A.; Ho, C. R.; Bell, A. T. *Acc. Chem. Res.* **2017**, acs.accounts.7b00354.

(8) Pomalaza, G.; Capron, M.; Ordomsky, V.; Dumeignil, F. *Catalysts* **2016**, *6* (12), 203–237.

(9) Angelici, C.; Velthoen, M. E. Z.; Weckhuysen, B. M.; Bruijnincx, P. C. A. *Catal. Sci. Technol.* **2015**.

(10) Kvisle, S.; Aguero, A.; Sneeden, R. P. A. *Appl. Catal.* **1988**, *43* (1), 117–131.

(11) Angelici, C.; Velthoen, M. E. Z.; Weckhuysen, B. M.; Bruijnincx, P. C. A. *ChemSusChem* **2014**, *7* (9), 2505–2515.

(12) Hayashi, Y.; Akiyama, S.; Miyaji, A.; Sekiguchi, Y.; Sakamoto, Y.; Shiga, A.; Koyama, T.; Motokura, K.; Baba, T. *Phys. Chem. Chem. Phys.* **2016**, *18* (36), 25191–25209.

(13) Di Valentin, C.; Del Vitto, A.; Pacchioni, G.; Abbet, S.; Wörz, A. S. S.; Judai, K.; Heiz, U. *J. Phys. Chem. B* **2002**, *106* (46), 11961–11969.

(14) Cavalleri, M.; Pelmenschikov, A.; Morosi, G.; Gamba, A.; Coluccia, S.; Martra, G. In *Oxide-based Systems at the Crossroads of ChemistrySecond International Workshop October 8-11, 2000, Como, Italy*; A. Gamba, C. C. and S. C. B. T.-S. in S. S. and C., Ed.; Elsevier, 2001; Vol. Volume 140, pp 131–139.

(15) Branda, M. M.; Rodríguez, A. H.; Belelli, P. G.; Castellani, N. J. *Surf. Sci.* **2009**, *603* (8), 1093–1098.

(16) Taifan, W. E.; Bučko, T.; Baltrusaitis, J. *J. Catal.* **2017**, *346*, 78–91.

(17) Chieregato, A.; Velasquez Ochoa, J.; Bandinelli, C.; Fornasari, G.; Cavani, F.; Mella, M. *ChemSusChem* **2014**, *8* (2), 377–388.

(18) Fan, D.; Dong, X.; Yu, Y.; Zhang, M. *Phys. Chem. Chem. Phys.* **2017**, *19* (37), 25671–25682.

(19) Sushkevich, V. L.; Palagin, D.; Ivanova, I. I. *ACS Catal.* **2015**, 4833–4836.

(20) Harris, J. W.; Cordon, M. J.; Di Iorio, J. R.; Vega-Vila, J. C.; Ribeiro, F. H.; Gounder, R. *J. Catal.* **2016**, *335*, 141–154.

(21) Boronat, M.; Concepcion, P.; Corma, A.; Navarro, M. T.; Renz, M.; Valencia, S. *Phys. Chem. Chem. Phys.* **2009**, *11* (16), 2876–2884.

(22) Boronat, M.; Concepción, P.; Corma, A.; Renz, M.; Valencia, S. *J. Catal.* **2005**, *234* (1), 111–118.

(23) Kantorovich, L. N.; Holender, J. M.; Gillan, M. J. *Surf. Sci.* **1995**, *343* (3), 221–

239.
(24) Chizallet, C.; Petitjean, H.; Costentin, G.; Lauron-Pernot, H.; Maquet, J.; Bonhomme, C.; Che, M. *J. Catal.* **2009**, *268* (1), 175–179.
(25) Chizallet, C.; Costentin, G.; Che, M.; Delbecq, F.; Sautet, P.; Surface, D.; Marie, P. *J. Am. Chem. Soc.* **2007**, No. 19, 6442–6452.
(26) Chizallet, C.; Costentin, G.; Che, M.; Delbecq, F.; Sautet, P. *J. Phys. Chem. B* **2006**, *110* (32), 15878–15886.
(27) Sushko, P. V.; Shluger, A. L.; Catlow, C. R. A. *Surf. Sci.* **2000**, *450* (3), 153–170.
(28) Bailly, M.; Chizallet, C.; Costentin, G.; Krafft, J.; Lauronpernot, H.; Che, M. *J. Catal.* **2005**, *235* (2), 413–422.
(29) Sushkevich, V. L.; Vimont, A.; Travert, A.; Ivanova, I. I. *J. Phys. Chem. C* **2015**, *119* (31), 17633–17639.
(30) Janssens, W.; Makshina, E. V. V.; Vanelderen, P.; De Clippel, F.; Houthoofd, K.; Kerkhofs, S.; Martens, J. A. A.; Jacobs, P. A. A.; Sels, B. F. B. F. *ChemSusChem* **2014**, *8* (6), 994–1008.
(31) Larina, O. V.; Kyriienko, P. I.; Trachevskii, V. V.; Vlasenko, N. V.; Soloviev, S. O. *Theor. Exp. Chem.* **2016**, *51* (6), 387–393.
(32) Zhu, Q.; Wang, B.; Tan, T. *ACS Sustain. Chem. Eng.* **2017**, *5* (1), 722–733.
(33) Golay, S.; Kiwi-Minsker, L.; Doepper, R.; Renken, A. *Chem. Eng. Sci.* **1999**, *54* (15), 3593–3598.
(34) Di Cosimo, J. I.; Díez, V. K.; Xu, M.; Iglesia, E.; Apesteguía, C. R. *J. Catal.* **1998**, *178* (2), 499–510.
(35) Phung, T. K.; Busca, G. *Catal. Commun.* **2015**, *68*, 110–115.
(36) Taifan, W.; Yan, G. X.; Baltrusaitis, J. *Catal. Sci. Technol.* **2017**, *7* (20), 4648–4668.
(37) Gao, M.; Jiang, H.; Zhang, M. *Appl. Surf. Sci.* **2018**.
(38) Zhu, Q.; Wang, B.; Tan, T. *ACS Sustain. Chem. Eng.* **2017**, *5* (1), 722–733.
(39) Kotov, S. V.; Nankeva, I. N. *Chem. Technol. Fuels Oils* **1994**, *30* (5), 240–245.
(40) Ho, C. R.; Shylesh, S.; Bell, A. T. *ACS Catal.* **2016**, *6* (2), 939–948.
(41) Mathur, L.; Saddam Hossain, S. K.; Majhi, M. R.; Roy, P. K. *Boletín la Soc. Española Cerámica y Vidr.* **2017**.
(42) Tavangarian, F.; Emadi, R. *Mater. Res. Bull.* **2010**, *45* (4), 388–391.
(43) Tavangarian, F.; Emadi, R. *Ceram. – Silikáty 54* (2), 122–127.
(44) Swanson, H. E.; Tatge, E. *J. Res. Natl. Bur. Stand. (1934).* **1951**, *46* (4), 318–327.
(45) ter Veen, H. R. J.; Kim, T.; Wachs, I. E.; Brongersma, H. H. *Catal. Today* **2009**, *140* (3), 197–201.
(46) Davydov, A. *Molecular Spectroscopy of Oxide Catalyst Surfaces*; John Wiley & Sons Ltd: West Sussex PO19 8SQ, England, 2003.
(47) Keturakis, C. Operando Molecular Spectroscopy during Catalytic Biomass Pyrolysis, Lehigh University, 2015.
(48) Knözinger, E.; Jacob, K.-H.; Singh, S.; Hofmann, P. *Surf. Sci.* **1993**, *290* (3), 388–402.
(49) Toussaint, W. J.; Dunn, J. T.; Jachson, D. R. *Ind. Eng. Chem.* **1947**, *39* (2), 120–125.
(50) Palagin, D.; Sushkevich, V. L.; Ivanova, I. I. *J. Phys. Chem. C* **2016**, *120* (41), 23566–23575.

(51) Ordomsky, V. V.; Sushkevich, V. L.; Ivanova, I. I. *J. Mol. Catal. A Chem.* **2010**, *333* (1), 85–93.

(52) Bian, S.-W.; Baltrusaitis, J.; Galhotra, P.; Grassian, V. H. *J. Mater. Chem.* **2010**, *20* (39), 8705.

(53) Busca, G.; Lorenzelli, V. *Mater. Chem.* **1982**, *7* (1), 89–126.

(54) Taifan, W.; Boily, J.-F.; Baltrusaitis, J. *Surf. Sci. Rep.* **2016**, *71* (4), 595–671.

(55) Lercher, J. A.; Grijndling, C.; Eder-Mirth, G. *Catal. Today* **1996**, *27*, 353–376.

(56) Lavalley, J. C. *Catal. Today* **1996**, *27*, 377–401.

(57) Vimont, A.; Thibault-Starzyk, F.; Daturi, M. *Chem. Soc. Rev.* **2010**, *39* (12), 4928–4950.

(58) Busch, O. M.; Brijoux, W.; Thomson, S.; Schüth, F. *J. Catal.* **2004**, *222* (1), 174–179.

(59) DeWilde, J. F.; Chiang, H.; Hickman, D. A.; Ho, C. R.; Bhan, A. *ACS Catal.* **2013**, *3* (4), 798–807.

(60) Da Ros, S.; Jones, M. D.; Mattia, D.; Pinto, J. C.; Schwaab, M.; Noronha, F. B.; Kondrat, S. A.; Clarke, T. C.; Taylor, S. H. *ChemCatChem* **2016**, *8*, 1–12.

(61) Joshi, S.; Kalyanasundaram, S.; Balasubramanian, V. *Appl. Spectrosc.* **2013**, *67* (8), 841–845.

(62) Kim, J.-W.; Lee, H.-G. *Metall. Mater. Trans. B* **2001**, *32* (1), 17–24.

(63) Echterhoff, R.; Knözinger, E. *J. Mol. Struct.* **1988**, *174*, 343–350.

(64) Echterhoff, R.; Knözinger, E. *Surf. Sci.* **1990**, *230* (1), 237–244.

(65) Angelici, C.; Meirer, F.; van der Eerden, A. M. J.; Schaink, H. L.; Goryachev, A.; Hofmann, J. P.; Hensen, E. J. M.; Weckhuysen, B. M.; Bruijnincx, P. C. A. *ACS Catal.* **2015**, *5* (10), 6005–6015.

Chapter 6

Role of transition metal promoters (Cu, Zn) on MgO/SiO_2 catalyst for Lebedev reaction

Abstract

Electronic structure and reactivity of Cu- and Zn-promoted wet kneaded MgO/SiO_2 catalysts was interrogated during ethanol reaction to 1,3-BD. A multimodal nature of characterization, including *in situ* or *operando* X-ray, electron, light spectroscopies and steady state reactivity measurements demonstrated critical new information on the temporal evolution of the catalyst active sites including key measurements performed *operando* using synchrotron source (EXAFS and XANES). *In situ* DRIFT spectroscopy allowed to decouple the aldol condensation and dehydrogenation reactive steps due to the promotion with enhanced ability to carry out aldol condensation, as correlated with the steady state reactivity experiments. . *In situ* UV-Vis spectroscopy presented a complex picture of the adsorbates with π- π^* electronic transitions due to the allylic cations, cyclic or aromatic species while also suggesting oligomeric CuO species were formed. *Operando* X-ray measurements combined with *ab initio* multiple scattering modelling performed as a function of temperature identified a new transient intermediate assigned to a 4-fold coordinate Cu species that was key leading to increase in Cu-Cu bond number. For the first time, two types of Zn bonds, namely Zn-O and Zn-Mg, were identified during X-ray analysis under operating conditions. With Zn nearly 6-coordinated when in the vicinity of Mg while Zn-O species coordinated to nearly 4 nearest neighbors. The data suggest that such supported catalyst deactivation might proceed not only via carbon coking mechanism but also through the dispersed Cu site diffusion and growth due to the nearest neighbor oxygen atoms loss. The results presented suggest intermediates for segregation/deactivation mechanisms for a broader set of supported Cu and Zn catalysts used for alcohol upgrading catalytic reactions.

1. Introduction

Catalytic conversion of ethanol to 1,3-butadiene (1,3-BD) is a promising green and renewable route for obtaining a commodity chemical that does not utilize a conventional petroleum-based feedstock.[1] The feedstock and technological process landscape in 1,3-BD production is undergoing changes due to the distinct industry shift from oil to C_4 hydrocarbon lean shale gas.[2] To this regard, ethanol is a very interesting *platform* molecule due to its steadily increasing production from biomass.[1] Two classes of catalysts have been used for ethanol conversion to 1,3-BD, namely ZrO_2-based and MgO/SiO_2-based (Lebedev catalyst).[3] The former have thoroughly been investigated using a combination of computational and spectroscopic methods[4,5] while the latter lack suitable spectroscopic characterization.[3] The overall reaction mechanism on MgO/SiO_2 is currently debated[3,6–8] and several recent attempts have been made to elucidate it.[6,9–12] These studies pointed towards aldol condensation as the most energetically favorable C-C bond formation mechanism, except for Chieregato *et al*. who suggested that C-C bond was formed via interaction of ethanol/acetaldehyde through a stable carbanion intermediate.[9] The latter mechanism was suggested to take place on pure, basic MgO sites based on a combination of infrared spectroscopy and theoretical DFT results.[9] The rate-determining step was found to be ethanol dehydrogenation[6,11] since an efficient dehydrogenating site was not present in MgO/SiO_2 catalysts. This suggests that an effective catalyst must possess multifunctional, i.e. acidic, basic and redox sites. MgO/SiO_2 catalysts are promoted with transition metal (oxides) to improve their dehydrogenation capability[2,13–17] where the choice of transition metal used as a promoter is determined by its dehydrogenation capability.[18–20] Au,[21,22] Ag,[23,24] and Cu[25,26] have been utilized to enhance the 1,3-BD yield.[2,27,28] Zn is another promoter that has been utilized to improve the yield of 1,3-BD.[13,15,29–31] The promotional effect was reported to originate from the improved availability of both Lewis acid sites and redox sites.[3,15] While Au and Ag promoters present economic constraints due to their high costs, Cu and Zn are relatively inexpensive and present an alternative for an efficient catalyst design. The work reported here provides new insights on the structure and reactivity of these sites under operating conditions.

Several theoretical and ultra-high vacuum (UHV) studies have been conducted on Cu-based catalysts to determine the structure of the active sites[32–39] but very few under operating conditions. UHV characterization and DFT revealed formation of isolated or clustered Cu^0 phases on the MgO surface[32,33] or a solid solution that contains Cu-Mg and Cu-O-Mg bonds.[34] For instance, on a perfect MgO (100) surface, DFT calculations showed that a single Cu adatom prefers to bond with a surface O atom with the possibility to spillover Cu.[32,33] Various cluster sizes of Cu (dimers, trimers, and tetramers) were observed depending on the surface coverage.[32] The formation of reduced Cu clusters on the surface was confirmed by Colonna *et al.* where Cu clusters, as evident by Cu-Cu bond length (2.55 Å), were observed as a thin layer on MgO using XANES during the UHV evaporation-deposition synthesis.[35] In a separate study, in addition to the observed Cu atoms on the MgO surface, both UHV XANES and DFT identified the formation of a solid solution between Cu and MgO that decreased the reactivity of the catalyst toward H_2S and SO_2 decomposition when compared to the supported Cu atom.[36,37] Larger charge transfer resulting in a strong ionic bond was observed when Cu was coordinated next to a defective MgO surface.[38,39] This shorter bond was due to the electron stabilization provided by the Cu atom.[38,39] UHV XANES of several transition metal-promoted MgO catalysts utilized for CH_3OH and RCH_2Z (where R=H and CH_3, Z=CN, COR', and COOR") coupling reactions confirmed the formation of Cu-MgO solid solution at 80 K and suggested that an octahedral coordination of the Cu species due to the pre-edge peak associated with 1s→3d transition was very small. This observation was accompanied by the extended X-ray absorption fine structure (EXAFS) analysis of the Cu-O and Cu-Mg atomic distances, 2.01 Å and 2.98 Å respectively, suggesting the formation of solid solution between Cu and MgO. Interestingly, all promoted MgO catalysts that showed worse catalytic activity toward the coupling reaction of CH_3OH and RCH_2Z (R=H and CH_3, Z=CN, COR', and COOR") were those that formed a solid solution with MgO.[34] Applicable to this study is *in-situ (operando)* characterization of a Cu-promoted catalyst for relevant alcohol reactions, such as methanol formation from syngas,[40] ethyl acetate production from ethanol[41] and ethanol steam reforming.[42] Cu-containing ternary oxide catalysts, e.g. Cu/ZrO-SiO_2, $CuMgAlO_x$ and Cu/MgO-SiO_2, were utilized for these and were well characterized.[28,43,44] *Operando* and *in-situ* characterization of these supported catalysts showed that Cu species could be present as both Cu^{2+} ions and CuO - the latter exhibiting lower-strength interaction with the SiO_2 support,[25,26] as a solid solution in the case of Cu-MgO/SiO_2[28] and Cu/ZnO/Al_2O_3,[45] as dimeric structures in the case of CuMgAl hydrotalcite catalysts[44] or as reduced species as in the case for $CuCrO_x$ and $CuZrSiO_x$ catalysts.[43,46] This suggests variety of active copper sites can be present under operating conditions[28,43–45] but very few studies, notably Angelici *et al.*,[26,28] attempted to decouple their reactivity during 1,3-BD formation or investigate the temperature effect on Cu site composition under reactive conditions.[28] ZnO/SiO_2 has been used as a model catalyst for many reactions, such as water-gas shift and methanol formation reaction,[47] but X-ray based catalytic site characterization during ethanol-to-1,3-BD are not existent to the best of our knowledge.[13,15,16] *In-situ* XAS and UV-Vis of this catalyst further showed the relevance of the precursor drying steps during the synthesis and that Zn was present both as a silicate (hemimorpite) and ZnO bulk phase at 10% Zn loading.[47] Ambient UV-Vis and TEM studies of a 1% ZnO/MgO catalyst demonstrated the formation of a highly-dispersed ZnO layer which had high activity for CO oxidation, affected by the quantum-confinement effect.[48]

In this work, we performed a comprehensive characterization on both Cu- and Zn-promoted MgO/SiO_2 catalysts. Details on the acid-base sites upon promotion with Cu and Zn, implications for the reaction mechanisms, as well as thorough infrared, UV-vis, electron and X-ray-based analysis of Cu and Zn local structure before, after, and during the reaction was elucidated. Complementary, if not contradictory, conclusions were reached for Cu-promoted MgO/SiO_2 to those available in the literature[28] while completely new X-ray data insights were obtained for Zn-promoted MgO/SiO_2 catalysts under operating conditions.

2. Computational results

2. 1. Model catalyst selection and analysis

Plenty literature of Cu-doped MgO catalysts characterization is available, both on computational and experimental studies. DFT calculation of small Cu cluster supported on a perfect MgO (100) surface revealed that for a single Cu adatom, the preferential adsorption site was on top of an O atom, whereas adsorption on a hollow site represented a saddle point for Cu spillover.[32,33] For a dimer Cu, there were two minimum states available with close optimized energies, parallel and linearly perpendicular to the surface. Two states were observed for the first case; one configuration where the dimer bond is 2.25 Å (stretched from 2.25 Å in its free form), and another one where the bond length is stretched even further, 2.34 Å. The linearly perpendicular states, however, had the single adatoms's Cu-O bond length, and free dimer's Cu-Cu bond length. Trimer Cu and tetramer Cu clusters preferred linear and rhombus geometry, respectively.[32] Cu/MgO DFT model had been used by Jose Rodriguez and coworkers.[36,37] When Cu was embedded into the surface, substituting an Mg atom with lower coordination, the catalyst was less reactive compared to when the Cu atom was adsorbed freely on the surface. When a SH or S molecule was adsorbed on the embedded Cu atom, the interaction was so strong that it pulled the Cu atom out of the surface plane.[36,37]

A significantly larger charge transfer was observed by Zhukovskii *et al.* and Matveev *et al.* when the metal was adsorbed on a defective MgO surface, meaning that the bonding was more ionic than that on the perfect surface.[38,39] The distance between Cu atom and the surface had decreased as well, from ~2 Å to 1.62 Å. This stronger bonding originated to the lower coordination atom, which would behave more like ions due to the lack of electronic relaxation. The defect sites used here are both Fs and Fs^+ sites, where an oxygen atom was removed from a perfect surface, along with a number of electrons accordingly to create the oxygen vacancy.

Experimental data carried out by Asakura and Iwasawa provided a different insight.[34] On a doped MgO catalyst, prepared using wet impregnation method, XANES spectra suggested an octahedral coordination for Cu^+ ions, deduced from the fact that the pre-edge peak of the spectra which was assigned to the 1s-3d transition was very small. The EXAFS spectra for Cu^+ ion, revealed that the M-O and M-Mg distances were observed to be 0.201 nm and 0.298 nm, respectively, away from the lattice constant of MgO, which further suggested that the Cu^+ ion would substitute an Mg site, i.e. supplanted into the lattice.[34] Colonna *et al.*[35], however, failed to replicate the XAS experiments when the surface was prepared using ion evaporation-deposition method in an UHV chamber. On monolayer coverage, the EXAFS data evidenced a Cu-Cu distance close to that of the bulk metal, due to the weak film-substrate interaction. Copper was also observed to be in its reduced state, and further, XANES spectrum showed a coordination number similar to the bulk value, indicating that the Cu^+ ions grew as a cluster on the MgO substrate.[35] Different preparation led to different geometry, as observed by Pascual *et al.*, which carried out X-ray measurement on Cu-doped MgO using arc fusion method, where MgO was melted before the dopant is mixed as CuO.[49] Both EXAFS and *Ab initio* calculation showed that the crystal is in D_{4h} geometry, associated with a compression of the original octahedron along the z-axis, indicating that the ions substituted Mg sites in the lattice.

Although the literature on Cu/MgO catalysts is very well-established, very limited study is available on promoted MgO/SiO_2 catalyst. Complications on how Cu would be added to the catalyst were brought upon by the presence of a second support material, i.e. SiO_2[28] or Al_2O_3[50]. The Cu could be present either as a surface species on SiO_2, as in the case of Cu/SiO_2 catalysts[28], or as a substitutional dopant, replacing Mg as in the case of the Cu/MgO catalysts. MgO/SiO_2, the Lebedev catalyst, was studied by Angelici *et al.*[28] Ex-situ XANES, EXAFS, FTIR, XRD, TEM, XPS, and UV-Vis showed that Cu species were not in planar geometry and were suggested to be located at crystal lattice sites. Formation of small $(CuO)_x$ clusters on MgO-containing materials was also advocated experimentally. XANES and EXAFS had also demonstrated the octahedral coordination of CuO and Cu-Mg bond distance of 0.298-0.302 nm, similar to the Mg-Mg distance in periclase phase.[28] Hydrotalcites ($Mg_xAl_yO_z$) were another class of catalysts that were routinely studied for ethanol upgrading. High resolution NMR study of Cu-promoted $Mg_xAl_yO_z$ was extensively studied and revealed that on low loading, Cu preferentially substituted for lattice Mg in the hydrotalcite structure, while at higher Cu content, the transition metal was also present on the surface as a bulk oxide.[50]

Studiy on the routinely used ZnO/SiO_2 catalysts showed that zinc was mostly present as Zn silicates in addition to small amount of ZnO bulk phase on the surface.[47] Extensive characterization of the catalyst was carried out with XAS, DRIFTS, and UV-Vis. Depending on the drying temperature, the small amount of bulk ZnO phase was formed on top of the catalyst after calcination. The calcination mostly resulted in the formation of Zn-silicate, hemimorphite in particular.[47] However, when MgO was added to the catalyst, i.e. Zn-doped Lebedev catalyst, more possibilities are now available, including the substitutional doping of Mg by Zn, formation of ZnO bulk phase on either MgO or SiO2, surface species formation on either support material, or preferential formation of Zn-silicate. Colloidal suspension synthesis method of 1% ZnO/MgO was shown to result in a very highly dispersed ZnO layer on top of MgO support, as confirmed by UV-Vis and TEM.[48] However, the catalyst synthesized in this study did not show the characteristic ZnO band gap and *operando* XANES-EXAFS characterization of the catalyst suggested that the local structure environment is very similar to Cu, indicating interaction with MgO, instead of SiO_2, resulting in a solid solution (*vide infra*). Hence, the model selection for both catalysts was chosen to be CuMgO and ZnMgO, with both transition metals to substitutionally dope an Mg atom. These models serve as a first approximation to the catalysts' model, simplifying the SiO_2 support effects, further eliminating the contribution of Mg-O-Si linkages and the accompanying hydroxyl groups.

Table 6.1 Different configurations tested for Zn(Cu)/MgO model catalysts. Various dopant location was chosen between the top and second layer, and compared for energy and Bader charge.

Scheme	Configuration	Dopant location	Cu-doped		Zn-doped	
			Energy (eV)	Bader Charge	Energy (eV)	Bader Charge
Cu(Zn)-1	Cu^{3C}-top layer	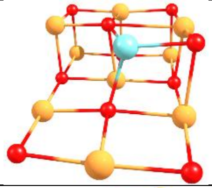	-659.48 (0.00)	0.72	-658.64 (0.00)	1.05
Cu(Zn)-2	Cu^{5C}-top layer	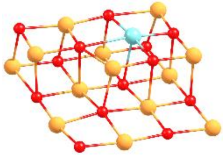	-659.28 (0.20)	0.82	-658.42 (0.22)	1.05
Cu(Zn)-3	Cu^{4C}-top layer	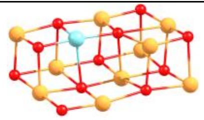	-659.22 (0.27)	0.82	-658.44 (0.20)	1.09
Cu(Zn)-4	Cu^{5C}-second layer	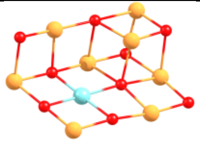	-658.97 (0.51)	0.94	-658.15 (0.49)	1.16
Cu(Zn)-5	Cu^{5C}-second layer	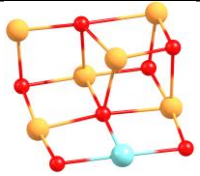	-658.89 (0.60)	0.92	-658.10 (0.54)	1.08
Cu(Zn)-6	Cu^{4C}-top layer	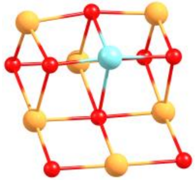	-659.13 (0.36)	0.81	-658.37 (0.27)	1.05
Cu(Zn)-7	Cu^{4C}-top layer	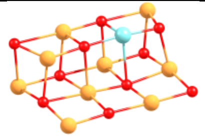	-659.45 (0.04)	0.91	-658.52 (0.12)	1.08
Cu(Zn)-8	Cu^{5C}-second layer	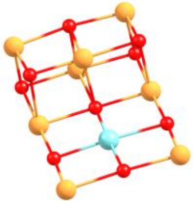	-658.83 (0.65)	0.92	-658.09 (0.55)	1.08

Cu(Zn)-9	Cu^{5C}-second layer	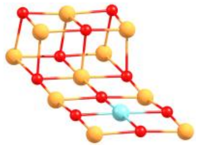	-658.73 (0.75)	0.96	-658.03 (0.61)	1.13
Cu(Zn)-10	Cu^{5C}-second layer	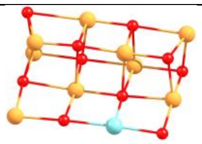	-658.75 (0.73)	0.93	-658.08 (0.57)	1.15

Table 6.1 shows the permutations tried for both dopants, i.e. Cu and Zn. The original kink model from Chapter 3 was used and modified with dopants substitutionally dope the catalyst's surface at different Mg atom locations. From all of the tried models, Cu (Zn)-1 possesses the lowest electronic energy. The Bader charge for the transition metal atom for each configuration was also calculated, with charge values of +0.72 and +1.05 for Cu and Zn. To discuss the effects of both Cu and Zn on the MgO model catalysts, Bader charges of the neighboring atoms were calculated as well and compared to the undoped MgO catalyst, shown in Figure 6.1.

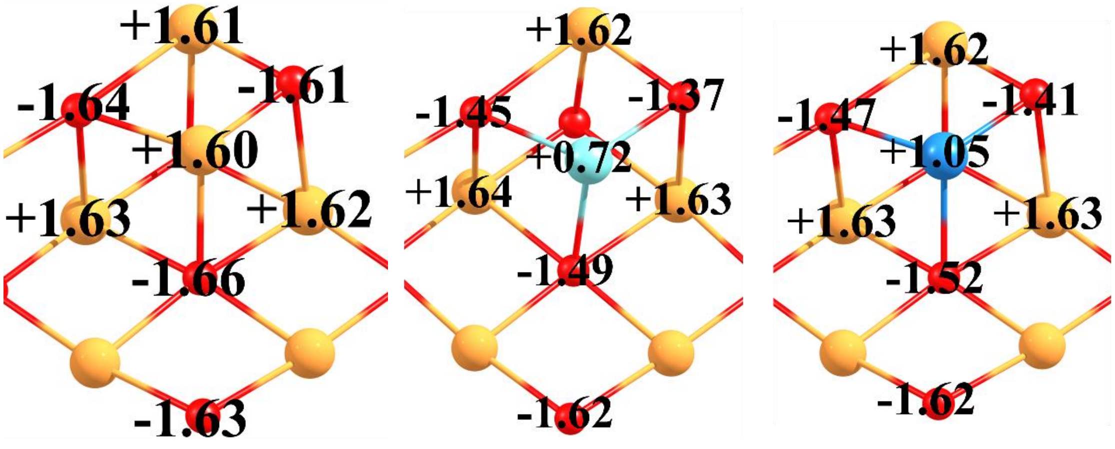

(a) (b) (c)

Figure 6.1. Local structure analysis of (a)MgO, (b)Cu-MgO, and (c)Zn-MgO. The Bader atomic charge on each atom is indicated by the boldfaced numbers.

The oxygen atoms neighboring both transition metals exhibited less negative charges than that of unpromoted MgO, with total charges of the 3 O atoms amounting to -4.91, -4.31, and -4.4 *e* for MgO, Cu-MgO, and Zn-MgO, respectively. The decreased atomic charges of O atoms neighboring the corner atoms indicates that the introduction of both transition metal atoms had lowered the basicity of the O atoms. The lowered basicity of the oxygen atoms neighboring the transition metal atoms was also observed both computationally and experimentally using XPS on Zn-promoted talc by Baba's group.[13] The neighboring Mg atoms and other oxygen atoms that are distanced from the transition metal dopants did not show any difference from the pristine MgO, which suggests that this lowered basicity effect is very localized, and hence calculation should be focused on this region.

The atomic charges observed for both Cu and Zn atoms are similar to what was previously observed on CuO[51] and ZnO[52] surfaces. Bader charges for CuO and ZnO are typically +0.57 – +0.84 and +1.13 – +1.20, respectively.[51,52] The very positive atomic charges for both means that these transition metal atoms are almost fully ionized in these model catalysts. The lowered atomic charges of both Cu and Zn from the ionized Cu^{+1} and Zn^{+2} are due to the charge transfer from the neighboring O atom. For Zn, the charge transfer is very straightforward, since both Mg and Zn possess +2*e* charge. The charge transfer for the corner Mg (Zn) from clean MgO (Zn-MgO) surface is equal to the difference between the Bader charge value and the charge of isolated Mg (Zn). These values are 0.4*e* and 0.95*e* for Mg and Zn, respectively. The difference of this value is equal to the difference of the summed charges on the neighboring O atoms between MgO and Zn-MgO, i.e. -4.91 and -4.4. The origin of charge density change is also acknowledged by Baba's group for the case of Zn/talc.[13] For Cu, however, this analysis fell apart, since the atomic charge of Cu is +1*e*, while Mg is +2*e*, and the lowered total charges on neighboring O atoms is different from the difference between Mg and Cu atomic charges.

2. 2. Reactive intermediates

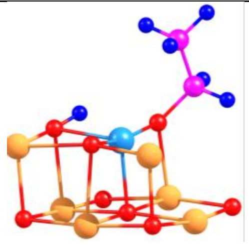	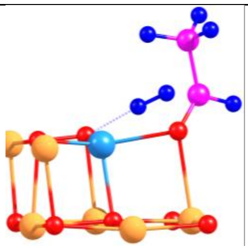	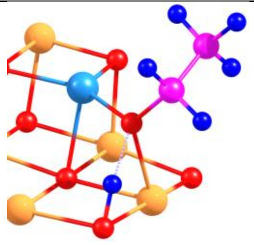	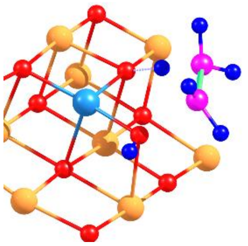
Zn-1A	Zn-1B (TS)	Zn-2A	Zn-2B (TS)
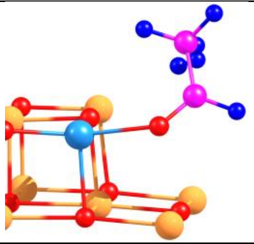		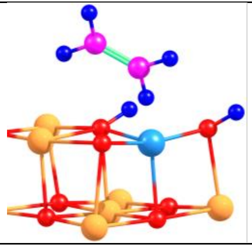	
Zn-1C		Zn-2C	
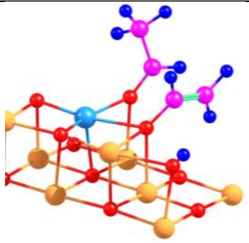	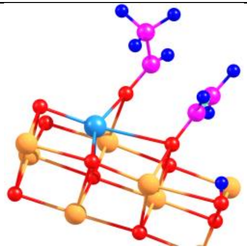	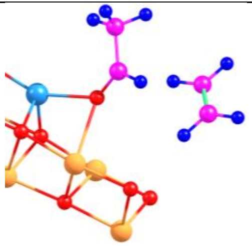	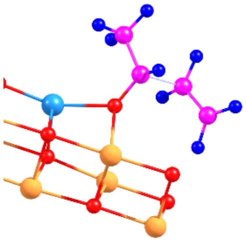
Zn-3A	Zn-3B (TS)	Zn-4A	Zn-4B (TS)
		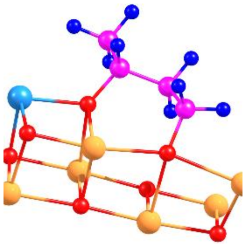	
Zn-3C		Zn-4C	

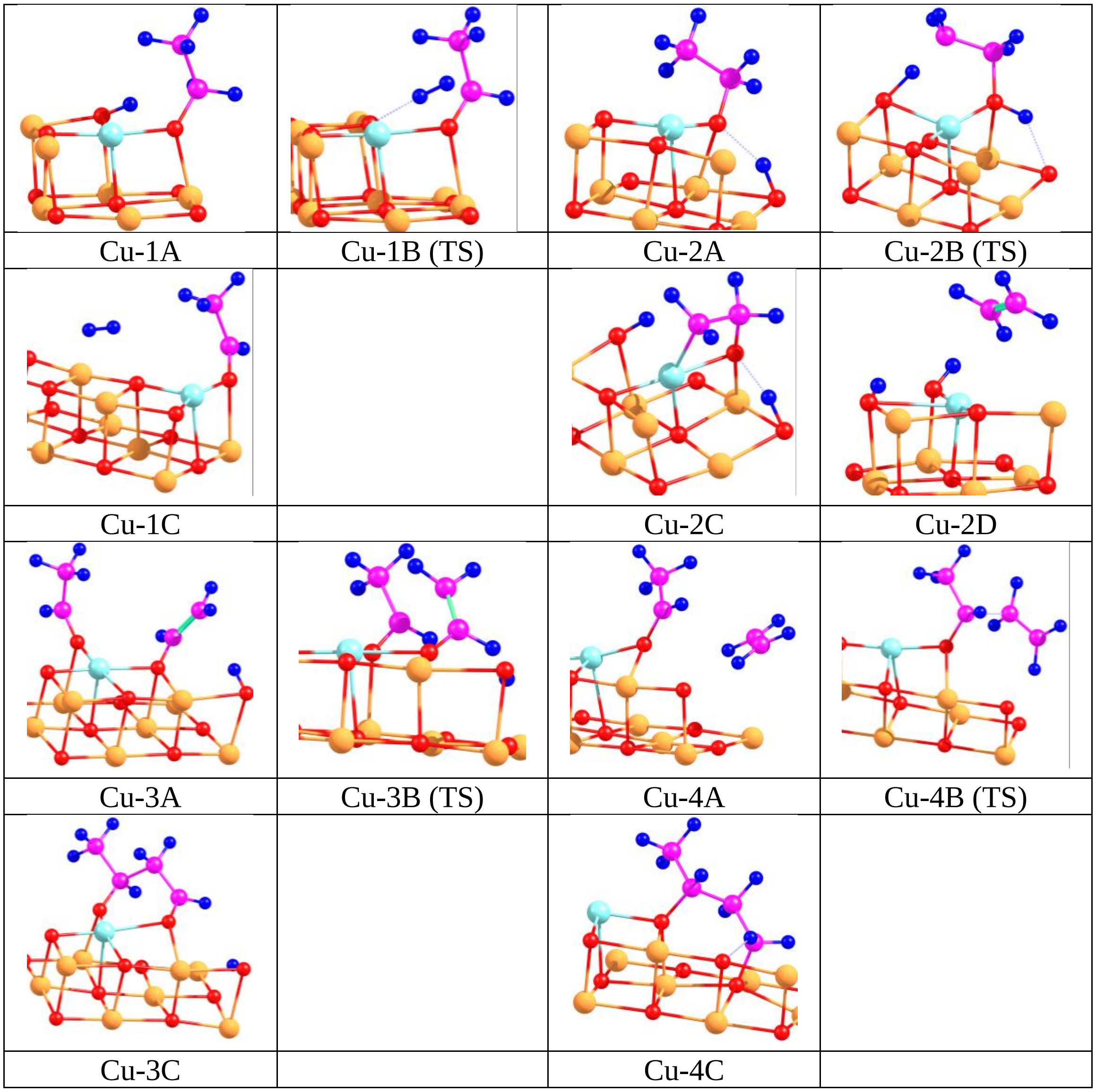

Cu-1A
Cu-1B (TS)
Cu-2A
Cu-2B (TS)
Cu-1C
Cu-2C
Cu-2D
Cu-3A
Cu-3B (TS)
Cu-4A
Cu-4B (TS)
Cu-3C
Cu-4C

Figure 6.2. All stable intermediates and transition states calculated following the reaction pathways. (1A-1C): ethanol dehydrogenation to acetaldehyde; (2A-2C): ethanol dehydration to ethylene; (3A-3C): C-C bond formation step in acetaldehyde aldol condensation to 3-hydroxybutanal (acetaldol); (4A-4C): C-C bond formation step in Prins condensation of acetaldehyde and ethylene. Calculations are carried over Zn/MgO model catalysts (prefix: Zn), and Cu/MgO model catalysts (prefix: Cu).

All optimized structures, including maxima and minima, are shown in Figure 6.2, while the corresponding electronic energies and Gibbs corrected free energies were tabulated in Table 6.2. The structures were optimized on the model Zn and Cu-doped MgO catalysts. To produce a comparable result, the optimization was done on the same site, i.e. corner Zn (Cu) atoms and the neighboring O atoms. The reaction steps that were studied are the key steps in both Prins and aldol mechanisms, i.e. dehydrogenation, dehydration, and C-C bond formation of both aldol and Prins condensation pathways.

Table 6.2. Referenced electronic and corrected Gibbs free energy for each species over MgO, Cu/MgO, and Zn/MgO catalysts.

Species	**MgO**		**Cu/MgO**		**Zn/MgO**	
	E (kcal/mol)	**G (kcal/mol)**	**E (kcal/mol)**	**G (kcal/mol)**	**E (kcal/mol)**	**G (kcal/mol)**
1a	-40.6	-13.50	-37.33	-18.72	-35.75	-8.10
1b	3.9	26.20	14.33	32.12	12.36	36.23
1c	-16.6	5.60	6.03	14.22	4.93	18.59
2a	-39.9	-10.50	-25.66	-1.96	-31.45	-4.30
2b	-2.6	23.00	4.97	21.48	5.99	31.54
2c	-32	-15.30	-26.19	-1.65	-26.45	-8.22
3a	-22.5	-23.70	-5.40	-14.32	-4.41	-4.21
3b	-15.9	-7.60	3.07	3.22	-4.24	0.75
3c	-19.4	-10.80	-2.89	-2.45	-8.72	-3.51
4a	11.6	-0.20	21.13	7.78	21.65	13.80
4b	25.6	28.60	34.17	31.13	33.81	35.49
4c	-34.8	-22.90	-0.31	9.29	-27.25	-15.61

For the dehydrogenation step, the intermediates are shown by Cu(Zn)-1A to 1C. On all MgO, Cu-MgO, and Zn-MgO, ethanol undergoes spontaneous dissociation to give surface ethoxide and a hydroxyl group. There was no visible difference from the model, and the electronic energies are not significantly different, i.e. ~35-40 kcal/mol. The Gibbs corrected free energies, however, are very different with Cu-1a is now the most stable species and Zn-1a being the least. The transition state for the dehydrogenation reaction did look very similar to the optimized structure on bare MgO catalyst (Chapter 3); the H-H and H-lattice O_{4C} distances are all of similar values.[6] The energetic values, however, differ a lot from the bare MgO, ~6-10 kcal/mol higher than the transition state found for the bare MgO. The very high values for both electronic and Gibbs' corrected energies indicate that these structures are very unstable. This observation is followed as well with the final state of the reaction, i.e. the adsorbed acetaldehyde and hydrogen as a product of the reaction when hydrogen is fully formed.

Ethylene production is an unwanted side reaction that accompanies 1,3-BD reaction pathway, and was even linked to as a reactive intermediate in the Prins mechanism.[53] Over MgO catalyst, ethanol to dehydration possessed lower activation energy than dehydrogenation, which confirms the experimental evidence.[6] Over Zn(Cu)-MgO, the initial state of this reaction, i.e. ethanol chemisorption, is very similar to the state observed on MgO catalyst. Common structural parameters, such as the supposedly elongated C-O bond, Cu(Zn) distance from the ethoxide O atom, and the bonding between O and planar Mg_{5C} are very similar to those in the bare MgO catalyst. Energetically, these intermediates are much less stable than the MgO-bound species, differing ~8-10 kcal/mol. These instabilities were also observed in the transition state and the final state of the reaction. Cu-MgO, in particular, exhibits a very high degree of affinity toward the ethylene product, as shown by the stabilized carbanion in Cu-2C. This intermediate then undergoes a C-Cu bond breaking transition step (not optimized here) to give off ethylene as the final product, i.e. Cu-2D. Cu-2D possessed referenced electronic energy of -27.54 kcal/mol, only 1 kcal/mol more stable than Cu-2C.

Probably the most debatable step in the reaction mechanism is the C-C bond formation. Aldol condensation had been widely accepted as the most possible mechanism, and we optimized all the transition states over the doped model catalysts, following the calculated structure over bare MgO.[6] Over the doped catalysts, the intermediates, i.e. minima, are all less stable than that on MgO. The stability achieved by the system when two acetaldehyde molecules are coadsorbed, i.e. initial state, on the surface is not replicated well on the doped MgO. Surprisingly, the activation energy of this step is much lower for Zn-MgO than Cu-MgO and bare MgO (discussed in detailed manner in Section 2.3). The viability of Prins mechanism again is questioned computationally. On all the optimized structures, similar activation energies were observed, i.e. ~21-29 kcal/mol. The computational method also favors the reaction step thermodynamically, with all catalysts giving exergonic reaction for the Prins step. This Prins mechanism, however, should be treated carefully, since experimental evidence pointed out that ethylene formation is very exclusive from 1,3-BD formation (Chapter 5).

2. 3. Potential energy surfaces

The potential energy surfaces for all computed reaction steps are presented in **Figure 6.3** and **6.4**, while the activation barriers and Gibbs' free energies of reactions are tabulated in **Table 6.3**. Based on our calculation, promotion with transition metals, i.e. Cu and Zn, did not achieve the intended lowered activation energy of ethanol dehydrogenation. Rather, these activation barrier increased for the case of Zn and Cu to 44.33 and 50.84 kcal/mol, respectively. For dehydration, dehydration activation energies are consistent with bare MgO, with similar values attained, especially for Zn-MgO. With the presented activation energies for both C2 reactions, i.e. dehydrogenation and dehydration, the reaction mixture at low temperature, will mostly consist of ethylene, instead of acetaldehyde, for all catalysts.

Table 6.3 Activation energy and thermodynamics consideration for key steps during ethanol conversion to 1,3-butadiene over MgO, Zn/MgO, and Cu/MgO catalysts.

Reaction steps	**ΔG_A (kcal/mol)**			**ΔG_{Rx} (kcal/mol)**		
	MgO	**Zn/MgO**	**Cu/MgO**	**MgO**	**Zn/MgO**	**Cu/MgO**
Dehydrogenation	39.60	44.33	50.84	24.61	26.68	32.94
Dehydration	33.47	35.84	23.44	-4.87	-3.92	0.31
Aldol C-C	16.10	4.96	17.55	19.07	0.70	11.87
Prins C-C	28.75	21.69	26.39	-22.74	-29.42	-1.87

Very surprisingly, aldol condensation is much more favorable over Zn-MgO, with the very low activation energy, as well as the lowered Gibbs' free energy of reaction value of 0.70 kcal/mol, which is almost aergonic. This lowered energetic barrier might be due to the duality of Zn, which presents as both redox site and as a Lewis acid site, which supposedly boost both dehydrogenation and aldol condensation step during the reaction.[3] Another unexpected observation is that of Prins mechanism, which continues to show viability computationally. Although this step does not have experimental ground, the theoretical calculation shows that this step is very feasible. According to our calculation, this step and ethanol dehydration are the two steps that have net positive rate constant (Chapter 3).[6] However, the calculation was carried out over model MgO catalyst, without considering the presence of SiO_2 and OH groups, therefore eliminating the other possible sites, such as the open and closed Lewis acid sites of Mg-O(H)-Mg and Mg-O(H)-Si, which were shown to actively catalyze the whole reaction steps (Chapter 5).[54]

The non-existence of hydroxyl groups in this idealistic model leads to very strong Lewis acid-base pairs, which is accentuated by the electron-deficient sites such as kink, corners, and edges. These highly unstable sites are typically stabilized by hydroxyl groups, and leads to softer acid-base pairs, due to the more distributed electron density.

Experimentally, the ethanol dehydrogenation step requires a weak basic site on the catalyst, as shown by the CO_2 and propionic acid cofeeding experiments, *in-situ* titration with CO_2 and pyridine, which is also supported by previous investigation.[2] The strong acid-base pairs used throughout the calculation inevitably stabilize electron rich or deficient structures, exhibited by the stabilized ethylene-acetaldehyde transition state that leads to the formation of a C4 oxygenate.[6] Furthermore, the proton abstraction steps that follow resulted in a carbanion, which is stabilized by the presence of corner Mg_{3C}^{2+}, which is undoubtedly a very strong electron acceptor.[6]

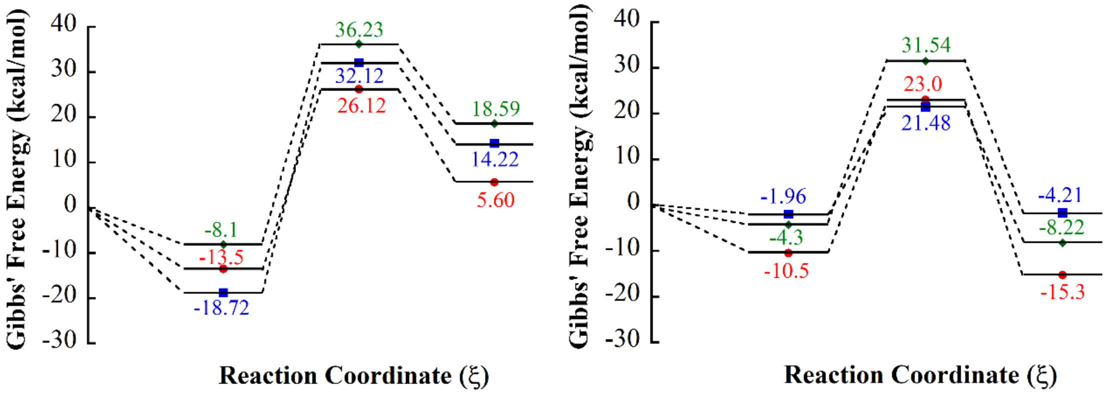

(a) (b)

Figure 6.3. Potential energy surface for ethanol (a)dehydrogenation and (b)dehydration over MgO, Zn/MgO, and Cu/MgO catalysts. (●)MgO, (■) Cu-MgO, (♦) Zn-MgO.

Another concerning discrepancy with experimental results are the dehydrogenation step. The reaction mechanism is widely believed to be dictated by ethanol dehydrogenation. The subsequent aldol condensation, dehydration, and MPV reduction steps were shown to be facile and spontaneous on unpromoted MgO/SiO_2 catalysts.[11] Promotion with Cu[14] and Zn,[15] among other transition metals,[2,16,27] are intended to lower the ethanol dehydrogenation step and to shift the rate-limiting step to MPV reduction step, which is already considerably fast. The calculated activation energies for this step on the Cu-MgO and Zn-MgO are, however, very similar to the bare MgO catalyst. On Cu-MgO, the activation energy is even ~10 kcal/mol more than the bare MgO. There are two possible sources of disagreement that is inherent to the model selection and the calculation nature. DFT calculations on transition metals, especially first row transition metals such as Cu and Zn, have to be treated carefully. Different DFT functionals had led to large variations in energies, of 20 kcal/mol or more.[55] The pure DFT functional used in this calculation (PBE) is known to overestimate the stability of low-spin forms. Improvement is usually achieved by including HF exact exchange, in expense of the prohibitively expensive calculation time, especially in the large system used for this study.[55] The assumption that the whole reaction steps are carried out on one site is oversimplification of this complex system. While this might be true on bare MgO, dehydrogenation over transition metal-promoted typically occurred on an isolated transition metal sites,[2,13,28] and the subsequent steps are over the Mg-O(H)-Si or Mg-O(H)-Mg, which will be shown in the next sections.

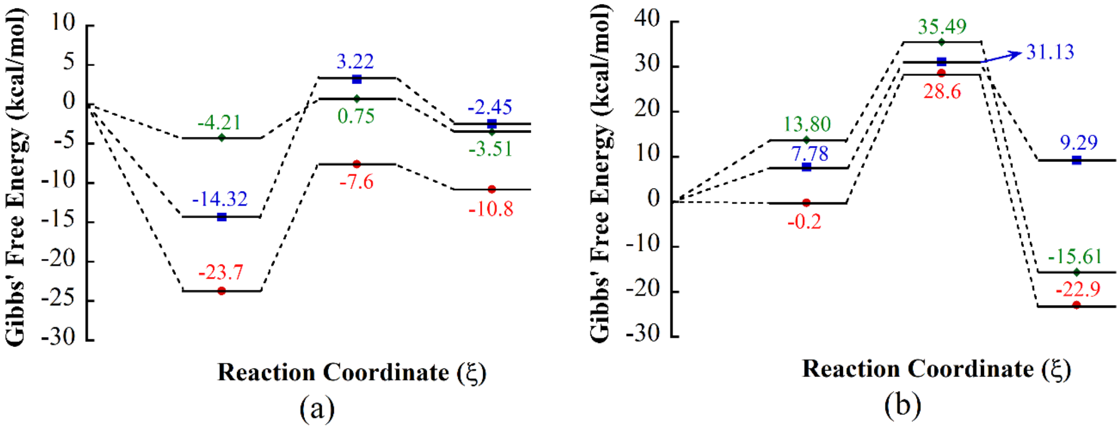

Figure 6.4. Potential energy surface for first C-C bond formation via (a) acetaldehyde aldol condensation and (b) Prins reaction between acetaldehyde and ethylene over MgO, Zn/MgO, and Cu/MgO catalysts.

3. Experimental results

3. 1 Catalyst characterization

The transition metal content in each catalyst was determined using both ICP-OES and XPS to infer bulk and surface concentration, respectively. Interesting agreement was found between the two characterization methods with ICP-OES determined Cu and Zn content of 0.8 % and 2.5 % virtually agreeing with those determined by XPS of 0.9 % and 2.7 % for each catalyst. These Zn and Cu concentrations are close to the intended high selectivity loading.[14,15] The starting support material, i.e. wet-kneaded MgO/SiO_2, possessed surface area of 120 m^2/g which was much lower than the fumed SiO_2 used (332 m^2/g). This lowering of the surface area has previously been observed by several other groups[14,27] and explained by the dispersion of low surface area MgO over SiO_2. Promoting the MgO/SiO_2 samples with transition metals led to the increase in the surface area. Zn and Cu-promoted samples exhibited surface area of 135 and 191 m^2/g, respectively. This significant enhancement of the catalyst surface area was not observed by Janssens *et al.*[27] Rather, Ag-promoted samples were shown to considerably lower the surface area of their calcined mesoporous support while in this study we used uncalcined hydroxide precursor. This increase in surface area was likely due to the impregnation step which was done before the support was calcined. The effect of calcination-impregnation order has previously been observed by Da Ros *et al.* with ZrZn-promoted MgO/SiO_2 catalysts.[16] This suggests that the metal promoters deposited via impregnation might act also as textural promoters, in addition to being electronic promoters.

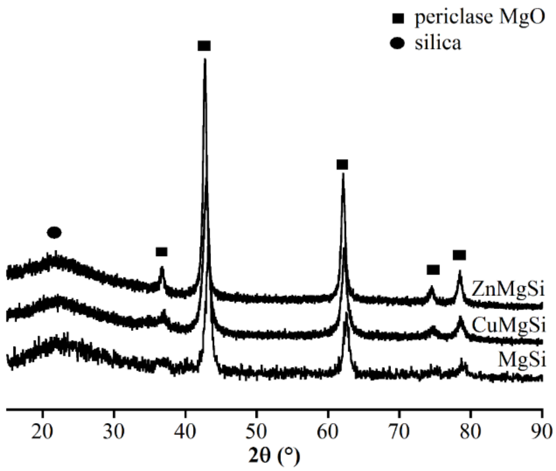

Figure 6.5. Comparison of XRD patterns between CuMgSi, ZnMgSi, and MgSi.

X-ray diffraction (XRD) pattern of the two promoted catalysts – CuMgSi and ZnMgSi – acquired under ambient conditions are shown in **Figure 6.5** together with the unpromoted MgSi. The unpromoted sample exhibited prominent peaks at 37.4, 43.5, 63, 75 and 79° which were due to the periclase MgO. Amorphous silica was also present in the XRD pattern as evidenced by the broad band in the lower 2θ of 20-30° region. The wet-kneading between MgO and SiO_2 did not produce new bulk crystalline phases in agreement with Angelici *et al.*[54] Magnesium silicate hydrate phase was previously observed by Shylesh *et al.* when MgO/SiO_2 catalyst was synthesized by impregnating Mg precursor on silica.[2] Careful examination on the XRD pattern showed that Zn significantly enhanced the intensity of the MgO peaks suggesting changes in its crystalline structure. For reference, several concentrations of ZnSi and ZnMg were prepared and also analyzed with XRD (**Figure S6.1**). ZnSi showed no new crystalline phases being formed up to 5% loading while ZnMg also revealed no new crystalline phases were formed at loading up to 10%. The Cu-promoted catalyst showed no change when compared to the support itself other than the peak broadening of the MgO periclase structure. However, no new peaks appeared in the Cu-promoted sample as they would appear even at low loading on individual SiO_2-support (**Figure S6.2**).[28] This also showed that Cu promoter was well dispersed on the catalyst surface with no detectable oxide nanoparticle formed on the surface.[28]

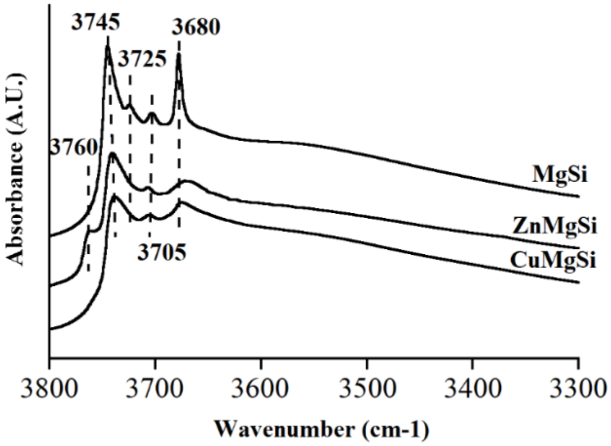

Figure 6.6. *In-situ* dehydrated DRIFTS of OH region of MgSi, CuMgSi, and ZnMgSi. Spectra were taken at 100°C under He flow after pretreatment at 500°C for 1 hour. Spectra were offset for clarity.

Figure 6.6 shows DRIFT spectra for dehydrated metal-promoted catalysts in the OH region, as well as that for the binary catalyst component compounds (ZnSi, ZnMg, CuSi, CuMg). The promoted MgSi catalysts show similar spectral features to the unpromoted MgSi. Detailed assignments of the four native OH groups can be found in the previous work.[11] Briefly, there are four prominent peaks on an MgO/SiO_2 catalyst, i.e. 3745 cm^{-1} assigned to both isolated MgO and silanol groups, 3725 and 3705 cm^{-1} ascribed to Mg-OH-Si with different OH coordination numbers and 3680 cm^{-1} peak assigned to a magnesium silicate species. Promoting the MgSi with Cu or Zn significantly reduced and broadened the native silica and the WK-signature peaks, i.e. isolated silanol at 3745 cm^{-1} and Mg-O(H)-Si group at 3680 cm^{-1}. This suggests that both transition metal promoters, Cu and Zn, interact strongly with this OH group as well. Displacement with Zn further results in a new OH site, as shown by the emergence of a peak at 3760 cm^{-1}, which was previously assigned to the isolated hydroxyl group of MgO.[11,56] This highly isolated hydroxyl group might form from broken Mg-O-Si linkages due to the introduction of Zn suggesting Zn interaction with O-Mg.

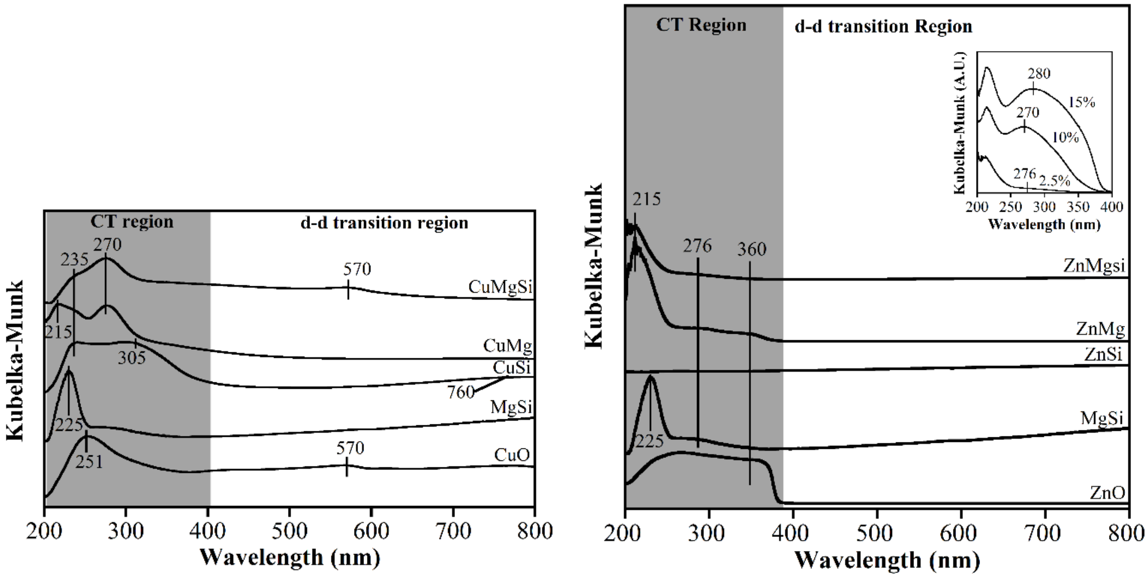

(a) **(b)**

Figure 6.7 *In-situ* UV-Vis DRS spectra of (a) dehydrated CuMgSi catalyst referenced with Cu/MgO (CuMg), Cu/SiO$_2$ (CuSi), CuO, and MgSi; (b) dehydrated ZnMgSi catalyst referenced with Zn/MgO (ZnMg), Zn/SiO$_2$ (ZnSi), ZnO, and MgSi. Inset: UV-Vis spectra of different loadings of Zn on MgO/SiO$_2$ catalysts.

The coordination and oxidation states of the metal promoters are further characterized by *in-situ* UV-Vis DRS under dehydrated conditions. **Figure 6.7a** shows a comparison between the Cu-promoted (CuMgSi) catalyst, MgSi and reference binary materials, such as CuMg, CuSi and bulk CuO. UV-Vis DRS spectra of the bulk CuO is characterized by the presence of a charge transfer (CT) peak at ~251 nm and a peak at 570 nm. The CT peak is assigned to the ligand-to-metal CT (LMCT) from O^{2-} to Cu^{2+} in octahedral coordination.[44] The peak at 570 nm can be assigned to either surface plasmon resonance from Cu^{0} or contributions from d-d transition.[57] Furthermore, a peak at 235 nm is present on all supported Cu samples, while the peak at 270 nm is present only on a Mg-containing support. The former represents LMCT peaks for a very isolated Cu-O species,[28,44] while the latter has been assigned to an oligomeric Cu-O species.[44] Analogously, the peak at 305 nm for CuSi is also assigned to the oligomeric Cu-O species.[28] This reference sample (CuSi, **Figure 6.7a**) also exhibits d-d transition peak at ~760 nm, indicative of Cu^{2+} species in a (distorted) octahedral field.[28] On the other hand, the CuMg reference exhibited an extra peak at 215 nm, possibly due to charge transfer between Mg^{2+} to silica surface.[27] This peak is not present on the CuMgSi catalyst which means that Cu promotion eliminated this exposed Mg species, consistent with DRIFTS observations. The CuMgSi catalyst exhibits a small peak at ~570 nm, which, as in the CuO reference case, might be due to the presence of a reduced species, i.e. Cu_2O or Cu^0. Lower geometry species are hardly encountered on mixed metal oxide and dehydration under inert atmosphere is more likely to induce partial reduction on the catalyst.[28] In agreement, a known adsorption peak in the 560-570 nm region is due to the plasmon resonance of metallic Cu nanoparticles.[57]

Tauc plots of CuO standard and the catalyst (CuMgSi) were derived from the UV-Vis DRS spectra, shown in **Figure S6.4.** Using the method previously described by Bravo-Suarez, *et al.*[44], identification of the oligomer is made possible by correlating the number of species to the edge energy. The plot in CuMgSi was deconvoluted into two species, isolated (0 nearest neighbors) and the oligomer that will be determined, with edge energies of 3.86 and 3.51 eV, respectively. The Tauc plot indicates that the reference oxide CuO exhibits an edge energy of 1.26 eV, close to the previously determined values at 1.17 ± 0.06 eV.[44,58] The value for the isolated CuO was higher than that reported for CuMgAl mixed oxide, which had been reported to be ~3 eV.[44] The difference originates from the coordination of the isolated CuO. In the previous report it was determined that the Cu species is in the Cu_2Al domains, instead of forming a solid solution with Mg.[44] Using isolated CuO species and standard CuO (6 nearest neighbors), the coordination number, i.e. number of Cu-O-Cu bond, was determined to be 0.8.

The Zn-promoted catalyst UV-Vis DRS spectra are shown in comparison with the reference samples, i.e., bulk ZnO, MgSi, ZnSi and ZnMg, shown in **Figure 6.7b**. The ZnMgSi catalyst shows a small peak at 276 nm. This small peak is down shifted ~100 nm, when compared to bulk ZnO at 360 nm. Additionally, ZnMgSi contains a peak at 215 nm, which resembles that of the CuMg UV-Vis DRS spectrum. This CT peak appears in almost all Mg containing samples, except for CuMgSi. That peak was located at almost the same wavelength, ~215 nm, for CuMg, ZnMg, and ZnMgSi, but shifted when MgSi support was used, i.e. at 225 nm. This peak can be assigned to a charge transfer from Mg^{2+} to O^{2-}, where a shift is expected when MgO is wet-kneaded with SiO_2.[59] However, introducing Zn to the MgSi support seems to negate this shift and it reverts back to ~215 nm. This phenomenon is consistent with DRIFTS data, as shown in **Figure 6.5,** where the OH peak at 3740 cm^{-1} disappeared when MgO was wet-kneaded to SiO_2, but reappeared when Zn is introduced to the surface. **Figure 6.7b inset** shows different Zn loadings on the wet-kneaded MgSi. At a higher loading, the peak at lower wavenumber, i.e. 215 nm, persists, while the ZnO peak started appearing at 270 and 280 nm for 10% and 15% Zn loadings, respectively. The shift in the CT peak is also followed by the shift in the edge energy cutoff. This shift with a higher Zn loading was also observed by Yoshida *et al.* on an SiO_2 support, although they describe this Zn site to have a distinct electronic structure from bulk ZnO, with XANES confirming that the ZnO is in a tetrahedral configuration.[60]

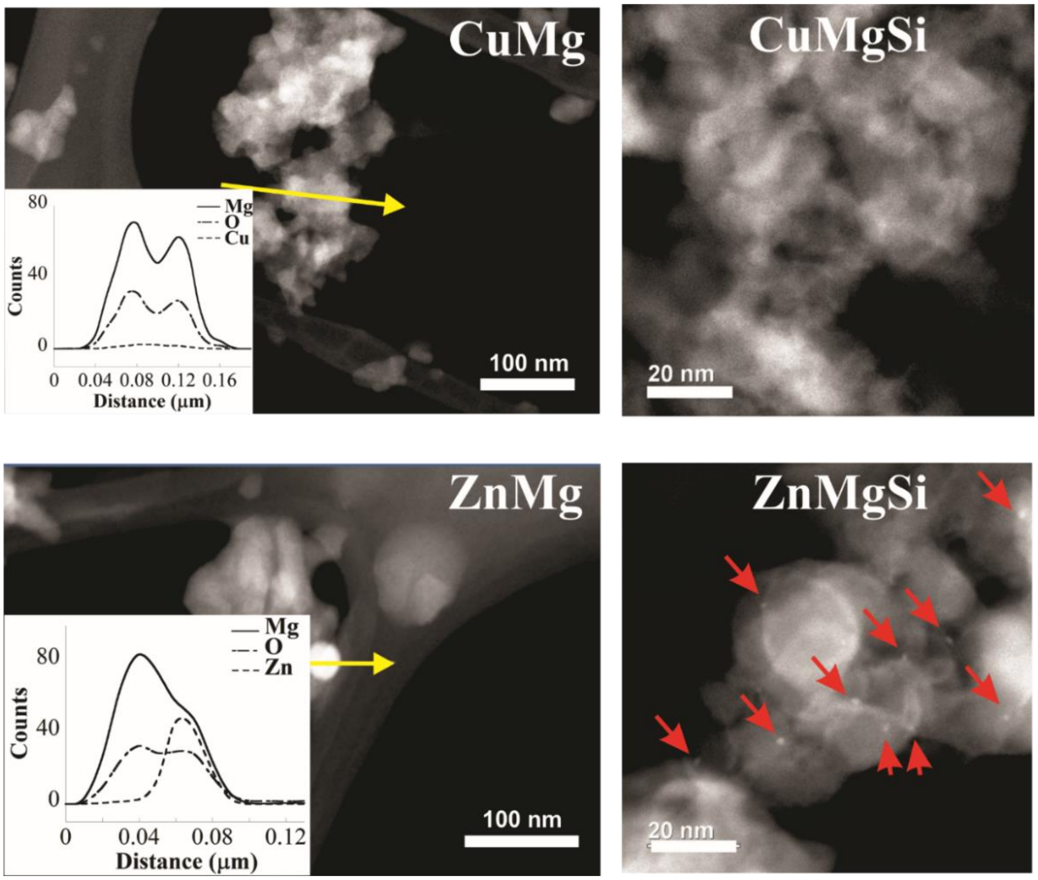

Figure 6.8. Scanning Transmission Electron Microscopy images of ZnMg, ZnMgSi, CuMg and CuMgSi samples. Energy Dispersive Spectroscopy profiles (smoothed) are also provided. Small ZnO nanoparticles are shown in ZnMgSi with red arrows.

The reference ZnMg and ZnSi samples further aided in peak assignments of the UV-Vis spectra of the ZnMgSi catalyst. In addition to the discussed 215 nm peak, the former exhibits two other peaks at 276 and 360 nm. The first peak could be associated with the defected Mg site of the catalyst, assigned to tri-coordinated O^{2-} ions on corner sites, which is also encountered in the MgSi sample.[27,59,61] Along with the peak at lower wavelengths, 215-225 nm, these peaks are indicative of the bulk MgO, also observed by

Sels and coworkers.[27] The second peak is likely to be assigned to bulk ZnO as a compared to the bulk ZnO reference spectra. The ZnMgSi catalyst, on the other hand, hardly shows any other peaks related to Zn-containing species, which rules out the bulk ZnO from active site consideration. Bulk ZnO nanoparticles might only be formed at a very small particle size. This is supported by STEM measurements in **Figure 6.8**. Chouillet *et al*. reported a similar observation, where UV-Vis shows bands of a bulk ZnO phase in the limit of 1.4-4.4 nm particle size, confirmed by TEM.[47] Highly dispersed ZnO nanoparticles have also been previously observed on MgO-supported catalysts.[48,62] Another possibility is that Zn might be present in a solid solution inside the lattice of the support *(vide infra)*, as previously reported in SiO_2[47,60] or in talc.[13] In particular, ZnMg shows large ~30 nm isolated ZnO crystals present. However, ZnMgSi shows very small ~1 nm crystals and the presence of isolated ZnO nanoparticles. This is consistent with the UV-Vis data shown in **Figure 6.7**. Isolated (monomeric) Cu sites, as well as oligomeric sites in both CuMg and CuMgSi, can't be detected using STEM/EDS in **Figure 6.8**, indicating high dispersion of these sites.

To confirm the presence of some reduced species on the surface, oxidative treatment was done post-inert treatment by flowing air (**Figure S6.5)**. The significant increase in the CT bands at 250 and 310 nm in expense of the peaks at 575 and 633 nm for CuMgSi indicates the presence of some native reduced species that became oxidized upon the introduction of air at higher temperature. Similarly, ZnMgSi shows the continuous increase in peaks at 230 and 340 nm, indicating the formation of both MgSi sites and bulk ZnO phases when oxidized.

3. 2 Steady state catalytic performance and acid/base chemistry of the catalyst active sites

The steady state reactivity comparison between MgSi, ZnMgSi and CuMgSi catalysts is shown in **Figure 6.9**. Here the activity of three catalysts is compared in the temperature range of 350-450°C. It can be seen that promotion with Cu and Zn significantly enhanced the 1,3-BD formation rate from <1 mmol/g_{cat} h to ~2 mmol/g_{cat} h throughout the investigated temperature range. Furthermore, ethylene formation was suppressed, more significantly in the case of Zn promotion. The origin of this promotional effect can be traced back to the production of acetaldehyde, which significantly increased in comparison to the unpromoted catalyst. This accumulation of acetaldehyde on the surface indicates that the Rate Determining Step (RDS) shifted for the case of promoted MgO/SiO_2. Quantitatively, this is confirmed by the decrease in apparent activation energy, E_a, as derived from the Arrhenius plot of each product formation rates. Acetaldehyde and 1,3-BD activation energy exhibits similar trend with promotion with Cu and Zn, with E_a (Zn) < E_a (Cu) < E_a (unpromoted). Apparent activation energy of ethylene, on the other hand, decreases with Cu promotion but not with Zn. With Zn, however, increasing temperature does not increase the formation rate of ethylene, which explains very low activation energy on this catalyst. The very low formation rate of ethylene must be due to very low rate constant of ethylene formation, since raising the reaction temperature does not have significant effect on the formation rate.

A similar increase in 1,3-BD production was previously reported by various investigators.[3] For instance, Weckhuysen and coworkers noticed a sharp increase (~20%) in both ethanol conversion and 1,3-BD yield upon promoting the wet-kneaded catalyst with

1% CuO. The productivity of their catalyst was very similar to that reported here: 0.48 mmol g_{cat}^{-1} hr^{-1} at 425°C and WHSV = 1.1 hr^{-1}.[14] When the reaction was carried out at more than 375 °C, the conversion over ZnMgSi approached 100%. This increase in conversion was previously observed when Zn was shown to provide more Lewis acidity and also suppressed the Brønsted acidity.[15,63] Zn-promoted catalysts, such as MgO/SiO_2[15] and talc[13], were reported to increase both the conversion and selectivity toward 1,3-BD. The latter showed the same productivity as our catalyst, ~1.1 mmol g_{cat}^{-1} hr^{-1} at an even lower reaction temperature (300°C) and a much higher WHSV (8.4 hr^{-1}).

The change in the surface chemistry of the catalyst induced by the presence of these metals, to the best of our knowledge, has not been thoroughly investigated. The general consensus is that the catalyst should have all redox, basic, and acidic sites on its surface. On Cu, extensive study on the local coordination of Cu by means of XAS was not accompanied by the identification of molecular coordination by other spectroscopic methods.[28] Further, promotional effects on Zn-promoted MgO/SiO_2 catalyst were not extensively investigated, i.e. studies were only focused on the activity change and the implication on acid-base characteristics of the catalysts.[15] Basic site poisoning using CO_2 and propionic acid can reveal the reactive site difference between the three catalysts. CO_2, a relatively weaker acid than propionic acid, will occupy the stronger basic sites[2,64] while propionic acid should non-discriminatively adsorb on all basic sites given its stronger acidity. Coflowing CO_2 with ethanol as a weak acid will mainly poison the strong basic sites and suppress any reactions that require participation of these sites. Propionic acid, being a stronger acid, will indifferently poison any basic sites, possibly suppressing all detectable reaction products. When switching to reactant-only flow, the weak bond established between the weak CO_2 molecules should be broken and therefore should eliminate the poisoning effect and revert the system back to its original state. For propionic acid, however, the strong basic sites should maintain strong bond with the probe molecule after flow is stopped and should irreversibly deteriorate the productivity of one or more reaction products that depend on the site availability.

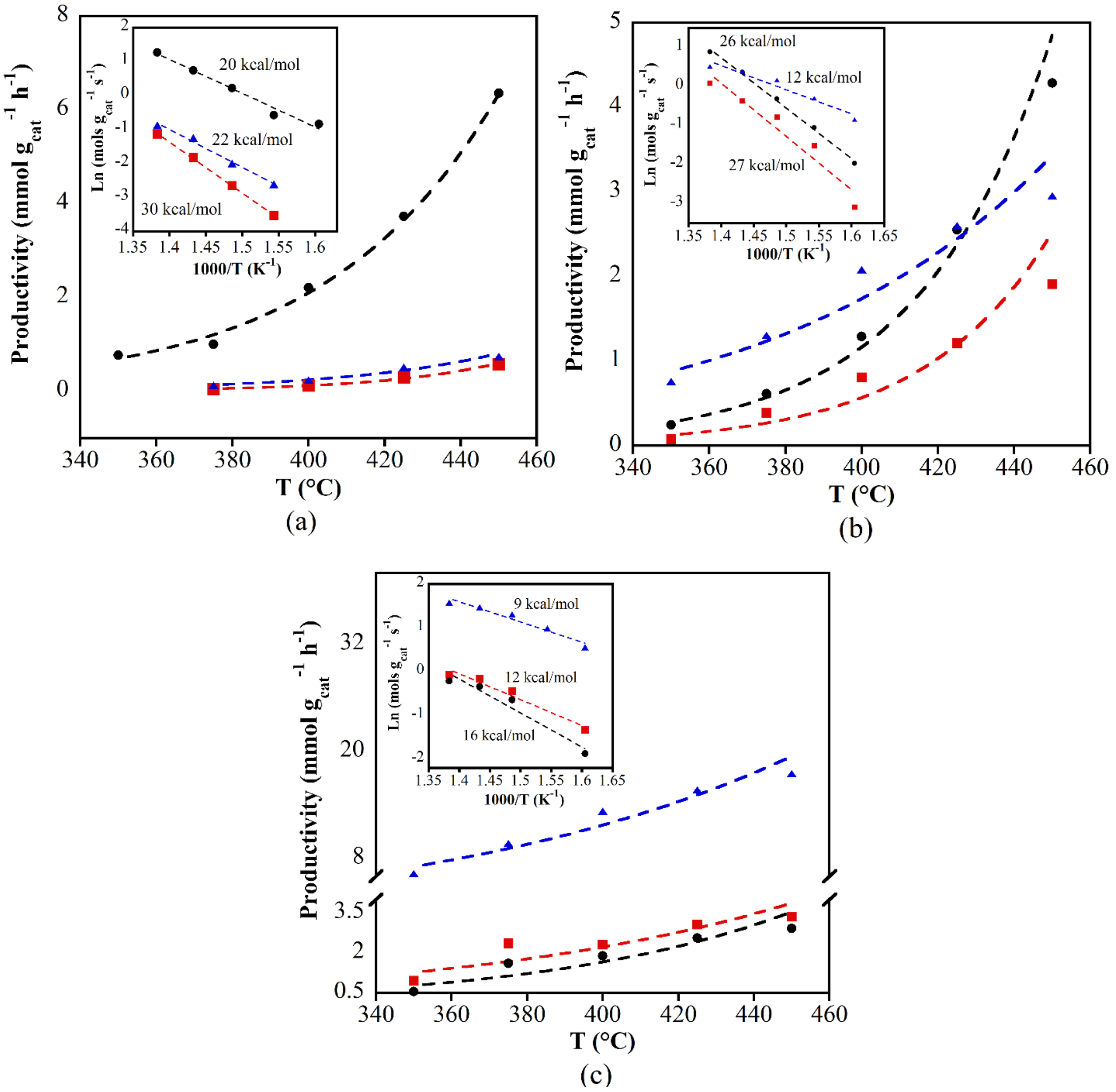

(a)

(b)

(c)

Figure 6.9. Productivity comparison of 1,3-BD (■), ethylene (●), and acetaldehyde (▲) over (a) MgSi, (b) CuMgSi, and (c) ZnMgSi. Dotted lines are meant to guide the eyes. Insets: Arrhenius plots to show apparent activation energies of the three (by)products. Reactions are carried out between 325 - 450°C, m_{cat} = 0.1 g, $p_{ethanol}$ = 1.8 kPa, total flow = 55 ml/min.

Fundamental acid-base study on both transition metal-promoted catalysts were investigated by both *in-situ* and *ex-situ* methods (**Section S6.2**). *In-situ* studies using propionic acid showed that all three catalysts possessed very limited amount of strong basic sites and that promotion with transition metals further decreased the amount of strong basic sites. The propionic acid cofeeding experiment showed that 1,3-BD productivity did not recover to its original formation rate which suggests the presence of some strong basic sites that maintain strong interaction with the leftover propionic acid.[2] With the wet kneaded support, the strong basic sites are limited and more medium basic sites are present. Both *in-situ* CO_2 poisoning and DRIFTS study confirmed the increased availability of the medium and weak basic sites. Our study aligns well with previous study using deuterated chloroform, with Cu-Mg solid solution being thought of as the origin of reduced strong basic sites.[28] The *in-situ* poisoning further unraveled the site requirements for every step of the reaction, i.e. acetaldehyde formation on weak basic sites, dehydration on any sites, aldol condensation and MPV reduction on strong basic sites. The reduced amount of strong basic sites is also the origin of RDS shift from acetaldehyde formation to MPV reduction. Total amount of acid sites were also reduced by promotion with Zn and Cu, as shown by both *in-situ* NH_3 poisoning and NH_3-DRIFTS experiment. While acid sites are responsible for the dehydration steps, the origin of acetaldehyde formation rate reduction is the competitive bonding between the available Cu^{2+} to NH_3, since Cu catalysts are routinely investigated as SCR catalysts.[65,66] This is further supported by the recovered acetaldehyde production. The acetaldehyde production was accompanied by Cu^{2+} successive reduction to Cu^0, as shown by *in-situ* XANES (*vide infra*) and was possibly the reason its productivity decreased overtime. Promotion with transition metals yielded similar results, where Lewis acid sites associated with Mg_{3C}^{2+} is removed, with enhancements on the M_{4C}^{2+} sites. This finding indirectly confirms the structural change in the catalyst itself, i.e. solid solution formation.

3. 3 Active sites under operating conditions

3. 3. 1. Temperature programmed infrared spectroscopy measurements (TP-DRIFTS)

The effect of metal promoters on ethanol to 1,3-BD reaction mechanism were probed using *in-situ* temperature programmed DRIFTS. This allowed to study the surface species participating during the reaction. Detailed assignments of the IR peaks can be found elsewhere.[11] Briefly, experiments utilizing different probe molecules, i.e. ethanol, acetaldehyde, crotonaldehyde, and crotyl alcohol, were performed. **Table 6.4** summarized the peak assignments from experiments done on MgSi catalyst. The *in-situ* DRIFT spectra in 1700 to 1300 cm^{-1} region of MgSi, ZnMgSi and CuMgSi catalysts are shown in **Figure 6.10 (insets)**. There were two very prominent peaks in the spectra at high reaction temperatures (>250°C), i.e. ~1575 cm^{-1} and 1440 cm^{-1}, previously assigned to the product of acetaldehyde aldol condensation and polymerization.[11] Noticeable difference between the unpromoted spectra and the promoted ones was in the exact position of the two peaks. On promoted catalysts, the C=C stretch shifted to 1587 cm^{-1} while the prominent peak for the C-H bending was at 1458 cm^{-1}. The 1587 cm^{-1} peak location is identical in the case for both CuMgSi and ZnMgSi, which indicates similar anchoring site on the catalyst. As will be discussed later some of the magnesium forms solid solution with both Cu and Zn, which is possibly the binding site of the reaction product, given the identical peak location.

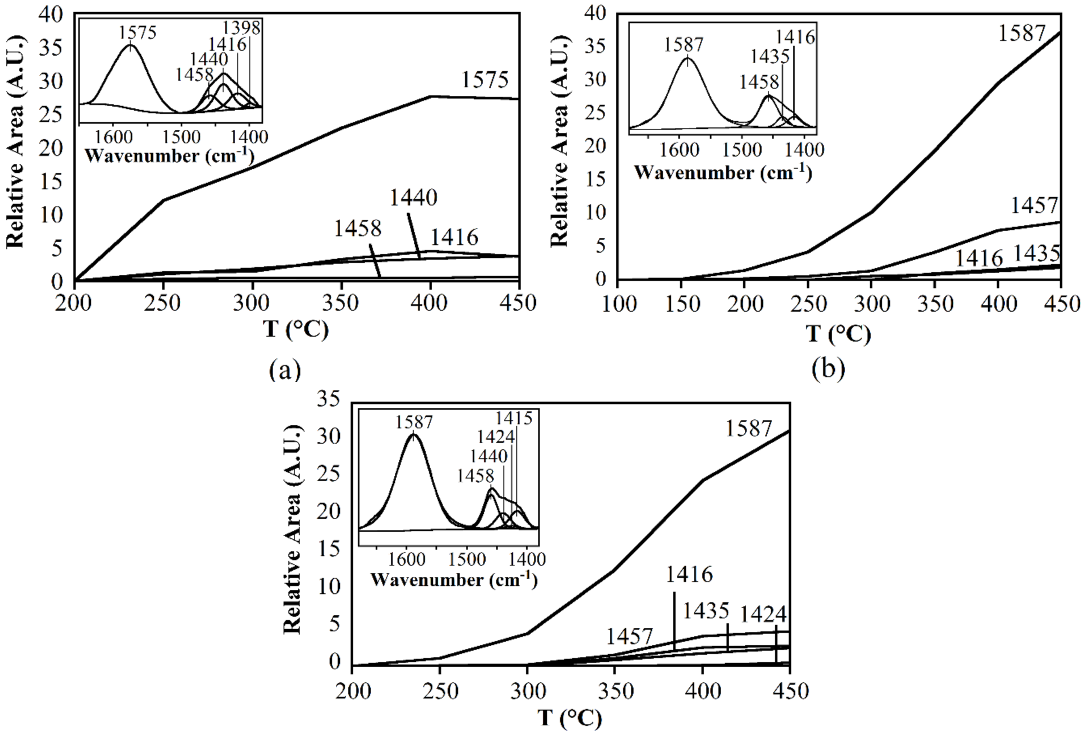

(a) (b)

(c)

Figure 6.10 Evolution of each peak during *in-situ* temperature-programmed ethanol DRIFTS over (a) MgSi, (b) CuMgSi, (c) ZnMgSi. Insets: original spectra of ethanol DRIFTS from where the peaks were deconvoluted.

The C-H bending peak was very complex since every reactive intermediate has a C-H group. Peaks were deconvoluted using CasaXPS software suite version 2.3.18PR1.1[67] into several different components. On the unpromoted catalysts, this broad envelope was deconvoluted into four peaks, i.e. 1458, 1440, 1416, and 1398 cm^{-1}. On metal-promoted catalysts, these peaks were less convoluted showing fewer species involved with only three prominent peaks existing. Interestingly, the peak at 1458 cm^{-1} was formed more rapidly in the case of promoted catalysts, while peaks at 1435 and 1416 cm^{-1} lagged, compared to the unpromoted catalyst. The growth of the peak at 1458 cm^{-1}, previously assigned to acetaldehyde (δ CH_3) and crotonaldehyde (ρ_w CH_3), is significantly enhanced over promoted catalysts. The reactive nature of acetaldehyde, which is the generally accepted first reactive intermediate, complicates analysis where multiple competing reactions, such as aldol condensation, acetate formation, and polymerization to take place at low to intermediate temperature.[68–73] The adsorbed acetate formation can't be fully ruled out due to the peaks at 1587-1575 cm^{-1} that appeared and grew almost at the same rate with the ~1400 cm^{-1} peak.[70] Together with polymerization of acetaldehyde and consecutive aldol condensation to C6 aldehydes, these reactions present side reactions that occur. The acetate formation is doubtful to take place in this experiment. In particular, if peak at 1587 (1575) cm^{-1} is assigned to the surface acetate the change in the growth after promotion with Zn (Cu) would apply to all the peaks in the 1460-1400 cm^{-1} region. In fact, the improvement in growth of peak at 1458 cm^{-1} after promotion is much more significant than that for the peak at 1587 (1575) cm^{-1}.

Hence, the peaks at 1587-1575 cm^{-1} and 1457 cm^{-1} can be used to characterize the degree of both aldol condensation and dehydrogenation that takes place on the surface, while the other peaks at ~1400 cm^{-1} to characterize the catalysts' basicity, i.e. its ability to readily polymerize the formed acetaldehyde. The resulting crotonaldehyde tends to stay on the surface and further undergo other reaction than to desorb as vapor-phase crotonaldehyde. The C4 intermediate can be further aldolized with acetaldehyde to form 2,4-hexadienal and stick on the surface and possibly deactivate the catalyst.[74] This insight can be further utilized to probe the abundance of the active sites of the catalyst, i.e. based on the accumulated 2,4-hexadienal which was characterized by the 1587 cm^{-1} peak. We carried out semi-quantificative analysis of the peaks at 1587 (1575), 1440, and 1458 cm^{-1}. The peaks at ~1400 cm^{-1} are summed together assuming that they result from similar class of reaction, i.e. polymerization that typically yield more than one product such as metaldehyde and paraldehyde.[74] The evolution of these peaks as a function of temperature was plotted in **Figure 6.10**. It can be seen that for all catalysts, there was no significant changes in the ~1400 cm^{-1} peak area. However, the promoted catalysts resulted in a higher intensity/area of the 1587 cm^{-1} peak with Cu higher than Zn. This indicates that promoting the catalyst with transition metal promoters enhances the ability of the catalyst to carry out aldol condensation, while at the same time keeping the unwanted polymerization constant with regards to the unpromoted catalyst. Another noticeable difference was the temperature where the peak started increasing in intensity. For Cu, the peak starts increasing at lower temperature, even at ~150 °C, while Zn lagged behind and showed similar reactivity to the unpromoted catalyst.

Overall, combination of both DRIFTS and steady state fixed-bed experiments showed a shift in the rate-limiting step. Without the promotion with transition metal, less acetaldehyde was produced in the product stream indicating the rapid consumption of the intermediate. Promoted catalysts, on the other hand, saw increase in acetaldehyde production, which suggested a bottleneck reaction. The accumulation of acetaldehyde in the steady-state reaction experiments suggested that aldol condensation is the RDS. The acidity and basicity of the catalyst was affected as well by promotion with transition metal. *In-situ* poisoning experiment with propionic acid and NH_3 showed that promoting increases the availability of the weak basic sites and total acid sites, as shown by the significant decrease in the production of all products during the coflow. *In-situ* DRIFTS of ethanol over the three investigated catalysts indicated that there was a change in the binding site during the aldol condensation, as manifested by the shift of C=C stretch peak at 1575 to 1587 cm^{-1}. This systematic change suggested that while the anchoring site was identical between the two promoted catalysts, a potential solid solution formation took place. Mechanistically, this semi-quantification confirms the steady-state experiment findings where the activation energy of the dehydrogenation step was significantly reduced leading to higher amount of acetaldehyde and products of aldol condensation. The change in the polymerization products was also an indication to the altered basicity of the catalyst.[68,69] Though the difference was not significant, the reduced polymerization products indicated that the basicity of the catalyst was slightly reduced.

Table 6.4. Vibrational frequencies in 1600-1400 cm^{-1} wavenumber range and their assignments for ethanol, acetaldehyde, crotonaldehyde and crotyl alcohol adsorption on WK (1:1)[11]

Assignment	Experimental (cm^{-1})				
	Ethanol	Acetaldehyde	Enolate	Crotonaldehyde	Crotyl alcohol
ν (C=C)	-	-	1600, 1578	1600, 1574	1602
δ (CH_2)	1454	-	-	-	1380
δ (CH_3)	1418	-	-	1456, 1434	1368
ρ_w (CH)	1380	-	-	-	-
ρ_w (CH_2)	-	-	-	-	1441
ρ_w (CH_3)	1338	1456, 1434, 1382	-	1346	1456

3. 3. 2. *In-situ* UV-Vis DRS study of MgSi catalysts

Figure 6.11 shows the *in-situ* UV-Vis DR spectra during ethanol conversion to 1,3-BD on (a) CuMgSi and (b) ZnMgSi. The spectra plotted are difference spectra referenced to 100 °C to better describe the dynamic changes. On CuMgSi it can be seen that with the reaction progressing there were four broad spectral bands. Increasing the temperature lead to the intensity increase at 248, 315 and 565 nm while the band at 276 nm showed decrease in intensity. Interestingly, inset in **Figure 6.11a** shows that the band at 211 nm reached a maximum at 300°C and decreased in intensity at higher temperature. To assist the peak assignments, we performed similar experiments on unpromoted MgO/SiO_2 catalyst (**Figure S6.12**). The UV-Vis spectra of the unpromoted catalysts showed changes on three bands at 210, 245, and 300 nm. These three peaks can be assigned to either CT bands of metal oxides, π- π* transitions of allylic cations, cyclic or aromatic species, or even neutral, uncharged aromatic species (for shorter wavelengths).[75,76] An alternative assignment for the two bands at 210 and 245 nm was the LMCT band of Mg to O on defect sites and to SiO_2, respectively.[27,59] The remaining peaks are at 276 nm that decreased at the expense of peak at 565 nm. The former was assigned to oligomeric CuO species (~0.8 Cu nearest neighbor), while the latter one was assignable to surface plasmon resonance of Cu also due to the rare occurrence of lower geometry CuO_x species in mixed oxide systems.[28,44] The indicated reduced CuO oligomeric species to surface Cu^0 will later be confirmed by X-ray methods since peak at 565 nm could also originate from substituted or unsubstituted benzene.[75]

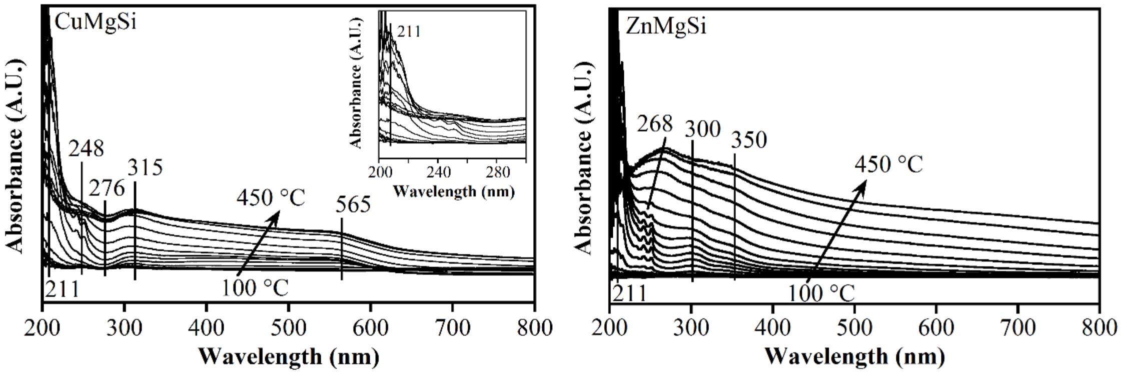

(a) (b)

Figure 6.11. *In-situ* UV-Vis DRS under constant ethanol flow over (a) CuMgSi and (b) ZnMgSi

On ZnMgSi, *in-situ* UV-Vis experiments showed the emergence of different intermediates as signified the by the bands at ~240 -shifted to 268 nm at higher temperature-, 300 and 211 nm. These bands were observed on the *in-situ* ethanol experiment over unpromoted MgO/SiO_2 catalyst as well. Another band with a cutoff at 350 nm also appeared. This band could be indicative of π- π* transitions of dienic allylic cations[75] or bulk ZnO formation since its emergence was also accompanied by the intensity increase of shoulder at ~230 nm, which alternatively can be assigned to CT between Mg^{2+} to SiO_2.[27] The alternative assignment can suggest that Zn was transformed from its solid solution state into bulk ZnO, as accompanied by the formation of CT band at ~230 nm.

3. 3. 3. *Operando* XAS studies of Cu, Zn-promoted MgSi catalysts

3.3.3.1. *Operando* XANES and EXAFS of Cu-promoted MgSi catalyst

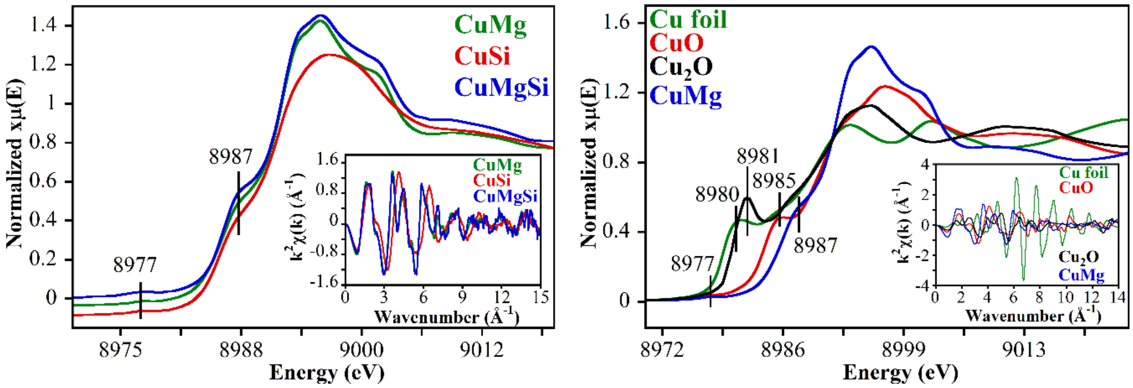

(a) (b)

Figure 6.12. Normalized XANES spectra of CuMg, CuSi, and CuMgSi (a) and Cu foil, CuO, Cu_2O, and CuMg (b). Inset: Cu K-edge k^2-weighted EXAFS data of corresponding spectra. XANES spectra in **Figure 6.12(a)** were offset vertically for clarity.

The XANES spectra of Cu catalysts and standards taken under ambient condition are shown in **Figure 6.12**. The XANES spectra for samples with Cu-promoted supports, i.e. CuMg, CuSi, and CuMgSi, show similar features with a weak pre-edge peak located at about 8977 eV and a shoulder peak at the rising edge at about 8987 eV (**Figure 6.12**, left). The weak feature at 8977 eV was previously assigned to the 1s → 3d transition, and is considered a signature for Cu^{2+} species.[28,77,78] For comparison, XANES spectra of the standards, i.e. Cu foil, Cu_2O, and CuO, are plotted along with CuMg XANES spectrum. The CuMgSi catalyst XANES spectrum strongly resembles that of the CuMg, and is very different from CuSi and Cu standards. Further, the EXAFS spectra in the inset are very similar for both CuMg and CuMgSi. The shoulder peak at 8987 eV, when compared to CuO, was shifted from 8985 eV. This shoulder peak is usually assigned to the 1s → 4p transition, and its position is associated with neighboring atomic geometry.[79] For CuMg, the shift in the shoulder peak was also observed. [28] Many reports attributed that shift to Cu being in octahedral or distorted octahedral geometry, occupying Mg lattice sites in a solid solution.[34,35,49]

Table 6.5. Best fitting results of Cu catalysts. The structural parameters of standards were listed for comparison.

Sample	**Bond**	**N**	**R (Å)**
CuMgSi	Cu-O	5.6±1.1	1.96±0.02
	Cu-Mg	7.0±1.8	3.01±0.02
CuMg	Cu-O	4.5±0.9	1.97±0.02
	Cu-Mg	7.1±2.0	3.00±0.03
CuO	Cu-O	4	1.96
	Cu-O	2	2.78
	Cu-Cu	4	2.9
	Cu-Cu	4	3.08
	Cu-Cu	2	3.18
Cu_2O	Cu-O	2	1.84
	Cu-Cu	12	3.01
MgO	Mg-O	6	2.11
	Mg-Mg	12	2.98
Cu foil	Cu-Cu	12	2.56

As shown in **Figure S6.13** (the Fourier transformed $k^2\chi(k)$ spectra of CuMgSi, Cu_2O, CuO and Cu foil), the R-space EXAFS spectra of CuMgSi have two distinct peaks in the range of 1-3 Å. The peak at about 1.5 Å is due to Cu-O contribution, and the peak at about 2.6 Å could be due to Cu-Cu contribution from Cu oxides or Cu-Mg contribution if Cu enters MgO lattice. To determine the local environment of Cu, EXAFS analysis was performed and two models were tested. Model A includes Cu-O and Cu-Cu path and Model B includes Cu-O and Cu-Mg path. The fitting k range is 2.0-11.0 $Å^{-1}$ and R range is 1.0-3.1 Å. The best fitting results were obtained by using Model B and are shown in **Table 6.5**. For comparison, the structural parameters for Cu foil, CuO, Cu_2O, and MgO were also listed in **Table 6.5**. The Cu-O bond parameters on both samples are similar to those of Cu-O bond in the CuO. The Cu-Mg bond lengths in both CuMg and CuMgSi are also similar to the Mg-Mg and Cu-Cu bond lengths of MgO and CuO standards, respectively. The Cu-Cu contribution was not detected for either CuMg or CuMgSi, which corroborates the insertion of Cu into MgO lattice. Coordination number of Cu-O shown in the EXAFS analysis was also in line with the (distorted) octahedral geometry. Previous investigations by Asakura *et al.* and Angelici *et al.* demonstrated that Cu-O coordination numbers were lower than 6.[28,34] Angelici, *et al.* found a coordination number of 4 and further assumed the presence of two additional oxygen atoms to simulate the XANES spectra which revealed another contribution from Cu-O bond at ~2.40 Å, which is characteristic of a separation between copper and apical oxygen atom in a CuO_6 complex.[28] For CuMg, the Cu-O contribution follows similar observation of Angelici *et al.* and Asakura *et al.*, i.e. less than 6.[28,34]

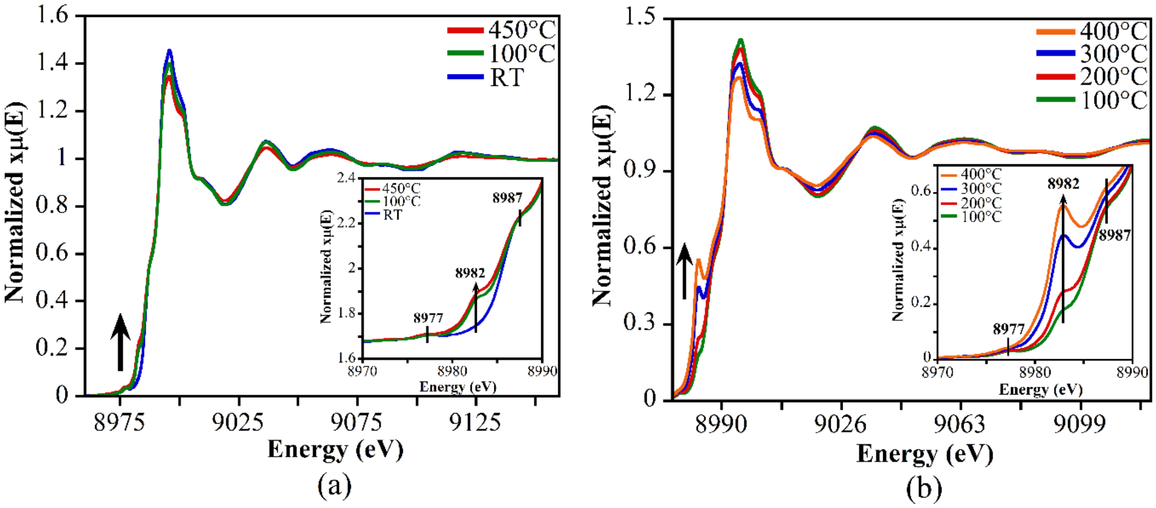

(a)

(b)

Figure 6.13 Normalized temperature-programmed *operando* XANES spectra of CuMgSi catalyst under He flow (a) and ethanol flow (b). Inset: enlarged region of the pre-edge features to elucidate changes at different temperatures.

Operando XAS experiments with flowing ethanol over CuMgSi were performed at different reaction temperatures to analyze the role of Cu species during the reaction, and at 400°C, multiple scans were performed to investigate the evolution of Cu species as the reaction progresses at constant temperature. **Figure 6.13** shows the XAS spectra of CuMgSi under both helium flow (a) and constant ethanol flow (b) at different temperatures. As shown in **Figure 6.13**, the pre-edge peak (at 8977 eV), which is a signature of Cu divalent species, remains almost unchanged after pretreatment, indicating Cu remains in the 2+ state after He treatment. Under helium at elevated temperatures, a new feature at 8982 eV appeared suggesting the change of the local environment of Cu after pretreatment. The position (8982 eV) of this peak is quite close to that (8981 eV) of the shoulder peak of Cu_2O, in which each Cu atom is surrounded by two O atoms in a collinear manner. The appearance of the 8982 eV peak thus implies the decrease of the average coordination number of Cu-O bond for Cu atoms in CuMgSi catalyst. During experiment with ethanol, significant increase in the intensity of 8982 eV peak was observed especially at high temperatures, suggesting the increased fraction of species in which the average Cu-O coordination number is low. We propose that such geometry is correlated with catalytic activity of CuMgSi catalyst. The corresponding MS data (**Figure S6.14**), shows that the acetaldehyde was made at very low temperature, i.e. starting as low as 100 °C, and increased significantly at ~250 °C. This increase is reflected as well by the spectra at 300 °C, where the increase is very significant from 200 °C. At the same time, the 1,3-BD started being produced at ~250 °C, which was lower than unpromoted catalyst, i.e. 300 °C.

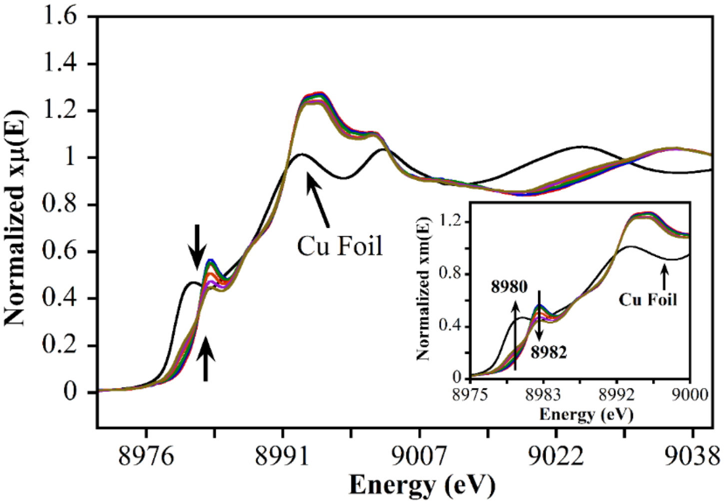

Figure 6.14. Normalized time-resolved *operando* XANES spectra of CuMgSi catalyst under ethanol flow at 400°C. Inset: enlarged region of the pre-edge features to elucidate changes at different temperatures.

When reaction temperature reached 400 °C, the temperature was held constant while XANES spectra were repeatedly taken to investigate any changes that take place during the reaction. The change in the copper species was recorded as a function of time, shown in **Figure 6.14**. A Cu foil XANES spectrum taken at ambient temperature was overlaid for comparison. As reaction proceeded, the peak at 8982 eV started decreasing in intensity, suggesting the re-arrangement of the local structure of Cu. Accompanied with this decrease, the peak at 8980 eV which is also a feature of Cu foil spectrum showed up and increased with time, suggesting the formation of Cu metallic phase. Basing on the above results, we conclude that changes in the local structure of Cu occurred throughout the reaction. The quantitative information on the local structure of Cu during the reaction conditions was obtained by performing EXAFS analysis and the results were summarized in **Figure 6.15**. **Figure 6.15** shows the change in the coordination numbers of Cu-Cu, Cu-Mg, and Cu-O bonds during the reaction. From 200-400 °C, a steady decrease in Cu-O bond coordination number takes place, which, as discussed above, is also manifested by the increase in the intensity of 8982 eV peak. There was no appearance of Cu-Cu bond until the steady-state condition at 400 °C. At 400 °C, the final EXAFS spectra show a significant increase of Cu-Cu coordination number from 0 to about 3. This indicates clustering of the Cu atoms after reaction has stabilized at 400 °C.

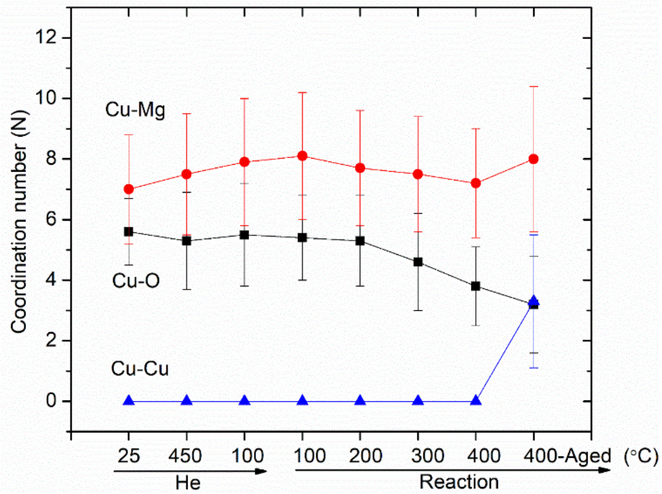

Figure 6.15. Coordination number changes during reaction of ethanol to 1,3-BD over CuMgSi

To confirm the correlation between the XANES features with the coordination number of Cu-O bond, XANES spectra simulations were performed using FEFF 9 code.[80]

Simulations were first performed on CuO and Cu_2O to find optimized simulation parameters, which were then applied in calculating the spectra of all models. For the as-prepared CuMgSi catalyst, according to EXAFS analysis, the coordination number of Cu-O was close to 6 and Cu is very likely taking the Mg sites in MgO lattice. We therefore built an MgO sphere which contains 251 atoms and has diameter of about 1.6 nm, and replaced the core Mg atom by a Cu atom. This model was named Model 1. In this model, Cu is octahedrally coordinated by 6 O atoms at the same distance. The calculated XANES spectrum of this model is plotted in **Figure 6.16**, and the shoulder peak at the rising edge is indeed shifted to higher energy compared to that of CuO, which agrees with the trend observed in experimental data. As shown by EXAFS results, under reaction conditions and at high temperatures, the average Cu-O decrease and is close to 4. We thus modified Model 1 by removing 2 oxygen atoms around Cu. In this modified model, Model 2, Cu is then surrounded by 4 oxygen atoms at the same distance forming a planar geometry. In the simulated XANES spectrum of Model 2, a shoulder peak appears in position between those of Cu_2O and CuO. Such trend was also observed in the experimental spectra. Therefore, the agreement between the experimental and theoretical XANES spectra suggests the shoulder peak at the rising edge of Cu spectra is related to the local oxygen environment around Cu. In the CuMgSi system, Cu replaces Mg in MgO lattice. When the reaction occurs, the octahedral Cu-O geometry will be distorted: most likely, part of oxygen atoms are pulling away from Cu, which could be then transformed to Cu metallic phase as detected in the final aged catalyst (**Figure 6.14**).

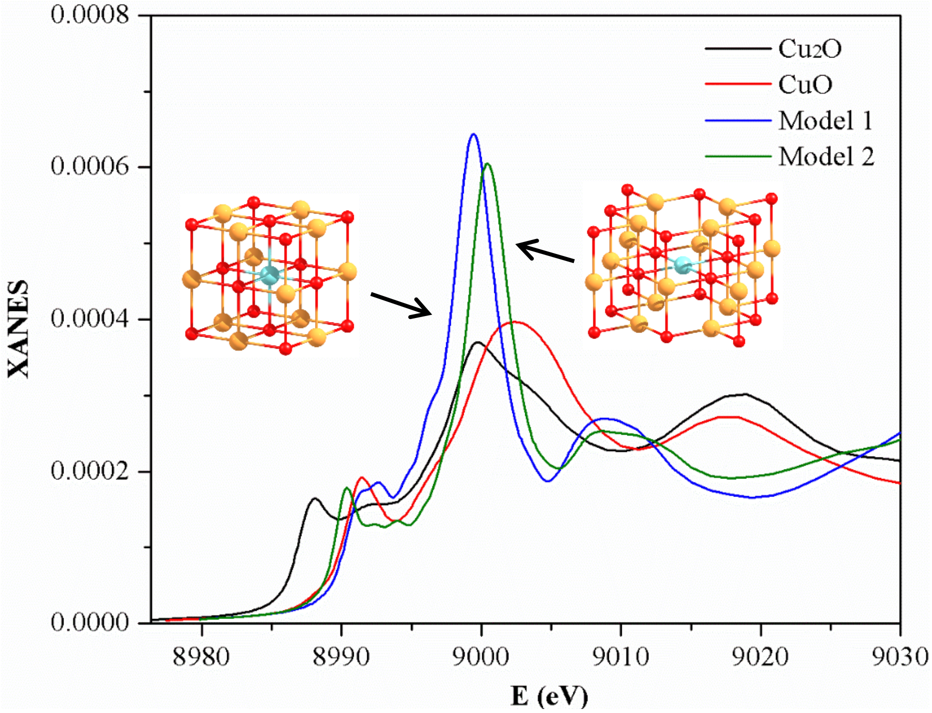

Figure 6.16. XANES spectra of the simulated CuO Model 1: Cu in a local environment surrounded by 6 oxygen atoms and Model 2: Cu in a local environment surrounded by 4 oxygen atoms.

A complementary view of this *operando* measurement was offered by Angelici *et al.*, where reactions were carried out at 400 °C under two different pretreatment conditions, i.e. inert flow and reducing atmosphere.[28] Under inert flow, the initial state of the catalyst consists of the native distorted octahedral Cu^{2+} species that was originally in the catalyst and another Cu^{2+} species that resembles to Cu^{2+} from CuO/SiO_2. This latter Cu^{2+} species was reduced to Cu^0 and transformed to the distorted octahedral Cu^{2+} species when pretreated at 425 °C under inert flow. Our observations show that there are new Cu species as evident by the peak at 8982 eV that appeared when catalyst was pretreated at high temperature even though the pre-edge feature at 8977 eV, assigned to the distorted octahedral Cu^{2+} from CuMgSi, barely changed. Interestingly, similar distribution between Cu^{2+}, Cu^+, and Cu^0 was observed after ethanol reaction without reducing pretreatment, after reducing pretreatment under H_2 and after ethanol reaction with reducing pretreatment.[28] Specifically, the three steps mentioned correspond to increasing amount of Cu^0 in the final state of the catalyst. This indicates that both ethanol and hydrogen have a competing reducing effect on the catalyst. The final state after the steady-state reaction under both pretreatment conditions revealed that there were some Cu^{2+} species on the catalyst even after extensive reaction with ethanol.[28] In our experiments, however, we observed a different outcome. The two pre-edge features at 8977 and 8987 eV behaved similarly with both of them barely changing during the reaction. Even after extensive reaction at 400°C, Cu-Mg coordination number did not change, while Cu-O coordination number decreased (**Figure 6.15**) to 4. The apparent increase in peak at 8987 eV is mostly due to the increase in peak at 8982 eV. We propose, based on data in **Figure 6.13-15,** that origin of the peak at 8982 eV, assigned to Cu^{2+} with less-than-6 oxygen neighbors, is from a bulk Cu^{2+} with six oxygen neighbors that catalyzed the reduction and lost bonding with two neighbor oxygens during interaction with ethanol, as indicated by the simulation (**Figure 6.16**). Furthermore, this new Cu species undergoes change in coordination number, decreasing to reduced Cu^0, possibly due to the depleted reducible Cu^{2+} that shifts the reaction active sites and further reduced all reducible copper species into Cu^0, as suggested by clustering of Cu (increase in Cu-Cu coordination number) as the reaction progressed at 400°C. The decreased reducibility of Cu^{2+}, evident from the presence of Cu^{2+} at the end of the reaction, was also observed previously on CuZn catalysts supported on MCM-41 and Al_2O_3, where co-presence of Zn^{2+} led to the formation of isolated Cu^{2+} species that was reduced at higher temperature.[42,81] Other factors that deteriorate Cu^{2+} reducibility can be attributed to the presence of solid solution phase and bulk CuO phase, such as that found in $CuMnZrO_2$ and

$CuMgAlO_x$ hydrotalcite catalysts, respectively.[44,78] The *operando* XANES and *in-situ* UV-Vis confirmed the presence of two Cu species on the catalyst prior to exposure to ethanol, i.e. distorted octahedral Cu^{2+} (possibly from solid solution) and reducible Cu^{2+} species, as suggested by *in-situ* dehydrated UV-Vis as well.

3.3.3.2. *Operando* XANES and EXAFS of ethanol over Zn-promoted MgSi catalyst

The XANES spectra of Zn catalysts and standards taken in ambient condition are shown in **Figure 6.17a**. The standards used in this study are Zn foil and ZnO to represent the reduced and oxidized states of the transition metal. Comparison between ZnMgSi, ZnSi (ZnO/SiO_2), and ZnMg (ZnO/MgO) reveals similarity between ZnMgSi and ZnMg. The silica-supported sample looks like those of willemite or hemimorphite, both Zn-silicates.[47] Chouillet *et al.* investigated the effect of drying temperature prior to calcination, and XANES spectra of all dried samples calcined at 450 °C, only 50 °C lower than our temperature, are nearly identical and indicative of zinc silicate formation.[47] The Zn foil exhibits a peak at 9660 eV, which was assigned to electron transition to empty d orbital. The absence of this feature indicates that all samples are fully oxidized.[55] For Zn standards (ZnO and Zn foil), there are two main features, the main edge, labeled as A, and feature B in the spectra. The main peak was assigned to 1s→4p electron transition with lesser peak intensity corresponding to decreasing coordination number of the cation.[82–84] The second feature was a multiple scattering resonance associated with medium range molecular structure around the target element; this feature was located differently for each sample, indicating difference in geometric molecular structure.[82,83]

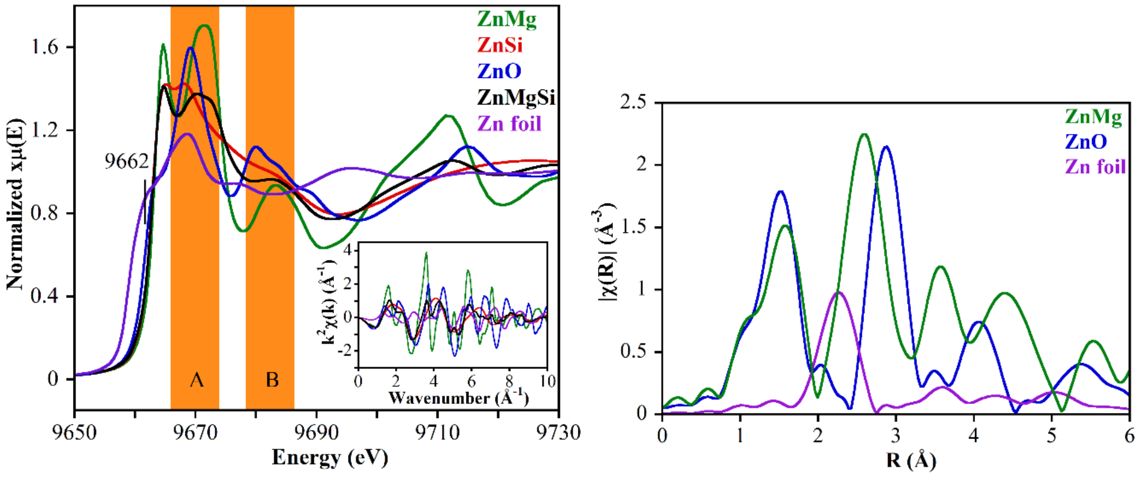

(a) (b)

Figure 6.17. (a) Normalized XANES spectra of ZnMg, ZnSi, ZnMgSi, Zn foil, and ZnO. Inset: Zn K-edge k^2-weighted EXAFS data of corresponding spectra. (b) Fourier transforms of the EXAFS spectra of ZnMg, ZnO, and Zn foil.

Both Mg-containing samples, i.e. ZnMg and ZnMgSi, exhibit splitting at the edge that was significantly larger than that of ZnSi. The splitting was previously observed on ZnO/Al_2O_3 and $ZnFe_2O_4$ as well and was attributed to a Zn^{2+} structure in a rigid environment nothing like ZnO.[83,85] EXAFS spectra of the samples show very similar spectral shape between the two samples although the oscillation magnitude of the ZnMgSi sample was much lower. The similarity indicates that the Zn in both samples possess very similar local structure. Fourier transform was applied to the EXAFS signal ($k^2\chi(k)$) of ZnMg to represent both samples and compared to ZnO and Zn foil (**Figure 6.17b**). Between 1-3 Å, there are two peaks at 1.40 Å and 2.40 Å. From the Fourier transformed spectra the first peak was attributed to Zn-O bond, while the latter was lower than Zn-Zn bond length in ZnO yet higher than Zn-Zn bond length in Zn foil. This implies that this was not due to the contribution of Zn-Zn bond and we predict this to be Zn-Mg bond. To confirm it, we did EXAFS analysis for the ZnMgSi catalyst and tested three models: Model A includes Zn-O and Zn-Zn paths; Model B includes Zn-O, Zn-Zn, and Zn-Mg paths;

Model C includes Zn-O and Zn-Mg paths. The fitting k range is 2.0-10.5 Å^{-1}, and R range is 1.0-3.2 Å. Model 3 provides us best fitting results, which confirms that Zn was singly distributed into MgO lattice. This Zn-Mg bond was ~0.2 Å shorter than that of Zn-Zn bond in the ZnO foil, which was also previously determined in $Zn_{(1-x)}Mg_xO$ alloy.[86] The bond length values for standards and samples are tabulated in **Table 6.6.**

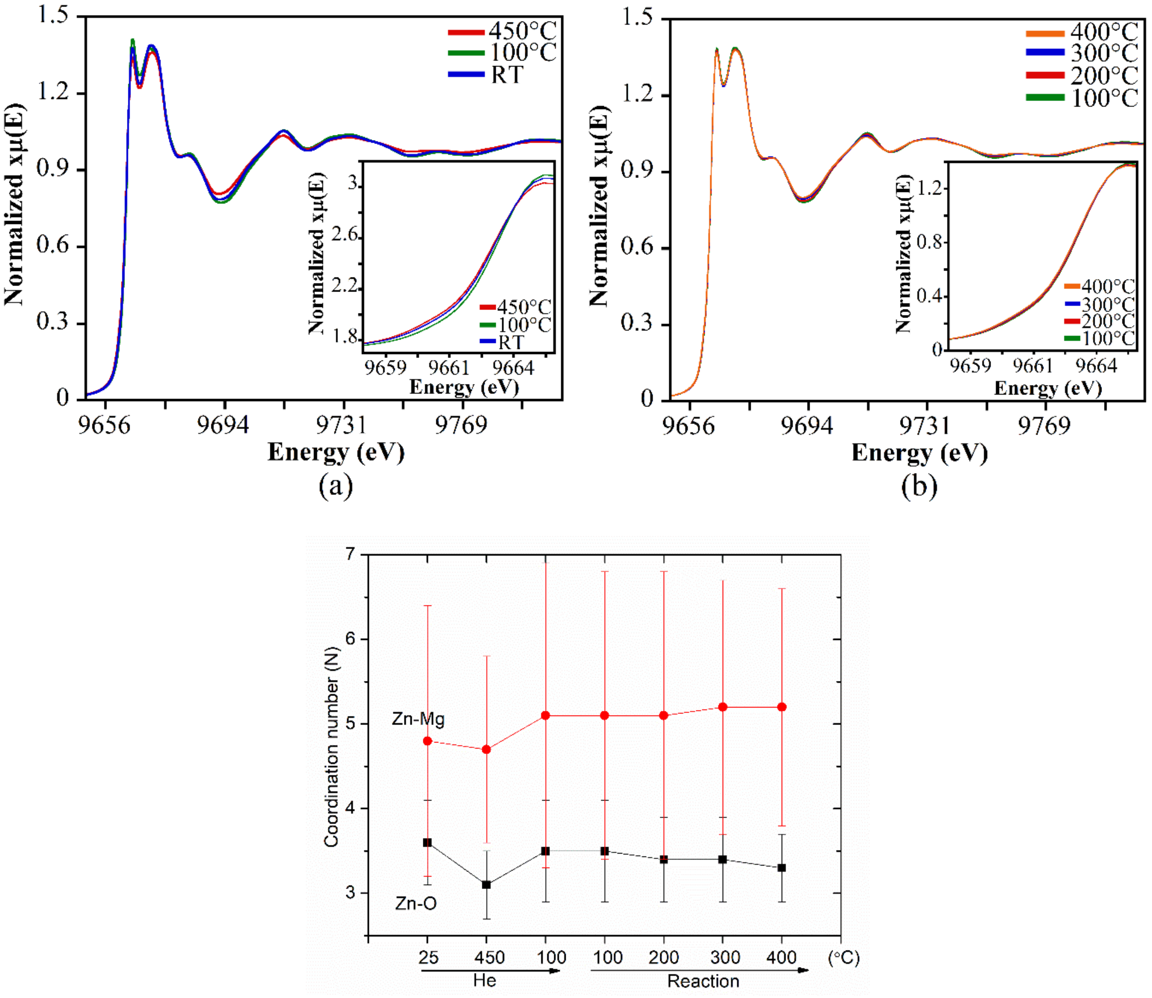

(a)

(b)

(c)

Figure 6.18. Normalized temperature-programmed *operando* XANES spectra of ZnMgSi catalyst under He flow (a) and ethanol flow (b). Inset: enlarged region of the pre-edge features to elucidate changes at different temperature. (c) Temperature-induced change in coordination number of Zn-Mg and Zn-O bonds during the reaction.

The *operando* XANES spectra during ethanol conversion are presented in **Figure 6.18**. Similar to study on CuMgSi, the experiment was conducted with increasing temperature under ethanol flow (**Figure 6.18b**). The MS data of the experiment shows similarities with CuMgSi. In particular, acetaldehyde was produced very early as well following the induction time between ethanol flowing into the reactor and the product stream entering the MS. The production of 1,3-BD follows similar trend, i.e. started being produced at lower temperature before really ramping up at ~300 °C. This sudden increase at 300 °C coincides with the increase in acetaldehyde production as well, which suggests that there are two active sites for ethanol dehydrogenation for both catalysts. The presence of these two sites on two promoted catalysts indicates that there are identical sites on both catalysts. When compared to unpromoted MgSi catalyst, the acetaldehyde production was found to dramatically increase at this temperature as well. This indicates that Zn and Cu both are present as an additional dehydrogenating site, and that the native weak basic sites responsible for the reaction are still present after promotion.

The Zn^{2+} local structure, however, shows a resilience nature with flowing ethanol, as shown in **Figure 6.18b (inset)**. There was no significant change under ethanol flow, compared to the thermal effect when only helium was flown (**Figure 6.18a**). **Figure 6.18c** further shows the analysis of the EXAFS spectra where there was no significant changes in Zn local coordination number (N) during the reaction. The identified Zn-Mg and Zn-O both remained intact with no change in the local state of the catalyst was observed. This indicates that the Zn-promoted catalyst should be relatively stable compared to Cu-promoted catalyst and possible deactivation is more likely to be related to the formation of carbonaceous deposit on the surface due to the higher activity exhibited by the additional redox and Lewis acid sites provided by the Zn dopant.[15]

Table 6.6. Best fitting results for ZnMgSi, ZnMg, ZnO, MgO and Zn. The structural parameters of standards were listed for comparison.

Sample	**Bond**	**N**	**R (Å)**
ZnMgSi	Zn-O	3.6±0.5	1.98±0.02
	Zn-Mg	4.8±1.6	3.09±0.04
ZnMg	Zn-O	4.7±1.0	2.09±0.04
	Zn-Mg	14.0±2.8	3.05±0.02
ZnO	Zn-O	4	1.94
	Zn-Zn	6	3.15
	Zn-Zn	6	3.2
MgO	Mg-O	6	2.11
	Mg-Mg	12	2.98
Zn foil	Zn-Zn	6	2.66
	Zn-Zn	6	2.88

4. Conclusions

Cu- and Zn-promoted wet kneaded MgO/SiO_2 catalysts were interrogated *in situ* and *operando* and provided new insights into the structure and reactivity of their catalytic sites during ethanol reaction to 1,3-BD. No distinct crystalline promoter phases were obtained according to XRD and STEM measurements and Cu and Zn was suggested to bind strongly with the native OH groups. Under dehydrated conditions, oligomeric Cu-O species were found to dominate CuMgSi while the combination of very small <4 nm ZnO nanoparticles and possibly solid Zn solution with MgO have been observed using a combination of UV-Vis and STEM measurements. The reduced amount of strong basic sites due to the metal promoter binding was found to affect RDS shift from acetaldehyde formation to MPV reduction. *In situ* DRIFT spectroscopy results allowed to decouple the aldol condensation and dehydrogenation fundamental steps that takes place on the surface suggesting that promoting the catalyst with transition metal promoters enhanced the ability of the catalyst to carry out aldol condensation as correlated with the steady state reactivity experiments. *In situ* UV-Vis spectroscopy suggested appearance of π- π* electronic transitions of allylic cations, cyclic or aromatic species on the catalysts while also providing insights on the oligomeric structure of the active sites. In particular, oligomeric CuO species with ~0.8 Cu nearest neighbor were found to decrease in intensity suggesting their involvement in ultimate catalytic Cu^0 species formation.

Our *operando* X-ray measurements were combined with *ab initio* multiple scattering modelling to unravel the exact electronic structure of the Cu and Zn promoters. These measurements were performed as a function of temperature and signified that Cu-Cu bond appeared at reaction temperatures of 400 ^oC on the aged (TOS of 6-7 hours) catalyst at the expense of Cu-O bonds. Cu replaced Mg in MgO lattice to eventually lead to Cu aggregates. This is akin to the literature reports where deactivation of Cu-containing catalysts was suggested due to the carbonaceous deposits rather than sintering of the promoter. Furthermore, the 8982 eV peak typically assigned to Cu^+ species, in our work was assigned to a 4-fold coordinate Cu species, rather than Cu_2O and is proposed as the key intermediate leading to increase in Cu-Cu bond number. It is transient and is only populated at temperatures lower than 400 ^oC and starts decreasing to yield Cu^0 during aging with ethanol. Two types of Zn bonds, namely Zn-O and Zn-Mg, were identified during X-ray analysis and showed resilience to ethanol under operating conditions. Particularly, Zn was nearly 6-coordinated when in the vicinity of Mg while Zn-O species showed nearly 4 nearest neighbors.

Chapter 7 – Supporting Information

S6.1 Catalyst Characterization

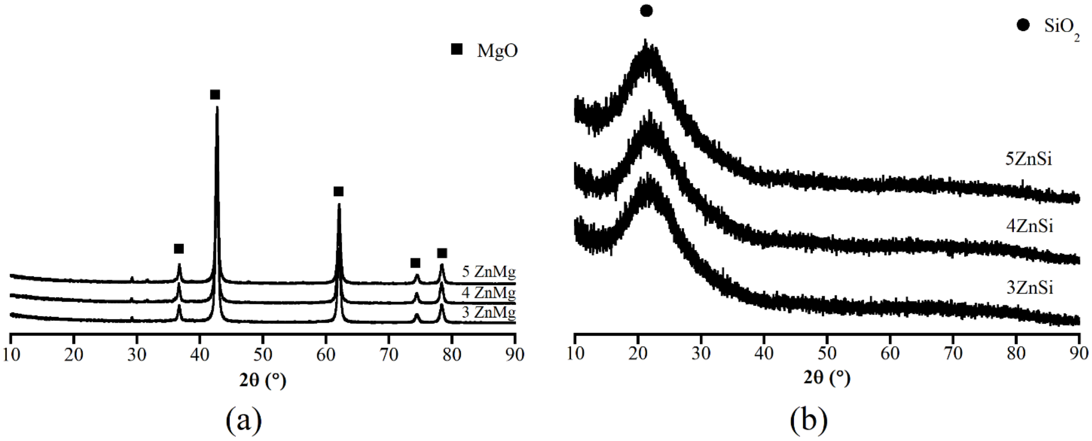

Figure S6.1. XRD patterns of (a) Zn/MgO and (b) Zn/SiO$_2$ at different loadings.

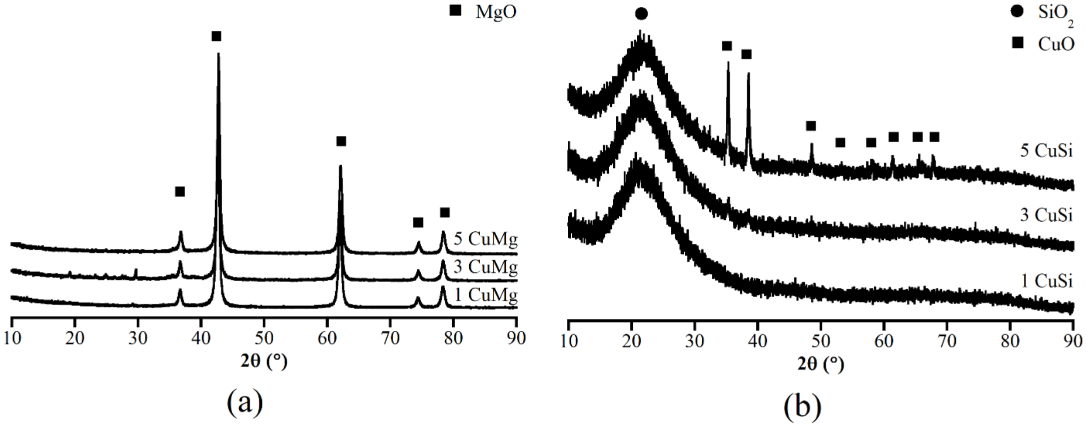

Figure S6.2. XRD patterns of (a) Cu/MgO and (b) Cu/SiO$_2$ at different loadings.

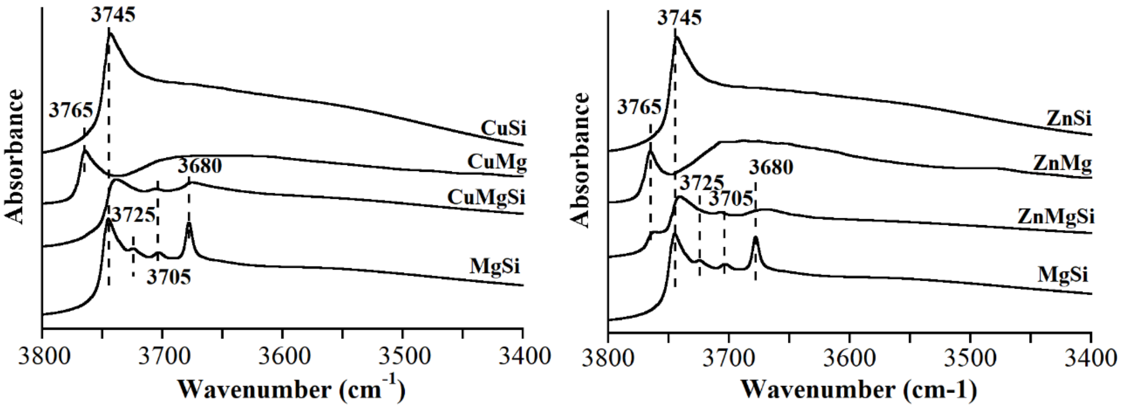

Figure S6.3. *In-situ* DRIFTS of OH region of dehydrated MgSi catalysts references at 100°C for Cu-promoted (left) and Zn-promoted (right). Spectra are offset for clarity.

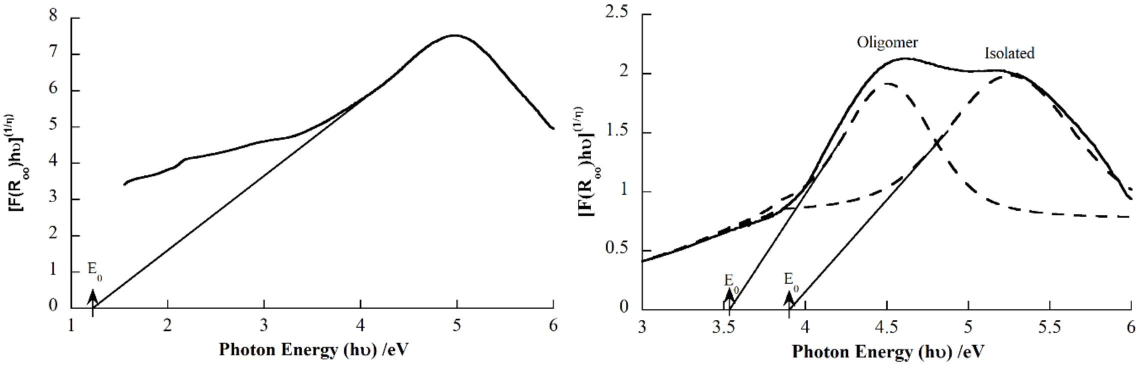

Figure S6.4. Tauc plot of CuO (left) and deconvoluted Cu species of CuMgSi catalyst (right) to determine the edge energy/band gap (E_0) for correlation with number of Cu coordination.

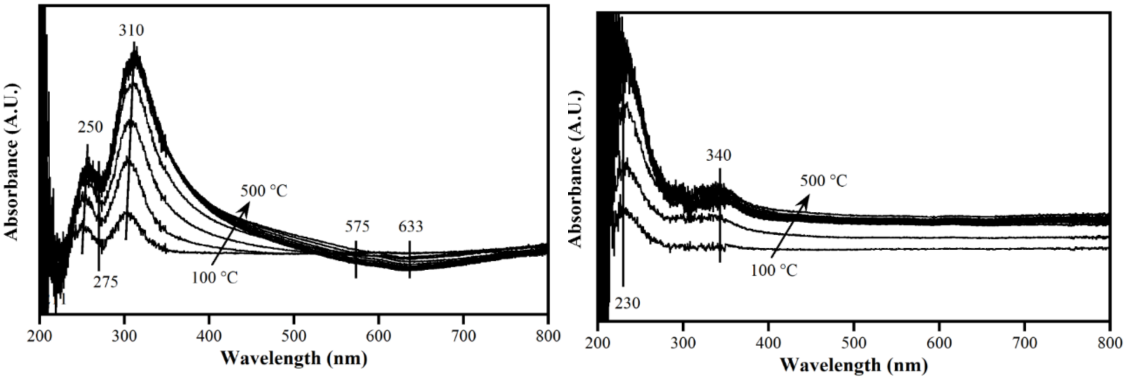

(a) (b)

Figure S6.5. *In-situ* UV-Vis difference spectra of oxidative dehydration of (a) CuMgSi and (b) ZnMgSi.

S6.2 Catalyst Acid-Base characterization

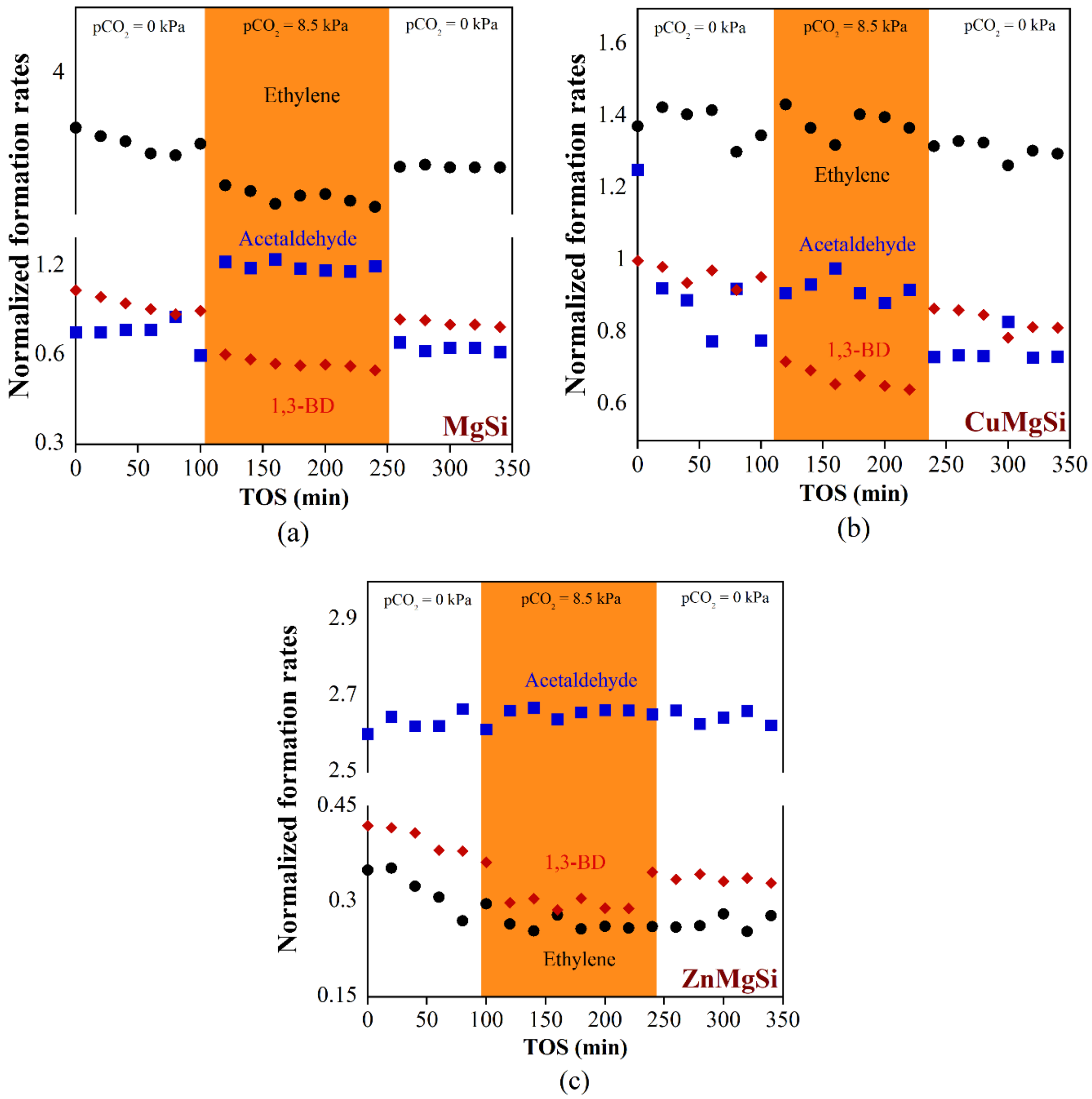

Figure S6.6. Poisoning reactivity testing using CO_2 to determine the role of basic sites during ethanol conversion to 1,3-BD over (a) MgSi, (b) CuMgSi, and (c) ZnMgSi. Reactions are carried out at 400 °C, $m_{cat} = 0.1$ g, $p_{ethanol} = 2.5$ kPa, total flow = 55 ml/min. All formation rates are normalized to initial 1,3-BD formation rate.

The CO_2 coflow is shown to inhibit 1,3-BD production on all catalysts while also increasing the production of acetaldehyde, except for ZnMgSi. CO_2 interacts only with strong basic sites, give its nature as a weak acid, and the change in acetaldehyde and ethylene production suggests the role of weak basic sites and strong basic sites in catalyzing the dehydrogenation and dehydration steps, respectively. The experiment on metal-promoted catalysts suggest that promotion with Cu or Zn decreases the strong basic sites since the ethylene production is not severely affected. The interaction between the catalysts' surface with CO_2 was studied by means of *in-situ* DRIFTS using CO_2 as a probe molecule. The experiment corroborates the *in-situ* poisoning experiments, where the amount of strong basic sites, demonstrated by the peaks assigned to monodentate and polydentate carbonate, are reduced upon introduction of transition metal promoters.[87] Upon introduction of the promoters, change in the stability of both monodentate and polydentate carbonate is lowered at higher temperature, with carboxylate species is now formed on the catalyst. CO_2 adsorption on transition metal oxides generally yields an additional carboxylate species, which is stabilized by back-bonding between d-orbitals of the metal ion and π^* orbital of the C=O bond.[88] Given its much lower stability, this carboxylate must indicate a weaker basic site that is present on the catalysts. Peak assignments of the CO_2 surface species are tabulated in **Table S1**.

Table S6.1. Peak assignments of surface CO_2 species identified on MgSi, CuMgSi, and ZnMgSi catalysts.

Species	**Vibrational mode**	**Catalysts**		
		MgSi	**CuMgSi**	**ZnMgSi**
Monodentate carbonate	υ_{as} OCO	1506	1500	1500
	υ_s OCO	1441	1440	1440
Bidentate carbonate	υ_{as} OCO	1663	1611	1611
	υ_s OCO	1362	-	-
Symmetrical	υ OCO	1425	-	-
Polydentate Carbonate	υ_{as} OCO	1571	1573	1566
	υ_s OCO	1380	1384	1391
Bicarbonate	υ_{as} OCO	1634	1644	1644
	υ_s OCO	1460	1464	1464
	δ OH	1280	1290	~1290
Carboxylate	υ_{as} OCO	N/A	1593	1593
	υ_s OCO	N/A	1374	1374

Poisoning using propionic acid shows significant reduction in 1,3-BD production for all catalysts. The reversibility nature of this change indicates that these catalysts in general had very little amount of strong basic sites. The experiments demonstrated that the acetaldehyde formation rate was more significantly affected during propionic cofeeding on promoted catalysts, i.e. CuMgSi and ZnMgSi. From **Figure S6.8**, it is apparent that the basicity was very different for the transition metal-promoted catalysts. Propionic acid was shown to interact more strongly with the transition metal sites deactivating active sites more readily, as shown by the degree of retardation it caused during propionic acid cofeeding.

Coflowing NH_3 resulted in poisoning of acid sites of the catalysts, and mechanistically, these sites are responsible for the dehydration steps that follow aldol condensation.[2] In this work, ethylene and 1,3-BD production were adversely affected in both ZnMgSi and CuMgSi, as opposed to MgSi. Which indicates the higher availability of total acid sites on unpromoted MgSi catalyst. The decrease in acetaldehyde production on

CuMgSi is due to competitive adsorption and activation of NH_3, since CuO catalysts are well-known SCR catalysts.[65,66] Zn promotion, on the other hand, showed a very strong dehydrogenation enhancement with acetaldehyde being accumulated on the catalyst and shifting the RDS to MPV reduction.

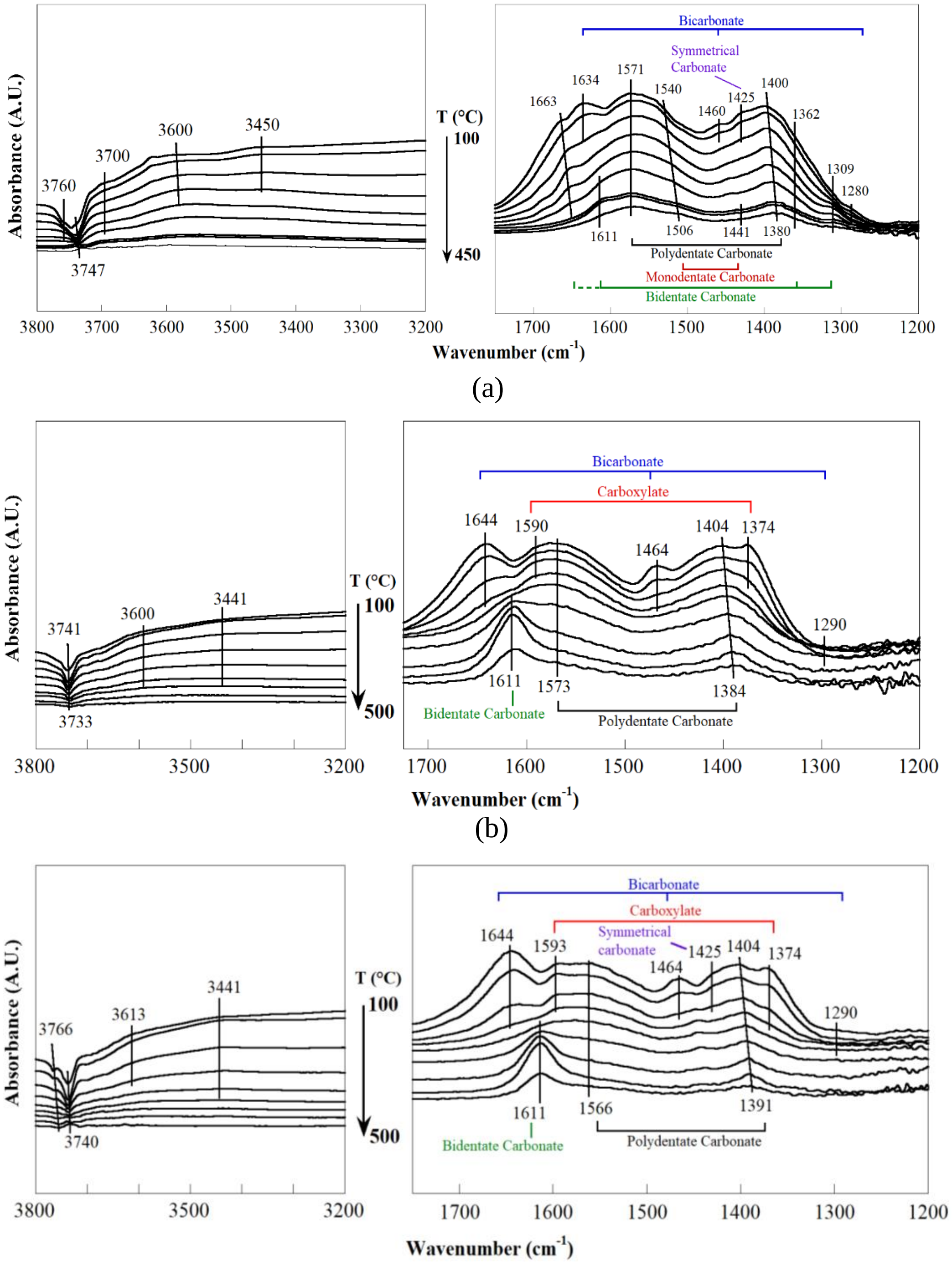

(a)

(b)

(c)

Figure S6.7. CO_2 Temperature Programmed-DRIFTS on (a) MgSi, (b) CuMgSi, and (c) ZnMgSi.

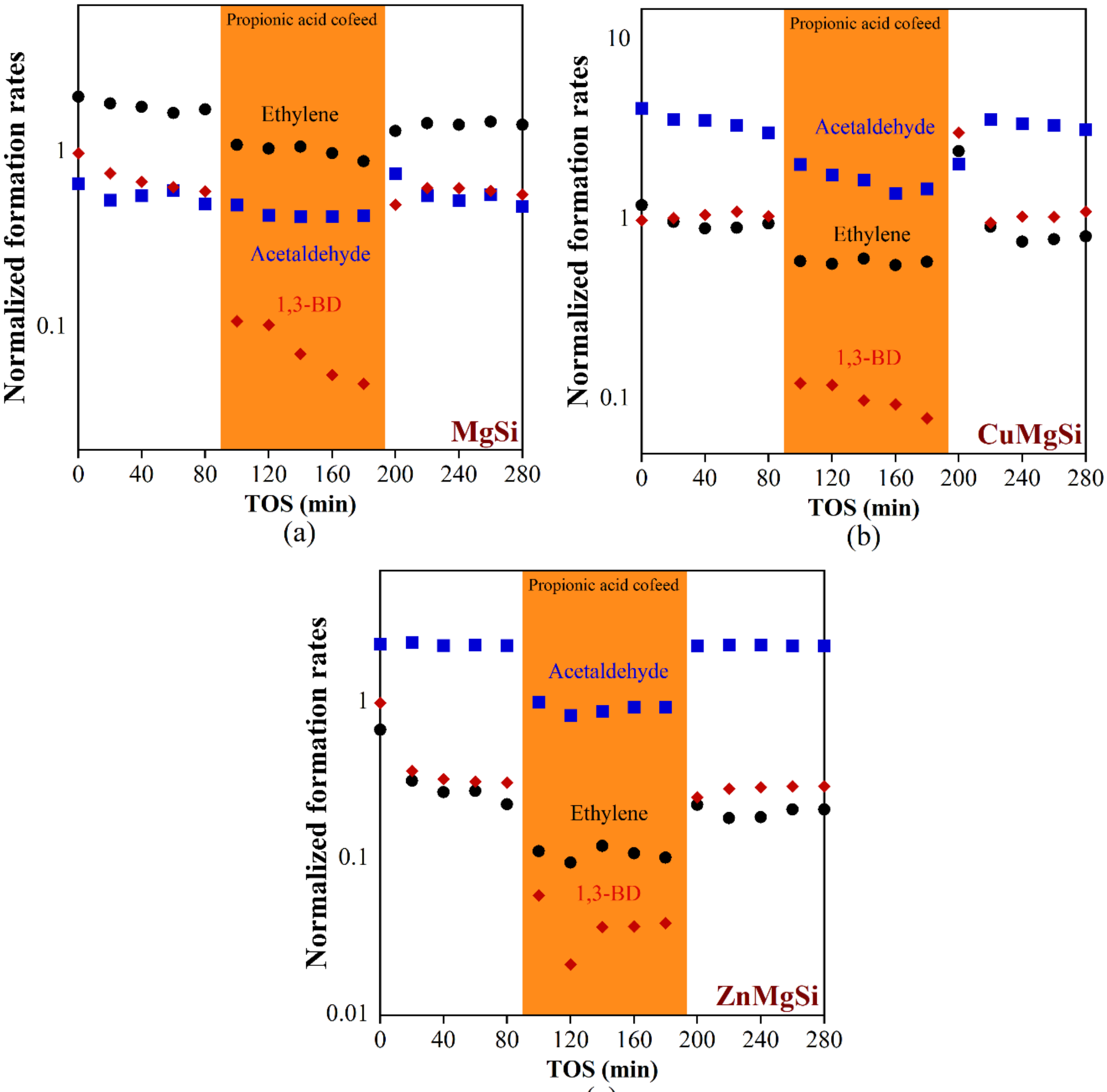

(a)

(b)

(c)

Figure S6.8. Poisoning reactivity testing using propionic acid to determine the role of basic sites during ethanol conversion to 1,3-BD over (a) MgSi, (b) CuMgSi, and (c) ZnMgSi. Reactions are carried out at 400 °C, $m_{cat} = 0.1$ g, $p_{ethanol} = 2.5$ kPa, total flow = 55 ml/min. All formation rates are normalized to initial 1,3-BD formation rate.

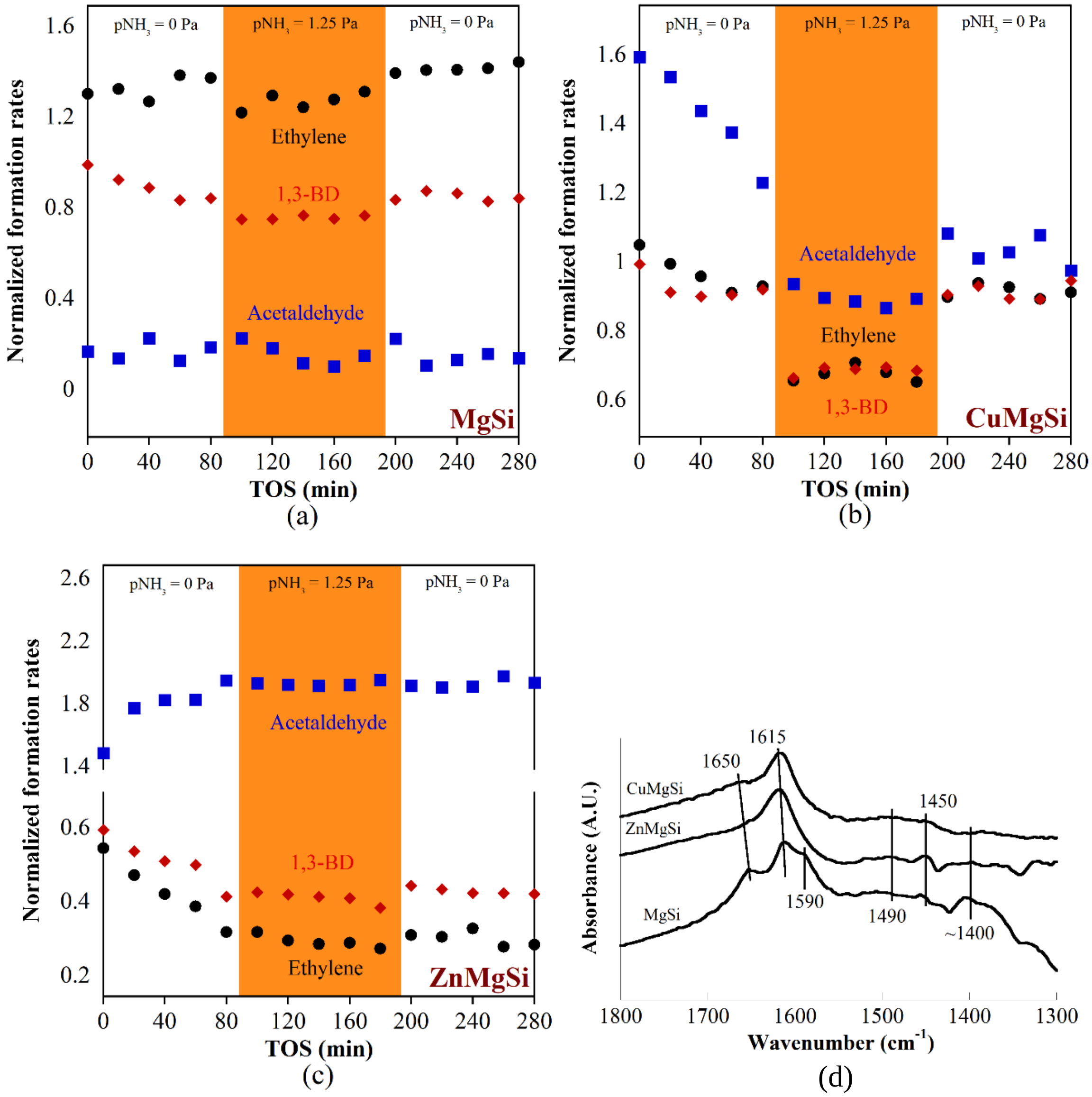

(a) (b) (c) (d)

Figure S6.9. Poisoning reactivity testing using NH_3 to determine the role of acid sites during ethanol conversion to 1,3-BD over (a) MgSi, (b) CuMgSi, and (c) ZnMgSi. Reactions are carried out at 400 °C, $m_{cat} = 0.1$ g, $p_{ethanol} = 2.5$ kPa, total flow = 30 ml/min (without NH_3), 55 ml/min (with NH_3). All formation rates are normalized to initial 1,3-BD formation rate. NH_3 desorption spectra on MgSi catalysts at 100°C are shown in (d).

The surface acidity of the catalysts was investigated with DRIFTS using NH_3 as a probe molecule. NH_3 is the most commonly used probe molecule, due to its small size, which can penetrate all sites available on the catalyst without being limited by catalyst geometry.[89–91] The Lewis acid sites are discriminated by the bending and stretching modes of the coordinated NH_3, i.e. NH_3 unpaired electron donated to metal sites and ammonium ion formed due to the strong OH acid sites.[90] From **Figure S6.9d,** peaks at 1650, 1615, and 1590 cm^{-1} are found in the N-H deformation region. The absence of peak at ~1450 cm^{-1} indicates the non-existence Brønsted acid sites, while the aforementioned peaks are assigned to two different Lewis acid sites. Using the help of DFT, peaks at 1650 and 1615 cm^{-1} are assigned to asymmetric N-H bending mode of Lewis-bound NH_3 species, while 1590 cm^{-1} is assigned to symmetric N-H bending mode of the Lewis-bound NH_3 species. In particular, 1650 cm^{-1} and 1590 cm^{-1} represent the same species that disappeared upon promotion with transition metal sites; assigned to Mg^{2+}_{3C} from our calculation, while the corresponding symmetric bending mode should be around ~1580 cm^{-1} give the split. Note that the DRIFTS simulation of both open and closed sites does not lead to proper discrimination of both sites, and hence this technique should not be used to differentiate both sites (**Table S2**). The Several other peaks at 1490, 1400, and 1370 cm^{-1} are associated with dissociative adsorption of NH_3 that takes place at low temperature.[89]

Table S6.2. DFT simulation of NH_3 on MgO slab. Simulation was done using VASP, PBE functionals on 2x2x1 k-point mesh.

Type	**Binding site**	**Vibrational mode**	
		δ_{as} NH_2	**δ_s NH_2**
Open	4C	1616	1590
	3C	1598	1557
Closed	4C	1612	1595
	3C	1645	1601

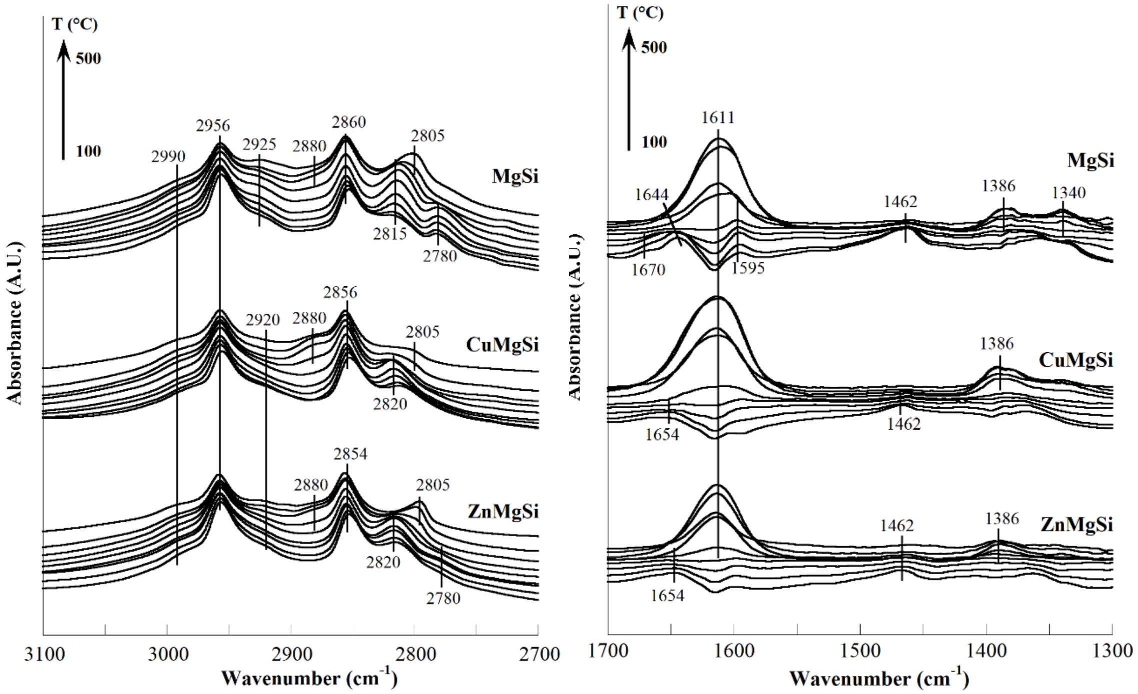

Figure S6.10. DRIFTS spectra in the C-H stretching (left) and bending (right) region of methanol desorption under He flow on unpromoted (top) and promoted (bottom) catalysts.

To further characterize the active sites on the MgSi catalysts, *operando* methanol DRIFTS-MS was carried out due to its versatility as a probe molecule.[92,93] On the basic sites methanol produces CO_2, acidic sites yield dimethyl ether (DME), while redox sites will form formaldehyde.[93] Hence, this *operando* testing allows further measurement of changes in catalyst redox properties, not directly available via CO_2 and NH_3 testing. The DRIFTS spectra of MgSi catalysts are shown in **Figure S6.10**. The C-H region (**Figure S6.10, left**) is typically used to identify the presence of surface methoxide.[92] Upon CH_3OH adsorption on the surface, several peaks showed up at 100 °C, i.e., 2990, 2965, 2920, 2860, 2820, and 2780 cm^{-1}. Methoxy species bounded to SiO_2 sites, such as Si-OCH_3, are indicated by the peaks at 2990, 2965 and 2860 cm^{-1}, assigned to υ_{as} (CH_3), υ_s (CH_3), and $2\delta_s$ (CH_3), respectively.[94] The analogs of these peaks for Mg-OCH_3 are located at 2920, 2820, and 2780 cm^{-1}.[95,96] The presence of the two kinds of adsorbed methoxy species have previously been observed by Wachs and coworkers.[94] In their study, it was shown that surface methoxide was present as Si- and V- bounded in the case of V_2O_5/SiO_2 catalyst. A shoulder at 2880 cm^{-1} is clearly seen on Cu- and Zn-promoted samples, but is lower in intensity for the unpromoted sample. This peak has previously been assigned to the υ_s (CH) of formaldehyde, formed by the readsorption of the redox product.[94] The peak at >350 °C, i.e., 2805 cm^{-1}, can possibly be attributed to surface formaldehyde υ (CH), based on Busca's work.[97]

Methanol typically adsorbs as two kinds of species, as surface methoxy (dissociative adsorption) and as a molecularly bonded species to Lewis acid site in a minor amount.[94] The asymmetric and symmetric methyl bends of the former are located around ~1450 and ~1430 cm^{-1}, while the second species is characterized by its OH bending at ~1360 cm^{-1} (**Figure S6.10, right**). These three peaks can be found on the spectra at low temperatures, while they disappear at higher temperatures. The adsorbed methoxy species further dehydrogenate into surface formate via C-H bond breaking on the redox site, and the basic site will perform another C-H bond scission to make carbonate.[93] The bicarbonate species, as explained before, is characterized by peaks at 1644 and 1464 cm^{-1}. The latter is overlapped by the methoxide methyl bending mode, but still apparent due to the broadness of the peak. An additional peak at 1670 cm^{-1} also occurred in these spectra, as it does for CO_2 adsorption, illustrated in **Figure S6.10**. At higher temperatures monodentate carbonate is apparent at 1386 cm^{-1} and is accompanied by a shoulder at ~1587 cm^{-1}. This is obscured by the intensity of the bidentate carbonate peak at 1611 cm^{-1}. The presence of surface formate in this experiment is revealed by the peaks at 1595 and a peak at around

~1340 cm^{-1}, assigned to υ_a (OCO) and υ_s (OCO), respectively.[97] The prevalence of surface formate on the unpromoted catalyst further demonstrates the basicity of the catalyst. The peaks at 1595 and 1340 cm^{-1} are much less pronounced in the spectra of the Cu- and Zn-promoted catalysts. This could indicate the spontaneous desorption of the produced formaldehyde, even though at higher temperatures, re-adsorption of formaldehyde is more pronounced in the case of promoted catalysts, as shown by the peak at 2880 cm^{-1} (**Figure S6.10, left**).

The corresponding MS data from the *operando* methanol spectroscopy are shown in **Figure S6.11**. As discussed, methanol adsorbs in two different ways, by dissociative adsorption and by molecular adsorption on Lewis sites. This is further corroborated by the vapor phase MS data, which shows a methanol peak (m/z = 31) for each catalyst, consisting of two different peaks. The symmetry of these peaks indicates that they consist of two peaks. A second peak, which is apparent as a shoulder at 300 °C, indicates the release of two adsorbed methanol species into the vapor-phase. The lower temperature peaks for the methanol occur at temperatures below 200 °C for each catalyst and are due to the strongly bound, yet molecularly adsorbed, methanol species on the Lewis acid site. The higher temperature peak is due to the recombination of the surface methoxide and surface hydroxyl group. The most striking observation is for the formaldehyde spectra (m/z=29), where the T_p values are situated close to their corresponding methanol T_p peaks. On redox sites, methanol dissociates to give surface methoxide ($CH_3O\cdot$) and surface hydroxyl group ($OH\cdot$). The surface methoxide will then perform a subsequent C-H bond breaking step and desorb as formaldehyde.[98] The un-promoted sample shows a very close T_p for both methanol and formaldehyde (190-193 °C), while the Cu-promoted and Zn-promoted samples show a significantly lowered temperature peak at 177°C. This shows that the redox capability of the catalyst has been improved by transition metal doping. The formaldehyde peak at lower temperature is very close to the methanol peak, at 182 and 185 °C for ZnMgSi and CuMgSi, respectively, which differs only by about 5-8 °C. Formaldehyde is known to re-adsorb onto the surface[94] so the second peak at a higher temperature originates from the desorption of this formaldehyde species.

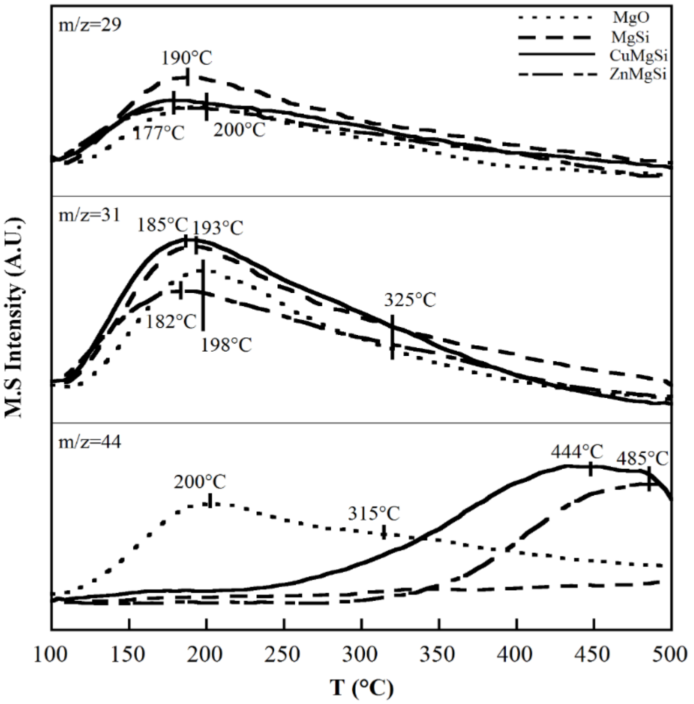

Figure S6.11. Online MS analysis during *operando* methanol DRIFTS of CuMgSi, ZnMgSi, MgSi and reference MgO

The CO_2 temperature profiles (m/z=44) are also shown in **Figure S6.11**. The mechanism of the methanol to CO_2 reaction is complex. Surface formate is required as a surface intermediate and this requires surface oxygen, since formaldehyde possesses only one oxygen atom. The re-adsorption of formaldehyde into surface formate is corroborated by the DRIFTS data shown in **Figure S6.10** and induced by the presence of the basic sites on the surface.[93] Subsequently, C-H bond breaking takes place and then CO_2 is released. Pure MgO is used in this experiment as a reference. On MgO the T_p peaks for methanol, formaldehyde and CO_2 are very close to each other, at 198, 200, and 200 °C, respectively. This indicates a competing, consecutive reaction for both formaldehyde and CO_2 formation. In this case, the desorption of formaldehyde from the surface after methoxy C-H bond breaking has a very similar rate with subsequent HCOO- formation and C-H bond breaking to give off CO_2. The redox capability of MgO is also acknowledged by Badlani and Wachs, where a steady-state reaction of MgO yields both formaldehyde and CO_2 with higher selectivity towards the former.[93] The presence of the second CO_2 peak at 315 °C represents the secondary formation of CO_2 from the re-adsorption of formaldehyde. The CO_2 peak never fully disappears, since there is a small amount of CO_2 being released from bulk magnesium carbonate.[99] Interestingly, this basicity of MgO is not reflected in the MgSi catalyst. The CO_2 peak is practically non-apparent as shown in **Figure S6.11**. SiO_2 is a very inert material, which should be the reason why there is very little CO_2 in the vapor-phase. This is mostly due to methanol thermal decomposition.[93] Wet-kneading with SiO_2 (1:1) should reduce the number of MgO basic sites and induce the formation of different sites, such as closed or open Lewis acid sites. These are formed from the Mg-O-Si linkages[11] and additional redox sites, as shown by the increased formaldehyde production for MgSi. The increased number of redox sites is apparently caused moreso by the higher formaldehyde productivity than by the pure MgO, which is why most MgO catalysts won't perform the ethanol-to-1,3-BD reaction. From our CO_2 DRIFTS experiment in **Figure S6.7,** it can be seen that the CO_2 peaks are present on all catalysts at elevated temperatures, with MgSi possessing the most integrated area. Un-promoted MgSi shows a better retention of

CO_2, demonstrated by the higher intensity of the carbonate peaks at a higher temperature, as compared to ZnMgSi and CuMgSi (**Figure S6.7**). It is likely that once the C-H bond of the surface formate is broken, the CO_2 formed is bound to an oxygen site on the unpromoted catalyst, whereas promotion with Zn or Cu reduced the electronegativity of the nearby oxygen site and released CO_2 at a higher rate than for the unpromoted sample.

A critical analysis done in this work is the comparison of the redox capability of the catalysts, which was done by evaluating the activation energy of the methanol dehydrogenation reaction to yield formaldehyde. The decomposition kinetics of the C-H bond breaking of surface methoxy is known to follow a first order reaction with pre-exponential factor of ~10^{13} s^{-1}.[100] The activation energy was calculated using the Redhead equation[101]

$$\frac{E_a}{RT_p^2} = \frac{\upsilon}{\beta} e^{\left(-\frac{E_a}{RT_p}\right)} \tag{1}$$

where E_a is the activation energy (J/mol), R is the gas constant (J/mol K), T_p is the TPSR temperature (K), β is the heating rate (10 °C/min), and υ is the pre-exponential factor (s^{-1}).

From equation (1), activation energies of 28.4, 27.7 and 26.7 kcal/mol for reference MgO, MgSi and the CuMgSi and ZnMgSi were calculated, respectively. The lowered activation energy explains the more reactive nature of the catalyst, since promotion of the catalyst has been shown to give a lower activation energy for the dehydrogenation reaction. Promotion with Zn and Cu enhances the alcohol dehydrogenation capability.[13,14] This promotional effect doesn't carry over to the ethanol dehydrogenation in a straightforward manner, since for ethanol, utilizing Zn and Cu promotion has shown a very profound effect on the ethanol dehydrogenation step of the reaction.[3] Similarly, the non-existence of DME as the product of the acidic sites can't be translated to the catalyst inability to carry out the dehydration reaction. DME formation requires two available sites that bind two ethoxy species, while for ethylene formation only one site is necessary. The absence of DME in the product goes along well with our steady-state experiment, where hardly any diethyl ether (DEE), an analog for ethanol bimolecular dehydration, is produced. The inability of the catalyst to produce DEE does not necessarily mean it is not acidic, since ethylene is prominently produced during the reaction. This experiment suggests that all the catalysts used in this work do not possess two neighboring acidic sites, which are required to dehydrate alcohols. Furthermore, the semi-quantification of the active sites for redox sites can be calculated by integrating the area under the peak, referenced to the surface area of the catalysts, which are calculated using BET method **(Table S6.3)**.

Table S6.3. Redox properties of the MgSi, CuMgSi and ZnMgSi catalysts and reference MgO obtained from MS measurements. These results have been normalized to the BET surface area (m_2/g) of each catalysts.

Catalysts	Redox site density relative to MgSi	Activation energy (kcal/mol)
Reference MgO	0.48	28.4
MgSi	1.00	27.7
CuMgSi	0.42	26.7
ZnMgSi	0.96	26.7

Promotion of the catalyst with a transition metal unexpectedly reduced the number of redox sites, which indicates the loss of these sites when the catalyst is promoted with transition metals. Promotion with Cu reduced the Redox site density significantly, while Zn barely modified the redox site density, which can be related to the superior ethanol reactivity in the steady-state experiment. The decrease in Redox site density further justifies explanations by previous reports that higher loading would be detrimental to the catalyst activity, as well as Zn's significant enhancement in the ethanol's conversion.[3]

S6.3 *In-situ* and *operando* characterization of Cu and Zn coordination on promoted MgSi catalysts

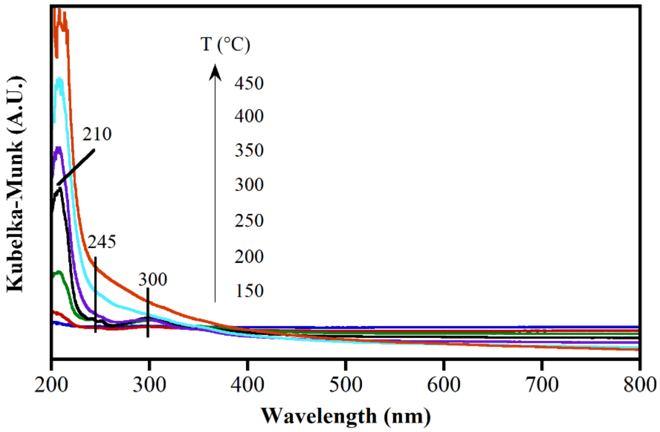

Figure S6.12. *In-situ* UV-Vis DRS of ethanol reaction on undoped MgO/SiO$_2$ catalyst. Difference spectra is shown, where catalyst spectra at 100°C with chemisorbed ethanol is used as a reference.

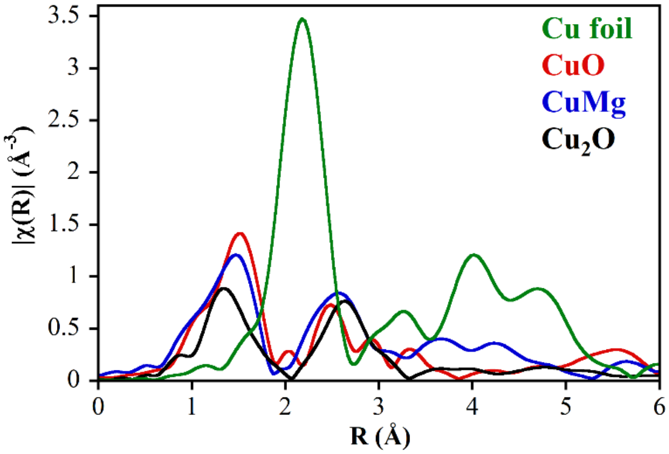

Figure S6.13. R-space EXAFS spectra of CuMg catalyst, in comparison to Cu foil, CuO, and Cu$_2$O

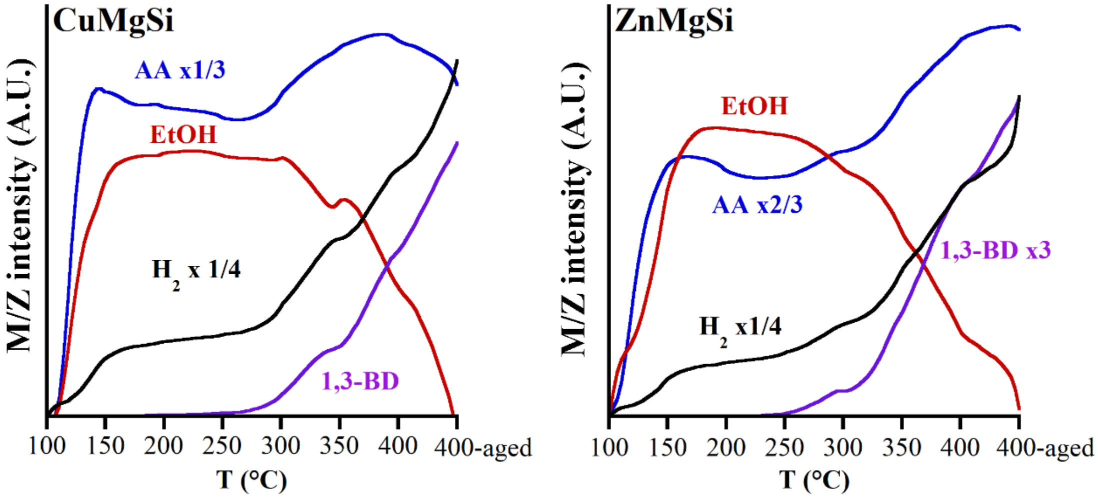

(a) (b)

Figure S6.14. Corresponding MS data of *in-situ* XANES-EXAFS for ethanol to 1,3-BD over (a) CuMgSi, (b) ZnMgSi

References

(1) Posada, J. A.; Patel, A. D.; Roes, A.; Blok, K.; Faaij, A. P. C.; Patel, M. K. *Bioresour. Technol.* **2013**, *135*, 490–499.

(2) Shylesh, S.; Gokhale, A. A.; Scown, C. D.; Kim, D.; Ho, C. R.; Bell, A. T. *ChemSusChem* **2016**, *9* (12), 1462–1472.

(3) Pomalaza, G.; Capron, M.; Ordomsky, V.; Dumeignil, F. *Catalysts* **2016**, *6* (12), 203.

(4) Sushkevich, V. L.; Ivanova, I. I. *ChemSusChem* **2016**, *9* (16), 2216–2225.

(5) Sushkevich, V. L.; Palagin, D.; Ivanova, I. I. *ACS Catal.* **2015**, 4833–4836.

(6) Taifan, W. E.; Bučko, T.; Baltrusaitis, J. *J. Catal.* **2017**, *346*, 78–91.

(7) Müller, P.; Burt, S. P.; Love, A. M.; McDermott, W. P.; Wolf, P.; Hermans, I. *ACS Catal.* **2016**, *6* (10), 6823–6832.

(8) Sushkevich, V. L.; Ivanova, I. I. *Appl. Catal. B Environ.* **2017**, *215*, 36–49.

(9) Chieregato, A.; Velasquez Ochoa, J.; Bandinelli, C.; Fornasari, G.; Cavani, F.; Mella, M. *ChemSusChem* **2014**, *8* (2), 377–388.

(10) Zhang, M.; Gao, M.; Chen, J.; Yu, Y. *RSC Adv.* **2015**, *5* (33), 25959–25966.

(11) Taifan, W.; Yan, G. X.; Baltrusaitis, J. *Catal. Sci. Technol.* **2017**, *7* (20), 4648–4668.

(12) Fan, D.; Dong, X.; Yu, Y.; Zhang, M. *Phys. Chem. Chem. Phys.* **2017**, *19* (37), 25671–25682.

(13) Hayashi, Y.; Akiyama, S.; Miyaji, A.; Sekiguchi, Y.; Sakamoto, Y.; Shiga, A.; Koyama, T.; Motokura, K.; Baba, T. *Phys. Chem. Chem. Phys.* **2016**, *18* (36), 25191–25209.

(14) Angelici, C.; Velthoen, M. E. Z.; Weckhuysen, B. M.; Bruijnincx, P. C. A. *ChemSusChem* **2014**, *7* (9), 2505–2515.

(15) Larina, O.; Kyriienko, P.; Soloviev, S. *Catal. Letters* **2015**, 1–7.

(16) Da Ros, S.; Jones, M. D.; Mattia, D.; Pinto, J. C.; Schwaab, M.; Noronha, F. B.; Kondrat, S. A.; Clarke, T. C.; Taylor, S. H. *ChemCatChem* **2016**, *8*, 1–12.

(17) Ohnishi, R.; Akimoto, T.; Tanabe, K. *J. Chem. Soc. Chem. Commun.* **1985**, No. 22, 1613–1614.

(18) Sushkevich, V. L.; Ivanova, I. I.; Ordomsky, V. V; Taarning, E. *ChemSusChem* **2014**, *7* (9), 2527–2536.

(19) Makshina, E. V.; Janssens, W.; Sels, B. F.; Jacobs, P. A. *Catal. Today* **2012**, *198* (1), 338–344.

(20) Jones, M. D.; Keir, C. G.; Iulio, C. Di; Robertson, R. A. M.; Williams, C. V; Apperley, D. C. *Catal. Sci. Technol.* **2011**, *1* (2), 267–272.

(21) Bond, G. C.; Thompson, D. T. *Catal. Rev. - Sci. Eng.* **1999**, *41* (3 & 4), 319–388.

(22) Guan, Y.; Hensen, E. J. M. J. M. *Appl. Catal. A Gen.* **2009**, *361* (1), 49–56.

(23) Wittcoff, H. A. A. *J. Chem. Educ.* **1983**, *60* (12), 1044.

(24) Sushkevich, V. L.; Ivanova, I. I.; Taarning, E. *ChemCatChem* **2013**, *5* (8), 2367–2373.

(25) Chang, F.-W.; Kuo, W.-Y.; Lee, K.-C. *Appl. Catal. A Gen.* **2003**, *246* (2), 253–264.

(26) Chang, F.-W.; Yang, H.-C.; Roselin, L. S.; Kuo, W.-Y. *Appl. Catal. A Gen.* **2006**, *304* (0), 30–39.

(27) Janssens, W.; Makshina, E. V. V.; Vanelderen, P.; De Clippel, F.; Houthoofd, K.; Kerkhofs, S.; Martens, J. A. A.; Jacobs, P. A. A.; Sels, B. F. B. F. *ChemSusChem* **2014**, *8* (6), 994–1008.

(28) Angelici, C.; Meirer, F.; van der Eerden, A. M. J.; Schaink, H. L.; Goryachev, A.; Hofmann, J. P.; Hensen, E. J. M.; Weckhuysen, B. M.; Bruijnincx, P. C. A. *ACS Catal.* **2015**, *5* (10), 6005–6015.

(29) Kyriienko, P. I.; Larina, O. V; Soloviev, S. O.; Orlyk, S. M.; Calers, C.; Dzwigaj, S.; Pisarzhevsky, L. V. *ACS Sustain. Chem. Eng.* **2017**, *5* (3), 2075–2083.

(30) Sekiguchi, Y.; Akiyama, S.; Urakawa, W.; Koyama, T.; Miyaji, A.; Motokura, K.; Baba, T. *Catal. Commun.* **2015**, *68*, 20–24.

(31) Baylon, R. a. L.; Sun, J.; Wang, Y. *Catal. Today* **2015**, 1–7.

(32) Musolino, V.; Selloni, A.; Car, R. *J. Chem. Phys.* **1998**, *108* (12), 5044.

(33) Pacchioni, G. *J. Chem. Phys.* **1996**, *104* (18), 7329.

(34) Asakura, K.; Iwasawa, Y. *Mater. Chem. Phys.* **1988**, *18*, 499–512.

(35) Colonna, S.; Arciprete, F.; Balzarotti, A.; Fanfoni, M.; De Crescenzi, M.; Mobilio, S. *Surf. Sci.* **2002**, *512*, L341–L345.

(36) Rodriguez, J. a.; Jirsak, T.; Chaturvedi, S. *J. Chem. Phys.* **1999**, *111* (17), 8077.

(37) Rodriguez, J. a.; Jirsak, T.; Freitag, A.; Larese, J. Z. *J. Phys. Chem. B* **2000**, *2* (100), 7439–7448.

(38) Zhukovskii, Y. F.; Kotomin, E. a.; Borstel, G. *Vacuum* **2004**, *74* (2), 235–240.

(39) Matveev, A.; Neyman, K.; Yudanov, I.; Rösch, N. *Surf. Sci.* **1999**, *426* (1), 123–139.

(40) Galadima, A.; Muraza, O. *J. Nat. Gas Sci. Eng.* **2015**, *25*, 303–316.

(41) Zonetti, P. C. C.; Celnik, J.; Letichevsky, S.; Gaspar, A. B. B.; Appel, L. G. G. *J. Mol. Catal. A Chem.* **2011**, *334* (1–2), 29–34.

(42) Velu, S.; Suzuki, K.; Okazaki, M.; Kapoor, M. P.; Osaki, T.; Ohashi, F. *J. Catal.* **2000**, *194* (2), 373–384.

(43) Ro, I.; Liu, Y.; Ball, M. R. R.; Jackson, D. H. K. H. K.; Chada, J. P. P.; Sener, C.; Kuech, T. F. F.; Madon, R. J. J.; Huber, G. W. W.; Dumesic, J. A. A. *ACS Catal.* **2016**, *6* (10), 7040–7050.

(44) Bravo-Suarez, J. J.; Subramaniam, B.; Chaudhari, R. V. *J. Phys. Chem. C* **2012**, *116* (34), 18207–18221.

(45) Vlaic, G.; Bart, J. C. J. C. J.; Cavigiolo, W.; Mobilo, S. *Chem. Phys. Lett.* **1980**, *76* (3), 453–459.

(46) Witzke, M. E. E.; Dietrich, P. J. J.; Ibrahim, M. Y. S. Y. S.; Al-Bardan, K.; Triezenberg, M. D. D.; Flaherty, D. W. W. *Chem. Commun.* **2017**, *53* (3), 597–600.

(47) Chouillet, C.; Villain, F.; Kermarec, M.; Lauron-Pernot, H.; Louis, C. *J. Phys. Chem. B* **2003**, *107* (15), 3565–3575.

(48) Didenko, O. Z.; Kosmambetova, G. R.; Strizhak, P. E. *Chinese J. Catal.* **2008**, *29* (11), 1079–1083.

(49) Pascual, J. L.; Savoini, B.; González, R. *Phys. Rev. B* **2004**, *70* (4), 45109.

(50) Hosoglu, F.; Faye, J.; Mareseanu, K.; Tesquet, G.; Miquel, P.; Capron, M.; Gardoll, O.; Lamonier, J. F.; Lamonier, C.; Dumeignil, F. *Appl. Catal. A Gen.* **2015**, *504*, 533–541.

(51) Laskowski, R.; Blaha, P.; Schwarz, K. *Phys. Rev. B* **2003**, *67* (7), 75102.

(52) Breedon, M.; Spencer, M. J. S.; Yarovsky, I. *Surf. Sci.* **2009**, *603* (24), 3389–3399.

(53) Gruver, V.; Sun, A.; Fripiat, J. J. *Catal. Letters* **1995**, *34* (3–4), 359–364.

(54) Chung, S.-H.; Angelici, C.; Hinterding, S. O. M.; Weingarth, M.; Baldus, M.; Houben, K.; Weckhuysen, B. M.; Bruijnincx, P. C. A. *ACS Catal.* **2016**, *6* (6), 4034–4045.

(55) Harvey, J. N. Kaltsoyannis, N., McGrady, J. E., Eds.; Springer Berlin Heidelberg: Berlin, Heidelberg, Heidelberg, 2004; pp 151–184.

(56) Chizallet, C.; Costentin, G.; Che, M.; Delbecq, F.; Sautet, P.; Surface, D.; Marie, P. *J. Am. Chem. Soc.* **2007**, No. 19, 6442–6452.

(57) Gawande, M. B.; Goswami, A.; Felpin, F.-X.; Asefa, T.; Huang, X.; Silva, R.; Zou, X.; Zboril, R.; Varma, R. S. *Chem. Rev.* **2016**, *116* (6), 3722–3811.

(58) Marion, M. C.; Garbowski, E.; Primet, M. *J. Chem. Soc.{,} Faraday Trans.* **1990**, *86* (17), 3027–3032.

(59) Coluccia, S.; Lavagnino, S.; Marchese, L. *Mater. Chem. Phys.* **1988**, *18* (5), 445–464.

(60) Yoshida, H.; Shimizu, T.; Murata, C.; Hattori, T. *J. Catal.* **2003**, *220* (1), 226–232.

(61) Cavalleri, M.; Pelmenschikov, A.; Morosi, G.; Gamba, A.; Coluccia, S.; Martra, G. In *Oxide-based Systems at the Crossroads of ChemistrySecond International Workshop October 8-11, 2000, Como, Italy*; A. Gamba, C. C. and S. C. B. T.-S. in S. S. and C., Ed.; Elsevier, 2001; Vol. Volume 140, pp 131–139.

(62) Valizadeh, H.; Azimi, A. A. *J. Iran. Chem. Soc.* **2011**, *8* (1), 123–130.

(63) De Baerdemaeker, T.; Feyen, M.; Müller, U.; Yilmaz, B.; Xiao, F.-S.; Zhang, W.; Yokoi, T.; Bao, X.; Gies, H.; De Vos, D. E. *ACS Catal.* **2015**, 3393–3397.

(64) Ho, C. R.; Shylesh, S.; Bell, A. T. *ACS Catal.* **2016**, *6* (2), 939–948.

(65) Liu, Q.; Liu, Z.; Li, C. *Chinese J. Catal.* **2006**, *27* (7), 636–646.

(66) Díaz, G.; Pérez-Hernández, R.; Gómez-Cortés, A.; Benaissa, M.; Mariscal, R.; Fierro, J. L. G. *J. Catal.* **1999**, *187* (1), 1–14.

(67) Baltrusaitis, J.; Mendoza-Sanchez, B.; Fernandez, V.; Veenstra, R.; Dukstiene, N.; Roberts, A.; Fairley, N. *Appl. Surf. Sci.* **2015**, *326*, 151–161.

(68) Georgieff, K. K. *J. Appl. Polym. Sci.* **1966**, *10* (9), 1305–1313.

(69) Bevington, J. C.; Norrish, R. G. W. *Proc. R. Soc. London. Ser. A. Math. Phys. Sci.* **1949**, *196* (1046), 363 LP-378.

(70) Song, H.; Ozkan, U. S. *J. Catal.* **2009**, *261* (1), 66–74.

(71) Inui, K.; Kurabayashi, T.; Sato, S. *Appl. Catal. A Gen.* **2002**, *237* (1–2), 53–61.

(72) Singh, M.; Zhou, N.; Paul, D. K.; Klabunde, K. J. *J. Catal.* **2008**, *260* (2), 371–379.

(73) Palagin, D.; Sushkevich, V. L.; Ivanova, I. I. *J. Phys. Chem. C* **2016**, *120* (41), 23566–23575.

(74) Ordomsky, V. V.; Sushkevich, V. L.; Ivanova, I. I. *J. Mol. Catal. A Chem.* **2010**, *333* (1), 85–93.

(75) Wulfers, M. J.; Tzolova-Müller, G.; Villegas, J. I.; Murzin, D. Y.; Jentoft, F. C. *J. Catal.* **2012**, *296*, 132–142.

(76) Nordvang, E. C.; Borodina, E.; Ruiz-Martínez, J.; Fehrmann, R.; Weckhuysen, B. M. *Chem. – A Eur. J.* **2015**, *21* (48), 17324–17335.

(77) Kang, M.; Park, E. D.; Kim, J. M.; Yie, J. E. *Catal. Today* **2006**, *111* (3–4), 236–241.

(78) Xu, R.; Wei, W.; Li, W. H.; Hu, T. D.; Sun, Y. H. *J. Mol. Catal. A Chem.* **2005**, *234* (1–2), 75–83.

(79) Choy, J.-H.; Kim, D.-K.; Hwang, S.-H.; Demazeau, G. *Phys. Rev. B* **1994**, *50* (22), 16631–16639.

(80) Rehr, J. J.; Kas, J. J.; Vila, F. D.; Prange, M. P.; Jorissen, K. *Phys. Chem. Chem. Phys.* **2010**, *12* (21), 5503–5513.

(81) Velu, S.; Wang, L.; Okazaki, M.; Suzuki, K.; Tomura, S. *Microporous Mesoporous Mater.* **2002**, *54* (1–2), 113–126.

(82) Galoisy, L.; Cormier, L.; Calas, G.; Briois, V. *J. Non. Cryst. Solids* **2001**, *293–295*, 105–111.

(83) Wang, H.-C.; Wei, Y.-L.; Yang, Y.-W.; Lee, J.-F. *J. Electron Spectros. Relat. Phenomena* **2005**, *144–147*, 817–819.

(84) Kelly, R. A.; Andrews, J. C.; DeWitt, J. G. *Microchem. J.* **2002**, *71* (2), 231–245.

(85) Waychunas, G. A.; Fuller, C. C.; Davis, J. A.; Rehr, J. J. *Geochim. Cosmochim. Acta* **2003**, *67* (5), 1031–1043.

(86) Jeong, E.-S.; Park, C.; Jin, Z.; Yoo, J.; Yi, G.-C.; Han, S.-W. *Journal of Nanoscience and Nanotechnology*. pp 1880–1883.

(87) Di Cosimo, J. I.; Díez, V. K.; Xu, M.; Iglesia, E.; Apesteguía, C. R. *J. Catal.* **1998**, *178* (2), 499–510.

(88) Busca, G.; Lorenzelli, V. *Mater. Chem.* **1982**, *7* (1), 89–126.

(89) T. Barzetti, E. Selli, D. Moscotti, L. F. *J. Chem. Soc. Faraday Trans.* **1996**, *92* (8), 1401–1407.

(90) Lercher, J. A.; Grijndling, C.; Eder-Mirth, G. *Catal. Today* **1996**, *27*, 353–376.

(91) Lavalley, J. C. *Catal. Today* **1996**, *27*, 377–401.

(92) Burcham, L. J.; Briand, L. E.; Wachs, I. E. *Langmuir* **2001**, *17* (20), 6164–6174.

(93) Badlani, M.; Wachs, I. E. *Catal. Letters* **2001**, *75* (3–4), 137–149.

(94) Burcham, L. J.; Deo, G.; Gao, X.; Wachs, I. E. *Top. Catal.* **2000**, *11–12*, 85–100.

(95) Di Valentin, C.; Del Vitto, A.; Pacchioni, G.; Abbet, S.; Wörz, A. S. S.; Judai, K.; Heiz, U. *J. Phys. Chem. B* **2002**, *106* (46), 11961–11969.

(96) Kondo, J.; Sakata, Y.; Maruya, K.; Tamaru, K.; Onishi, T. *Appl. Surf. Sci.* **1987**, *28*, 475–478.

(97) Busca, G.; Lamotte, J.; Lavalley, J. ciaude; Lorenzelli, V. *J. Am. Chem. Soc.* **1987**, *109* (17), 5197–5202.

(98) Kim, T.; Wachs, I. E. *J. Catal.* **2008**, *255* (2), 197–205.

(99) Angelici, C.; Velthoen, M. E. Z.; Weckhuysen, B. M.; Bruijnincx, P. C. A. *Catal. Sci. Technol.* **2015**.

(100) Feng, T.; Vohs, J. M. *J. Catal.* **2002**, *208* (2), 301–309.

(101) Redhead, P. a. *Vacuum* **1962**, *12* (4), 203–211.

Chapter 7

Conclusions and future outlook

1. Conclusions

Chapter 3

A complex reactive mechanism of ethanol to form 1,3-butadiene was explored using periodic quantum chemical methods. Three reaction mechanisms, in particular, were tested using DFT, namely Prins condensation, aldol condensation, and hemiacetal rearrangements. Based on the thermodynamic and kinetic data determined within this study we identified four rate important steps in the overall process, namely ethanol dehydrogenation and dehydration to acetaldehyde and ethylene, respectively, aldol condensation between adsorbed enolate and physisorbed acetaldehyde, and finally carbanion stabilization between ethylene and acetaldehyde. In particular, ethanol dehydration to form ethylene possessed lower energy barrier than dehydrogenation to yield acetaldehyde suggesting competing reactive pathways. Aldol condensation step to form acetaldol was preceded with forward free-energy barrier of 16.1 kcal/mol but limited thermodynamically with endergonic reaction free energy of 12.9 kcal/mol. The energetic barrier for the first C-C bond formation step in the Prins condensation mechanism at 28.8 kcal/mol also demonstrated the viability of this mechanism over an idealized MgO defect sites. The model employed here represents a simplified, ideal defected MgO surface, without taking into account participation of the formed Mg-O-Si bonds resulting from interaction between MgO-SiO_2 and OH groups, significantly affected the acidity-basicity of the catalyst.

Chapter 4

Surface chemistry of WK (1:1) catalyst during the reaction of ethanol and the corresponding reactive intermediates, including acetaldehyde, crotonaldehyde, crotyl alcohol, was investigated using *in situ* DRIFTS measurements combined with DFT calculations. Involvement of the native hydroxyl groups was shown to be transient, mostly due to the hydrogen bonding with the intermediates. The stability of these OH groups suggested that interaction between the catalyst and intermediates might be due to the interaction between the Lewis metal heteroatom with the intermediates, instead of with the OH groups. Ethanol adsorbed as both physisorbed and chemisorbed surface species, while acetaldehyde, when formed exhibited high reactivity to yield crotonaldehyde but the excess resulted in strongly bound surface species assigned to surface acetate, and/or 2,4-hexadienal or polymerized acetaldehyde due to the basicity of the surface. Crotonaldehyde was more likely to be reduced by ethanol to yield crotyl alcohol than desorbing, even at relatively high temperatures. DRIFTS study of crotyl alcohol further elucidated the nature of its interaction with the catalyst, where dissociative adsorption led to the deprotonation of the molecule and C-O bond scission to yield 1,3-BD. Altogether, the data presented unraveled a complex interplay between the surface hydroxyl groups, gaseous reactants and surface bound reactive intermediates of 1,3-BD formation.

Chapter 5

MgO/SiO_2 catalyst active surface sites were analyzed using *in situ* DRIFTS (using complementary DFT calculations), TPRS and steady state reactor in combination with bulk XRD and surface LEIS measurements. Combination of *in-situ* probing with CO_2 and pyridine and *in-situ* poisoning demonstrated the site requirement for the catalyst. In particular, it was determined that the weak basic sites were responsible for ethanol dehydrogenation, strong basic sites for aldol condensation and MPV reduction, while stronger acid sites catalyzed acetaldol and crotyl alcohol dehydration reactions and weak acid sites catalyzed the undesired ethanol dehydration. Furthermore, through a combination of NH_3-TPD and DFT the presence of *open* and *closed* LAS was identified while further elaborating Mg coordination, as adopted from LAS classification of zeolitic materials.[1–3] The MgSi-WK catalyst was shown to have both *open* LAS with both Mg_{3C} and Mg_{4C} as the anchoring LAS, and a very isolated *closed* LAS (Mg_{3C}).

Chapter 6

Cu- and Zn-promoted wet kneaded MgO/SiO_2 catalysts were interrogated *in situ* and *operando* and provided new insights into the structure and reactivity of their catalytic sites during ethanol reaction to 1,3-BD. *In-situ* UV-Vis revealed the presence of Cu^{2+} species with dimeric coordination, while for Zn-promoted MgO/SiO_2 catalyst, bulk ZnO phase and Zn-MgO solid solution were observed. Promotion with metals showed increases in weak basic sites, with Zn contributing to more Lewis acid sites that are responsible for the enhanced activity. *In-situ* DRIFT spectroscopy results allowed decoupling of the aldol condensation and dehydrogenation fundamental steps that took place on the surface suggesting that promoting the catalyst with transition metal promoters enhanced the ability of the catalyst to carry out aldol condensation as correlated with the steady state reactivity experiments. *In-situ* UV-Vis spectroscopy suggested appearance of π-π^* electronic transitions of allylic cations, cyclic or aromatic species on the catalysts while also providing insights on the oligomeric structure of the active sites. Our *operando* X-ray measurements were combined with *ab initio* multiple scattering modelling to unravel the exact electronic structure of the Cu and Zn promoters. Change in the local coordination of Cu indicates the presence of more than one Cu^{2+} species, with only one contributes to the reaction. This Cu^{2+} species was reduced to Cu^0 during reaction via a Cu species that was identified as a Cu species with reduced Cu-O coordination number. Zn-promotion, on the other hand, resulted in a very stable catalyst with stable Zn local coordination, barely changed during the reaction. However, this catalyst exhibited very high reactivity, which results in the formation of carbonaceous deposit that further deactivated the catalyst.

2. Future Outlook

The most important issue in the Lebedev reaction is to design a selective catalyst that possesses an optimum combination of redox, basic, and acid sites. The lack of suitable spectroscopic methods hampers comprehensive characterization of MgO/SiO_2 catalysts. Up until now, structure-activity relationship has not been achieved yet, with previous investigators can only indirectly correlate the amount of layered hydrous magnesium silicate phase to the 1,3-BD yield.[4] Work by Hayashi, *et al.* further proves that SiO_2 is not fundamentally required for this reaction, which suggests that more comprehensive characterization is necessary to directly correlate the molecular structure of the catalyst that actively catalyze the reaction.[5] The presence of both *open* and *closed* Lewis acid sites discovered in this work further open a new research pathway, where combination of spectroscopic method and probe molecules is necessary to unravel their participation during reaction. Further study to confirm the reaction mechanism is also important to further elucidate the need of specific active sites. Understanding the mechanism of this cascade reaction, combined with elucidation of the molecular structure of the catalyst will lead to a more rational design of the catalyst. In particular, the presence of water and acetaldehyde during the reaction needs to be investigated.[6,7]

This system is still on an early stage, with no consensus on which preparation method, Mg/Si ratio, optimum transition metal loading, and calcination temperature achieved. The synthesis parameter leads to different acidity and basicity of the catalyst, which suggests the need to optimize these parameters. Optimized parameters will lead to a superior catalyst with the best selectivity, and combined with knowledge of reaction mechanism, a kinetic rate expression can be modeled to engineer an appropriate reactive system.

References

(1) Harris, J. W.; Cordon, M. J.; Di Iorio, J. R.; Vega-Vila, J. C.; Ribeiro, F. H.; Gounder, R. *J. Catal.* **2016**, *335*, 141–154.

(2) Boronat, M.; Concepcion, P.; Corma, A.; Navarro, M. T.; Renz, M.; Valencia, S. *Phys. Chem. Chem. Phys.* **2009**, *11* (16), 2876–2884.

(3) Boronat, M.; Concepción, P.; Corma, A.; Renz, M.; Valencia, S. *J. Catal.* **2005**, *234* (1), 111–118.

(4) Chung, S.-H.; Angelici, C.; Hinterding, S. O. M.; Weingarth, M.; Baldus, M.; Houben, K.; Weckhuysen, B. M.; Bruijnincx, P. C. A. *ACS Catal.* **2016**, *6* (6), 4034–4045.

(5) Hayashi, Y.; Akiyama, S.; Miyaji, A.; Sekiguchi, Y.; Sakamoto, Y.; Shiga, A.; Koyama, T.; Motokura, K.; Baba, T. *Phys. Chem. Chem. Phys.* **2016**, *18* (36), 25191–25209.

(6) Velasquez Ochoa, J.; Bandinelli, C.; Vozniuk, O.; Chieregato, A.; Malmusi, A.; Recchi, C.; Cavani, F. *Green Chem.* **2016**, *18*, 1653–1663.

(7) Zhu, Q.; Wang, B.; Tan, T. *ACS Sustain. Chem. Eng.* **2017**, *5* (1), 722–733.

Curriculum Vitae

William E. Taifan

Address: 9 Duh Drive #131, Bethlehem, PA 18015
Phone: +1 510-219-0716; +62 812-1601-1180
Email: williamtaifan@gmail.com
Place of Birth: Surabaya, Jawa Timur, Indonesia
Date of Birth: September 25, 1991
Parents: Fantasi Pola and Ernie Gonawan

Experience

Research Assistant at Lehigh University

August 2014 – present

Ethanol-to-chemicals catalysis research. Presently focused in n-butanol and 1,3-butadiene synthesis, as well as ethanol as a hydrogenating agent for bio-oil. Side projects including CO_2 capture and theoretical work on oxidative coupling of methane (OCM) catalyst.

Intern at Chemisence, Inc.

February 2014 - June 2014 (5 months)

Research internship at an upcoming green tech startup in Silicon Valley. Research focused on developing chemical sensors based on carbon black conductivity and affinity with polymers.

Undergraduate Research Assistant at Biochemical Engineering Lab ITS

August 2012 - August 2013 (1 year 1 month)

Undergraduate research on separation and purification of an ester from a bio-oil.

Technical Expertise

- Matlab, Vienna Ab-initio Simulation Package (VASP) and Gaussian09
- Catalyst synthesis, testing and characterization
- Spectroscopy (IR, UV-Vis)
- GC, GC-MS

Academic Qualifications

Doctor of Philosophy (PhD) in Chemical Engineering

Lehigh University *2014-2018*

Dissertation Title:

Advisor: Professor Jonas Baltrusaitis

Master of Science in Chemical Engineering

University of California at Berkeley *2013-2014*

Bachelor of Engineering (with Honor)

Institut Teknologi Sepuluh Nopember Surabaya, Indonesia *2009-2013*

Publications

"Operando structure determination of Cu and Zn on supported MgO/SiO2 catalysts during ethanol conversion to 1,3-butadiene"
ACS Catalysis, submitted
Authors: William E. Taifan, Yuanyuan Li, John P. Baltrus, Anatoly I. Frenkel, Lihua Zhang and Jonas Baltrusaitis

"In-situ spectroscopic insights on the molecular structure of the MgO/SiO2 catalytic active site during ethanol conversion to 1,3-butadiene"
Journal of Physical Chemistry C, submitted
Authors: William Taifan and Jonas Baltrusaitis

"Surface chemistry of MgO/SiO2 catalysts during the ethanol catalytic conversion to 1,3-butadiene: in situ DRIFTS and DFT study"
Catalysis Science & Technology, 2017, 7(20), 4648-4668
Authors: William E. Taifan, George X. Yan, Jonas Baltrusaitis

"CH4 and H2S reforming to CH3SH and H2 catalyzed by metal promoted Mo6S8 cluster: a first-principles micro-kinetic study"
Catalysis Science & Technology, 2017, 7 (16), 3546-3554
Authors: William E. Taifan, Adam A. Arvidsson, Eric Nelson, Anders Hellman and Jonas Baltrusaitis

"Minireview: direct catalytic conversion of sour natural gas (CH 4+ H 2 S+ CO 2) components to high value chemicals and fuels"
Catalysis Science & Technology, 2017, 7 (14), 2919-2929
Authors: William E. Taifan and Jonas Baltrusaitis

"Catalytic conversion of ethanol to 1,3-butadiene on MgO: a comprehensive mechanism elucidation using DFT calculations"

Journal of Catalysis, 2017, 346, 78–91
Authors: William E. Taifan, Tomas Bucko, Jonas Baltrusaitis

"Surface chemistry of carbon dioxide revisited"
Surface Science Reports, 2016, 71 (4), 595-671
Authors: William E. Taifan, Jean-Francois Boily, Jonas Baltrusaitis

"CH4 conversion to value added products: Potential, limitations and extensions of a single step heterogeneous catalysis"
Applied Catalysis B: Environmental, 2016, 198, 525–547
Authors: William Taifan and Jonas Baltrusaitis

"Dairy wastewater for production of chelated biodegradable Zn micronutrient fertilizers"
ACS Sustainable Chemistry & Engineering, 2016, 4 (3), 1722-1727
Authors: Hanyu Zhang, Megan Frey, Criztel Navizaga, Courtney Lenzo, Julian Taborda, William Taifan, Abdolhamid Sadeghnejad, Alfredas Martynas Sviklas, Jonas Baltrusaitis

"Elucidation of ethanol to 1,3-butadiene reaction mechanism: Combined experimental and DFT study"
Conference paper at Energy and Fuel – Biomass, ACS 2016 Fall Meeting at Philadelphia
Conference paper at Catalysis and Reaction Engineering Division, AIChE 2016 annual meeting
Conference paper at North American Catalysis Society, 2017 annual meeting at Denver

Award and Honors

2016 Chevron Scholar Awards Lehigh Chemical Engineering
2017 Kokes Scholar Award – *North American Catalysis Society*
2017 John C. Chen Fellow – Lehigh University

Students Mentored (Past 4 Years)

- George X. Yan, B.S. Chemical Engineering, Lehigh University, Ph.D. Student, UCLA
- Paige Rockwell, B.S. Physics, Lycoming College
- Yiying Sheng, B.S. Chemical Engineering, Lehigh University